DESIGN AND PERFORMANCE OF COLD BENT GLASS

KYRIAKI DATSIOU

Department of Engineering

Lucy Cavendish College, University of Cambridge

November 2017

This dissertation is submitted for the degree of

Doctor of Philosophy

Φύσις κρύπτεσθαι φιλεί.

Ηράκλειτος / Heraclitus 535-475 BC

ACKNOWLEDGEMENTS

I would like to express my gratitude and appreciation to all individuals and organisations that made this thesis possible. Their contribution is gratefully acknowledged in this section.

I would sincerely like to thank my academic supervisor, Dr Mauro Overend for giving me the opportunity to undertake my doctoral studies under his supervision, at the University of Cambridge, for his guidance and support and encouragement in becoming an independent researcher. This PhD project would not have been the same without his valuable input.

I would also like to express my gratitude to the Engineering and Physical Sciences Research Council UK (EPSRC), Eckersley o'Callaghan, the Onassis Foundation and the Research Fund for Coal and Steel of the European Community for their financial support. Funding for attending and presenting my work at the Challenging Glass and Engineered Transparency conferences, from the Lucy Cavendish College and the Engineering Department of the University of Cambridge, is also thankfully acknowledged.

I am grateful to all past and current members of the Glass and Façade Technology Research Group, Marco Z., Isabelle, Fabio, Shelton, Belarmino, Caroline, Jacopo, Alessandra, Marco D., Carlos, Mark and Hanxiao for their direct and indirect contribution to my project and for creating a friendly environment that extended beyond the office walls. Special thanks goes to the technicians of the Structures and Materials laboratories and especially to Phil, Len, Martin, Lorna and Dave for their valuable help and the fun discussions during the experimental parts of this work.

I am thankful to team of Eckersley o'Callaghan and especially to James O'Callaghan, Peter Lenk and Graham Coult for sharing their expertise and providing technical support. I would also like to thank my academic advisor, Keith Seffen for his counsel during this project.

On a personal note, it is a pleasure to thank all my friends for the wonderful times we spent together in Cambridge and beyond. Special thanks goes to Eleni, Isabelle, Marilena, Carlo, Marco, Phil, Thanos, Dia, Eri and Fotini for their company and the enthusiasm they shared in making these last 4 years beautiful with travelling, hiking and climbing adventures.

I would also like to thank Vassilis for proofreading and for his love, patience and support, encouraging me through the stressful steps of this PhD journey.

Last but not least, I would like to thank my parents, Maria and Giorgos and my brother, Zacharias for their endless love and support all these years. I dedicate this dissertation to you.

Kyriaki Corinna Datsiou

April 2017, Cambridge

DECLARATION

The author wishes to declare that, except for commonly understood and accepted ideas, theories, and engineering principles, or where specific reference is made to the work of others, the content of this dissertation is her own work and includes nothing that is the outcome of work done in collaboration. General assistance received is stated in the Acknowledgements section.

This dissertation has not been submitted previously, in part or in whole, to any university or institution for any degree, diploma, or other certification. It does not exceed the word limit for the degree committee and contains approximately 64,251 words, 109 figures, 25 tables and 222 pages.

ABSTRACT

The demand for flat glass is high and increasing significantly. The building industry has by far the largest share of this market, and accounts for around 80% of all the flat glass produced. This increase is a direct result of the recent architectural requirements for additional lightness, transparency and natural light in new buildings. Current architectural trends increasingly require the use of glass in curvilinear forms to produce smooth free-form façades. Two principal challenges arise from this trend: (a) to produce the desired curvature in glass in a cost effective manner and; (b) to ensure its safe performance after exposure to ageing mechanisms.

The recent availability of high strength toughened glass (in the form of chemically toughened or heat treated glass) provides an opportunity to address the first challenge by developing cold bent glass surfaces. Cold bending of glass involves the straining of relatively thin glass components, (typically plates), at ambient temperatures, and is a low energy and cost effective manner of creating curvilinear forms. However, cold bending is not yet widely established as a reliable method for bending glass. The aim of this thesis is to develop the understanding of cold bent glass plates during the bending process and to evaluate their mechanical performance after ageing (to address the second challenge indicated above). In doing so, it is necessary to fill the gaps in the available knowledge as described in the next paragraphs.

This thesis, firstly, focuses on the experimental and numerical investigation of the mechanical response of monolithic glass plates during the cold bending process. The stability of heat treated and chemically toughened cold bent glass is investigated experimentally by bending the glass in double curved anticlastic shapes in order to identify local and global instability phenomena during the bending process. This is additionally investigated in a parametric numerical analysis that involves different boundary conditions, geometrical characteristics of the plate, load locations and plate orientation/initial imperfections. The principal outcome of this research is that a previously unreported local instability which is now termed cold bending distortion occurs when certain displacement limits are exceeded in the bending process. This instability could degrade the optical quality of cold bent glass as a function of the amplitude of the cold bending distortion. Nonetheless, the results shows that high optical quality cold bent glass can be achieved when certain applied displacement criteria are met during the design process. An optical quality evaluation procedure is formulated in this thesis to set limits and therefore, aid designers and manufacturers to predict the cold bending response and the resulting optical quality of the glass.

Cold bent glass is subjected to permanent bending stresses throughout its service life and therefore, its strength degradation after exposure to ageing mechanisms needs to be quantified carefully. The strength of annealed and fully toughened glass is obtained with destructive tests in

a conventional Coaxial Double Ring set-up. Experimental and numerical investigation is undertaken in this thesis to identify a novel set-up for the destructive testing of thin chemically toughened glass to avoid stress concentrations that arise when conventional destructive tests are used. Analytical investigation is additionally, undertaken to investigate the influence of sub-critical crack growth during the destructive tests, to identify the best goodness-of-fit yielding method for fitting glass strength data to a 2-parameter Weibull distribution and to determine the minimum number of specimens that are necessary to obtain reliable strength predictions.

However, the limited availability of naturally aged toughened glass and the absence of a reliable artificial ageing standard for glass impede the evaluation of its aged performance. Therefore, the investigation of artificial ageing methods (falling abrasive and scratching) on annealed glass is also undertaken in this thesis. The aim is to identify a method that could introduce equivalent levels of damage to that found in a single source of naturally aged annealed glass which was exposed to erosive action during its service life. An experimental parametric analysis is performed to identify the influence of different artificial ageing parameters on glass strength by means of optical microscopy, surface profilometry, destructive testing and fractographic analysis. A procedure for the evaluation of the strength of aged glass is finally, formulated to allow the selection of artificial ageing parameters that correspond to a target level of erosion.

The knowledge on artificial ageing and glass strength prediction acquired in the previous sections is finally implemented on different types of glass to determine their strength after ageing and assess their safe use in cold bending or other load bearing applications. Artificial ageing, destructive tests and fractographic analysis are therefore undertaken to evaluate the strength of aged fully (thermally) toughened, chemically toughened and annealed glass. The investigation evaluates the erosive resistance and the strength degradation in all types of glass showing that fully (thermally) toughened glass has a superior performance to chemically toughened or annealed glass.

Overall, the research presented in this thesis demonstrates that high quality cold bent toughened glass plates can be created when certain applied displacement limits are respected. These can be used as a safe, cost-effective and energy efficient replacement to the more conventional hot bent glass. However, cold bending and other similar load bearing applications in which the stressed glass surface is exposed to ageing, require glass with a relatively high case depth such as fully toughened or bi-tempered glass. Further research is however, needed to investigate the mechanical response of cold bent monolithic glass during its service life and cold bent laminated glass and cold bent insulated glass units during their production and when subjected to transient service life loads.

CONTENTS

LIST OF FIGURES

LIST OF TABLES

NOMENCLATURE

Greek characters:

α: flaw depth; α_i: initial depth; α_f: final depth; α_{TH}: crack growth threshold depth; α_r: radial/median crack depth and; α_{ef}: depth w/o radial / median cracks

β: shape factor of the 2-parameter Weibull distribution

Γ: Gaussian curvature

γ: safety factor

$\delta_{AC,z}$: applied displacement on each of each free corner during the cold bending

δ_{dist}: applied displacement limit on each of the free corner that triggers cold bending distortion

δ_E: deflection at the centre of the plate

E: Young's modulus

ε: strain and; ε_{pl}: plastic strain beyond the yield point

θ: scale factor of the 2-parameter Weibull distribution

κ: curvature and; κ_{edge}: curvature of the plate's edge

λ: significance level for Weibull distribution

M_r: sample moments in *MME*

$\overline{\mu}$: mean of the distribution

μ'_r: raw moments in *MME*

μ_r: central moments in *MME*

ν: Poisson's ratio

σ_{cb}: permanent stress arising from the cold bending process

σ_f: failure stress ($\sigma_{f,0.008}$: design strength for P_f=0.008 and $\sigma_{f,0.50}$: mean strength for P_f=0.50)

$\sigma_{f,eq}$: equivalent failure stress for reference time

$\sigma_{t,max}$: maximum tensile stress

σ_r: residual surface compression

σ_u: location parameter of the 3-parameter Weibull distribution

φ: parametric angle at the flaw boundary

Φ: cumulative distribution function for the normal distribution

Latin characters:

A: area of the flaw perpendicular to the opening stress

A_{dist}: amplitude of the cold bending distortion

B: width of confidence interval for the Weibull distribution

c: half of the flaw width

CV: coefficient of variance

D_L: diameter of loading ring in CDR test

D_R: diameter of reaction ring in CDR test

d_c: case depth of residual surface compression in toughened glasses

E_i: probability estimator

F_n: empirical distribution function

G: shear modulus

$f_{AN,d}$: design strength of annealed glass

h: thickness of specimen

H: drop height in falling abrasive method

$K_{I\text{-}III}$: stress intensity factors for crack propagation modes I-III

K_{IC}: fracture toughness

K_{TH}: stress intensity factor at crack growth threshold

k: sample size

k_n: un-biasing constant in the *GLUE*s method

L: likelihood function

m: mass of abrasive medium

n: static fatigue constant

P: applied load

P_f: probability of failure

p: percentage of gravel (%) in abrasive medium

p_{AD}: observed significance level for the Anderson Darling goodness-of-fit

R: radius of curvature

R_a: average surface roughness

s: largest integer of $0.84k$ in the *GLUEs* method

t_c: curing time after artificial ageing

t_{IN}: the time limit between inert conditions and the commencement of sub-critical crack growth

t_f: time to failure

t_r: the time when the applied tensile stress is equal to the residual surface compression

t_{ref}: reference time for equivalent failure stress

t_{TH}: crack growth threshold time limit

T: temperature (T_g: transition temperature and T_m: melting temperature)

v_0: crack velocity

W: weight function of the *WLR* method

w_{AD}: weight function for the Anderson Darling goodness-of-fit

Y: geometry factor of critical flaw; $Y_{LEFM:}$ linear elastic fracture mechanics computation (Y_{SCG}: during sub-critical crack growth and Y_{IN}: during inert conditions); Y_{MUR}: Murakami model and; Y_{NR}: Newman-Raju model

ABBREVIATIONS

AD: Anderson Darling goodness-of-fit
ALS: Alumino-silicate
AN: Annealed Glass
AR: Aspect ratio
CS: Clamped Supports
CTG: Chemically Toughened Glass
CDF: Cumulative Distribution Function
CDR: Coaxial Double Ring
EDF: Empirical Distribution Function
FEA: Finite Element Analysis
FTG: Fully Toughened Glass
F&T: Faucher and Tyson's weight function
*GLUE*s: Good Linear Unbiased Estimators
GSR: Grain size range of abrasive medium
IGU: Insulated Glass Unit
LEFM: Linear Elastic Fracture Mechanics
LP: Load Points
LR: Length ratio (Chapter 3)
LR: Least Square Regression (Chapter 4)
MLE: Maximum Likelihood Estimation
MME: Method of Moments Estimation
MGS: Maximum grain size of abrasive medium
NA: Naturally Aged Glass
PS: Pin Supports
PVB: Poly Vinyl Butyral
RH: Relative Humidity
RR: Rotation Rate in falling abrasive set-up
RS: Roller Supports
SA: Sand Abraded
SC: Scratched
SCALP: Scattered Light Polariscope
SCG: Sub-critical crack growth
SGP: Sentry Glass Plus ©
SLS: Soda lime silica
TDF: Theoretical Distribution Function
WLR: Weighted Least Square Regression

1. INTRODUCTION

Glass is one of the oldest materials in the building industry as a result of its transparent nature which presents a twofold advantage of introducing natural day light in buildings and increasing their aesthetic appeal and levels of indoor comfort. However, the surface flaws that inevitably accumulate during its service life lead to a significant reduction in the intrinsic tensile strength of glass. For this reason, the use of glass was traditionally confided to infill/fenestration applications where relatively small stresses (e.g. self-weight, wind loads) are expected during their service life.

However, the role of glass in the building industry has evolved over the last decades from functional and decorative to structural as a result of technological improvements in glass processing methods; high strength / toughened glass (chemically toughened or heat treated) is produced by introducing a thin layer of residual compression on the surface of glass. The surface compression increases its tensile capacity because surface flaws cannot grow and induce fracture unless the surface compression is exceeded. Therefore, the use of glass expanded to other structural applications where higher stresses than those typical induced on infill plates, need to be borne. Such applications involve staircases, canopies, beams, floors etc. (Fig. 1.1).

(a) (b)

Fig. 1.1: Structural glass: (a) glass floor (Cologne airport) and; (b) glass staircase (Shanghai Apple IFC, ©EOC).

In addition to the requirements for durable, high-strength glass, the recent architectural trends require free form geometries and curvature in glass (Fig. 1.2). The production of curved glass so far has been predominantly based on heating the glass above its transition temperature and subsequently bending it in shape. However, heat bending methods are usually energy intensive and costly whilst the optical quality of the final product is a function of the quality of the mould or the rollers used during the bending process. Therefore, the new challenges that emerge in load bearing curved glass are: (a) to reduce manufacturing costs and energy; (b) to ensure good optical quality of the curved glass plate and; (c) to ensure its strength after exposure to ageing mechanisms.

Fig. 1.2: Curved façade in Oxford Street (London).

Cold bending of glass is an alternative and relatively recent method that has the potential to address these challenges. Cold bending introduces a controlled amount of strain and associated stress in flat glass at ambient temperatures to create the desired curved shape (Fig. 1.3). Glass is therefore, elastically bent to suit and subsequently fixed in a frame or substrate with mechanical fixings or structural adhesives. Toughened glass (chemically toughened or heat treated glass) is typically used in such applications to successfully withstand the permanent stress arising from the cold bending process. However, instabilities could be triggered during the bending process or its service life as a result of the high slenderness of the glass elements. These instabilities could create additional serviceability and/or limit state limits causing a detrimental effect on the shape and the optical quality of the cold bent glass and/or even trigger failure of the curved glass. Therefore, the stability of cold bent glass needs to be investigated to ensure its safe and functional performance.

However, there is limited knowledge on the strength of all forms of aged glass, particularly on toughened / chemically toughened glasses. This is an important limitation as the case depth of the residual surface compression is relatively small compared to the total thickness of the toughened glass. Therefore, the surface flaws that will inevitably accumulate during the service

life of the glass, if deep enough, will reduce the favourable effect of the residual surface compression. Therefore, the need to evaluate the strength of aged toughened glass has arisen.

The availability of high strength glass in the form of heat treated or chemically toughened glass presents an unprecedented opportunity to create novel cold bent glass units and reduce production costs and energy for curved glass. This will be possible when the strength of aged toughened glass and the stability and the optical quality of the cold bent glass units are ensured. Due to their form and lightweight nature, these glass units, will have the potential to be applied in the architectural, automotive and aerospace industries.

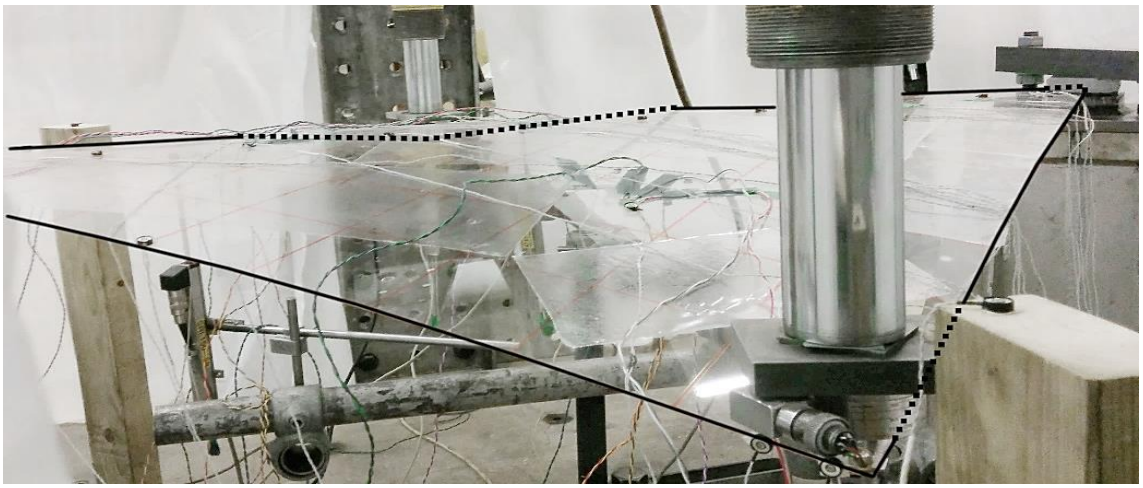

Fig. 1.3: Cold bending of glass plate.

2. Flat & Curved Glass: State of the Art

2.1 Introduction

The demand for glass plates is high and increasing significantly; since 2009 float glass production has increased by 5% per annum to meet this demand. The building industry has by far the largest share of this market, and accounts for around 80% of all the flat glass produced [1]. This increase is a direct result of the recent architectural requirements for additional lightness, transparency and natural light in new buildings, leading to an increased demand for larger glass plates. In addition, architectural trends increasingly require the use of glass in curvilinear forms to produce smooth free-form facades [2]. The use of curved glass in such applications has a twofold advantage: (i) to enable complex architectural ideas and; (ii) to improve the structural behaviour of the glass panel with respect to that of flat glass; curvature leads to an increase in stiffness which enables the activation of membrane stresses and thereby improves its structural efficiency.

However, challenges arise during the design, construction and service life of free form façades in order to form the curved glass plate in a cost effective manner, to ensure its geometric stability and optical quality and its aged mechanical performance. Chapter 2 (Fig. 2.1) focuses on the main components of available knowledge (glass types and properties, curved glass, glass strength and aged performance) that can be used to address these challenges, revealing gaps in knowledge that will be addressed in the subsequent chapters. Finally, Section 2.8 presents the aims of this thesis.

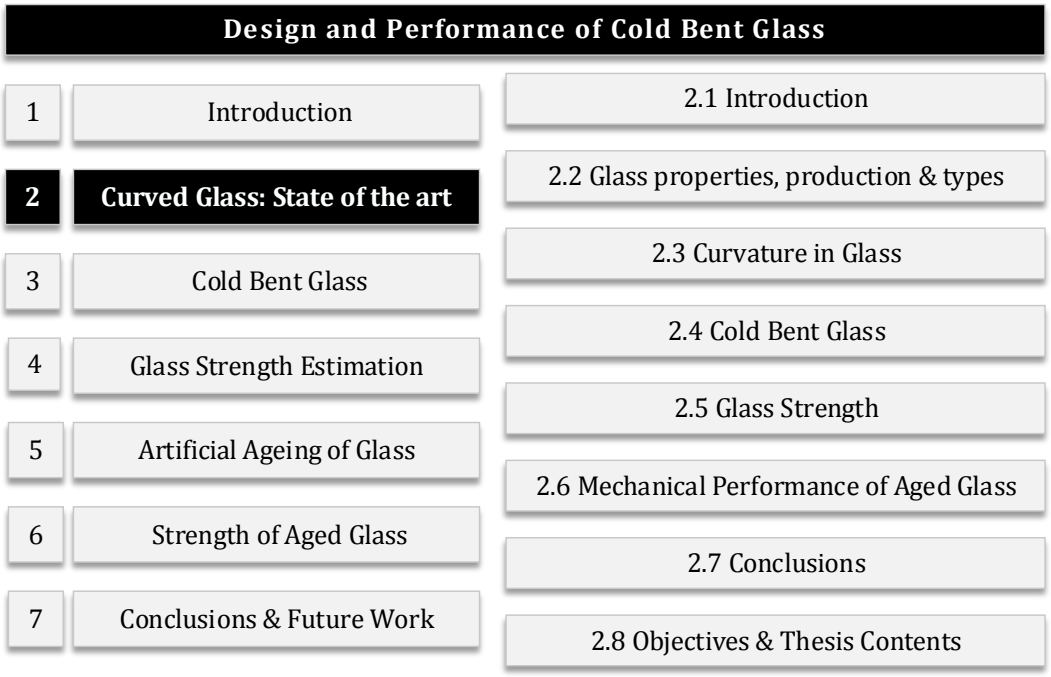

Fig. 2.1: Contents of Chapter 2.

2.2. Glass: properties, production and types

2.2.1 Glass properties

Glass is an inorganic and non-crystalline solid i.e. glass lacks the ordered, three dimensional molecular network of repeating structures that are traditionally found in crystalline solids, but instead comprises an amorphous molecular network without any particular order.

Glass properties depend on its chemical composition and temperature. Dissimilar to crystalline solids that solidify instantaneously once cooled below their melting temperature (T_m), glass undergoes a transition phase that comprises the following steps (Fig. 2.2):

(a) $T_m > T > T_1$: glass is transformed to a super cooled liquid during cooling i.e. its viscosity increases but the molecules are still able to rearrange their position and achieve the equilibrium liquid structure;

(b) $T_1 > T > T_2$: the viscosity of glass increases considerably; this hinders the movement of the molecules compared to stage (a), resulting in longer durations for achieving equilibrium and;

(c) $T_2 > T$: the viscosity increases so much that the position of the molecules is considered fixed and therefore, the molecular structure is now independent of the temperature.

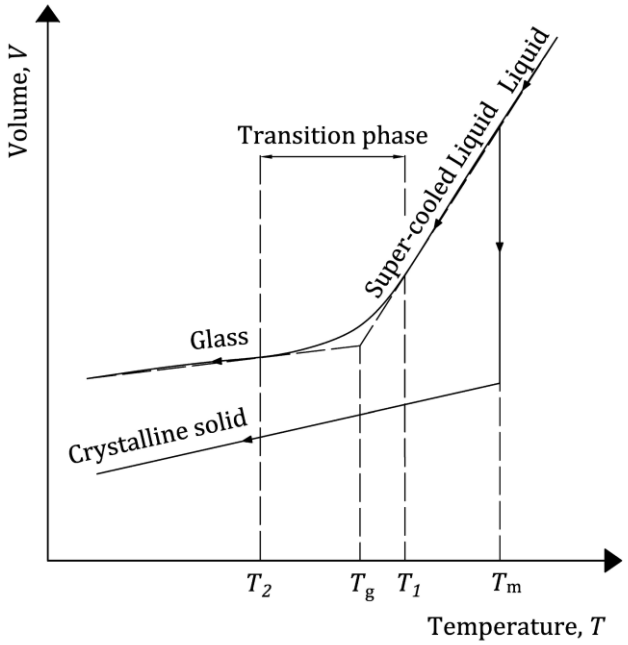

Fig. 2.2: Glass transition phase.

Temperatures T_1 and T_2 set the limits for the transition phase. In particular, the transition temperature T_g is defined as the intersection temperature between the lines describing the super-cooled liquid state and the glass state. The transition temperature is a function of the composition

of glass. Soda lime silica glass (SLS) is the most commonly used glass in the building industry. The molecular structure of SLS glass (Fig. 2.3a) comprises a 3d network of network-formers and network-modifiers. The strength of glass is attributed to silicon (Si^{4+}) which acts as the network former and creates strong, covalent bonds with oxygen anions (O^{2-}) in tetrahedral formation. Alkali oxides (in this case sodium Na_2O) are introduced in the glass to change its physical properties (hardness, workability, thermal expansion, density etc.) and act as network modifiers. Alkalis break the glass network and form metallic bonds with oxygen anions.

High strength / chemically toughened glass of alkali alumino-silicate composition (ALS) is also available. In this case aluminium (Al^{3+}) replaces silicon in molecular network acting as a network modifier and a network former. However, the Al-O tetrahedron has a valence of -1 and therefore, another cation (alkali) is needed to achieve neutrality. An example of an ALS molecular structure is given in Fig. 2.3b, however, this only applies when the number of Al-O tetrahedral is equal to the number of alkali cations. More information on the molecular structure of ALS glass can be found in [3–5]. Table 2.1 summarizes some of the physical properties for SLS and ALS glasses.

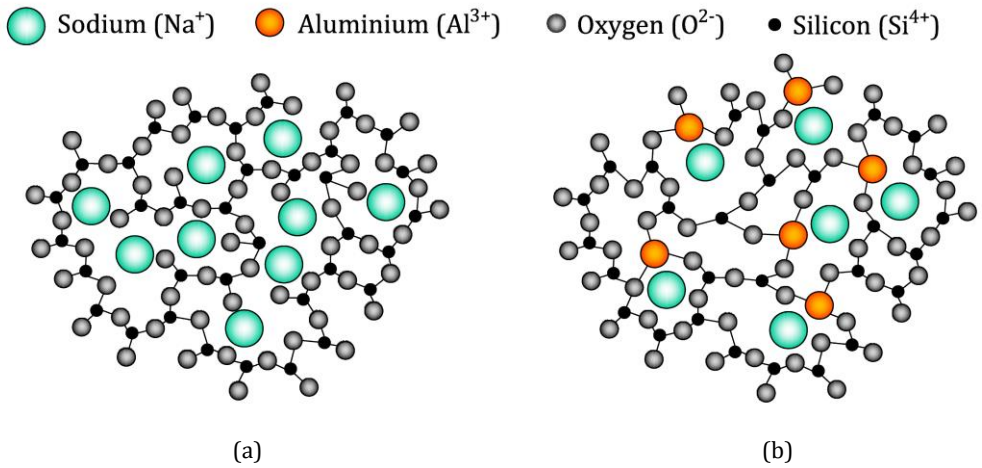

Fig. 2.3: Molecular structure for: (a) SLS glass and; (b) ALS glass (additional oxygens exist in 3d space forming covalent bonds with each silicon and aluminium).

Table 2.1: SLS and ALS glass properties [3,6–10].

Property	Abbr.	Soda lime silica glass	Alkali-alumino-silicate glass
Transition temperature	T_g	550-600°C	720-790°C
Annealing temperature	T_a	520-600°C	710°C
Melting temperature	T_m	1500°C	1600°C
Young's modulus	E	70 GPa	70-90 GPa
Poisson's ratio	ν	0.2-0.25	0.2-0.25
Density	ρ	2500 kg/m^3	2300-2600 kg/m^3
Fracture toughness	K_{IC}	0.72-0.82 MPa·m$^{1/2}$	0.96 MPa·m$^{1/2}$

2.2.2 Glass production

The float process was developed by Pilkington in 1959 [11]. The process (Fig. 2.4a) involves melting of raw materials (sand, limestone, sodium carbonate, dolomite, iron oxide and sodium sulphate etc.) and glass cullet in a furnace at a temperature T_m=1500 ^{0}C. The molten glass is then allowed to flow on a bath of molten tin at a temperature of 1100 ^{0}C, creating a flat surface. Tin is chosen due to its higher specific gravity with respect to glass. A solid ribbon of glass of even thickness exits the tin bath drawn by rollers [3]. The thickness of the glass is a function of the speed of the flow and the speed of rollers. The glass sheet is then transferred into an annealing lehr where the glass is gradually cooled (from the annealing temperature T_a=600°C, i.e. the temperature at which the internal stresses are relieved in a matter of a few minutes, to T=100°C) to relieve residual stresses. The surface quality glass is then inspected before being cut to size.

The Fusion Downdraw process (Fig. 2.4b) is another glass production process which was first introduced by Dockerty in 1967 [12]. The main difference with the float process is that glass is produced in a vertical configuration. The molten glass (1500°C) is fed in a V-shaped trough; when the through is filled, molten glass is allowed to overflow over the edges of the trough at a uniform rate. The two overflowing streams of glass fuse at the end of the trough to form a single sheet of glass. The glass is drawn downwards by rollers and is then transferred to an annealing lehr (600°C) to remove residual stresses before being cut. This process offers higher surface quality than the float process because the glass avoids contact during its production with any other material that could potentially introduce flaws on its surface (e.g. contact with tin in the float process). This method is mostly used for the production of thin glass (100 μm < h <15 mm) as a uniform thickness is easier to achieve.

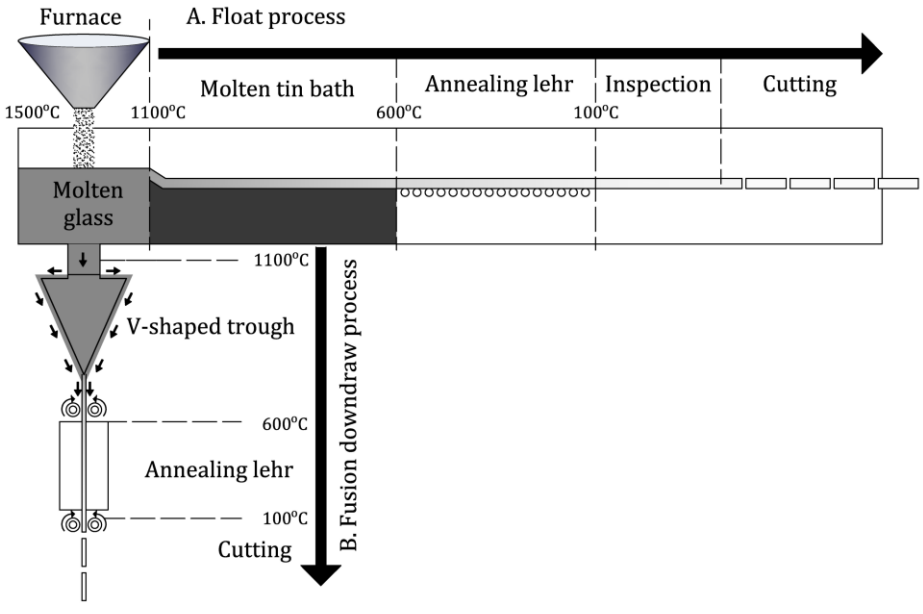

Fig. 2.4 Glass production: (a) Float process and; (b) Fusion Downdraw process.

2.2.3 Types of glass

Annealed glass

Annealed glass (*AN*) is float glass that has been gradually cooled in the annealing lehr to minimize residual stresses in the glass. Annealed glass does not undergo any further treatment and its fracture pattern consists of large fragments (Fig. 2.6a).

Toughened glass

High strength glass is produced with a toughening process that introduces an advantageous stress profile through the thickness of the glass, which is characterized by tensile stress in the core of the glass and compressive stress in the outer surfaces (Fig. 2.5). Flaws situated on the outer surface of the glass do not grow or initiate fracture when in compression i.e. when the flaw depth does not exceed the case depth, d_c i.e. the depth of the compressive layer. Flaws are not usually expected in the glass core (apart from nickel sulphide inclusions - refer to fully toughened glass below) and therefore, the core tensile stresses do not initiate fracture. Apart from the protective layer of residual surface compression in toughened glasses, their increased strength is also partially attributed to the thermal healing of flaws on the surface of glass during the toughening process [13] and the increased resistance (erosive or scratching) to the induction of flaws (shown in Section 6.4.3).

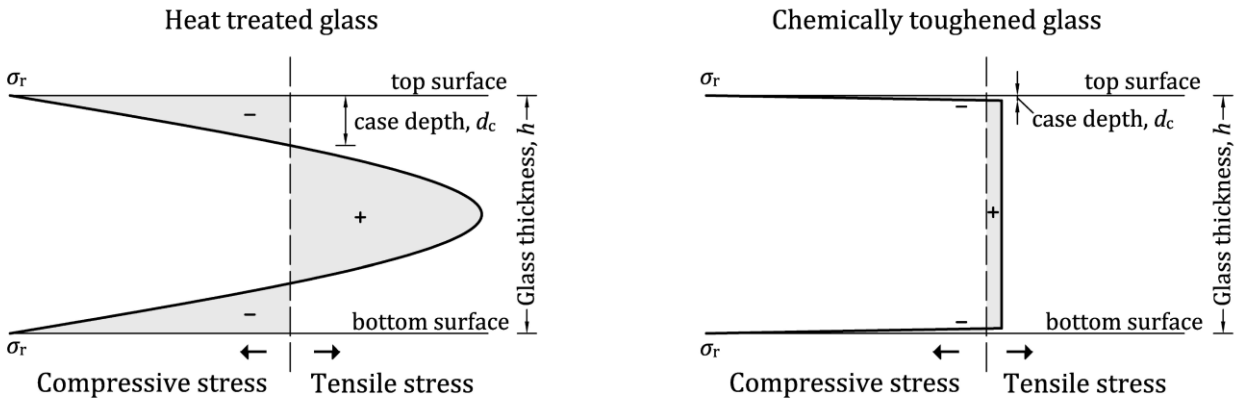

Fig. 2.5: Residual stress profiles for: (a) heat treated and; (b) fully toughened glass.

Heat treated glass

Heat treated glass is typically soda lime silica glass, produced by heating the glass above its transition temperature followed by rapid cooling with jets of cold air. Hence, the external faces of the glass solidify with a faster rate than the glass core leading to shrinkage of the outer layer and introduction of a parabolic residual stress profile through the thickness of the glass (Fig. 2.5a,

detailed description of the physical interpretation of the process is available in [14,15]). The residual surface compression is a function of the cooling rate which defines the type of glass: fully toughened glass and heat strengthened glass.

Fully toughened glass

High cooling rates are used for fully toughened (*FT*) glass, achieving a surface compression of the order of $69 \leq \sigma_r \leq 170$ MPa [8] while σ_r=120 MPa is set in EN12150-1[16]. The minimum requirement for fully toughened glass, prescribed in ASTM C1048-12 [17], is σ_r=69 MPa and $\sigma_{r,ed}$=67 MPa for surface and edge compression respectively. The case depth, d_c, i.e. the depth of compressive layer (Fig. 2.5a) for fully toughened glass, is about 20% of the glass thickness [18].

Fully toughened glass is also known as safety glass, as it fractures into small, relatively harmless fragments (1 x 1 cm), the edges of which are rounded (Fig. 2.6b). However, failures in fully toughened glass can still pose a risk of human injury e.g. when used in overhead glazing. The number of fragments in the standard test area (fragment density) depends on the degree of toughening; during fracture part of the stored elastic energy is converted into surface energy of the newly formed surfaces and thereby, higher degrees of toughening and stored energy result in higher number of fragments.

Fully toughened glass may experience spontaneous failure due to nickel sulphide inclusions in the glass mass. Nickel sulphide inclusions can undergo a phase change under temperature increase which causes volumetric expansion; the combination of this expansion with the residual tensile stress in the glass core can lead to spontaneous fracture. Destructive quality assurance tests, called heat soak tests, are performed for this reason to reduce the possibility of nickel sulphide failures by slowly heating the fully toughened glass and then maintaining the temperature for several hours [19].

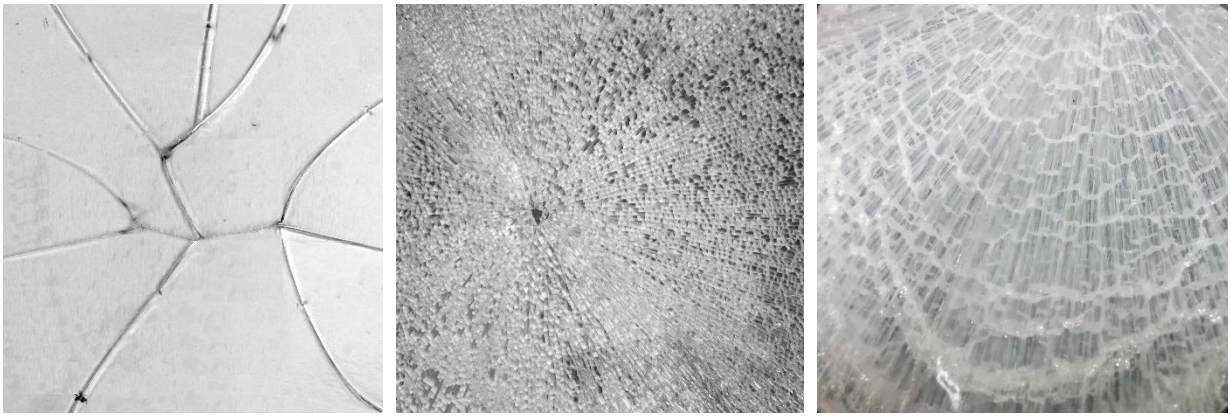

(a) (b) (c)

Fig. 2.6: Fracture pattern of: (a) annealed; (b) fully toughened and; (c) chemically toughened glass (subjected to high loads).

Heat strengthened glass

Heat strengthened glass is quenched with lower cooling rates than those used for fully toughened glass thereby, resulting in lower levels of surface compression. Typical values of surface compression range between $40 \leq \sigma_r \leq 80$ MPa [8] or $24 \leq \sigma_r \leq 52$ MPa as prescribed in ASTM C1048-12 [17]. Heat strengthened glass breaks in larger fragments than fully toughened glass due to the lower levels of stored elastic energy, while its fragments are smaller with respect to those of annealed glass (Fig. 2.6).

Chemically toughened glass

Chemical toughening of glass involves a process of ion exchange between the alkali of the glass surface and those of a bath of molten alkali salt and can be performed in both soda-lime-silica and alumino-silicate glasses given that a sufficient amount of alkali is present. High temperatures facilitate the diffusion process during which volumetrically larger alkalis replace volumetrically smaller alkalis of the glass surface (e.g. sodium/potassium to replace lithium or potassium to replace sodium), creating compression in the outer surface of the glass (Fig. 2.5b, [20]). The case depth and surface compression depends on the temperature of the molten bath (which typically ranges between 350-470°C), the duration of the ion exchange process (which typically ranges between 1-12 hrs) and the composition of the glass. High temperatures, high alumina content and long durations increase the ion diffusion rate [21–23]. However, as the temperature increases close to the level of the glass transition temperature (T_g=550°C), stress relaxation occurs and the surface compression can be significantly reduced [24,25]. The case depth for chemically toughened glass (CTG) is significantly smaller than that of heat treated glass whilst its surface compression is significantly higher. Case depths of about $40 \leq d_c \leq 90$ μm and surface compression of about $350 \leq \sigma_r \leq 500$ MPa are usually found in chemically toughened soda lime silica glasses [21,26,27] while larger case depths of the order of 50 μm $\leq d_c \leq$ 1 mm and surface compression of $300 \leq \sigma_r \leq 1000$ MPa are found in chemically toughened alkali alumino-silicate glasses [26]. The fragmentation pattern of chemically toughened glass consists of a small number of fairly large and sharp fragments as those in annealed glass. However, the fragment density is a function of the energy required to cause failure. Therefore, high strength chemically toughened glass with high surface quality can fracture into a large number of small sharp fragments e.g. Fig. 2.6c.

Bi-tempered glass

The advantageous properties of the high residual surface compression in chemically toughened glasses and the large case depth and the safe fragmentation pattern of fully toughened glasses can be combined in bi-tempered glass [28]. Bi-tempered glass is a novel type of glass which is developed by thermal toughening followed by chemical toughening of the glass.

Laminated glass

The post fracture performance of glass is improved by bonding glass panes together with interlayers that hold the glass fragments upon fracture. Lamination is typically achieved in an autoclave at a temperature of approximately 140°C. The most commonly used interlayers are Poly Vinyl Butyral (PVB), a soft co-polymer and Sentry Glass Plus (SGP), an ionoplast interlayer. SGP exhibits a stronger and stiffer response with respect to PVB. *T*he tensile strength is 20 MPa for PVB and 34.5 MPa for SGP while the elongation at failure is 300% for PVB and 400% for SGP at room temperature [8]). Ethylene Vinyl Acetate (EVA) is a less common interlayer, but popular for photovoltaic panels, since it does not require lamination in an autoclave which would damage the solar cells.

Interlayers are viscoelastic materials, i.e. their properties are temperature and time dependent. Fig. 2.7 shows the time and temperature dependency for the shear modulus, *G*, of *SGP*, based on the experimental data in [29].

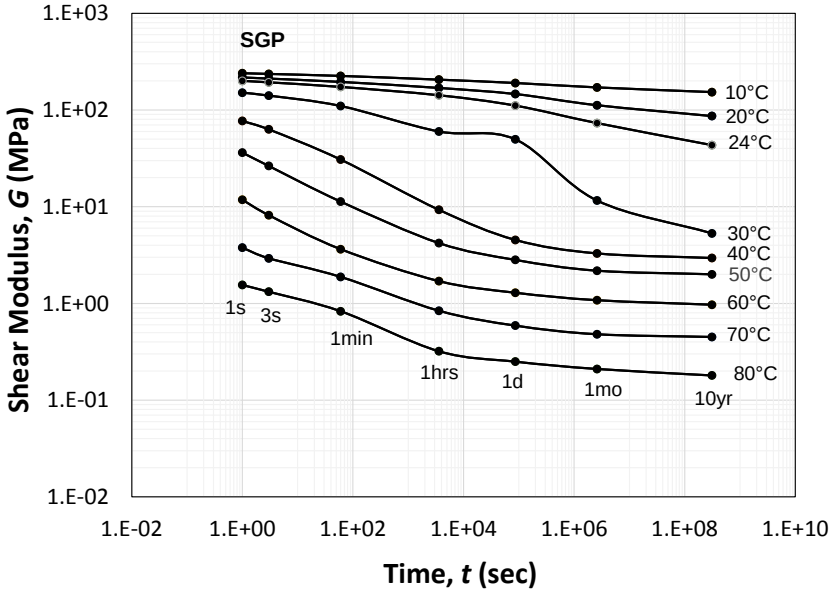

Fig. 2.7: Master curve for SGP (data found in [29]*).*

The flexural response of laminated glass depends on the level of shear coupling between the interlayer and the glass plates. Therefore, its mechanical behaviour lies between two bounds or configurations [30]:

(a) a layered configuration (Fig. 2.8a, $G \rightarrow 0$) where the system responds as an un-bonded unit with the glass plates free to slide on top of one another and;

(b) a monolithic configuration (Fig. 2.8 b, $G_{int}=G_{glass}$) where shear coupling is fully achieved between the interlayer and the glass so that the unit responds in a similar way to monolithic glass with a thickness equal to that of the laminated unit.

Even though the shear modulus of the interlayer is significantly lower than that of glass, some shear coupling is expected between the glass plates and the interlayer. Therefore, the response of the system is in-between the layered and the monolithic configuration (Fig. 2.8c) and depends strongly on the load duration and the temperature [31,32]; a close to monolithic response is expected for short load durations and/or low temperatures while a close to layered response for long load durations and/or high temperatures.

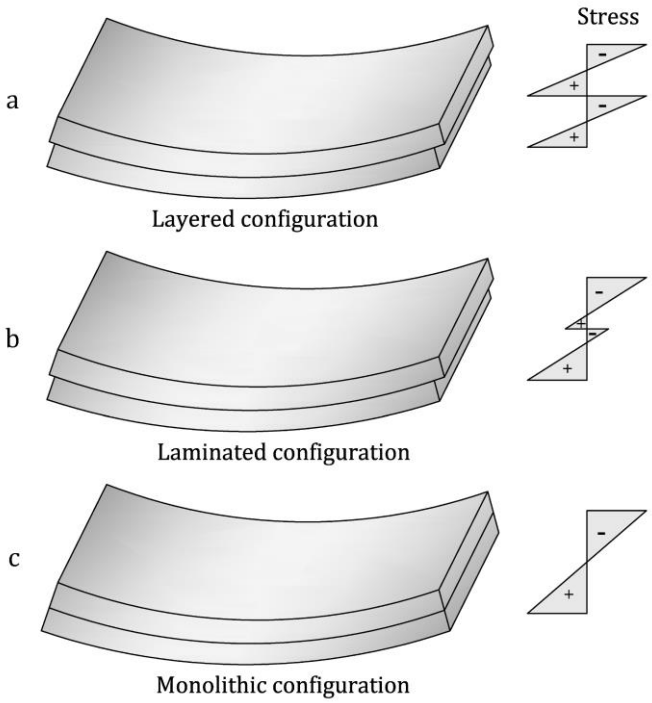

Fig. 2.8: Stress profile for the: (a) layered; (b) monolithic and; (c) laminated configuration (interlayer not shown due to its small thickness).

Two approaches commonly describe the response of the interlayer:

(a) the interlayer is considered as a linear elastic material with properties that correspond to a specific set of load duration and temperature. This approach is followed in ASTM E1300-12 [33] and prEN16612 [34] where a shear transfer coefficient and an effective thickness need to be calculated in order to transform the laminated unit in a monolithic configuration. The effective thickness approach is generally thought to provide more conservative results, however, there are cases e.g. a corner supported plate, where results are underestimated and are thereby, considered unsafe [35]. An enhanced effective thickness approach has been also proposed in Galuppi and Royer-Carfagni (2012, [35]) to be used in statically indeterminate systems.

(b) rheological models can also be used to describe the viscoelastic response of the interlayer. The generalised Maxwell model (Fig. 2.9) is perhaps the most common [36,37], connecting in parallel a hookean spring and multiple Maxwell elements which in turn are series of a hookean

spring and a Newtonian dashpot. Prony series (Eq. 2.1) are used in this case to describe the shear modulus of the interlayer:

$$G(t) = G_{\infty} + \sum_{i=1}^{n} G_i \cdot e^{-t/\tau_i} \qquad \text{(Eq. 2.1a)}$$

$$G_0 = G_{\infty} + \sum_{i=1}^{n} G_i \qquad \text{(Eq. 2.1b)}$$

where G_∞: the long term shear modulus (t→∞), G_i: the shear modulus of a Maxwell element, τ_i: the relaxation time of the dashpot of the Maxwell element, $\tau_i = \eta_i / G_i$ where η_i: the dashpot viscosity and; G_0: the instantaneous or glassy shear modulus (t=0).

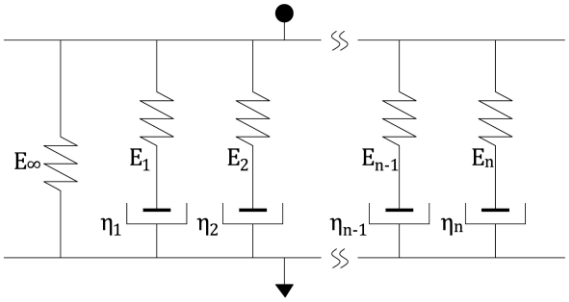

Fig. 2.9: Generalised Maxwell model.

These two methods can been used for the analysis of simple systems for which an analytical solution is available (for a given geometry, load case and boundary conditions) e.g. [35,36,38–40]. However, finite element modelling is typically preferred in complex cases where analytical solutions are difficult to obtain. The laminated unit can be numerically modelled: (a) as a composite unit with a viscoelastic interlayer whose material properties are described by Prony series [41,42]; (b) a composite unit with an elastic interlayer that corresponds to specific load durations and temperature [43,44] and; (c) an equivalent monolithic glass unit using the effective thickness approach [45].

2.3 Curvature in Glass

2.3.1 Introduction

Curvature indicates the deviation from flatness i.e. the deviation from a straight line for a 2D curve or a flat plane for a 3D surface. For a 2D plane, curvature can be expressed with an arc (Fig. 2.10); let M and M_1 be two points on the arc and *ds:* the length of arc between them. The curve between these points can be approximated by fitting a unique circle for M_1 and M_2; the intersection point O, of the 2 perpendicular lines to the tangent lines at M and M_1 denotes the centre of this circle

which is also known as the centre of curvature while *OM* and OM_1 are the radii of curvature, *R* (Eq. 2.2a). Curvature is defined as the inverse of the radius of curvature (Eq. 2.2b).

$$R = \frac{ds}{d\phi} \quad \text{and} \quad \kappa = \frac{1}{R} \qquad \text{(Eq. 2.2a-b)}$$

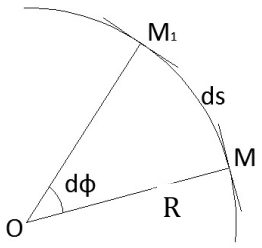

Fig. 2.10: Radius of curvature for a 2D arc.

However, for 3D surfaces, there is an infinite number of possible radii of curvature that may be obtained for each point of the surface as there is an infinite number of normal lines that can be drawn from that point. The maximum and minimum values of the radii of curvature correspond to the principal radii of curvature (R_1, R_2) while their inverses provide the principal curvatures for that point (κ_1, κ_2 respectively). The product of the two principal curvatures gives the Gaussian curvature of a 3D surface at that point (Eq. 2.3).

$$\Gamma = \kappa_1 \cdot \kappa_2 \qquad \text{(Eq. 2.3)}$$

The Gaussian curvature is used to classify surfaces in single and double curved. Single curvature characterizes all developable forms that are created through uniaxial bending of a planar surface and has zero Gaussian curvature (Fig. 2.11a). Typical examples of single curved surfaces are cylinders, cones and developable surfaces.

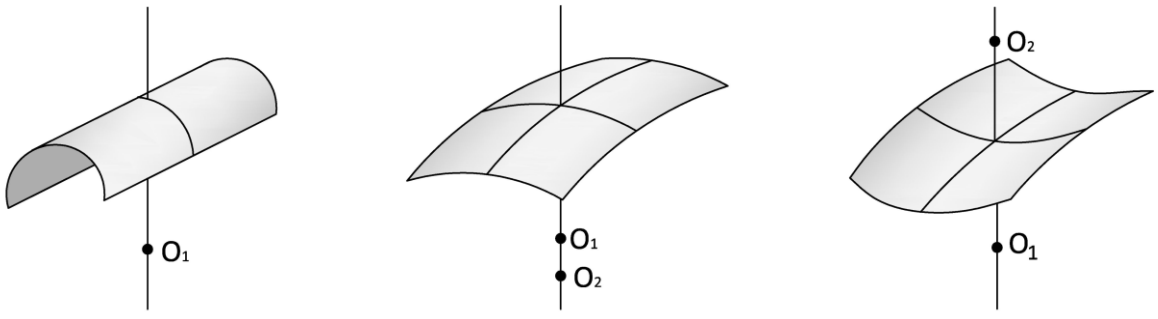

(a) (b) (c)

Fig. 2.11: Curved surfaces: (a) Single curved, (b): Double curved synclastic, (c): Double curved anticlastic.

Double curved surfaces are formed by bending about two axes and are divided in synclastic and anticlastic. The principal curvatures are of the same sign in synclastic surfaces (e.g. paraboloid geometry) i.e. both centres of principal curvatures are located on the same side of the surface and

their Gaussian curvature is positive ($\Gamma > 0$, Fig. 2.11b). Whereas in anticlastic surfaces (e.g. hyperparaboloid geometry) the centres of principal curvatures are on alternate sides of the surface and thereby, their Gaussian curvature is negative ($\Gamma < 0$, Fig. 2.11c).

Free form façades consist of free form surfaces that can be mapped with parameter lines to support the spatial impression of the surface and to divide the surface in smaller sections of known curvature (single or double curved) [46].

2.3.2 Curved glass technologies

The processes available for producing curved glass can be divided in two categories based on whether heat is involved in the process: hot bending and cold bending. The bending method has a significant influence on its optical quality, the ability to process it further after the bending (e.g. lamination) and the dimensions of the final product.

Static mould bending

Static mould bending (also known as sag bending) involves heating the glass plate above the transition temperature (T > 550°C), so that it becomes viscous. Consequently, the desired curvature is obtained by allowing the heated flat plate to sag under its self-weight, onto a concave or convex mould (Fig. 2.12).

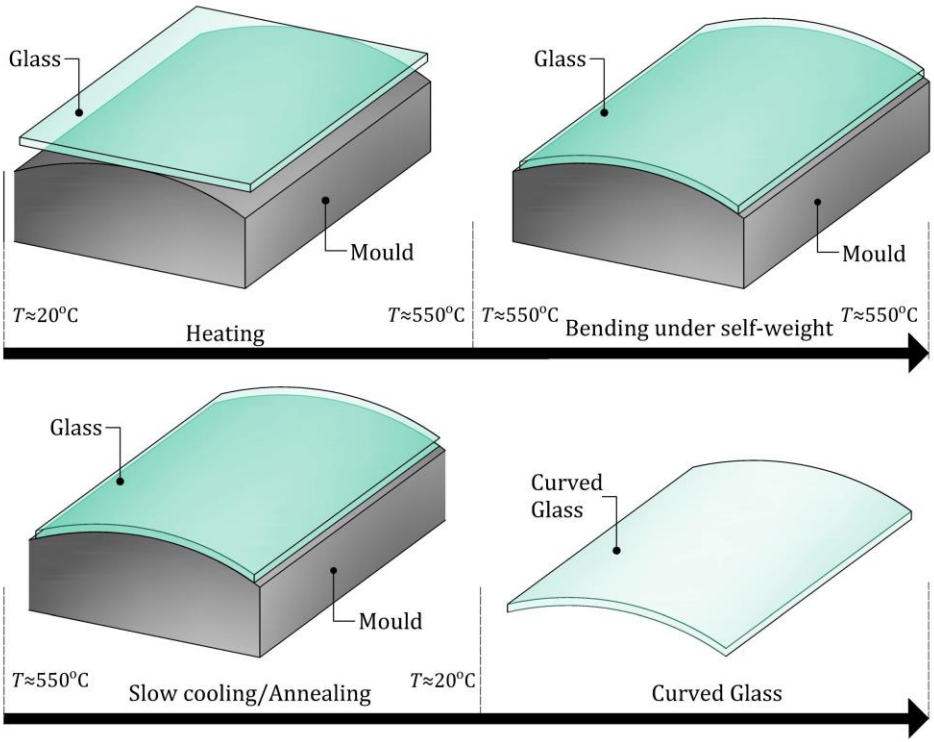

Fig. 2.12: Static mould bending of glass.

The mould is usually made with steel tubes covered by refractory fibres. The heating temperature depends on the desired radius of curvature. Higher temperatures are required for smaller bending radii. This is a well-established glass bending method. However, different moulds are required for plates of different curvature therefore, this method is neither energy nor cost effective. Furthermore, the optical quality of the curved glass plate is very sensitive to imperfections in the mould and the transportation of the curved plates is not easy and practicable.

Roller bending

Roller bending is an alternative method of hot bending performed in a horizontal or vertical set-up. The former is performed in a horizontal bending toughener (Fig. 2.13) during the toughening process of glass; the heated glass (T_g=550°C) is transported horizontally along its longitudinal axis to the bender. The bender comprises a roller bed with circular cylindrical roller cores around which flexible mantels are allowed to rotate. Initially the roller bed is flat; when the glass plate reaches the bender, the rollers lift/move out of plane pressing the glass in the desired curved shape. After the bending, the glass plate is quenched with jets of cold air to create the favourable residual stress profile of toughened glass. During this process the rollers move back and forth to avoid any "black spots". This technique is used in order to create a circular cylindrical bending and is called tilted roller bending.

During vertical toughening bending, the glass is lowered into the furnace in a vertical position and is pressed onto the mould before being toughened.

The advantage of roller bending methods over static mould bending is that adjustable and re-usable "moulds" are employed. However, the most important limitation of the roller bent process is that the optical quality of the roller bent glass plates is very sensitive to the straightness of the rollers and their position relative to one another, leading to roller wave distortion. The optical quality of glass can be assessed qualitatively with the use of a zebra board plate (i.e. a board of black and white stripes). The waviness of the reflected image on the surface of the glass plate is used to assess whether the level of distortion is acceptable. However, this method is subjective as it relies on the experience of the inspector and is very sensitive to the position of the glass. More recent quantitative methods include: (i) in-contact with the glass gauges (flat bottom or 3-way-contact gauge) that are conveyed along the direction of the distortion while measuring peak to valley height [16,47]; (ii) non-contact distortion measuring systems involving the use of computer vision (i.e. automated processing and analysing of digital images) and high-resolution cameras [48]. Recommendations such as those set in EN 12150-1:2000 [16] are often used to determine whether the optical quality of the curved plate is acceptable. These limit the amplitude of the roller wave distortion in fully toughened glass to 0.5 mm over a length of 300 mm. It is currently, possible to manufacture toughened glass with significantly smaller roller wave

distortion amplitudes. In fact, a limit of 0.25 mm is often prescribed for high-end applications.

More information on thermal bending processes (static mould bending and roller bending) can be found in [49–55].

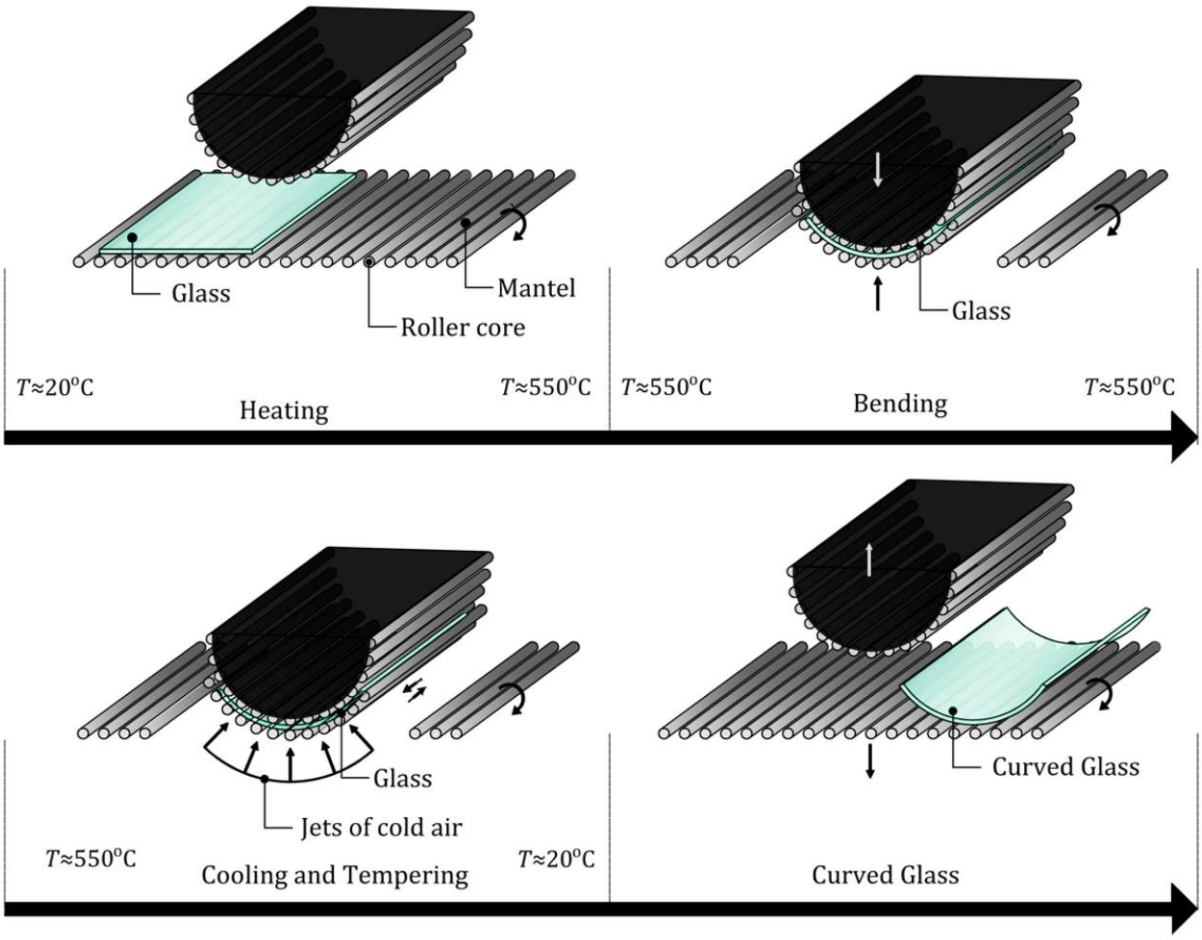

Fig. 2.13: Roller bending of glass.

Cold bending

Cold bending is an alternative, and relatively recent technique of creating curved glass plates. During this process, the curvature is induced elastically with out-of-plane loads at ambient conditions (Fig. 2.14) with a relatively small amount of equipment, thereby, making the process energy efficient and allowing the bending to be executed on site.

Cold bent glass can be used to generate either single or double curved forms. Single curvature / developable glass surfaces are easier to form, but they are not as popular in architectural design as double curved glass which provides a much larger architectural freedom and can be used to create smooth, free form, transparent façades. The glass plates of various curvatures that are required in this kind of applications can be cold bent in shape without any requirement for moulds, therefore, minimizing their cost and making cold bending an attractive method for

creating curved glass surfaces. Apart from energy savings and cost related benefits, it is also thought that cold bending does not affect the optical quality of the glass from its flat state because, unlike thermal bending, viscous flow is not required.

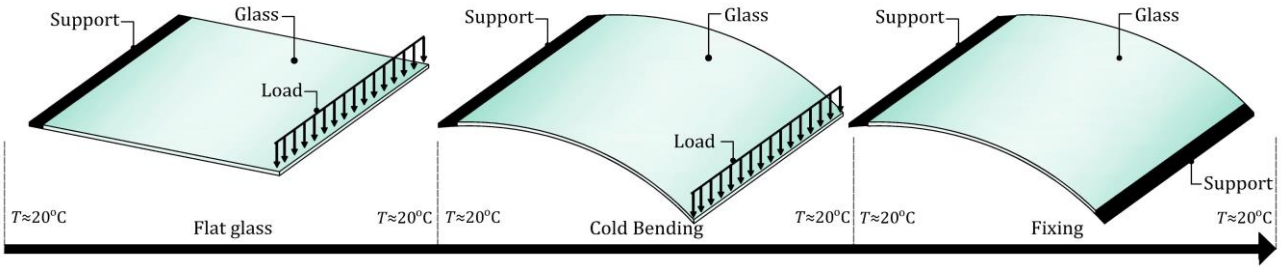

Fig. 2.14: Cold bending of glass.

Cold lamination bending [56,57] is a variation of the cold bending process used to restrain the curved glass plate during the cold bending of laminated glass and involves: (a) bending the un-bonded unit of glass plates and interlayer(s) in the desired shape and restraining it by mechanical means; (b) laminating the un-bonded bent unit in an autoclave and; (c) removing the mechanical supports (Fig. 2.15). In this case, the interlayer preserves the shape of the glass in place though partially, since initial spring-back is expected when the restraints are removed after the lamination.

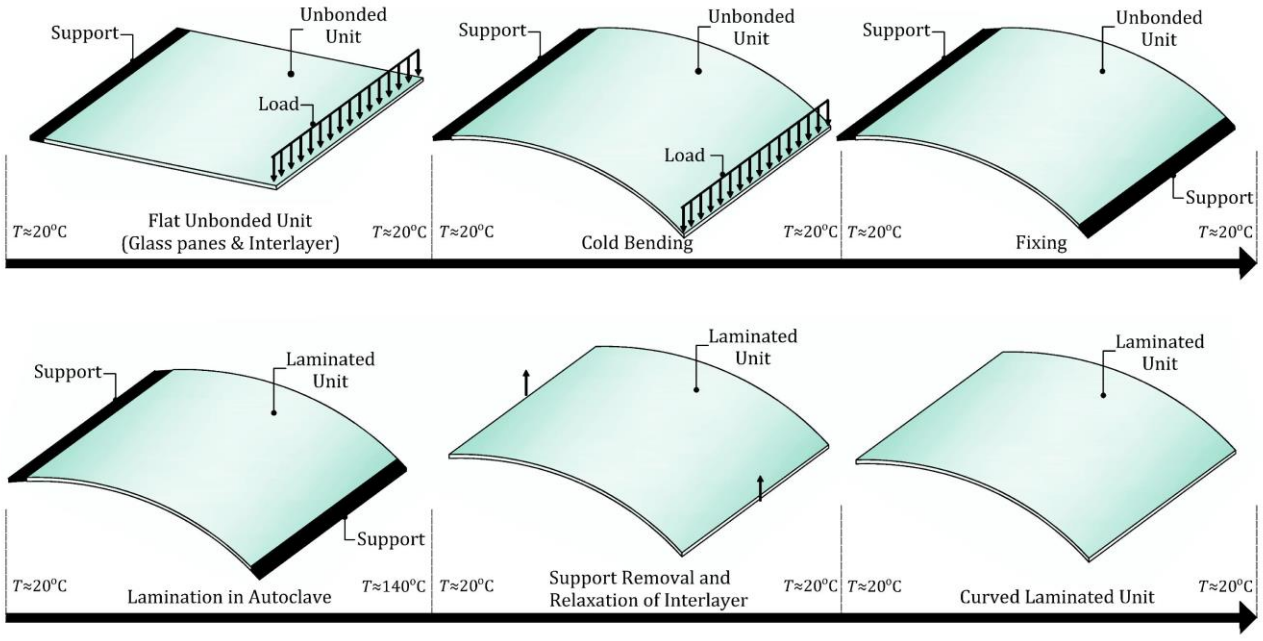

Fig. 2.15: Cold lamination bending of glass.

2.3.3 Curved glass in architecture

Architectural trends for curvilinear forms and complex geometries in façades have prevailed over the last decades. The first "curved" glass façades comprised flat glass plates positioned in such a

way to mimic curvature. However, the end result is facetted and angular and thereby, fails to fulfil requirements for smoothness. An example of this technology is the Moor House (Fig. 2.16) in the City of London designed by Foster and Partners architects and Arup engineers in 2004.

Increasing demands for smooth curved façades eventually led to the use of curved glass in the building envelopes. Curved glass produced with hot bending is traditionally used in such applications. Two examples of this technology are: (a) the façade at 61 Oxford street in London designed by the Allford Hall Monaghan Morris architects and Walsh engineers in 2015 (Fig. 2.17a); the wave design of the façade is created with single curved double glazed units with 2 ply laminates of 6 mm annealed glass and; (b) the three double curved canopies on the Canary Wharf Underground Station designed by Foster and Partners and Arup engineers in 1999 that consist of single curved 12 mm/0.52 mm PVB/12 mm annealed laminated glass (Fig. 2.17b).

Fig. 2.16: Curvature attained by flat glass plates in Moor House (London).

(a) (b)

Fig. 2.17: Hot bent glass: (a) 61 Oxford Street (London) and; (b) Canary Wharf Station (London).

(a) (c)

(b)

Fig. 2.18: Cold bent glass: (a) IAC Headquarters (New York, © www.contemporist.com); (b) train station (Strasbourg, [59]*) and; (c) Victoria and Albert Museum (London).*

However, more recent architectural trends involve free form façades where glass plates of different curvature are needed. Hot bending is not an economic option in this case since moulds of different curvature need to be created and roller bending usually degrades the optical quality of the curved glass. Therefore, cold bent glass becomes an attractive method. Prominent examples of the cold bending technology are:

(a) the IAC Headquarters in New York designed by Frank Gehry and DeSimone engineers in 2006 to resemble a boat's sails at full mast (Fig. 2.18a). Approximately 1,400 double glazed units were cold bent on-site by Permasteelisa to achieve unique shapes by fixing 3 corners of the unit and manually forcing the fourth in place. The maximum out-of-plane rotation from top to ground is 150° in the units at the back of the building [58];

(b) the train station in Strasbourg which was designed in 2007 by the architect Jean-Marie Duthilleul and the RFR engineers (Fig. 2.18c). Cold lamination bending was used to form single curved 2 ply laminates comprising 6 mm heat treated glass. The radii of curvature range between $11 \leq R \leq 30$ m and the façade covers an area of 6,000 m^2 [59] and;

(c) the roof at the Victoria and Albert Museum (Fig. 2.18b): MUMA Architects and Dewhurst

Macfarlane Engineers designed in 2009 the new glass roof for the Medieval and Renaissance Galleries of the museum. The main structure of the roof comprises 73 laminated 10-meter long glass beams of heat treated glass while the roof comprises a 370 m^2 surface of cold bent insulated glass units that are point fixed in the glass seams [60].

2.4 Cold Bent Glass

2.4.1 Introduction

Cold bending involves the application of out-of-plane loads on the glass surface to create the desired curved shape of the glass plate at ambient conditions. The cold bent glass needs to be restrained in its curved shape when the cold bending loads are removed to avoid spring back to its initial flat position as a result of its linear elastic nature. The glass is therefore, subjected to a permanent state of stress throughout its service life.

The relatively low tensile strength of annealed glass makes it inappropriate for cold bending applications, as the radius of curvature that can be safely introduced in an annealed glass plate is generally too large to produce significant curvature in the glass plate. Therefore, toughened glass in the form of heat treated (heat strengthened or fully toughened) or chemically toughened glass is often used in such applications. The maximum curvature that can be achieved in cold bent glass has thus far been limited by the maximum surface stresses, generated during the cold bending process (σ_{cb}) that can be safely resisted by the toughened glass throughout its service life (semi-probabilistic method – Section 2.5.4):

$$\sigma_{cb} \leq \frac{\left(f_{AN,d} - \frac{\sigma_r}{\gamma_{M,r}} - \sigma_{app} \cdot \gamma_{f,app} \right)}{\gamma_{f,cb}} \qquad \text{(Eq. 2.4)}$$

where $\left(f_{AN,d} - \frac{\sigma_r}{\gamma_{M,r}} \right)$ is the design strength of toughened glass [8,61,62], which is the sum total of the design strength of annealed glass, $f_{AN,d}$, and the design compressive residual surface stress (σ_r<0) induced by the thermal/chemical toughening $\left(\frac{\sigma_r}{\gamma_{M,r}} \right)$; $\sigma_{app} \cdot \gamma_{f,app}$ is the maximum design stress on the surface of the glass induced by loads imposed on the glass during its service life and; $\gamma_{f,cb}$ is an appropriate safety factor to account for variability during the cold bending process.

Eekhout et al. [63] suggest that the maximum tensile stress arising from the cold bending should not exceed 25-50% of the residual surface compression of the toughened glass ($\max\sigma_{CB} < 0.25\sigma_r$ or $\max\sigma_{CB} < 0.50\sigma_r$) depending on the magnitude of the service life loads and the consequence

class of the application [64]). The remaining 75-50% of the residual surface compression remains available for successfully withstanding service life loads e.g. wind loads. An example of the stress profile for a cold bent plate is illustrated in Fig. 2. 19.

The curved shape of cold bent glass is typically preserved by means of mechanical fixings or structural adhesives. Mechanical fixings are usually made of steel or aluminium and involve: (a) traditional clamping systems; however, these systems are not very efficient for cold bent laminated glass as the imposed permanent compression that is applied on the glass, could result in unwanted creep of the interlayer and; (b) bolted connections: these systems may lead in high stress concentrations in the glass and thereby, increase the requirements for its thickness for the stress to be successfully accommodated.

Structural adhesives are preferable in this regard, since stress in the connection is evenly distributed on the glass plate without high stress concentrations, even though creep phenomena in the adhesive might still apply. The most commonly used adhesives are structural silicone and epoxy or acrylic resins. Structural silicone though, may interfere with the aesthetic appeal of the design due to its black colour and the wider bonding areas when required to transfer higher loads.

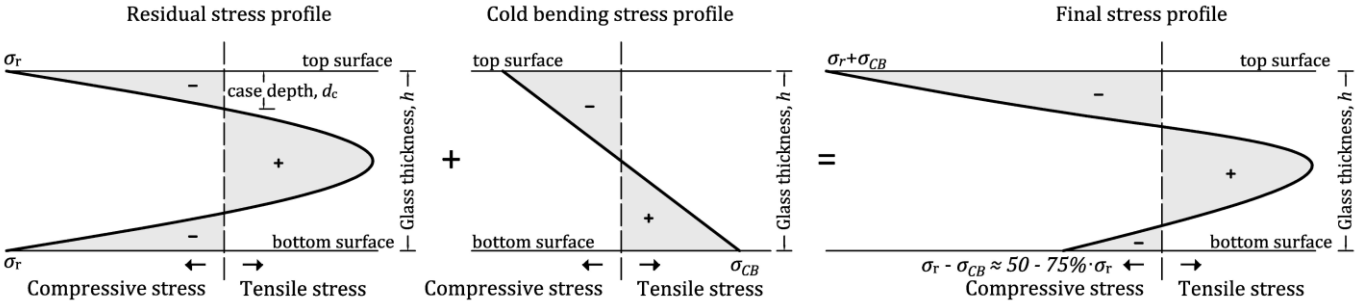

Fig. 2. 19: Example of stress profile in cold bent glass.

2.4.2 Cold bending of monolithic glass plates

Cold bending of glass may be a cost efficient and attractive method for creating curved glass surfaces, but the limited research conducted on cold bent monolithic glass plates to-date indicates that it can result in geometric instabilities [65–67]. Staaks and Eekhout [65,66] reported that the free edges of the glass plate change their shape from straight to curved during the cold bending process. Their bending process involved forcing two corners of the plate out-of-plane while the other two were point fixed (Fig. 2.20), thereby creating a double curved surface. In particular, two deformation modes were reported. In the first deformation mode, both diagonals were curved and the edges preserved their initial straightness (Fig. 2.20b). However, when the out-of-plane displacement at the two corners exceeded 16 times the thickness of the plate, a change in the deformation mode was observed [66]; the plate buckled as one diagonal straightens and the

edges become curved (Fig. 2.20c). This phenomenon is noteworthy because curved edges could result in difficulties when fixing the plate to the frame and / or aligning the edges of adjacent glass plates.

A simplified analytical model was also proposed by Eekhout and Staaks [65,66] to predict this buckling instability. The plate was considered as a system of two diagonal strips spanning between the corners of the plate and intersecting at the centre of the plate, and four rods, one along each of the four edges of the plate. By forcing two corners out of plane, bending increases in the diagonals while the rods connecting the corners are stretched creating an additional axial compression in the diagonals. A change in the deformation mode (instability) occurs when the critical Euler buckling stress is exceeded in one diagonal. However, Eekhout and Staaks were unable to obtain good agreement between their simplified analytical model and their numerical results.

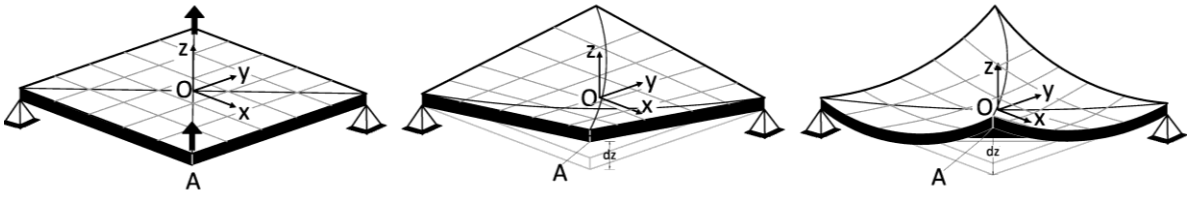

(a) (b) (c)

Fig. 2.20: Deformation modes during cold bending: (a) flat; (b) 1st mode; (c) 2nd mode (adapted from [66]*).*

This change of curvature has also been described by Galuppi *et al.* [67] as snap-through buckling. Snap-through buckling, in the case of a plate, is a sudden change of deformation in the direction of the load in the central regions of the plate. Their analytical and numerical investigations involved a plate loaded at its four corners; downward loading (negative z) was applied at two diagonally opposite corners and upward (positive z) at the other two. Their results show that the hyperbolic paraboloid form of the deformed plate changes abruptly and its axes of symmetry are reduced from two to one. This occurs as one of the diagonals straightens while the curvature of the other continues to increase and the edges display significant curvature. An analytical model [67,68], validated by finite element modelling, was proposed by the same authors using a combination of Mansfield's inextensional plate theory and beam theory to account for the double cylindrical shape of the plate. However, the surface quality resulting from the cold bending process is not quantified or investigated, their analytical results have yet to be validated experimentally, and the influence of different boundary conditions have not been investigated.

Apart from energy and cost related benefits, it is thought that cold bending does not affect the optical quality of the glass from its flat state because, unlike thermal bending, viscous flow is not required. However, it was recently reported that optical distortions [69] and unwanted

reflections [70] could appear during the bending process thereby bringing into question the optical quality of cold bent glass plates. This geometric instability and the resulting surface quality in monolithic glass plates seem to be overlooked in the limited number of experimental studies on cold bent glass to-date.

Additionally, research on the influence of the residual stress on the mechanical response of toughened glass plates, typically used in cold bent applications, during the bending process could not be found. However, previous research on cantilevers of semi-conducting materials (e.g. gallium arsenide) suggests that residual stresses can affect their mechanical behaviour [71–74]. In particular, their findings show that the strain independent part of stress i.e. the residual stress, influences the resonant frequency and consequently, the stiffness of the material. Nonetheless, the effect of the residual stress was only investigated at a microscale level and conflicting views on the influence of residual stresses are found in [75].

2.4.3 Cold bending of laminated glass plates

Even though monolithic cold bent glass applications exist (e.g. Town hall of Alphen aan den Rijn), safety reasons traditionally dictate the use of laminated cold bent glass [45,63,76]. Bending in this case can be performed using the cold lamination bending method (the un-bonded glass plates and in-between interlayer(s) are first cold bent and temporarily fixed in place before being laminated in an autoclave, Section 2.3.2). The advantage of this method is that the curvature in the laminated unit is retained by the interlayer after lamination. Many studies focus on the spring-back effect of the curved unit and relaxation of the interlayer once the boundary conditions used prior and during lamination are removed and the ability of the interlayer to maintain the curved shape throughout its service life [56,57,77,78].

However, cold bending of laminated glass can also follow after the lamination process in a similar way to which monolithic glass is cold bent. In such cases the cold bent laminated unit needs to be restrained in shape by mechanical fixings or structural adhesives. The advantage of this is that it facilitates execution on site. An alternative approach suggests mildly heating the laminated unit (45-60°C) to reduce the interlayer's stiffness and ease the cold bending process which follows subsequently [76,79].

Belis et al. [79,80] investigated the behaviour of cold bent laminated glass units of single curvature consisting of two layers of fully toughened glass bonded together with different types of PVB. Their results showed that the mechanical behaviour of these units is dependent on the type and the thickness of the interlayer, the speed with which the load is applied and the temperature during the bending process. The mechanical performance of cold bent laminated glass has been also investigated numerically simulating a monolithic plate based on the effective

thickness approach (Section 2.2.3) [45], a monolithic plate considering full shear coupling of the unit [78] or a composite unit wherein the interlayer is modelled as a linear elastic material with properties corresponding to a specific combination of temperature and load duration [79].

However, instability phenomena during the cold bending of laminated glass were disregarded in the previous studies and its optical quality was overlooked.

2.4.4 Cold bending of insulated glass units

An Insulated Glass Unit (IGU) is a unit that consists of two or more plates of monolithic/laminated glass. The glass plates are held apart with spacers forming a cavity between the glass plates. The air in the cavity can be replaced by a gas of lower thermal conductivity than air e.g. argon, krypton or xenon to improve the thermal insulation of the unit.

Cold bending of IGUs is more complicated with respect to cold bending of monolithic or laminated glass as their mechanical behaviour is not only influenced by the response of the cold bent glass plates and/or the relative movement between the glass plates and the interlayer encountered in cold bent laminated glass. However, issues also arise on the choice of the structural adhesive and the frame; bonding the glass plates to the frame; the integrity of the edge seal; the energy performance of the whole unit etc. Research on cold bending of IGUs is very limited to-date and has primarily focused on the durability of the primary and the secondary seals of the cold bent IGUs [81] or structural performance of the IGU and the adhesive [82].

2.5 Glass strength

2.5.1 Introduction

The intrinsic strength of glass is very high and estimated around 32 GPa [8] based on the external forces required to break the covalent bonds between silicon and oxygen. However, glass strength is not a material constant, but depends strongly on the process quality and the condition of the glass surface. Griffith was first to propose that fracture in glass does not initiate from a flawless surface but is caused by pre-existing imperfections known as Griffith flaws [83]. Surface flaws accumulate during manufacture and service life of the glass and act as stress concentration points that significantly reduce the strength of glass to its extrinsic strength.

Crack propagation can be triggered under one of the following fracture modes (Fig. 2.21a-c): (a) Mode I (*opening mode*): tensile forces act perpendicular to the crack plane and result in crack opening; (b) Mode II (*in-plane shearing or sliding mode):* fracture occurs due to shear forces acting in parallel to the crack plane and; (c) Mode III (*tearing mode*): fracture occurs as a result of out-of-plane shear forces.

Stress intensity factors, K (Eq. 2.5, [84]) are used to describe the elastic stress intensity near the tip of the crack. Instantaneous fracture occurs when the stress intensity factor becomes equal to or exceeds a critical value known as the fracture toughness, K_{IC} ($K_I \geq K_{IC}$). The fracture toughness ranges between $0.72 \leq K_{IC} \leq 0.82$ MPa $m^{1/2}$ for soda lime silica glass (Table 2.1).

$$K_I = Y\sigma_{zz}\sqrt{\pi a}, \quad K_{II} = Y\sigma_{zy}\sqrt{\pi a} \quad and \quad K_{III} = Y\sigma_{zx}\sqrt{\pi a} \qquad \text{(Eq. 2.5)}$$

where Y: the geometry factor based on the configuration of the flaw, α: the flaw depth and σ: the failure stress normal to the flaw's plane.

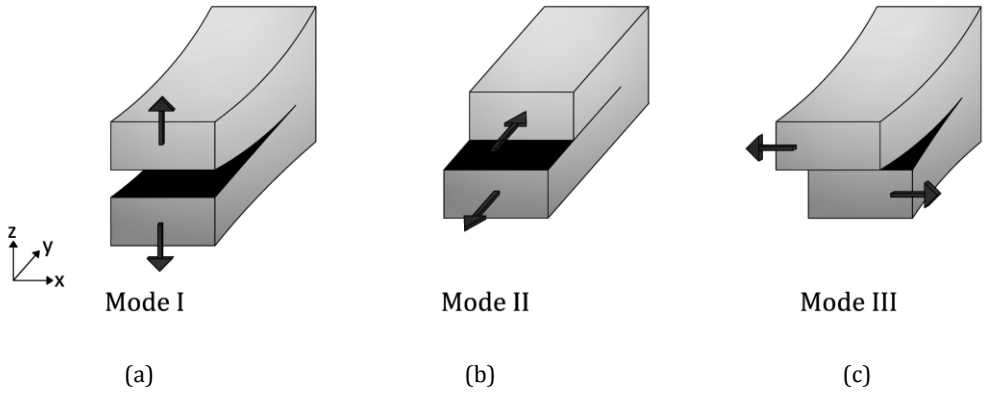

Fig. 2.21: Fracture modes: (a) mode I: opening; (b) mode II: sliding and; (c) mode III: tearing.

However, surface flaws can also grow at stress levels below the strength of glass or stress intensity factors below the fracture toughness of glass in non-inert conditions. Crack growth largely depends on the humidity and the stress rate during the service life / testing of the glass and is characterised by one of the following three regions (Fig. 2.22, [85]):

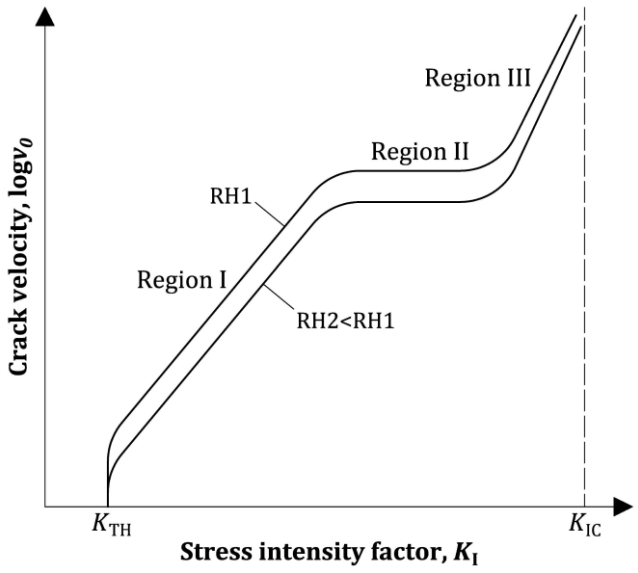

Fig. 2.22: Crack growth regions.

Region I: the crack velocity is highly influenced by the chemical reaction between the hydroxyl ions of the water molecules and the Si-O tetrahedra of the glass surface [86]. Therefore, increase in humidity levels leads to a corresponding increase in crack velocity. This phenomenon is known as sub-critical crack growth or stress corrosion. The depth of flaws increase under the influence of sub-critical crack growth, until they reach their critical size and eventually initiate fracture of the glass [87,88]. Subcritical crack growth depends on the surface stress history and environmental conditions (humidity, temperature and pH [89]) during testing/service life of the glass. The lower limit of Region I is set by the crack growth threshold, K_{TH} i.e. the stress intensity level below which crack growth does not occur or is very minor to detect; a change in the chemical composition of the crack tip (alkali leaching from the glass surface after interaction with water, [90]) is the potential reason behind this phenomenon. The crack growth threshold is a function of the environmental conditions, and in particular the pH and the composition of the glass.

Region II: the crack velocity depends on the supply rate of water to the crack tip but is independent to the applied loading as its value remains constant for increasing stress intensities;

Region III: the crack growth depends on the applied loading but is independent to humidity as the $\log v_0$-$\log K_I$ curves converge to a straight line for testing in environments with different levels of humidity.

Sub-critical crack growth is suppressed (i.e. $\alpha_i \approx \alpha_f$) when the glass is loaded in inert conditions i.e. when there is no influence from environmental conditions or stress history (e.g. experimental tests in a dry-nitrogen or vacuum chamber), or when fracture is induced rapidly (for very short durations of loading, more information shown in Chapter 4, Section 4.3).

Two approaches are available for the estimation of glass strength [62]: (a) an explicit approach: linear elastic fracture mechanics can be used for a given flaw morphology and; (b) a stochastic approach: this involves destructive testing of a sufficient number of specimens and statistical analysis of their failure stress. Strength estimates can be subsequently obtained for different probabilities of failure, P_f. A detailed description follows for each method.

2.5.2 Explicit approach

For annealed glass specimens with a critical flaw of known geometrical characteristics, glass strength is given by Eq. 2.6a [62,91]. The upper limit of Eq. 2.6a corresponds to the inert strength of glass i.e. Region A in Fig. 2.23a-b ($0 \leq t_f \leq t_{IN}$) within which sub-critical crack growth is suppressed while the lower limit of Eq. 2.6a corresponds to the threshold strength, below which the glass will not fail irrespective of the stress duration i.e. Region C in Fig. 2.23a-b ($t_{TH} \leq t_f \leq \infty$).

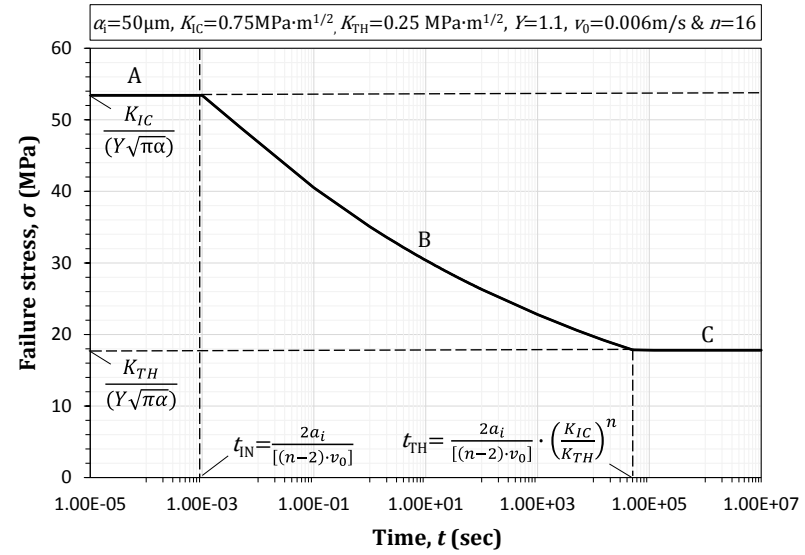

(a)

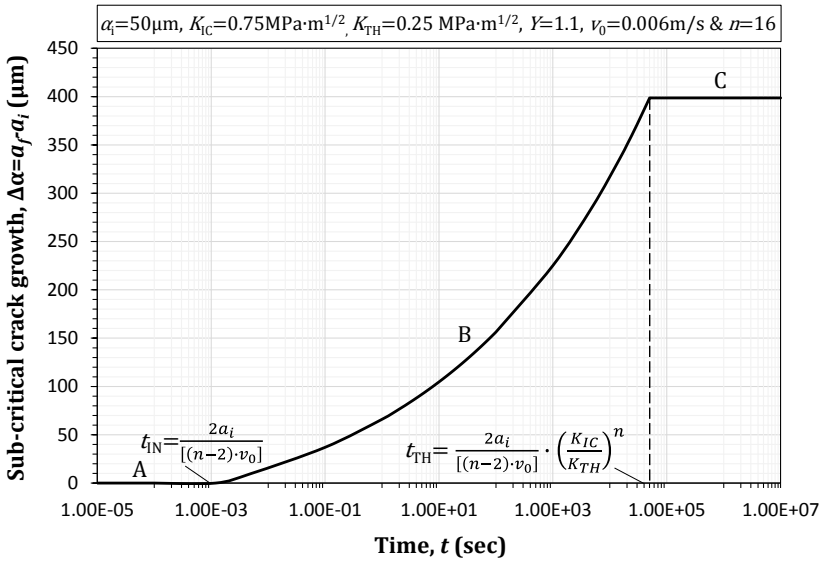

(b)

Fig. 2.23: Sub-critical crack growth (SCG) regions: A → Inert; B → SCG and; C → SCG threshold: (a) stress vs. time and; (b) crack growth vs. time.

$$\int_0^{t_f}\left(\sigma^n(t)\right)dt=\left\{\left[\frac{2}{(n-2)v_0K_{IC}^{-n}(Y\sqrt{\pi})^n a_i^{(n-2)/2}}\right]\cdot\left[\frac{1-\left(\frac{a_i}{a_f}\right)^{(n-2)/2}}{1-\left(\frac{a_{TH}}{a_i}\right)^{(n-2)/2}}\right]\right\} \qquad \text{(Eq. 2.6a)}$$

where: σ_f: the surface stress due to external loading, t_f: the time to failure a_i: the initial crack depth, a_f: the critical crack depth for K_I=K_{IC}=0.75 MPa·m½, a_{TH}: the threshold crack depth for K_{TH}=K_I=0.25 MPa m $^{1/2}$, v_0: the crack velocity and n: the static fatigue constant.

Eq. 2.6a is transformed to Eq. 2.6b for toughened glass to account for the suppression of subcritical crack growth when $0 \le t \le t_r$ i.e. the time during which the applied tensile stress is less than the residual surface compression ($|\sigma_{app}| \le |\sigma_r|$, $\sigma_r<0$).

$$\int_0^{t_f - t_r} \left[(\sigma_f + \sigma_r)(t)\right]^n dt = \left[\frac{2}{(n-2)v_0 K_{IC}^{-n} (Y\sqrt{\pi})^n a_i^{(n-2)/2}}\right] \cdot \left[\frac{1-\left(\frac{a_i}{a_f}\right)^{(n-2)/2}}{1-\left(\frac{a_{TH}}{a_i}\right)^{(n-2)/2}}\right] \quad \text{(Eq. 2.6b)}$$

2.5.3 Stochastic approach

The characteristics of the critical flaw are often unknown or difficult to determine. In such cases, a stochastic approach is adopted for the estimation of strength of annealed or toughened glass. There is a large variation in fracture strength obtained from seemingly identical specimens which are produced, stored and tested destructively under the same conditions. Therefore, destructive testing of several nominally identical glass specimens and the subsequent statistical analysis of their strength data is essential for establishing an accurate design strength corresponding to a sufficiently low probability of failure. As indicated in Section 2.5.2, glass is susceptible to sub-critical crack growth, therefore in order to normalise the effects of glass specimens failing at different load durations, the fracture strength data from the destructive tests are often converted to equivalent strengths. This is achieved by converting the stress history exerted during the destructive test to an equivalent constant stress, $\sigma_{f,eq}$, for a reference time period, t_{ref}, (60 sec is a typical value) using Eq. 2.7a for annealed glass (Fig. 2.24a) and Eq. 2.7b for toughened glass to account for the suppression of sub-critical crack growth when $|\sigma_{app}| \le |\sigma_r|$ (Fig. 2.24b).

$$\int_0^{t_f} \sigma^n(t)dt = \int_0^{t_{ref}} \sigma_{f,eq}^n dt \quad \text{(Eq. 2.7a)}$$

$$\int_0^{t_f - t_r} \left[\left(\sigma_f + \sigma_r\right)(t)\right]^n dt = \int_0^{t_{ref} - t_r} \left(\sigma_{f,eq} + \sigma_r\right)^n dt \quad \text{(Eq. 2.7b)}$$

There are three distributions that have historically been used for describing glass strength data; the Weibull, the normal and the lognormal distribution. The 2-parameter Weibull distribution is by far more popular since: (a) it is more effective in describing glass strength data [92] providing better goodness-of-fit and; (b) is more conservative at the tail of the distribution, than the lognormal and the normal distributions [92,93]. Conservative estimates are more desirable for engineering design applications and therefore, the Weibull distribution has traditionally been used to describe glass strength data [13,94–97].

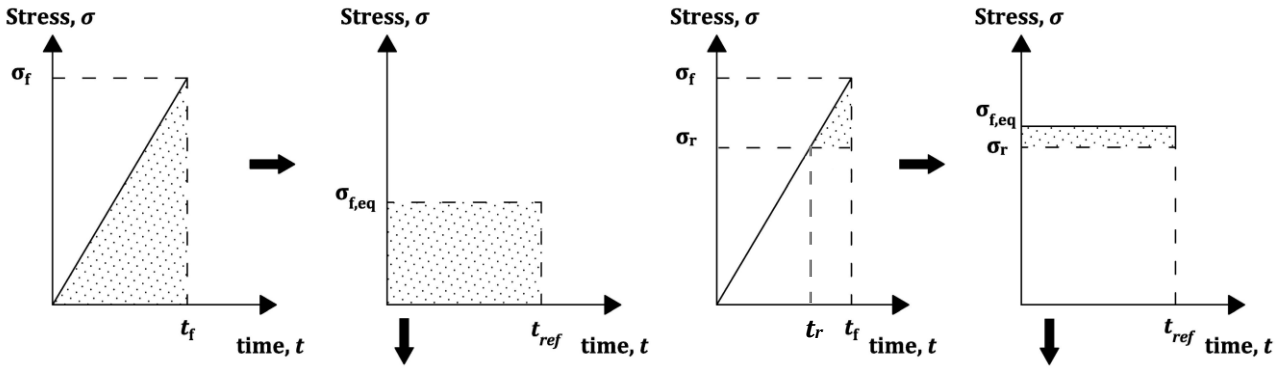

$$\sigma_{f,eq} = \sigma_f \cdot \left[\frac{t_f}{t_{ref} \cdot (n+1)} \right]^{1/n} \qquad \sigma_{f,eq} = -\sigma_r + (\sigma_f + \sigma_r) \cdot \left[\frac{t_f - t_r}{(t_{ref} - t_r) \cdot (n+1)} \right]^{1/n}$$

(a) (b)

Fig. 2.24: Failure stress to equivalent stress for a reference time in: (a) annealed and; (b) toughened glass.

The general equation for the cumulative distribution function (CDF) of the Weibull distribution [98] is:

$$P_f(\sigma_{f,eq}) = 1 - \exp\left[-\left(\frac{\sigma_{f,eq} - \sigma_u}{\theta} \right)^{\beta} \right] \qquad \text{(Eq. 2.8)}$$

where β is the shape parameter, θ is the scale parameter and σ_u is the location parameter.

The location parameter, σ_u, represents the stress level below which the material never fails (i.e. P_f=0). Safety reasons dictate that σ_u is set to 0 as recommended in [99] for brittle materials. This specifically applies for annealed glass. However, a three-parameter Weibull distribution could be potentially useful for toughened glass where the location parameter could be equal to the residual surface compression (σ_u=σ_r), below which glass is not expected to fail. Nonetheless, Eq. 2.8 is reduced to a two-parameter Weibull function for annealed glass (and toughened glass) and the CDF can be linearized (Eq. 2.9) in the form of y=bx+c by taking the logarithm of each side twice:

$$\ln\left(\ln\left(\frac{1}{1-P_f} \right) \right) = \beta \cdot \ln\sigma - \beta \cdot \ln\theta \qquad \text{(Eq. 2.9)}$$

Hence, the CDF becomes a linear plot of $\ln\left(\ln\left(\frac{1}{1-P_f} \right) \right)$ vs. $\ln\sigma$ as illustrated in Fig. 2.25 and where the gradient of the distribution is equal to the shape parameter, β and the intercept is -β·lnθ. The shape parameter, β, indicates the variability of the data and thus, higher values of β lead to a steeper CDF which represents a smaller scatter of strength in the data. The scale parameter, θ, is sufficient to dictate the position / stress level below which 63.2% of the

specimens fail. However, the shape parameter, β, is needed to determine the position of other points on the CDF.

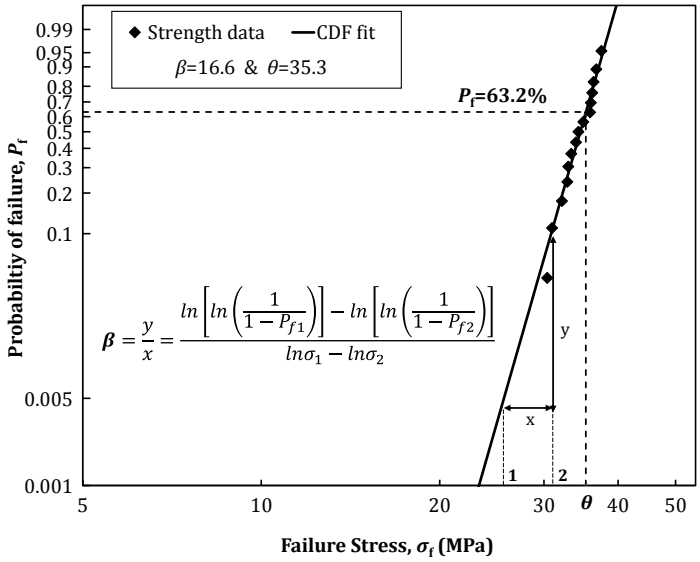

Fig. 2.25: CDF of glass strength data.

2.5.4 Reliability analysis

The following reliability methods / levels are used for glass design:

Deterministic method (Level 0): the resistance (strength), *R*, of the material is defined based on historical or empirical data and should exceed the actions (loads), *E*. The ratio between the resistance and the action represents the safety factor for the specific application i.e $E_k \le R_k/\gamma$.

Semi-probabilistic: (Level I): Design values are obtained using characteristic values for actions and resistances and partial safety factors: $\mathrm{E}_d \le R_d \Rightarrow \gamma_F \cdot E_k \le R_k/\gamma_{\mathrm{M}}$. This approach is prescribed in prEN1374 [100] for glass where actions are defined based on EN 1991 [101] and design strengths are given by Eq. 2.10a for annealed glass and Eq. 2.10b for toughened glass:

$$f_{g,d} = \frac{k_{\mathrm{mod}} \cdot k_{sp} \cdot f_{g,k}}{\gamma_{\mathrm{M,A}}} \qquad \text{(Eq. 2.10a)}$$

$$f_{g,d} = \frac{k_{\mathrm{mod}} \cdot k_{sp} \cdot f_{g,k}}{\gamma_{\mathrm{M,A}}} + \frac{k_v \cdot (f_{b,k} - f_{g,k})}{\gamma_{m,v}} \qquad \text{(Eq. 2.10b)}$$

where $k_{\mathrm{mod}} = 0.663 \cdot t^{-1/16}$: the modification factor for load duration *t*; k_{sp}: the modification factor for glass surface; $\gamma_{\mathrm{M,A}}$=1.6: the material safety factor; $\gamma_{\mathrm{m,v}}$=1.2: the surface compression safety factor; $f_{\mathrm{g,,k}}$=45 MPa the characteristic glass strength of annealed glass and; $f_{\mathrm{b,k}}$=120 MPa: the characteristic strength for fully toughened glass.

1st order reliability analysis (FORM, Level II): The strength and the actions correspond to a specific probability of failure and probability of occurrence, respectively so that $P_f = P(R-E<0)$. These could be chosen to suit the recommendations of existing standards at design level. For example:

- EN 1990:220 [64] the design resistance is defined as $P_f = P(R \le R_d) = \Phi(-a_R \cdot \beta)$ and the design action as $P_o = P(E > E_d) = \Phi(+a_E \cdot \beta)$

  where R: the effective resistance and R_d: the design resistance, a_R=0.8 is the sensitivity factor for resistance; β is the reliability index; Φ the cumulative distribution function for the normal distribution and; a_E=0.7: the sensitivity factor for actions. For instance, the reliability index is β=3.8 and β=4.7 for buildings with a 50-year and a 1-year reference period respectively and a consequence class 2, and thereby:

  $P_f = \Phi(-0.8 \cdot 3.8) = \Phi(-3.04) = 0.0012$ and $P_O = \Phi(-0.7 \cdot 3.8) = \Phi(-2.66) = 0.0039$

  $P_f = \Phi(-0.8 \cdot 4.7) = \Phi(-3.76) = 0.0001$ and $P_O = \Phi(-0.7 \cdot 4.7) = \Phi(-3.29) = 0.0005$

- ASTM 1300-12 [33] assigns a probability of failure of 0.8% or less for glass resistance at design level.

The FORM approach will be followed in Chapter 5 and Chapter 6 for the estimation of the design strength which will correspond to a probability of failure of P_f=0.008 as indicated in ASTM 1300-12 [33].

2.6 Mechanical performance of aged glass

2.6.1 Introduction

The strength of glass is highly dependent on the condition of its surface (Section 2.5). For example, for a typical half penny shaped flaw with a depth a=50 μm on the surface of the annealed glass and K_{IC}=0.75 MPa m$^{0.5}$ and Y=0.713, the extrinsic strength of glass is reduced to σ_f= 83.9MPa (Eq. 2.5). Therefore, a 99.7% reduction is noticed with respect to the intrinsic strength of glass if one considers σ_{intr}=32 GPa [8]. Strength reduction in cold bent glass or other load bearing applications during its service life could be detrimental and lead to failure when the permanent stresses can no longer be accommodated. Therefore, the long term mechanical performance of aged glass must be evaluated carefully.

The long term mechanical performance of glass can refer to: (a) the influence of sub-critical crack growth on pre-existing flaws that grow under long-term loads e.g. flaws that grow sub-critically on the inner / protected glass surface of an insulated glass unit and; (b) the nucleation of new flaws, in addition to the pre-existing ones, on the surface of glass during its service-life e.g. flaws

that accumulate on the external / exposed surface of an insulated glass unit. The latter i.e. the mechanical performance of aged glass is investigated in this section.

2.6.2 Mechanical durability of annealed glass

Damage that accumulates during the service life of glass is a result of natural ageing caused by contact, abrasion or impact and typically depends on the level of exposure. Previous research has shown a reduction of 35-85% in extrinsic strength with respect to the extrinsic strength of as-received annealed glass [94,95,102,103]. Therefore, the mechanical performance of aged glass becomes essential when designing with glass. However, only a few studies are available on the strength of weathered annealed glass [94,95,102,104,105] and even fewer on the strength of weathered toughened glass [106]. Frequently, research on the durability of glass components focuses on the response of the interlayer in laminated glass and its viscoelastic response to load duration and environmental conditions in order to investigate the monolithic/layered response of the laminated glass component [107–110].

The mechanical durability of the glass itself can be divided into erosive resistance and scratch resistance. The erosion of glass occurs when glass is exposed to flying projectiles that repeatedly impact its surface (e.g. a glass panel in a façade) and lead to material removal. The risk increases in cases of extreme wind and locations where windstorms are common. The most common types of flying projectiles in urban areas are roof gravel, roof tiles and timber [111]. Sand abrasion is used for the evaluation of the erosive resistance of glass. This can be achieved either: (a) in a sand trickling set-up ([96,112–115]) where sand is allowed to fall freely from a controlled height onto the surface of the glass or; (b) with sandblasting ([116–119])) i.e. propelling of sand by compressed air towards the surface of the glass. The erosive resistance of the glass is a function of the particle size, impact velocity, duration of abrasion and mass of abrasive medium [119]. Damage increases with higher quantities of abrasive medium, impact angles and speed of impact. However, the erosive resistance was mainly evaluated in these studies with non-destructive tests (roughness characterisation, optical transmission and mass loss) disregarding glass strength. Basic strength data are shown in [113,114], however, a comprehensive statistical analysis of glass strength is only available in [103] reporting a 59% reduction in as-received characteristic strength (P_f=0.05) after sand-abrasion with 6 kg of sand dropped from a height of 1 m. However, further experimental testing and a subsequent detailed statistical analysis on glass strength due to erosive ageing mechanisms is needed to determine the influence of the artificial ageing parameters during the sand abrasion and their correlation to naturally induced damage.

Glass elements are also vulnerable to scratches when objects of higher hardness are forced into the glass and dragged along its surface. Scratches can be induced due to mishandling of the glass during transportation/installation processes, cleaning and in-service conditions. Scratch

resistance is typically evaluated with indenters and commercially available scratching devices that can accommodate geometrically different indenter tips [120–122]. Depending on the level of damage and their configuration, scratches can be described with one of the following regimes [123]: (a) *micro-ductile*: permanent deformation and potential lateral cracks (Fig. 2.26) are induced in the glass.; (b) *micro-cracking*: radial / median cracks (Fig. 2.26) are formed while lateral cracks extend and occasionally intersect with the surface; (c) *micro-abrasive*: radial and median cracks are also formed in this regime while the intersection of the lateral cracks with the surface is continuous along the length of the scratch and accompanied by material removal, known as chips (debris, Fig. 2.26).

The scratch resistance of glass and the associated regimes depend on the geometry of the indenter, the chemical composition of the glass, the environmental conditions and the curing time of the scratch, and the scratching speed ([120–124]). Scratches in the micro-ductile regime are more likely to form in glasses with higher silica content. Sharp indenters (e.g. 60°) also result in scratches in the micro-ductile regime while realistic scratches approximating those induced during cleaning (micro-cracking regime) are induced with 90° or 120° conical indenters. Strength recovery after scratching, known as crack healing, was found to occur particularly during the first 24 hours of curing time after inducing flaws on the glass surface. The crack healing led to an increase in mean strength of 32% and 42% for curing at ambient conditions (RH=50%) and curing under water, respectively [124].

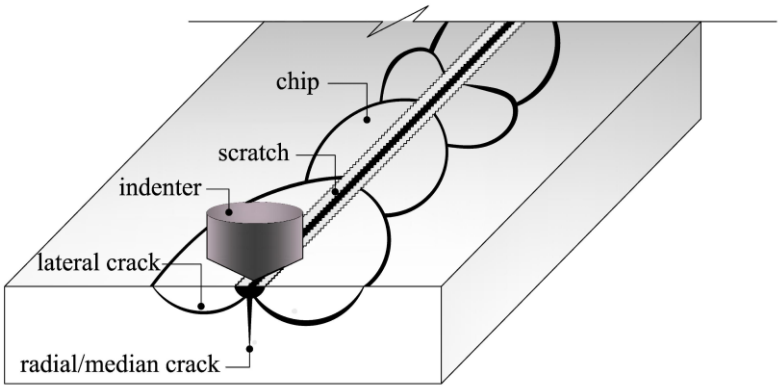

Fig. 2.26: Morphology and types of cracks.

2.6.3 Mechanical durability of toughened glass

The ability of toughened glass to retain a safe level of its beneficial residual stress profile (Fig. 2.5) during its service life is essential. This is true especially when glass is used in cold bent or other applications where higher loads than those typically expected for a traditional infill panel need to be borne. The residual surface compression in toughened glass is expected to enhance its structural behaviour as surface flaws will not grow or initiate fracture when in compression.

However, flaws that accumulate on the surface of toughened glass have a twofold detrimental effect: (i) they act as stress-concentration points similarly to annealed glass and; (ii) they impose the stress concentration at a depth, α, from the surface, where the compressive residual stress is lower than that found on the surface for flaw depths $\alpha \leq d_c$: $|\sigma_r(\alpha)| < |\sigma_r(h)|$, Fig. 2.27a) or eliminate the residual surface stress for flaw depths $\alpha > d_c$: $\sigma_r(\alpha) > 0$, Fig. 2.27b).

The mechanical durability of toughened glass can be divided into scratch and erosive resistance. Realistic linear scratches similar to those found in chemically toughened glass could be reproduced with indenters of 90°, 120° or 136° (Vickers) tip angles [120,125]. Similar values of vertical deformation were found for scratches in annealed and fully toughened glass indicating that their hardness does not differ [120]. However, micro-abrasive regime i.e. chip formation along the direction of the scratch, occurs at lower loads for fully toughened glass than annealed glass indicating the superior scratch resistance of the latter [120]. The pattern of crack formation during scratching of chemically toughened glass was found to differ from heat treated (fully toughened and heat strengthened) glass in that lateral cracks preceded the formation of radial/median cracks in the former [126]. Unsurprisingly, strength reductions were reported for heat treated and annealed glass after scratching; scratched heat treated glass was stronger than scratched annealed glass indicating that the depth of the flaws induced was smaller than the case depth [127].

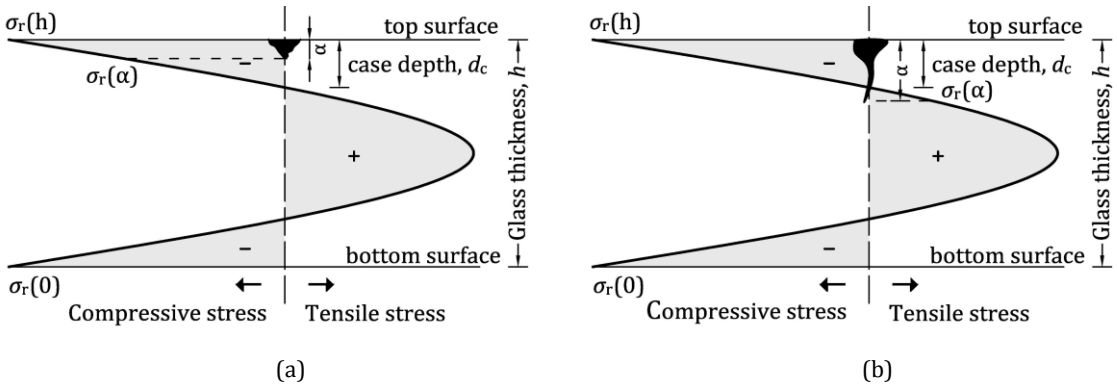

Fig. 2.27: Flaw in fully toughened glass.

Erosive resistance tests (surface abrasion) were proposed for assessing the mechanical performance of chemically toughened glass in [23,125]. Its erosive resistance was found to be a function of the mass of the abrasive medium and the time and temperature used in the toughening process [128]. Chemical toughening was found to offer only a slight improvement over the performance of annealed glass when exposed to erosive action for small masses of abrasive medium, in terms of mass loss, surface roughness and optical transmission but the strength of glass was not assessed [118]. Additionally, the erosive damage in the above studies was chosen arbitrarily with no apparent correlation to natural damage.

The mechanical performance of aged toughened glass can be evaluated by testing naturally aged specimens. However, sourcing of naturally aged toughened glass is difficult, due to the relatively recent use of toughened glass in the building industry. In fact, only a single study appears to exist on the weathering action on fully toughened glass [106] wherein, weathered fully toughened glass was found to meet the strength requirements set in ASTM E1300-12A [33] after 20 years of exposure. However, a comprehensive statistical analysis of strength data is not available. No such study on chemically toughened glass could be found.

Artificial ageing methods can be used to expedite the process of natural ageing. However, despite the existing research on erosive and scratch mechanisms in annealed and toughened glass, a comprehensive and reliable method for the artificial ageing of glass has yet to be established. The selection of a suitable artificial ageing method should depend on the level of exposure / type of application where the glass is to be installed and correspondingly on the expected type of critical flaw (i.e. caused by scratching or erosion). For example, the induction of scratches is preferred in [124] over other abrasion methods; scratches were found to be a better optical match, based on dye penetrant inspection used to reveal flaws in the naturally aged glass of that study and additionally in [124].

DIN 52348 [129] (similar to ASTM D968-05 for organic coatings [130]) is currently the only standard on the artificial ageing of glass. This standard proposes a sand trickling test for the artificial ageing of glass and the evaluation of its durability. However, DIN 52348 and similarly ASTM D968-05 have some important limitations, namely: (a) there is no published research on the basis of the sand trickling parameters proposed in the standard; (b) there is no published research on the correlation between damage induced artificially and the damage generated by natural phenomena and; (c) the durability of glass is evaluated in terms of light transmission and the magnitude and scatter of the resulting strength data is disregarded.

2.7 Conclusions – Gaps in knowledge

Chapter 2 provides the state-of-art knowledge for curved glass. The aim of this Chapter was to present the available knowledge and to identify gaps related to curved glass. Cold bending of toughened glass was identified as an attractive method for creating curved glass surfaces minimizing energy requirements and costs. However, it was shown that even though some research is available on cold bent glass, there are still several unknowns that need to be addressed for cold bending to be established as a reliable method for creating curved glass surfaces. These involve, but are not limited to: the evaluation of the optical quality and the stability during the bending process and the service life of the glass and; the assessment of its mechanical performance / strength degradation after exposure to natural ageing mechanisms.

Cold bending is thought to result in high optical quality curved glass surfaces. However, the high slenderness of cold bent glass elements makes them prone to instabilities under the production and the service life loads. Such instabilities could potentially degrade the optical quality of cold bent glass and exceed serviceability or even ultimate limit state limits. Some instability phenomena have been identified during the production process in the existing literature, however, their influence is not yet fully characterised.

Toughened glass is often required for cold bending applications, but uncertainties also arise on the ability of toughened glass to preserve the favourable effect of the residual surface compression in cold bent or other load bearing applications. The flaws that accumulate on the glass surface during the service life could compromise the residual surface compression. However, the strength of aged toughened glass is not well documented and the availability of naturally aged toughened glass for destructive testing is very limited. Therefore, the two main areas that could be investigated further, are: (a) to establish a reliable artificial ageing method for the evaluation of the strength of aged glass and; (b) to implement this method on toughened glass to evaluate their strength after ageing.

The estimation of the strength of glass (aged or as-received) can be achieved with a stochastic approach when the geometry of the critical flaw is unknown and an explicit approach for morphologically known critical flaws. The Weibull distribution has been identified as the most effective distribution for describing glass strength data [92,93] in the stochastic approach. However, several methods are available for estimating the Weibull parameters and no clear conclusion has been reached thus far, as to which parameter estimation method is more effective for small samples of glass strength data.

2.8 Research aim / Main objectives

This project endeavours to address the above listed challenges by developing the understanding of cold bent glass with the ultimate aim to develop novel, lightweight and durable curved glass units. This project will particularly focus on uncertainties related to the bending process and the aged performance of cold bent glass. Even though its performance during its service life is considered equally important, it is not investigated here as it is thought to be more project-specific, and dependent on the type of application and the expected service life loads.

Cold bending of glass in double curved anticlastic shapes will therefore be investigated experimentally and numerically to identify (global and local) instability phenomena that could potentially cause changes in the shape of the curved glass unit, degradation of its optical quality or even fracture during its production process. This is achieved experimentally and numerically by deforming monolithic fully toughened and thin chemically toughened glass plates at ambient

temperatures with out-of-plane loads. The influence of boundary conditions, geometrical characteristics of the glass plate, number of load points and set-up will be also investigated numerically. The real world usefulness of this research is to establish displacement limits in order to avoid: unwanted instabilities and subsequent problems in retaining the curved shape and; loss of the optical / visual quality of the curved monolithic glass plate. Results will be subsequently compiled in a user-friendly set of guidelines that will make a useful tool for designing / producing cold bent glass.

The mechanical performance of aged toughened glass will be also investigated in this thesis to assess its safe use in cold bent or other load bearing applications. It is difficult to source naturally aged toughened glass specimens and especially chemically toughened glass because of their recent use in structural applications. Therefore, the first step in the evaluation of the performance of aged toughened glass will be to devise an artificial ageing method that introduces realistic damage. Accelerated ageing with a falling abrasive method and an alternative technique involving a scratching method will be used aiming to introduce equivalent levels of damage to those found in the naturally aged annealed glass. The damage induced will be evaluated by means of destructive testing, surface profilometry and pre-fracture and post-fracture optical microscopy.

The best-performing artificial ageing method will be subsequently implemented on toughened glass to evaluate its mechanical performance after exposure to ageing mechanisms. The practical outcome of this investigation is to determine the effectiveness of toughened glass in structural and / or cold bent glass applications and its ability to bear design loads successfully throughout its service life.

2.8.1 Thesis contents

This thesis is divided into 7 chapters. **Chapter 1** comprises the introduction and sets the context of the investigation that will follow in the next chapters.

The present chapter, **Chapter 2** provides an overview of the state of the art for curved glass. The types of glass used in this study are presented in Section 2.2. Section 2.3 describes the available glass curving technologies and discusses the advantages of cold bent glass over conventional heat bending methods. Section 2.4 focuses on the cold bending of glass to identify gaps in knowledge that need to be addressed in the following chapters. Section 2.5 presents an overview of glass strength estimation methods that will be subsequently used in Chapters 4, 5 and 6 for the evaluation of the mechanical performance of aged glass. Section 2.5 provides an overview of the existing research on the mechanical performance of aged glass that could be extrapolated for the evaluation of the strength of cold bent aged glass.

Chapter 3 focuses on the experimental and numerical investigation of the mechanical behaviour of glass during the cold bending process. Cold bending of monolithic fully toughened and thin chemically toughened glass in anticlastic shapes is undertaken experimentally to evaluate their stability and to validate numerical models of the cold bending process. The validated numerical models are then extended for different combinations of set-up and geometries to identify their influence on stability and optical quality during the bending process.

Chapter 4 focuses on the determination of glass strength. The selected method for the destructive testing of glass and the associated numerical models to convert failure load to failure stress are initially presented. Further investigation establishes: (a) the influence of sub-critical crack growth for the chosen stress rate using linear elastic fracture mechanics and fractographic analysis; (b) the most effective method for the statistical analysis of glass strength data and; (c) the minimum number of specimens that are required to obtain reliable strength predictions. These findings are subsequently used in Chapters 5 and 6 for the estimation of glass strength.

Chapter 5 presents an experimental study to evaluate different artificial ageing methods of glass. The aim is to identify a method that can be used to reliably and realistically artificially age annealed glass. A falling abrasive and a scratch-inducing method are trialled to replicate naturally induced damage. The methods are evaluated with non-destructive and destructive techniques. Results are subsequently condensed in a set of guidelines that permit the selection of an artificial ageing method and its parameters for ageing of as-received glass for a target level of exposure.

Chapter 6 presents an experimental study to evaluate the strength of aged toughened glass. The guidelines introduced in Chapter 5 for the artificial ageing of glass are used to artificially age as-received annealed, fully toughened and chemically toughened glass and evaluate their strength after exposure to ageing mechanisms. The ultimate aim of this Chapter is to assess the safe use of annealed and toughened glass in load bearing applications (e.g. cold bent applications).

Finally, **Chapter 7** summarizes significant observations and conclusions of the previous Chapters and proposes directions/areas of future research.

3. Cold Bent Glass

3.1 Introduction

Chapter 2 indicates that cold bending is a simple, energy and seemingly cost effective method for creating curved glass surfaces compared to traditional heat bending methods. However, uncertainties arise on the safe use, stability and optical quality of cold bent glass.

Chapter 3 (Fig. 3.1) aims to address uncertainties related to the stability and the optical quality of cold bent glass by characterising the mechanical behaviour of monolithic glass plates during the cold bending process. In particular, Section 3.2 and 3.3 respectively focus on the cold bending of monolithic fully toughened glass plates and chemically toughened glass plates in double curved anticlastic shapes. The aim is to identify any local and global instability phenomena in the glass that could be triggered during the bending process under different combinations of bending parameters and to investigate the optical quality of cold bent glass. Finally, Section 3.4 summarizes important results and conclusions.

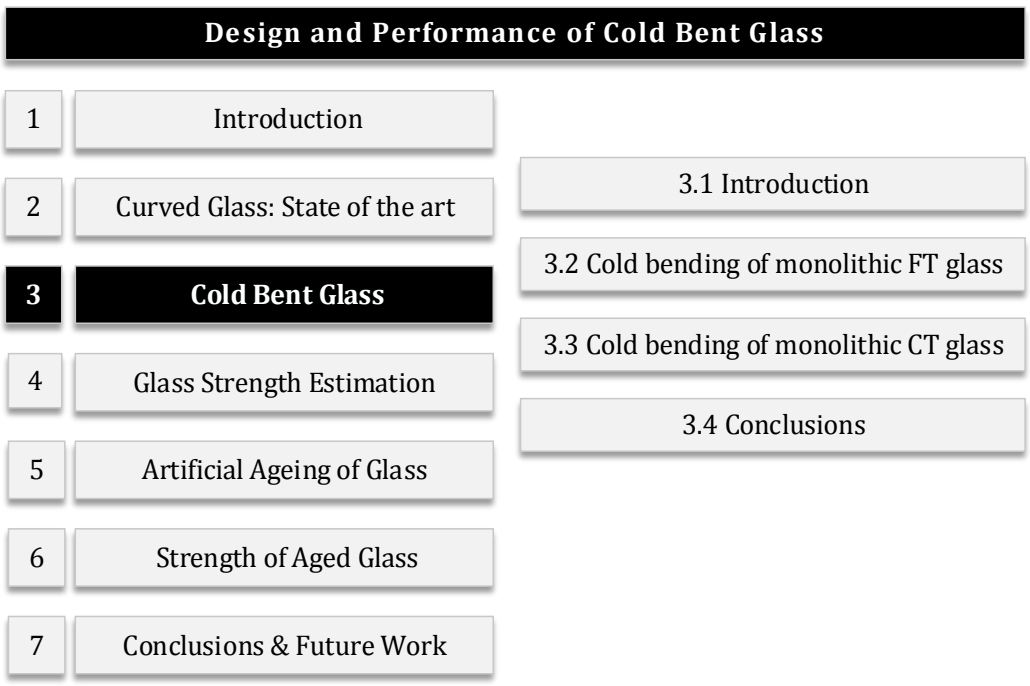

Fig. 3.1: Contents of Chapter 3.

3.2 Cold bending of monolithic fully toughened glass

3.2.1 Introduction

The experimental and numerical research described in this section aims to investigate the mechanical response of point-supported, monolithic glass plates, cold bent into anticlastic shapes. This develops the fundamental understanding of monolithic cold bent glass that will eventually provide the basis for future research on the more complicated subjects of cold bent laminated glass and cold bent insulated glass units. The objective is to identify instabilities that could occur during the cold bending process and may lead to permanent optical distortions or trigger failure. Three different cases of boundary conditions, are tested experimentally and modelled numerically, at the supported corners of the plate. Details of these methods and their results are provided in Section 3.2.2-3.2.4. A further interpretation of the results follows in Section 3.2.5 that infers the response of the plate during the bending process. The validated numerical model is further modified in Section 3.2.5 to investigate the influence of geometrical characteristics of the plate; orientation of the plate and; load locations during the cold bending process. Finally, an optical quality assessment procedure is proposed in Section 3.2.6 to aid designers/manufacturers in achieving cold bent glass with an acceptable optical quality.

3.2.2 Experimental investigation

Cold bending tests were conducted to produce anticlastic shapes frequently required in free form façades. Anticlastic shapes can be achieved imposing out-of-plane forces along the four edges of the plate. The forces may be placed in a variety of locations e.g. continuously along the edges, at intermediate district locations etc.

The simplest configuration was adopted in this research wherein two corners of the plate (B and D, Fig. 3.2a) were restrained locally while the remaining two corners (A and C) were subjected to vertical, out-of-plane, loads that were applied incrementally by means of hydraulic jacks (Fig. 3.2b) actuated by a single manually-operated hydraulic pump. The load was applied at a rate of 1.5-2.5 N/sec. However, the geometric response of the monolithic plate is not deemed to be sensitive to the loading rate. Loading was applied up to fracture of the glass plate in order to capture the full extent of the geometric instabilities. The glass plate consisted of 1000 x 1000 x 5 mm fully toughened glass and no roller wave distortion was detected on the surface of the specimens. The edges were polished prior to toughening in order to reduce the possibility of premature failure from edge flaws.

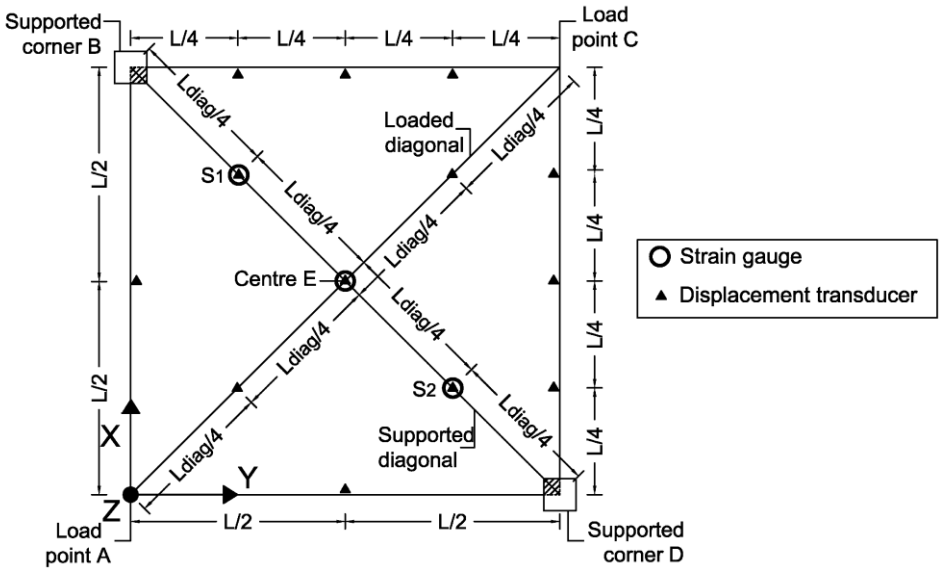

(a)

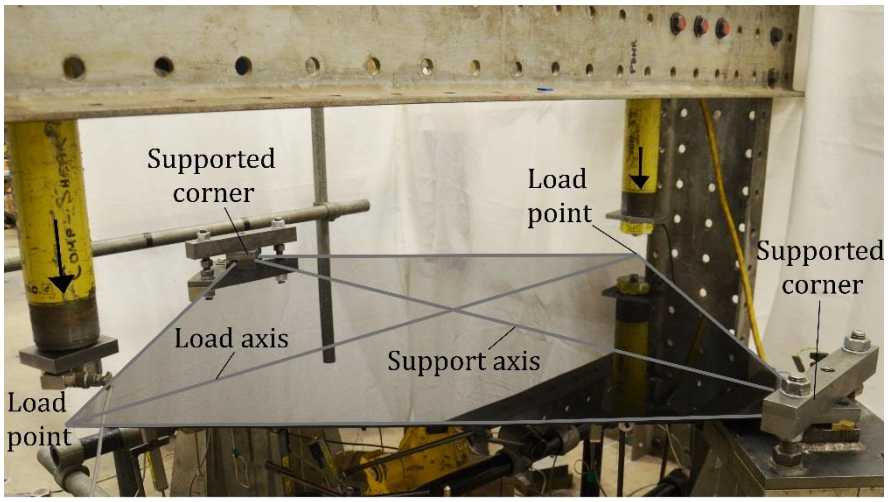

(b)

Fig. 3.2: Cold bending set-up: (a) instrumentation (plan view) and; (b) experimental set-up.

The following three sets of alternative boundary conditions were used at the locally supported corners B and D (Fig. 3.3): clamped supports (CS); pin supports (PS) and; roller supports (RS). Table 3.1 provides an overview of the restrained degrees of freedom for each case. Translational restraints were achieved for Cases CS and PS by clamping the glass between two steel plates; the contact area of which was 37.5 by 37.5 mm (Fig. 3.3a). Additionally, in case PS, rotational freedom was provided by an articulated joint in the clamping system (Fig. 3.3b). Finally, in Case RS, corners B and D were simply supported on spherical supports that were in turn attached to a sliding bearing, thereby allowing rotation and in-plane translation (Fig. 3.3c); even though the translation in the +Z direction of corners B and D was not restrained mechanically, lifting of the plate from the spherical supports is not an issue in this instance because the reaction forces are not expected to change direction during the testing.

Table 3.1: Translational and rotational restraints at corners B and D (U=translation; R=rotation).

Case	Description of supports	Restrained DOF	Area (mm)	Glass dimensions (mm)	No. of tests
CS	Clamped (fixed translation and rotation)	U_x, U_y, U_z, R_x, R_y, R_z	37.5 x 37.5	1000 x 1000 x 5	3
PS	Pin (fixed translation, free in rotation)	U_x, U_y, U_z	37.5 x 37.5	1000 x 1000 x 5	3
RS	Roller (free rotation and translation)	U_z	37.5 x 37.5	1000 x 1000 x 5	3

(a) (b) (c)

Fig. 3.3: Boundary conditions: (a) Case CS: clamped; (b) Case PS: pin and; (c) Case RS: roller supports.

Prior to testing, the residual stress profile through the thickness of the fully toughened glass was obtained by means of a scattered light polariscope (SCALP-05, GlasStress Ltd. [36]). Three spot readings were taken on each glass plate, coinciding with the location of the strain gauges that were subsequently attached to the top and bottom surface of the glass plate (Fig. 3.2a). The mean residual compressive surface stress recorded was σ_r=85 ± 6 MPa. Three nominally identical glass plates were tested per case of boundary conditions to ensure repeatability of the results. The mean failure load (mean failure corner displacement) recorded at the end of the testing was: (a) 486 ± 37 N / (84 ± 8 mm) for Case CS; (b) 645 ± 11 N / (119 ± 1 mm) for Case PS and; (c) 701 ± 19 N / (135 ± 2 mm) for Case RS.

Displacements and surface stresses were obtained from LVDT displacement transducers and rosette strain gauges, respectively (Fig. 3.2a). The vertical (out-of-plane) profile of the support axis was acquired by a custom-made surface profilometer that comprised a horizontal wire gauge and a vertical LVDT displacement transducer, to measure the in-plane location, $l_{x,y}$, and out of plane deflection, δ_z, respectively. The surface profilometer was deployed along the support axis at 100 N load intervals.

3.2.3 Numerical investigation

Numerical models (Fig. 3.4a) of the experimental set-ups were constructed within Abaqus/CAE 6.12-2, using a static Riks analysis [131] in order to capture any geometric instability that may occur during the cold bending process.

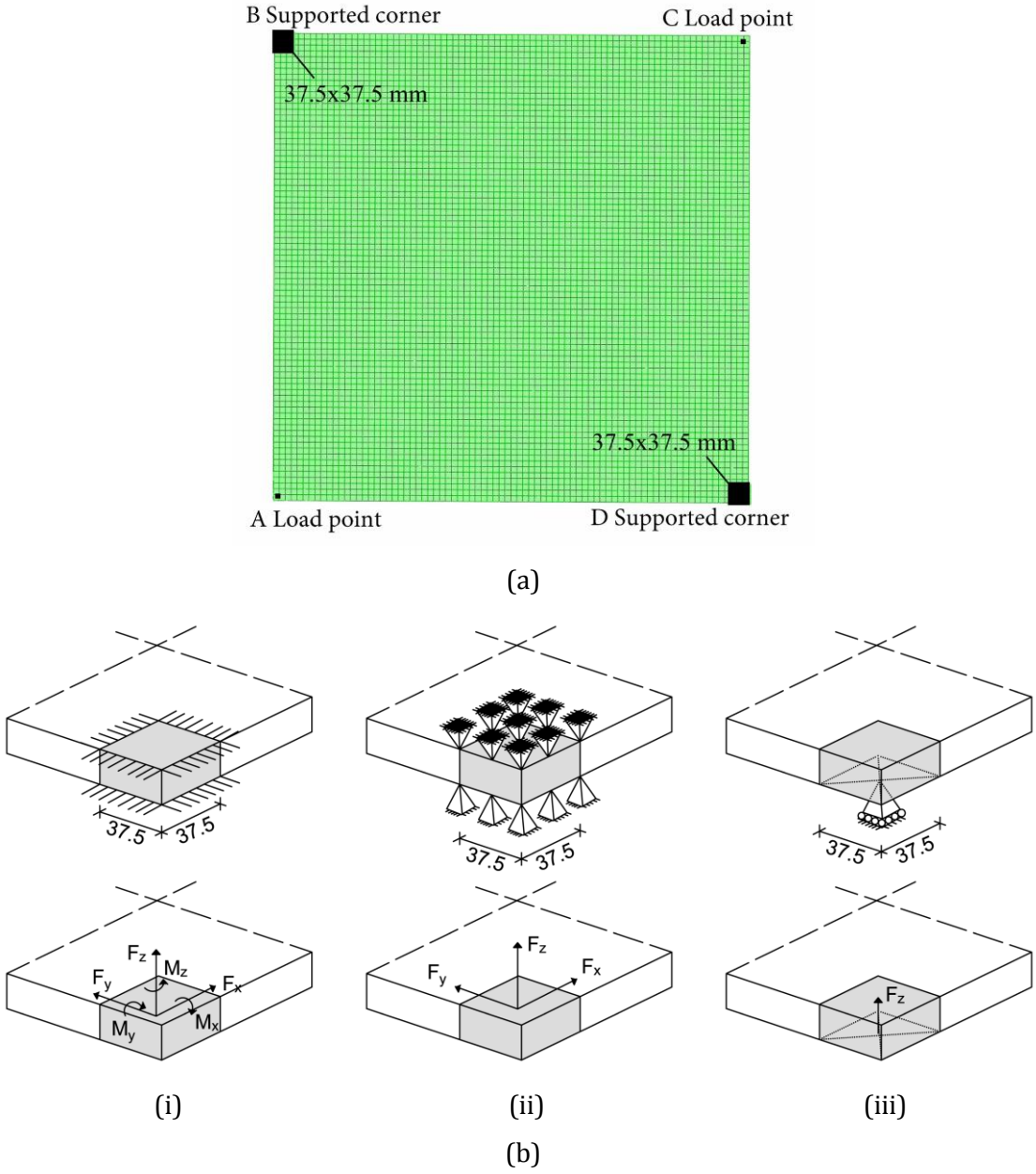

Fig. 3.4: Finite element analysis: (a) numerical set-up and; (b) boundary conditions and reaction forces for (i) clamped supports; (ii) pin supports and; (iii) roller supports.

The Riks method is an incremental analysis used in non-linear problems. In this method the applied displacements and corresponding deflections are unknowns for each increment and the progress of the solution is evaluated using the arc-length. The ratio of the initial arc length, Δl_{in}, i.e. the percentage of the total displacement applied on the first increment of the analysis (set to

0.01), over the total arc length, l_{period} (set to 1.0), provides the initial displacement proportionality factor, ($\Delta\lambda_{in}=\Delta l_{in}/\ l_{period}$) which determines the first increment of the analysis. Consequently, the procedure consists of a prediction and a corrective phase for each increment. In the prediction phase a suitable starting point is computed for each increment; this point is based on the tangential stiffness derived from the previous converged point on the load-deflection path and the distance along the tangent path that is specified by the arc length. The iterative process of the corrective phase follows subsequently to minimize / eliminate the drift error that is produced by the prediction phase until the solution converges to the equilibrium path. This procedure is automatically implemented in Abaqus with an integrated algorithm. The analysis was displacement controlled and set to stop when the displacement at the loaded corners exceeded 100 mm. The self-weight of the plate was modelled as a gravity load, applied prior to the forced displacements at the loaded corners.

The element type and mesh density were selected on the basis of displacement and stress convergence tests in order to provide a good balance between accuracy and computational time. The model consists of twenty-node, quadratic, brick elements with reduced integration properties to prevent shear locking. The glass plate is modelled as 2 elements thick, 80 elements wide and 80 elements long, giving a total of 12,800 elements.

To simulate the boundary conditions that were tested experimentally, the degrees of freedom indicated in Table 3.1 were restrained accordingly at the 18 solid elements (9 on each layer through the thickness of the plate) within the contact area of the supports. In particular, all of the top and bottom surface nodes of the 18 elements within the 37.5 x 37.5 mm contact areas of the supports were restrained for Case CS and PS (Fig. 3.4b i-ii). Contrary, only the bottom surface nodes of the central element (12.5 x 12.5 mm) within the contact area (37.5 x 37.5 mm) of the support were restrained for Case RS (Fig. 3.4b iii); this simulates the area over the sphere of the spherical support that was restrained from displacing vertically in the experimental set-up. Forced displacements up to 100 mm were applied at the two load points. The residual surface stress of fully toughened glass was not included in the numerical model as it is not expected to influence its mechanical behaviour, when in equilibrium. However, this is investigated in detail in Section 3.3.3.

Further numerical analyses beyond the experimental set-ups (Table 3.2) were performed by modifying the validated numerical model to: (i) quantify the influence of geometrical characteristics, orientation of the plate and load locations on the optical quality of the glass plate and; (ii) propose brief design guidelines.

Table 3.2: Numerical models: (a) Square plates and; (b) Rectangular plates.

(a)

Boundary Conditions	Length ratio *LR*	Thickness *h* (mm)	No. of load points	Orientation of the plate during cold bending	No. of FEA models
Case PS	1.00	5*	2	horizontal	1
Case RS	1.00	5*	2	horizontal	1
Case CS	1.00	2, 3, 4, 5*, 6, 7, 8	2	horizontal	7
Case CS	1.00	5	1	horizontal	1
Case CS	1.00	5	2	vertical, horizontal-reverse loading	2
Case RS	1.00	5	2	vertical, horizontal-reverse loading	2
Case CS	1.50	2, 3, 4, 5, 6, 7, 8	2	horizontal	7
Case CS	2.00	2, 3, 4, 5, 6, 7, 8	2	horizontal	7
Case CS	2.50	2, 3, 4, 5, 6, 7, 8	2	horizontal	7
Case CS	3.00	2, 3, 4, 5, 6, 7, 8	2	horizontal	7

(denotes model corresponding to experimental set-up).*

(b)

Boundary Conditions	Aspect ratio *AR*	Thickness *h* (mm)	No. of load points	Orientation of the plate during cold bending	No. of FEA models
Case CS	0.50	2, 3, 4, 5, 6, 7, 8	2	horizontal	7
Case CS	0.75	2, 3, 4, 5, 6, 7, 8	2	horizontal	7
Case CS	1.25	2, 3, 4, 5, 6, 7, 8	2	horizontal	7
Case CS	1.50	2, 3, 4, 5, 6, 7, 8	2	horizontal	7
Case CS	1.75	2, 3, 4, 5, 6, 7, 8	2	horizontal	7
Case CS	2.00	2, 3, 4, 5, 6, 7, 8	2	horizontal	7

3.2.4 Experimental and numerical results and observations

The salient results and observations contain the effect of boundary conditions on the load-displacement response and on the final curved shape of the plate; the validation of numerical results; changes in relative stiffness; local changes in curvature; and surface stress-deflection-load results. These are described in-turn in this section.

The variation of deflection at the centre of the plate (point E, Fig. 3.2a), $\delta_{E,z}$, versus the load, P, applied on each of the free corners is shown in Fig. 3.5a.

Each case of boundary conditions produced different initial central deflections caused by the self-weight of the glass plate and the influence of the specific boundary conditions. Fig. 3.5a also reveals that the boundary conditions have a significant effect on the response of the plate during the bending process. When in-plane displacement is unrestrained at the supported corners (Case RS), the load, P, vs. centre deflection, $\delta_{E,z}$, relationship is almost linear throughout, but when it is restrained the initial linear relationship between load and centre deflection is followed by an end

of the proportionality (P=110 N for Case CS and P=130 N for Case PS). When this load is exceeded, the centre of the plate remains approximately stationary until the applied load reaches a value of 150 N for both cases (Fig. 3.5b). As the load increases further, the deflection of the centre of the plate decreases gradually towards its unloaded position. Furthermore, case CS has a stiffer response compared to the other cases of boundary conditions (Fig. 3.5c).

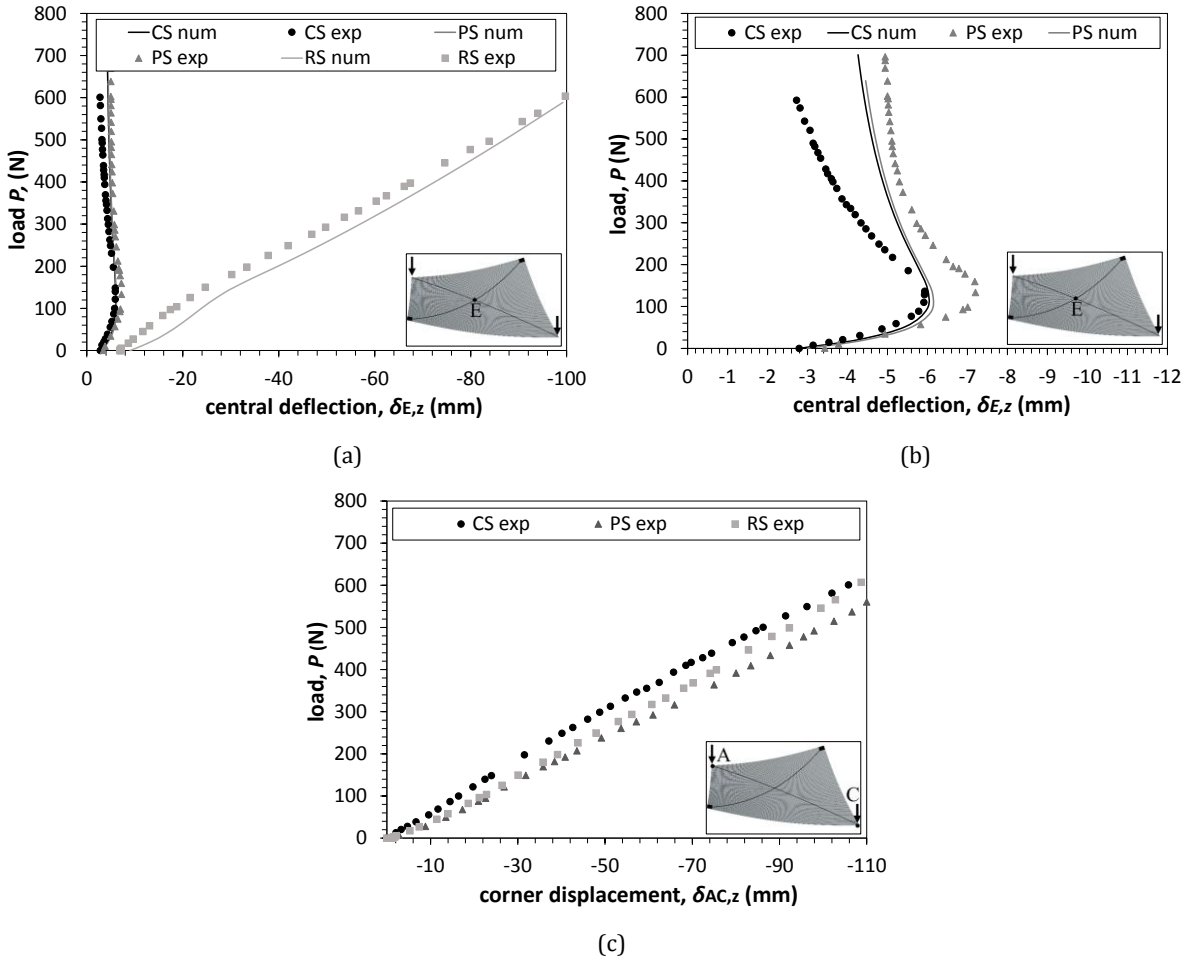

Fig. 3.5: (a-b) Load vs. centre deflection and; (c) Load vs. applied displacement for different boundary conditions.

It was also observed that the final curved shape of the plate is a function of the boundary conditions (Fig. 3.6). The surface geometry acquired during the cold bending process is doubly curved. Double curvature, involves bending about two axes and could be either synclastic or anticlastic. In synclastic surfaces (e.g. paraboloid geometry), the principal curvatures are of the same sign i.e. both centres of principal curvatures are located on the same side of the surface. Whereas in anticlastic surfaces (e.g. hyperparaboloid geometry) the centres of principal curvatures are on alternate sides of the surface. The curvature for Case RS was anticlastic throughout the experiment (Fig. 3.7e-f). This was also observed in the early stages of the bending for the other two cases (Cases CS and PS). However, even though the global anticlastic curvature

is preserved, the curvature in the central regions of the plate becomes synclastic in Cases CS and PS when the applied load, *P,* at each corner exceeds approximately 250 N (Fig. 3.7a-d). Some asymmetries are evident in Fig. 3.7 which can be attributed to minor deviations from symmetry in the initial experimental set-up and are therefore, considered negligible.

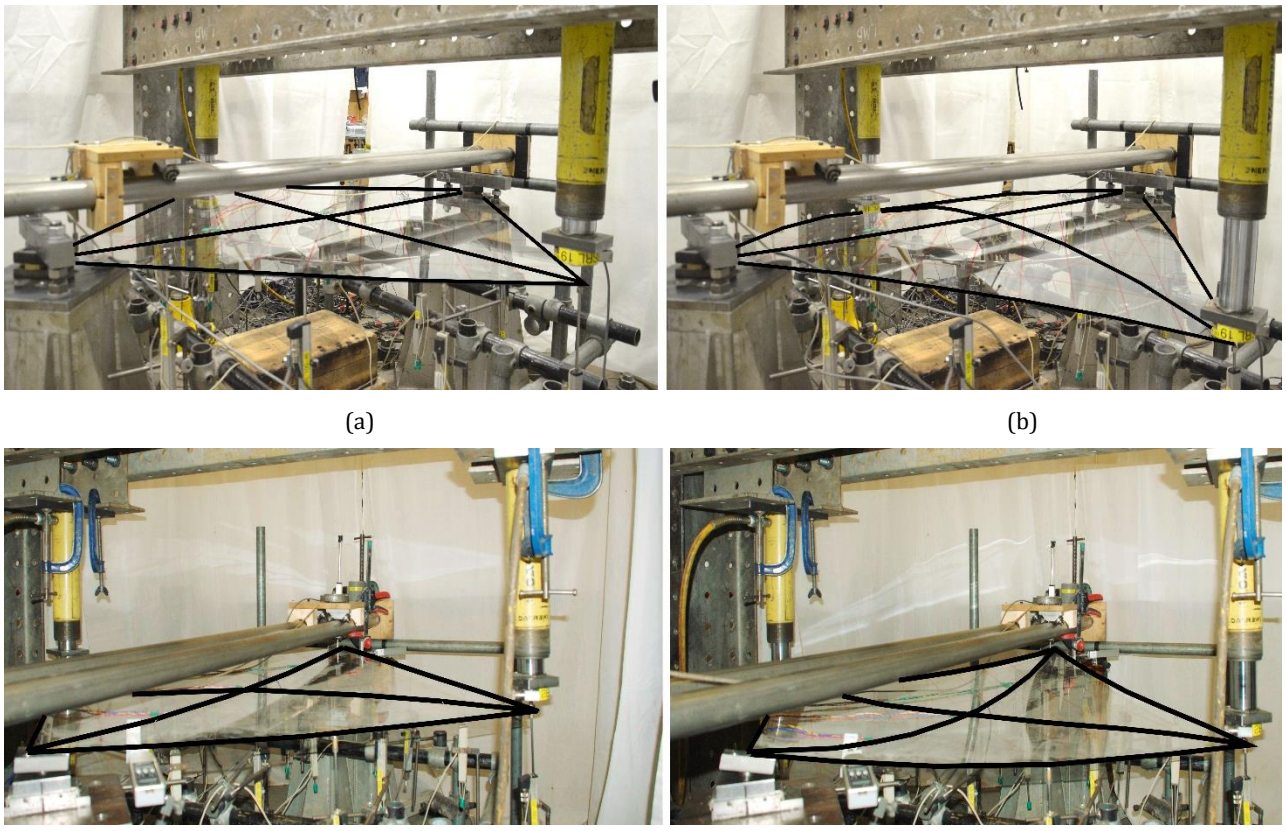

(a) (b)

(c) (d)

Fig. 3.6: Initial and deformed shape: (a-b) for CS and; (c-d) for RS.

The numerical results (Fig. 3.5a & b) show adequate agreement with the experimental data. Differences appear when the numerical model fails to accurately predict: (a) the post-buckling behaviour of the plate for Case CS, where the numerical model results in smaller relative deflections and; (b) the load at which the maximum deflection of the centre of the plate occurs for Case PS. These deviations between experimental and numerical results can be attributed to small imperfections in the experimental set-up. Indeed, it was found that minor misalignments in the boundary conditions during iterations of experimental testing resulted in slightly different experimental results but the overall load-displacement responses remained largely unchanged.

A change in the deformation mode was also observed for all three cases of boundary conditions as the curvature of one diagonal increases while the curvature of the other decreases or remains almost unchanged throughout the bending process. In particular for:

(a) *Case CS and PS*: a reduction in the curvature of the support axis occurs after 150 N while the curvature in the load axis continues to increase. The support axis experiences a reduction in absolute values of deflection increments, between subsequent load steps (Fig. 3.7 & c) whereas the deflection increments of the load axis are almost constant throughout the testing (Fig. 3.7b & d). This indicates that substantial deflection is confined to the load axis (Fig. 3.7b & d);

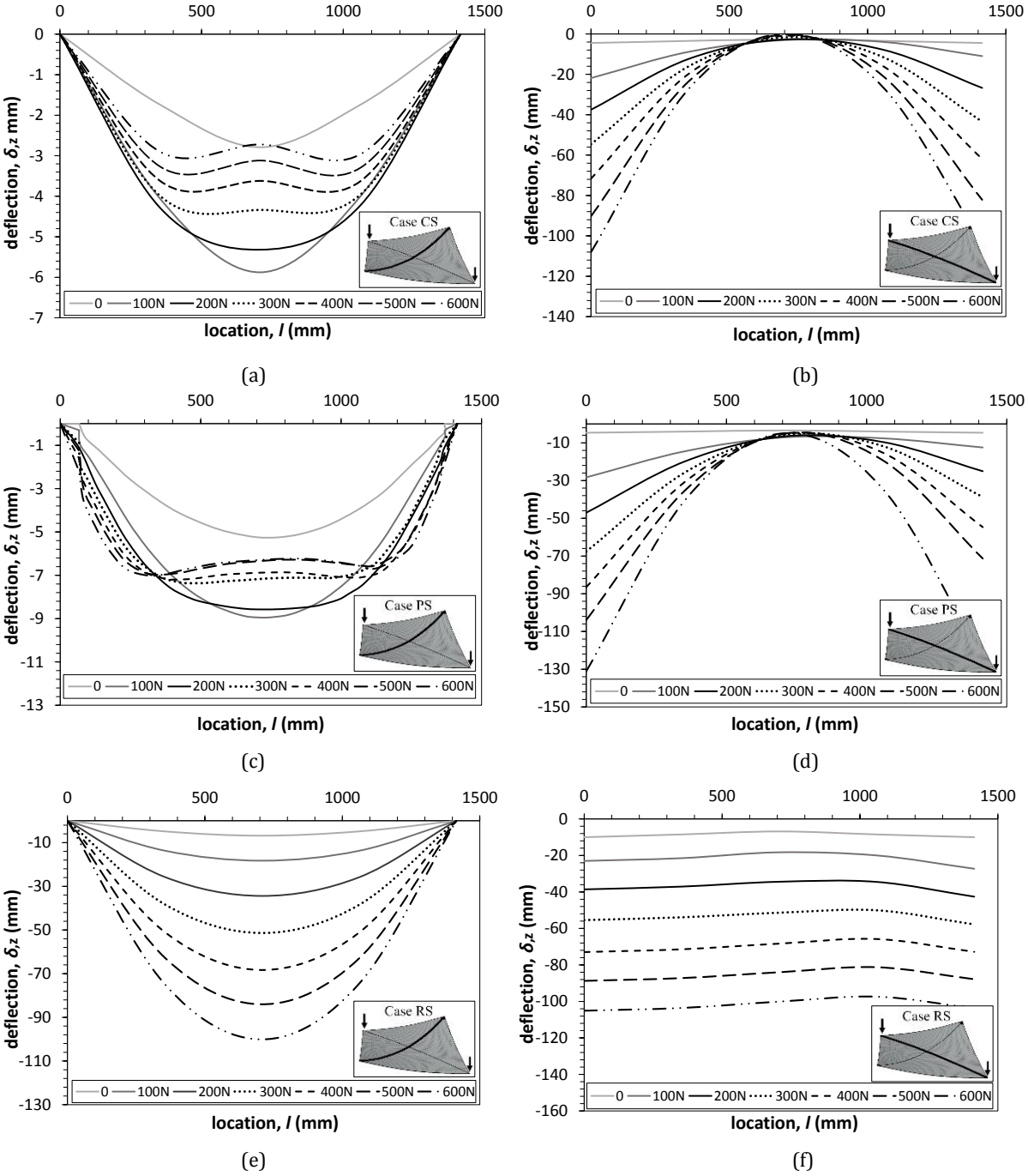

Fig. 3.7: Support and load axis profiles (100N increments) for:(a-b) CS; (c-d) PS and; (e-f) RS (exp. data).

(b) *Case RS*: an increase in the curvature of the support axis occurs during the bending process while the curvature of the load axis remains almost constant and relatively small (Fig. 3.7e & f).

Perhaps even more significantly, a change of sign of curvature was observed along the central third of the length of the support axis for Case CS and PS as the load increases beyond 200 N at each corner; the anticlastic curvature is converted to synclastic locally so that the support axis takes the shape of a two-trough ripple (Fig. 3.7a & c). At this load, the curvature of the central regions of the plate becomes synclastic. This ripple observed in cold bent glass is henceforth referred to as cold bending distortion and can have an undesirable effect on the optical quality of the curved glass similar to roller wave distortion in fully toughened glass.

Qualitative images showing the optical distortion on the surface of the glass were captured during the experimental testing. This was achieved by means of a "zebra" board; the bottom surface of the glass plate was spray-painted black to maximize the clarity of the reflected image on the top surface of the glass and to create a mirror-like effect. Fig. 3.8a shows the distorted reflection of the black and white stripes as well as the distorted reflection of the edge of the zebra board that reveal the cold bending distortion on the cold bent glass plate. Fig. 3.8b shows the distortion resulting from the numerical model in top and side view.

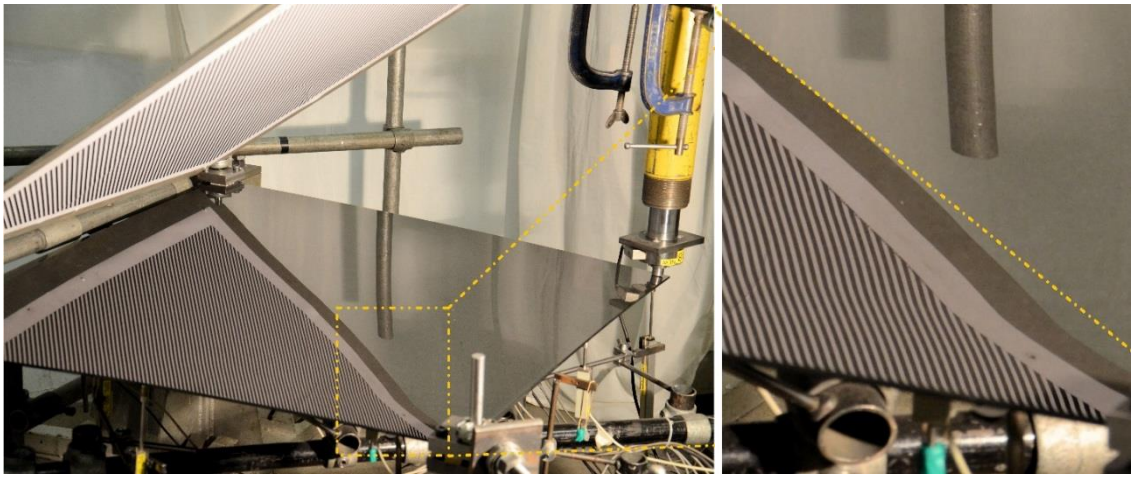

(a)

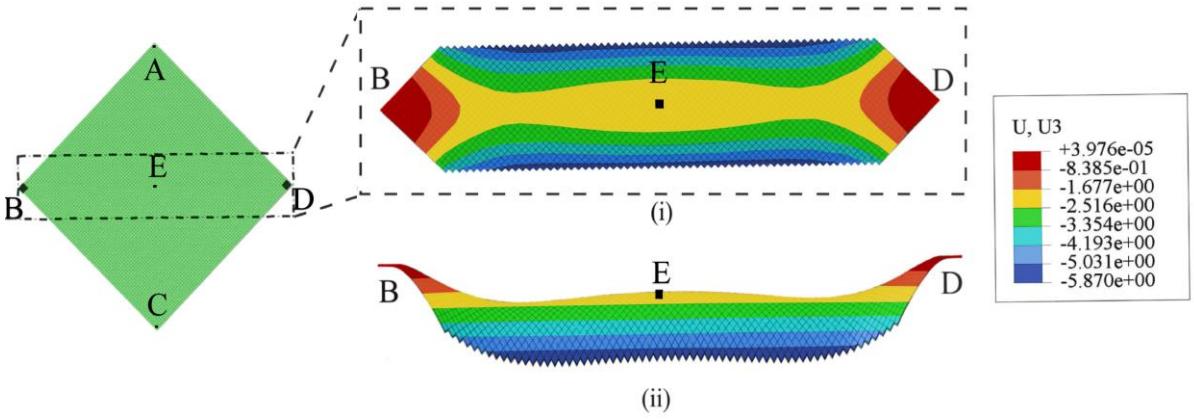

(b)

Fig. 3.8: Cold bending distortion captured: (a) experimentally (distorted reflection on cold bent glass) and; (b) numerically: (i) top view and; (ii) side view (exaggerated 40x vertically).

Stress and deflection data are used in the following four load ranges to describe the mechanical response of a cold bent glass plate for Case CS under increasing load. Principal strain data obtained from strain gauges showed that the directions of the principal strains are aligned to the support and the load axes. In particular, the angle between the support axis and the direction of the maximum principal stresses, θ, is relatively small and ranges between -4.3° and 1.6° during the testing for all the top and bottom stresses for points E and S_1 (Fig. 3.2a). Therefore, the in-plane shear strain between the two axes is negligible. All strain and stress data presented below, refer to the direct principal values in the direction of the support axis.

(i) *$0 \le P \le 110$ N:* During the initial stages of the bending process, the central regions of the plate displace away from the initial flat position creating an anticlastic shape, until the applied load reaches 110 N (Fig. 3.5b). Strain gauge data and the corresponding stresses, at the top surface of the plate along the direction of the support axis BD (Fig. 3.2a), σ_{sd}, show that up to this load, in-plane compressive stresses are present along its length (Fig. 3.9a).

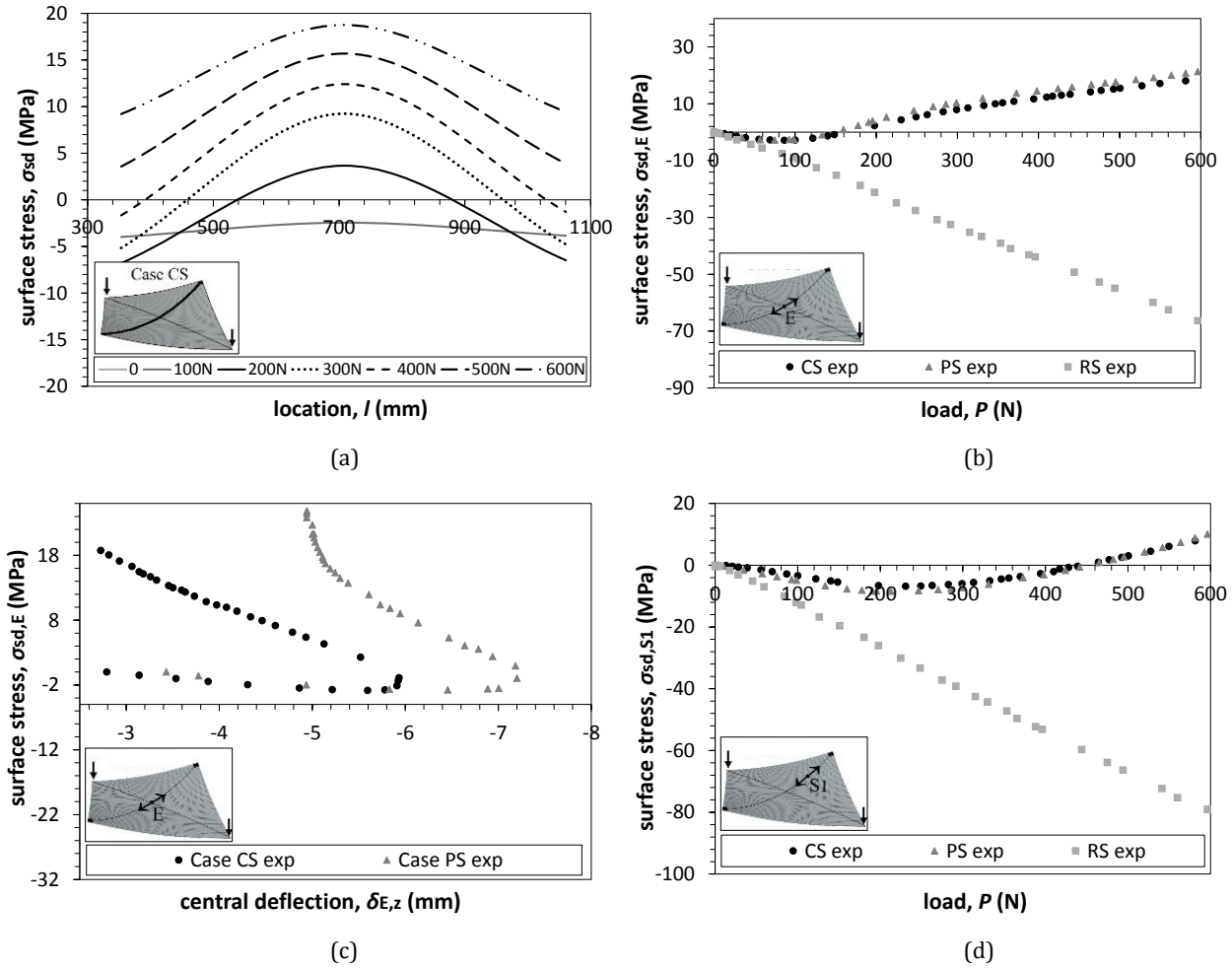

Fig. 3.9: Surface stress (exp.) along support axis for case CS: (a) support axis (100N increments); (b-c) point E; and; (d) point S_1.

(ii) *110 < P ≤ 150 N:* When the load exceeds *P* > 110 N the central regions of the plate cease to deflect vertically and remain relatively stationary up to a load of 150 N (Fig. 3.5b). This is accompanied by a corresponding reduction in the top surface compressive stresses at the centre of the plate (Fig. 3.9b), whereas the top surface compression in the outer third regions (point S_1 and S_2 in Fig. 3.2a) of the support axis continues to increase (Fig. 3.9d).

(iii) *150 < P ≤ 250 N:* As the load increases beyond *P* > 150 N, a change in the deformation mode occurs; the load axis continues to acquire more curvature, while the curvature of the support axis diminishes (Fig. 3.7a & b). Within this load range, the centre of the plate starts to deflect back towards its unloaded position (Fig. 3.5b). This coincides with the accumulation of top surface tensile stresses in the central regions of the plate, $\sigma_{sd,E}$, (Fig. 3.9a, b & c). However, even after this change in the deformation mode, top surface compressive stresses still dominate the outer third parts of the support axis (points S_1 and S_2 in Fig. 3.2a, Fig. 3.9a & d). The maximum value of compression (7 MPa) at S_1 and S_2 is reached at the load of *P*=250 N (Fig. 3.9d).

(iv) *P > 250 N:* At *P*=250 N, the top surface compressive stresses along the support axis start to decrease, as seen at points S_1 and S_2 (Fig. 3.9d). At this load a gradual change of the double curvature of the plate from synclastic to anticlastic occurs in the central regions of the plate. This leads to the appearance of the cold bending distortion that manifests itself as a sinusoidal deformation along the support axis BD (Fig. 3.7a & b). The amplitude of the cold bending distortion, A_{dist}, i.e. the height difference between its highest and lowest point (peak to trough), continues to increase with increasing load until the end of the test at 600 N (Fig. 3.10a). The same applies to the curvature of the edges, κ_{edge}, of the plate (BA, BC, DA and DC in Fig. 3.2a).

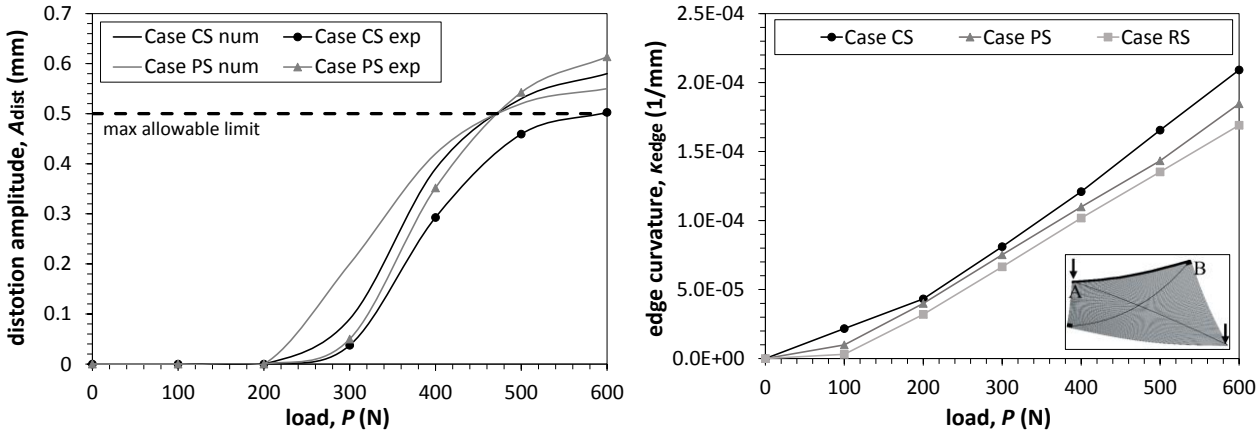

(a) (b)

Fig. 3.10: (a) Cold bending distortion amplitude for CS & PS (exp. & num.) and; (b) edge curvature (exp.).

A response similar to that described above was observed for Case PS. However, for Case RS, neither the cold bending distortion nor the corresponding tensile stresses on the top surface of the support axis were observed. The top surface stresses in the central regions of the RS plate

therefore remained in compression throughout the cold bending process (Fig. 3.9b).

3.2.5 Discussion

Interpretation of the mechanical response of the plate

Two phenomena of interest were observed during the cold bending process: (a) a change in the deformation mode and; (b) the cold bending distortion. The cold bending distortion was only apparent in Cases CS and PS. The response for Case CS can be interpreted as follows:

The development of surface tensile strains in the central regions of the plate ($150 \leq P \leq 250$ N, Fig. 3.9b) confines significant deflections to the load axis AC whereas the support axis starts to decrease in curvature (occurrence of change in the deformation mode, Fig. 3.7a & b).

Strain profiles at points S_1 and E (Fig. 3.11 a-b), reveal that membrane effects are significant along the support axis while the load axis is predominantly subjected to bending effects, as indicated also by Mansfield in [132]. The axial force that is developed at points S_1 and E during the testing can be determined from the membrane strains at these points (Fig. 3.12). The results show that the axial compression initially increases for both points S_1 and E until a load of P=100 N. Above this load the axial force decreases at point E and is finally transformed to axial tension (P=180 N) while the axial compression continues to increase at point S_1. Eventually, the axial compressive stress at point S_1 reaches a critical value of 25 N/mm at a load of P=250 N (Fig. 3.12), and eventually leads to a local instability (local buckling) and the corresponding gradual change of the double curvature from anticlastic to synclastic in the central regions of the plate (occurrence of cold bending distortion, Fig. 3.7a). The sharp peak of axial tension that is developed at point E (Fig. 3.12) at P= 250 N is a manifestation of this instability.

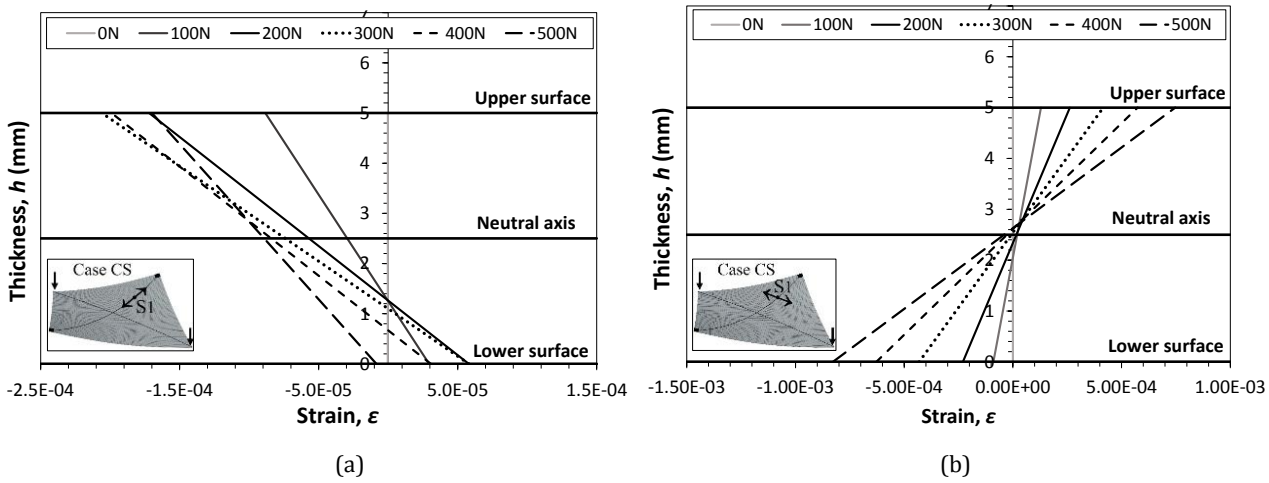

Fig. 3.11: Cross-sectional strain for point S_1 along: (a) the support axis and; (b) the load axis (exp.).

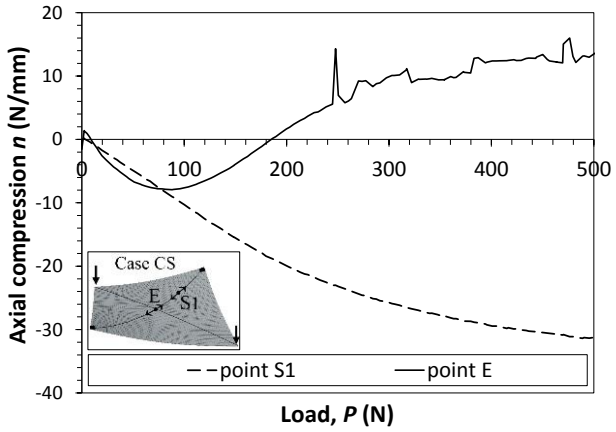

Fig. 3.12: Axial force along the support axis for points S_1 and E during cold bending.

The difference in Case RS is that the supported corners of the plate (B and D) are free to displace in-plane. The absence of in-plane reaction forces allows the support axis to acquire significantly smaller radii of curvature than those of in Cases CS or PS (Fig. 3.7a, c, & e). As the load increases, the curvature of the support axis increases while the load axis retains a constant curvature (change in the deformation mode). The cold bending distortion is not triggered in Case RS when the load is applied in the same direction as the self-weight. However, as shown further down in Section 3.2.5, the cold bending distortion in Case RS is sensitive to the direction of the load with respect to initial imperfections. Therefore, the cold bending distortion can be attributed to the forcing of the plate into a non-developable surface generated by the plate geometry, the boundary conditions and out-of-plane loads.

The numerical and experimental results of the progress of the cold bending distortion during the bending process for Case CS and PS are summarised in Table 3.3. The cold bending distortion initially occurs when the applied load *P* exceeds 200 N at each of the two free corners. At this load, the maximum tensile stress, $\sigma_{t,max}$, on the surface of the glass plate, is 54.9 MPa and 55.6 MPa for Case CS and PS, respectively. This is significantly lower than the design strength of fully toughened glass which can be approximately estimated using part of Eq. 2.4 as follows:

$$f_{AN,d} - \frac{\sigma_r}{\gamma_{M,r}} = 30 - \frac{-85}{1.20} = 100.8 MPa$$

where σ_r is derived from the SCALP measurements.

Therefore, in both cases the cold bending distortion precedes the fracture of the glass plate and potentially exceeds a serviceability limit due to the optical distortions occurring in the curved plate. The amplitude of the cold bending distortion, A_{dist}, can indicate whether distortions are visually acceptable or not. European standards limit the amplitude of roller wave distortion in fully toughened glass to no more than 0.5 mm [16]. This limit is exceeded during the cold bending

process at an applied load of: P=420 N (experimental and numerical data) for Case PS and; P=480 N (numerical data) and P=600 N (experimental data) for Case CS (Fig. 3.10a).

Overall, the experimental and numerical results support Galuppi's [67,68] and Staaks's [65,66] observation that one diagonal straightens during the bending while the other becomes more curved (Fig. 3.7a-f). However, this change in the deformation mode occurred gradually with increasing load and no general limit point buckling (snap-through instability), such as that suggested by Galuppi [67] was observed in these cases (Fig. 3.5b). It is however, shown (refer to Section 3.2.5) that snap-through buckling could be triggered under a specific case of boundary and loading conditions. Additionally, the increase in the curvature of the edges, κ_{edge}, (BA, BC, DA and DC in Fig. 3.2a) also occurred gradually without any sudden change in shape (Fig. 3.10b).

Table 3.3: Num. and exp. data for stress and amplitude of the cold bending distortion.

Case CS					**Case PS**				
P	$\delta_{AC,z,num/exp}$	$A_{dist,num}$	$\sigma_{t,num,max}$	$A_{dist,exp}$	P	$\delta_{AC,z,num/exp}$	$A_{dist,num}$	$\sigma_{t,num,max}$	$A_{dist,exp}$
N	mm	mm	MPa	mm	N	mm	mm	MPa	mm
0	0	0.00	0.0	0.00	0	0	0.00	0.0	0.00
100	-18	0.00	35.9	0.00	100	-18	0.00	40.7	0.00
200	-32	0.00	54.9	0.00	200	-40	0.00	55.6	0.00
300	-47	0.19	70.0	0.04	300	-55	0.20	68.2	0.05
400	-61	0.39	83.4	0.29	400	-69	0.42	79.7	0.35
500	-76	0.54	95.8	0.46	500	-84	0.52	95.6	0.54
600	-90	0.64	107.5	0.50	600	-105	0.55	105.7	0.61

Parametric analysis

The onset of the cold bending distortion is expected to be a function of the geometrical characteristics, the orientation of the plate and the load locations during the bending process. These parameters were investigated by modifying the numerical model to suit (Table 3.2); the results are discussed in-turn.

Geometrical characteristics of the plate

Further numerical simulations were performed to investigate the influence of the initial geometry of the glass plate (thickness, edge length and aspect ratio) on the cold bending distortion. Forced displacements up to 200 mm were applied at the two free corners of the plate for Case CS.

The results show that the cold bending distortion occurs at smaller values of applied displacement during the cold bending process for thinner plates (Fig. 3.13a). However, cold bending of thicker glass plates leads to larger values of maximum distortion amplitude. The recommended limit for roller wave distortion (A_{dist}=0.5 mm) is exceeded when the thickness of

the glass plate exceeds $h \geq 4$ mm. This may compromise the optical quality of the cold bent plate.

Square plates with different edge length and a thickness of h=5 mm were also investigated. This was done by varying the length ratio i.e. the ratio of the edge length of the tested plate, L_p, over the edge length of the reference plate, $L_{p,0}$=1000 mm, $LR=L_p/L_{p,0}=L_p/1000$. Numerical results showed that the cold bending of plates with larger length ratio, *LR,* produces smaller values of cold bending distortion amplitudes under the same bending conditions (Fig. 3.13b). The maximum distortion amplitude for plates with an edge length $L_p \geq 2000$ mm and a thickness of h=5 mm does not exceed the limit of roller wave distortion (A_{dist}=0.5 mm) up to an applied corner displacement of $\delta_{\text{AC,z}}$=200 mm.

The change in the deformation mode was also found to be a function of the aspect ratio, *AR,* of the plate (Fig. 3.14). It was found that square plates required the smallest magnitude of forced displacement at the free corners, δ_{dist}, to trigger cold bending distortion (Fig. 3.14b), and exhibited the smallest distortion amplitude among the aspect ratios investigated ($0.5 \leq AR \leq 2.00$).

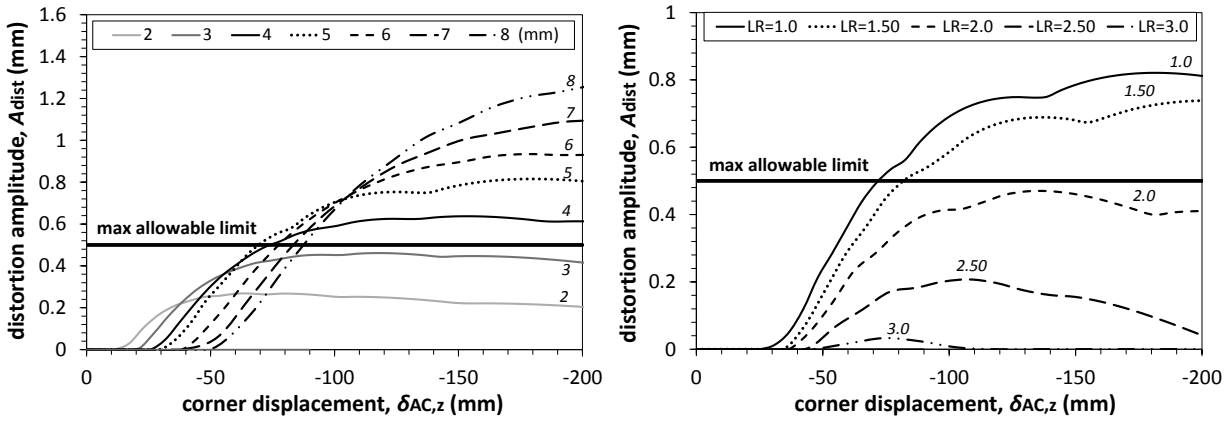

(a) (b)

Fig. 3.13: Cold bending distortion amplitude (num.) for plates of different: (a) thickness (1000 x 1000 x h mm) and; (b) length ratio (L_p x L_p x 5 mm).

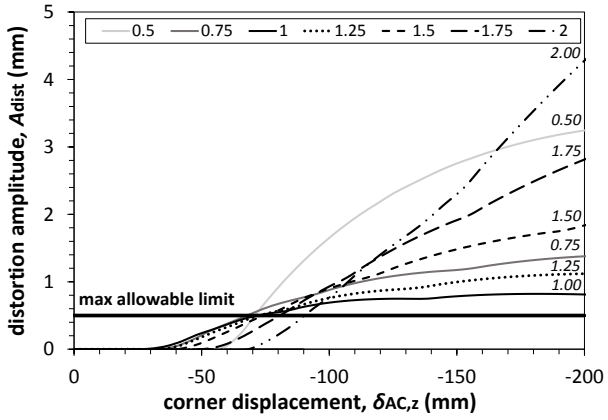

Fig. 3.14: Cold bending distortion amplitude for plates of different aspect ratio ($L_{p,1}$ x $L_{p,2}$ x 5 mm, num.).

Cold bending orientation and load locations

Possible influences of plate orientation with respect to gravity and load locations were also investigated numerically on a 1000 x 1000 x 5 mm glass plate. In particular, the orientation of the plate was considered pertinent as it changes the influence of the self-weight on the cold bending distortion. The plate was modelled for Case CS and RS: (a) horizontally (*Hor*), with the corner displacement applied in the same direction as the self-weight (this is identical to the experimental and numerical models described previously in Sections 3.2.2 - 3.2.4); (b) horizontally (*Hor-reverse*), with the corner displacement applied in the opposite direction to the self-weight and; (c) vertically (*Ver*), so that the self-weight acts in the plane of the glass plate and its influence can be considered negligible.

The results show that initial deviations from the plate's flatness induced by the self-weight have an important influence in the mechanical response of the plate. In *Hor* and *Ver* testing, global instabilities do not occur (Fig. 3.7a-b and Fig. 3.7e-f and Fig. 3.15a-b and Fig. 3.15c-d). However, in *Hor reverse* testing the plate exhibits a change of sign of curvature in both the load and the support axis (Fig. 3.15e-f and g-h). This is observed at a load of P=63 N and a corner displacement of $\delta_{AC,z}$=10 mm for Case CS, while for Case RS the load and corner displacement are P=78 N and $\delta_{AC,z}$=15 mm, respectively. Fig. 3.16a-b shows the deformed plate shape before and after the snap-through instability for Case RS. Therefore, snap-though instabilities are triggered when the out-of-plane loads are applied in a direction opposite to the initial out-of-plane deflection induced by self-weight (or other surface imperfections) of the plate.

Overall, one of two possible configurations occur during the initial stages of the cold bending process, shown in Fig. 3.7e-f / Fig. 3.15e-f for Case RS and Fig. 3.7a-b /Fig. 3.15 g-h for Case CS. The resulting configuration is based on the direction of the external cold bending loads with respect to gravity; when the self-weight acts in the same direction as the external loads, the configuration that is initially formed as a result of the self-weight alone, is maintained when the external loads are applied and global instabilities are prevented (Fig. 3.7a-b & e-f); however, snap-through instability occurs when the self-weight and the external loads act in opposite directions as the plate changes suddenly from one configuration to the other (Fig. 3.15e-f & g-h). In both cases where snap-through instability is noticed, increasing the applied corner displacement further, eventually leads to cold bending distortion (Fig. 3.16c) (CS and RS).

Table 3.4 summarizes both instability phenomena (snap-through instability and cold bending distortion) for the different plate orientations for Case CS and RS. It is clear that cold bending distortion always follows snap through buckling, but that snap-through buckling is not always a precursor of cold bending distortion. Finally, Fig. 3.17 shows that snap-through buckling has a negligible effect on the amplitude of the cold bending distortion.

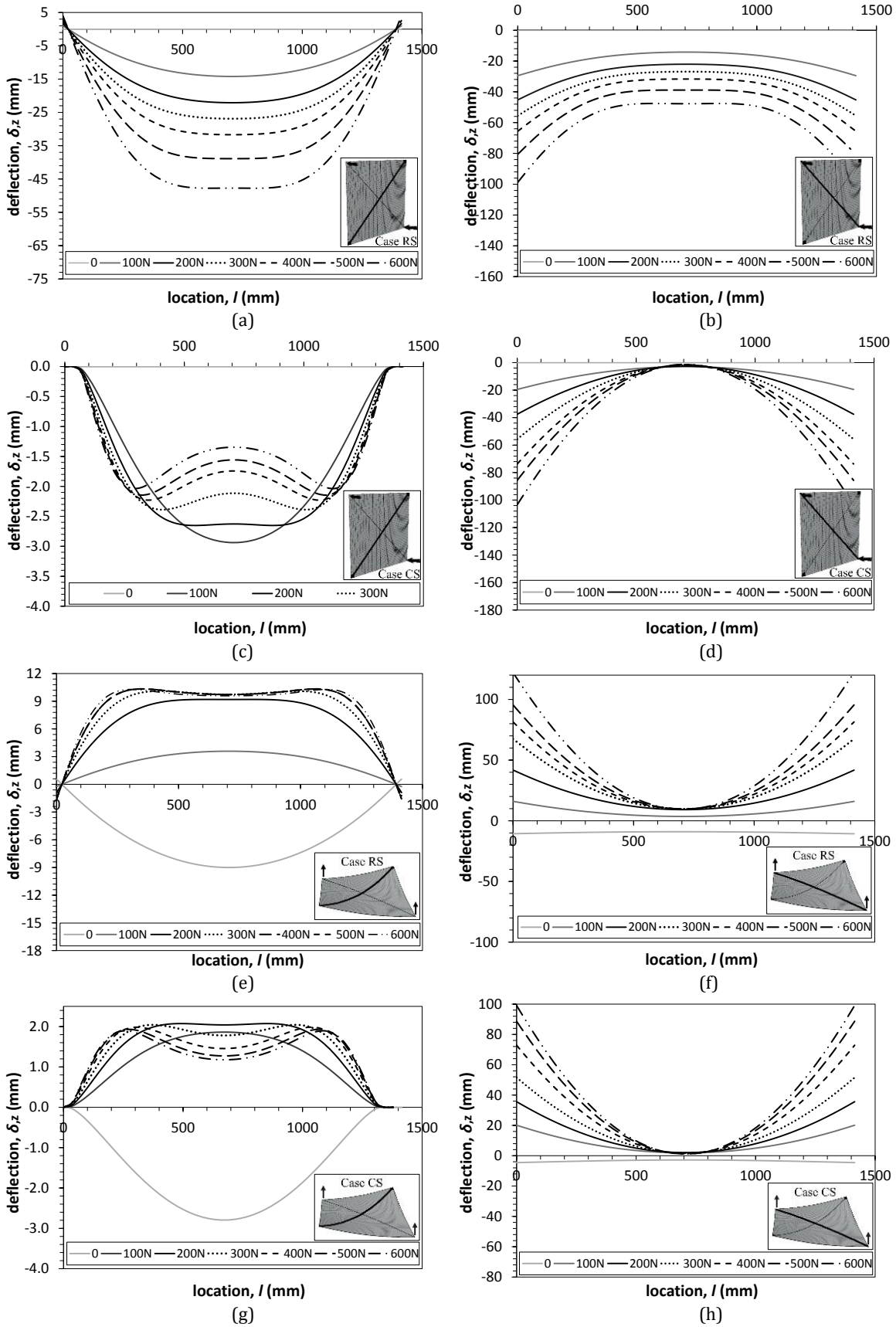

Fig. 3.15: Support and load axis profiles (100 N increments): (a-b) Ver testing-RS; (c-d) Ver testing-CS; (e-f) Hor-reverse testing-RS; (g-h) Hor-reverse testing-CS (num.).

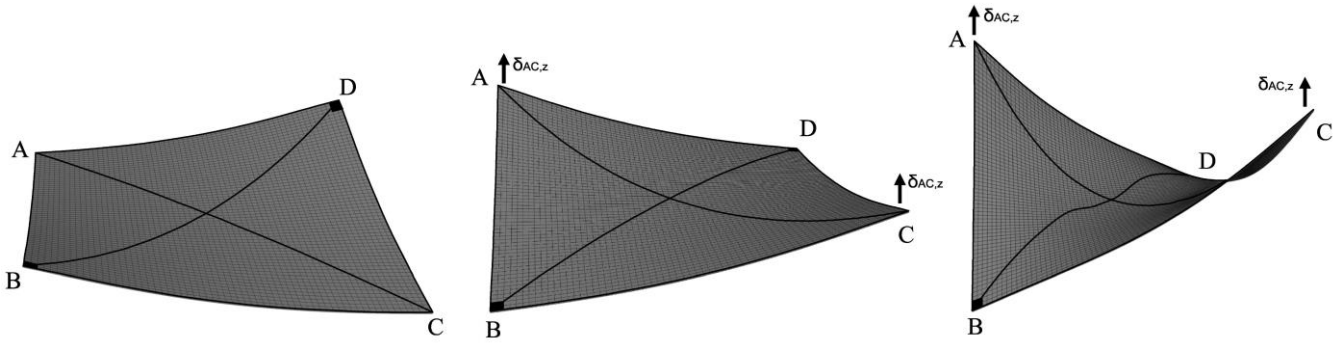

Fig. 3.16: Deformed shape for RS-Hor-reverse testing (exaggerated 30x vertically): (a) self-weight effect before bending; (b) snap-through instability ($\delta_{AC,z}$=15 mm); (c) cold bending distortion ($\delta_{AC,z}$= 63 mm).

Table 3.4: Snap-through instability & cold bending distortion for Case CS & RS.

Boundary Conditions	**Case CS**			**Case RS**		
Plate orientation	Hor	Hor-reverse	Ver	Hor	Hor-reverse	Ver
Snap-through buckling	✗	✓	✗	✗	✓	✗
Cold bending distortion	✓	✓	✓	✗	✓	✗

(✓→occurrence, ✗→absence)

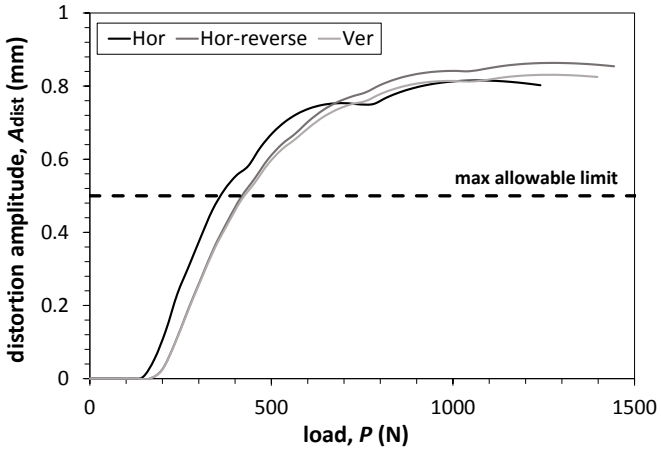

Fig. 3.17: Cold bending distortion amplitude for plates of different orientation for Case CS.

The influence of the number of the load points, *LP,* was also investigated numerically for Case CS. An increase in the plate's stiffness is observed when the number of load points, *LP,* is decreased to one and the number of supported corners is simultaneously increased to three. The onset of the cold bending distortion occurs at larger applied displacement values during the bending process ($\delta_{AC,z}$=50 mm of applied displacement in comparison to $\delta_{AC,z}$=30 mm) while the value of the distortion amplitude is significantly reduced and is, in this instance, below the recommended limit for roller wave distortion (Fig. 3.18).

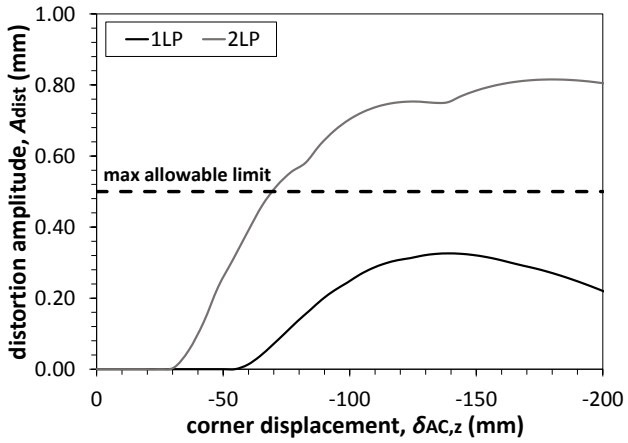

Fig. 3.18: Influence of the number of load points on the amplitude of the cold bending distortion.

3.2.6 Evaluation of the optical quality of cold bent monolithic glass plates

An optical quality evaluation procedure for predicting cold bending distortion in cold bent monolithic glass plates in anticlastic shapes is proposed in this section. This evaluation procedure is not a comprehensive design guide for cold bent glass, because among other things, the strength of glass is not considered. The evaluation procedure therefore provides the serviceability limit checks required to achieve an acceptable optical quality of the curved monolithic plate at the end of the cold bending process. Results are only provided for glass plates that are supported at two corners with the boundary conditions of Case CS. The evaluation procedure is based on a numerical parametric analysis that was performed for plates of different geometrical characteristics.

In particular, plates of different thickness h, aspect ratio AR for rectangular plates, or length ratio LR for square plates of different size, were considered in order to populate three dimensional charts. Two dimensional views taken from these charts and shown in Fig. 3.20 and Fig. 3.21. The charts are useful for establishing the applied corner displacement, δ_{dist} at which the cold bending distortion occurs and for determining the amplitude of the cold bending distortion, A_{dist}. This evaluation procedure is valid for: (a) square plates with: edge length ranging between $1000 \leq L \leq 3000$ mm and thickness ranging between $2 \leq h \leq 8$ mm and; (b) rectangular plates with one edge length ranging between $500 \leq L_{p,1} \leq 2000$ mm while the other edge length is $L_{p,2}$=1000 mm. Their thickness also ranges between $2 \leq h \leq 8$ mm.

The proposed procedure for assessing cold bending distortion is as follows (Fig. 3.19):

(1) Define the geometrical characteristics of the glass plate. These include the thickness of the plate, h, the length ratio, LR for square plates or the aspect ratio, AR, for rectangular plates;

(2) Define the desired cold bending characteristics i.e. the curvature, κ, and consequently the forced displacement, $\delta_{AC,z}$, that is to be applied at each of the two free corners of the plate to produce the desired curvature. These would typically be determined from a finite element analysis of the plate on a case-by-case basis or from simple geometrical calculations based on the desired radius of curvature;

(3) Determine the applied displacement δ_{dist}, that triggers the onset of the cold bending distortion (Fig. 3.20);

(4) Establish whether cold bending distortion occurs in the process of achieving the desired cold bending geometry i.e. whether $\delta_{\text{dist}} < \delta_{\text{AC,z}}$ (Fig. 3.20 a/b);

(4a) for $\delta_{\text{dist}} > \delta_{\text{AC,z}}$ the desired geometrical and cold bending characteristics do not cause cold bending distortions and the optical quality is therefore unaffected;

(4b) for $\delta_{\text{dist}} \leq \delta_{\text{AC,z}}$, cold bending distortion occurs and the distortion amplitude, A_{dist}, should be quantified in order to determine whether it exceeds an acceptable value of distortion (e.g. limits set in EN12150-1:2000);

(5) Use the desired forced displacement at the free corners, $\delta_{\text{AC,z}}$, in Fig. 3.21a-f to quantify the distortion amplitude;

(6) Determine whether the distortion amplitude exceeds $A_{\text{dist}} > 0.25$ mm or another user-prescribed value;

(6a) for $A_{\text{dist}} < 0.25$ mm, the amplitude is considered acceptably low and its effect on the optical quality is negligible;

(6b) for $0.50 \geq A_{\text{dist}} \geq 0.25$ mm, the cold bending distortion could be visible depending on the location and the incidence of reflections on the glass;

(6c) for $A_{\text{dist}} > 0.50$ mm, the cold bending distortion will be clearly visible and is deemed unacceptable;

(7) If A_{dist} obtained from step 6, is considered unacceptable for the specific application, the geometrical and/or bending parameters should be modified accordingly and the cold bending distortion should be re-assessed from step (3) until acceptable optical quality is achieved.

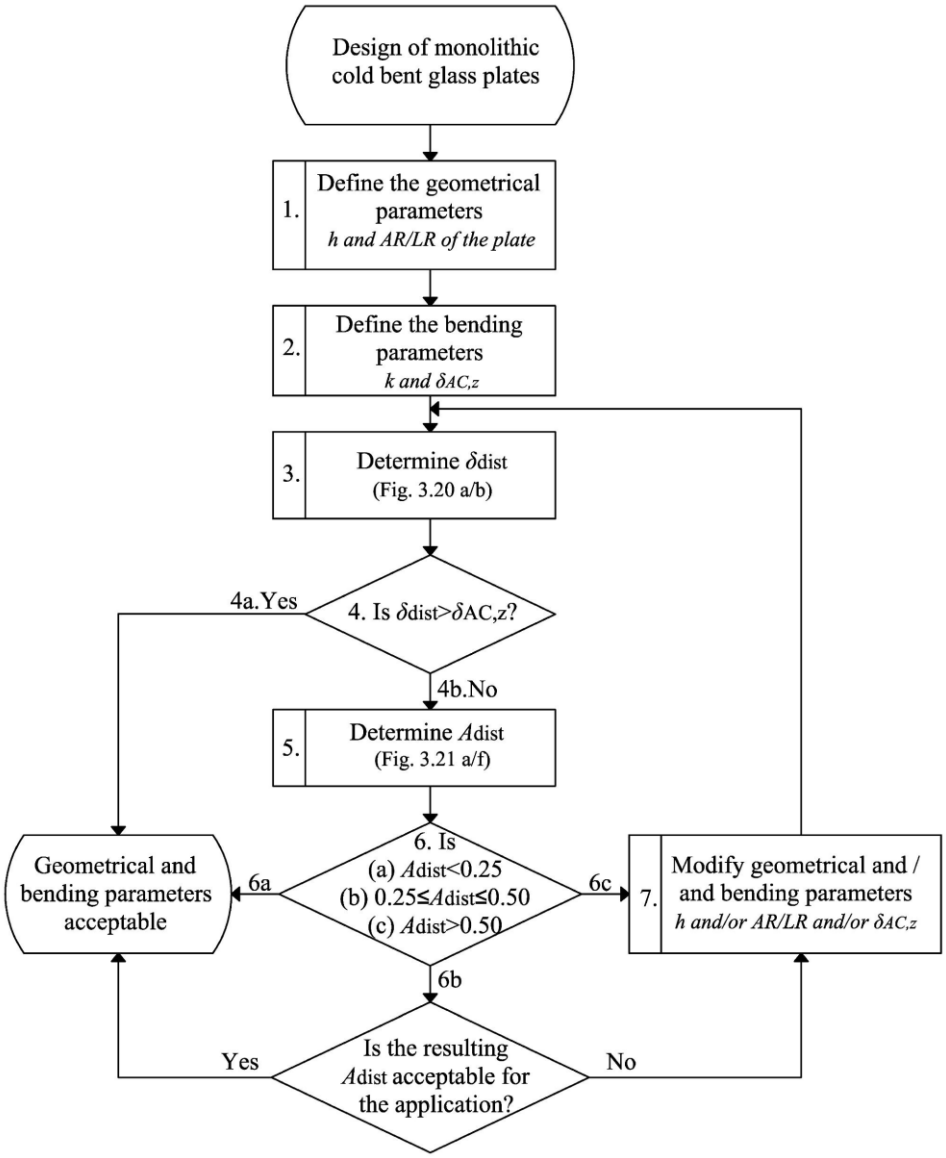

Fig. 3.19: Optical quality evaluation procedure for cold bent monolithic glass plates.

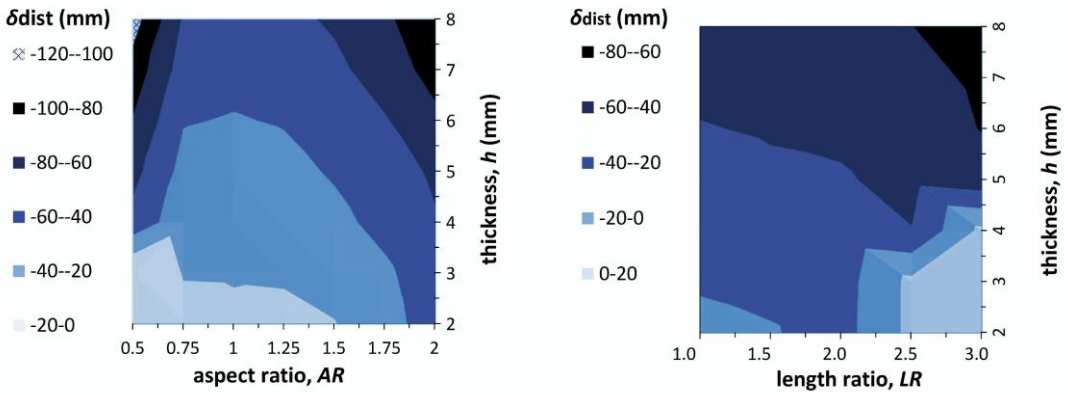

(a) (b)

Fig. 3.20: Applied displacement at the cold-bending-distortion onset for plates of different thickness and: (a) aspect ratio and; (b) length ratio (num.).

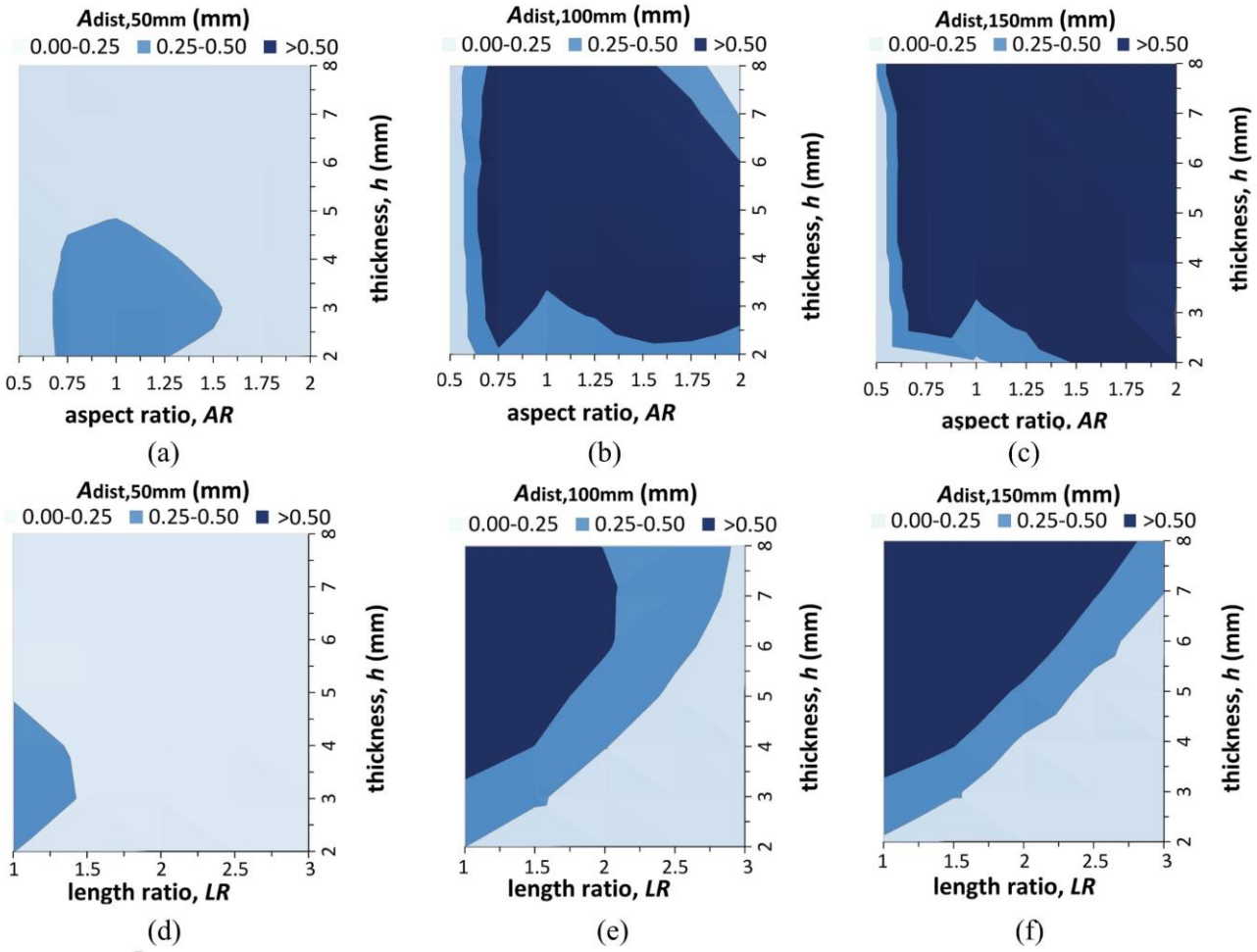

Fig. 3.21: Cold bending distortion amplitude for plates of different thickness and: (a-c) aspect ratio and; (d-f) length ratio for: (a&d) 50 mm; (b&e) 100 mm and; (c&f) 150 mm of applied displacement (num.).

3.2.7 Conclusions on the cold bending of fully toughened glass

Cold bending of monolithic, corner-supported, fully toughened glass plates in double curved anticlastic shapes with out-of-plane loads revealed that a change in the deformation mode and two un-related instability phenomena could be triggered during the cold bending process.

The change in the deformation mode appears as the curvature of one diagonal continues to increase while, depending on the choice of boundary conditions, the curvature of the other diagonal decreases or remains constant. When in-plane displacement is restrained at the supported corners (Case CS & PS), significant deflections are restricted along the support axis during the change in the deformation mode, due to the membrane action mobilised by the boundary conditions at the supported corners. Therefore, significant deflections are confined to the load axis. This phenomenon occurs at an even earlier stage during the cold bending process if rotation is also restrained at the supported corners. However, when in-plane displacement is

unconstrained (Case RS), the load axis does not show any significant increase in curvature compared to the support axis.

Global instabilities (snap-through buckling) were only observed when the out-of-plane loads on the two free corners were applied in a direction opposite to the initial out-of-plane deflection induced by self-weight (or other surface imperfections) of the plate. This phenomenon appeared in the early stages of the cold bending process as an abrupt change of the direction of curvature in both diagonals and can be considered as a particular case of this change in the deformation mode.

The second phenomenon of interest during the cold bending process is the occurrence of a local instability (buckling). As the applied displacement at the loaded corners increases beyond the change in the deformation mode in Case CS and PS, a sinusoidal ripple, termed cold bending distortion, appears along the length of the support axis. This phenomenon followed in all the cases where snap-through instability had occurred i.e. even when in-plane displacement was allowed at the supported corners (Case RS). Therefore, the cold bending distortion is a function of boundary conditions and preceding global instabilities that are influenced by the combination of the self-weight and the direction of the applied load. This ripple can have a detrimental effect on the aesthetic quality of the curved plate as it may cause unwanted optical distortions, thereby triggering a serviceability limit state failure of cold bent glass.

The amplitude of the cold bending distortion can be used to evaluate the optical quality of the curved glass plate as recommended in EN 12150-1:2000 [16]. The parametric analysis performed, revealed that the amplitude of the cold bending distortion is very sensitive to the choice of boundary conditions, geometrical characteristics of the plate and load locations. Larger distortion amplitudes were found in plates with pin supports (Case PS), larger thickness or larger aspect ratio.

All of the above parameters should be taken into account during the design of cold bent glass plates in order to avoid snap-though instabilities and to ensure the optical quality of the curved plate. An optical quality evaluation procedure was proposed for the cold bending of glass plates in a horizontal position, with two clamped corner supports (Case CS) and loaded at the remaining two free corners in the direction of the self-weight to avoid snap-through instabilities. This evaluation procedure can be used to determine the applied displacement at which cold bending distortion occurs and to quantify its amplitude, thereby providing a measure of the optical quality of the cold bent glass plate.

3.3 Cold bending of monolithic thin chemically toughened glass

3.3.1 Introduction

Experimental and numerical investigation were undertaken to characterise the response of monolithic thin chemically toughened glass plates. The aim of this Section is to identify differences, if any, in the response of chemically toughened glass with that of fully toughened glass (Section 3.2) and to investigate the influence of its smaller thickness and its higher level of residual surface compression. Section 3.3.2 and 3.3.3 describe in turn the experimental and numerical results. Finally, Section 3.3.4 provides salient conclusions.

3.3.2 Experimental investigation and results

Experimental set-up

A 1000 x 1000 x 2 mm, alumino-silicate chemically toughened glass plate was cold bent into a double curved anticlastic shape as was done for fully toughened glass in Section 3.2.2. The plate was clamped on two opposite corners (over a contact area of 37.5 x 37.5 mm on each corner, Fig. 3.3a & Fig. 3.22b). The cold bending set-up for chemically toughened glass was identical to that of the fully toughened glass plate with the exception that the central regions of the plate were vertically supported prior to the bending to stabilize the glass and facilitate clamping due to the flexible nature of the glass. The temporary central supports were removed after clamping to allow the action of the self-weight to take place. Similarly to the fully toughened glass plate, the chemically toughened glass was subsequently cold bent in shape by incrementally applying out-of-plane loads at the two remaining, free corners with hydraulic jacks that were operated simultaneously through a manually handled pump with a loading rate of 1.5-2.5 N/sec.

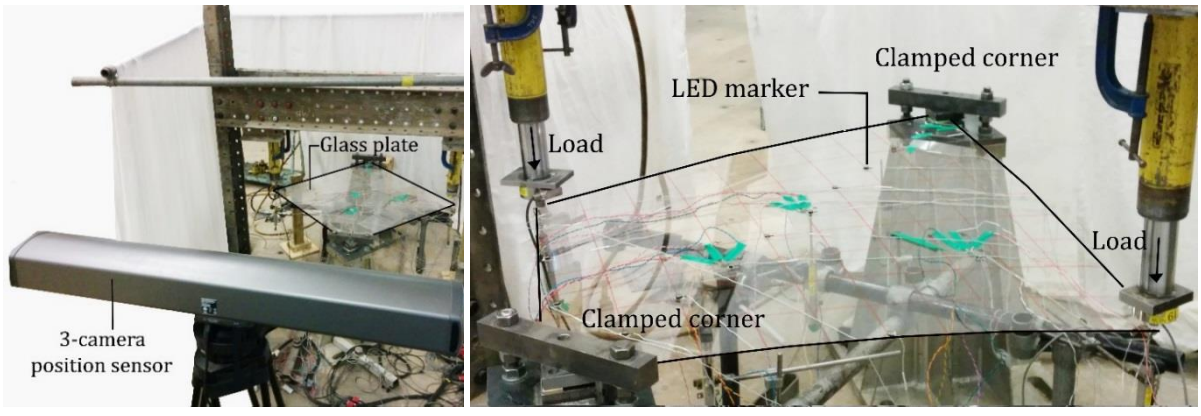

(a) (b)

Fig. 3.22: Cold bending of chemically toughened glass: (a) 3D camera system and; (b) cold bent glass set-up.

Strain gauges were positioned on the centre and at one/fourth intervals of the two diagonals on top and bottom surfaces to capture the stress behavior of the plate and to allow distinction

between bending and membrane components in the cross section. An optical measurement system (Optotrak, NDI Ltd.) was used for displacement data; this system (Fig. 3.22a-b) incorporates three cameras within a single position-sensor to obtain the 3D coordinates of LED markers on the glass surface that flash at a frequency of 1000 Hz. The readings obtained by this system were validated with LVDT displacement transducer readings (results were found to be within ±2% of each other).

Experimental results

The change in the deformation mode and the cold bending distortion found in fully toughened glass (Section 3.2) are also evident in chemically toughened glass plates. In particular, the initial change in the deformation mode occurs as the curvature of the load axis increases while the support axis decreases in curvature; this phenomenon is followed by the onset of the local instability / cold bending distortion i.e. a sinusoidal effect (Fig. 3.23a) along the length of the support axis, that depending on its amplitude, could degrade the optical quality of the cold bent glass. This phenomenon is attributed to a build-up of axial compression (Fig. 3.23b) along the direction of the support axis which eventually triggers this local instability as was also found for the fully toughened glass plates (Section 3.2).

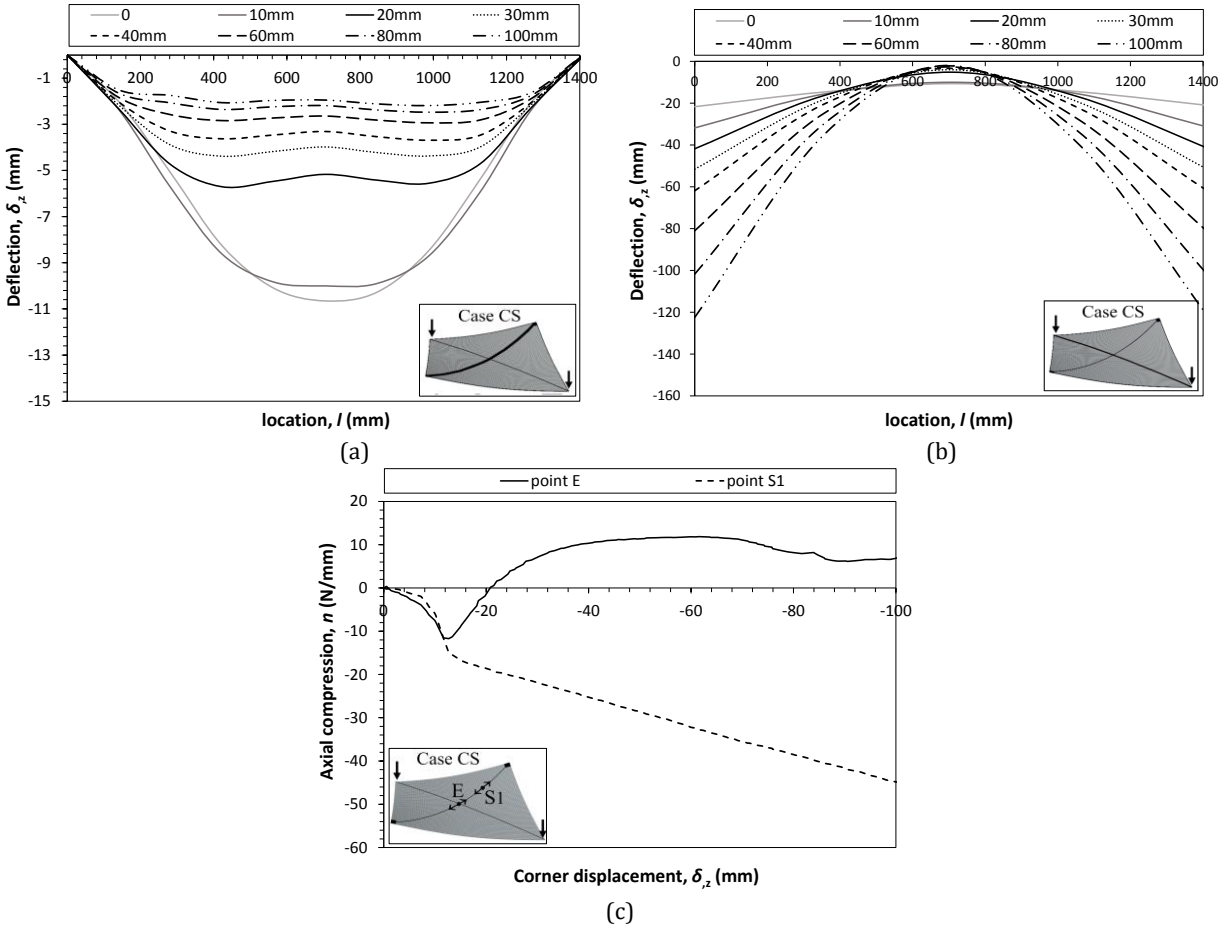

Fig. 3.23:(a-b) Support and load axis profiles and; (c) axial force at points S_1 & E along support axis.

3.3.3 Numerical investigation and results

Cold bending of thin chemically toughened glass is investigated numerically in this section. The differences with the numerical model developed in Section 3.2.3 for fully toughened glass, lie in the higher Young's modulus of alumino-silicate glasses, the higher level of residual surface compression and the smaller thickness. These will be investigated in this section.

Material properties

The numerical model of Section 3.2.3 was modified to suit the thickness and material properties of alumino-silicate chemically toughened glass (h=2 mm and E=72 GPa, v=0.21 and d=2440kg/m^3, Table 2.1).

The results show that the numerical model predicts a similar trend with the experimental response however, significant discrepancies are present (Fig. 3.24a-b). In particular, the numerical model predicts larger initial deflections under the effect of the self-weight at the centre of the glass plate, (Fig. 3.24a) while the change in the deformation mode occurs at higher loads (Fig. 3.24b).

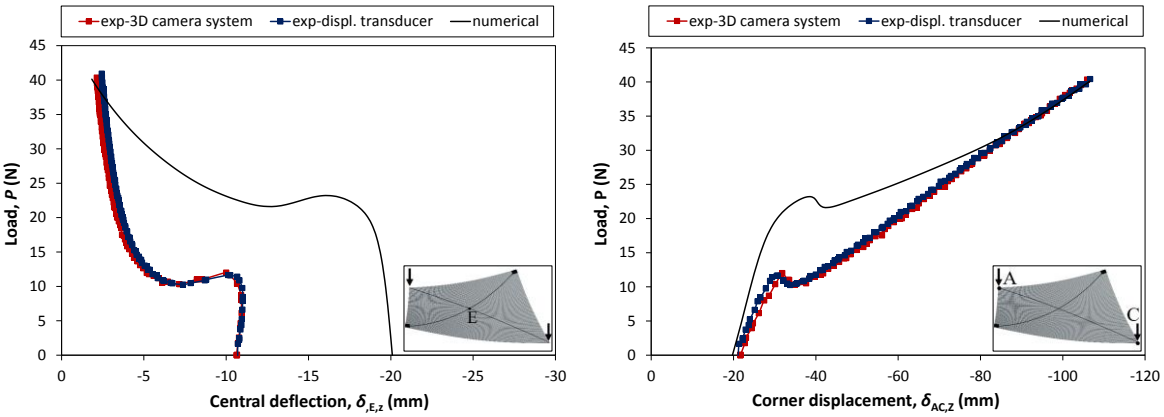

(a) (b)

Fig. 3.24: Load vs. central deflection for case CS and; (b) load vs. applied displacement.

The discrepancies between experimental and numerical results could be attributed to: (a) the high residual surface compression of chemically toughened glass as previous research on semi-conducting materials indicates (Section 2.4.2); (b) in-accurate material properties for the chemically toughened glass and; (c) deviations between the experimental set-up and the numerical model; small modifications / misalignments in the experimental set-up may result in large deviations due to the small thickness of the glass. Scenario (c) is potentially the most likely among the three; experimental clamping of the plate in its flat position with temporary central supports that prevent gravity imperfections (Section 3.3.2) could result in locking of axial stress

and therefore, the change in the deformation mode and the subsequent instability occur at lower loads. However, scenario (a) is investigated further in the following section.

Level of residual surface compression

The influence of residual surface stress is investigated numerically in this section at a macroscopic level, by incorporating the residual stress profile of toughened glass in the cold bending model that was developed previously in Section 3.2.3. This is achieved with the following steps:

(i) a FORTRAN script file (e.g. FORTRAN.for) is created within Visual Studio to describe the imposed stress field. This script file refers to SIGINI, an Abaqus subroutine which is specifically designed to assign a stress array to each integration point through the plate's cross section. The residual stress is then extrapolated to each node within the model. Two such FORTRAN scripts are shown in Appendix A: one for fully toughened and one for chemically toughened glass;

(ii) the Abaqus model for the cold bending (Section 3.2.3) is modified to incorporate an additional analysis step prior to the bending step; this step is used to extrapolate the residual stress to the nodes;

(iii) the Abaqus input file (e.g. INPUT.inp) created in the previous step (ii) is subsequently, manually modified to include the user-defined stress field; the following text is added below the steps section (i.e. below the definition of the additional step and the bending step) in the input file:

*INITIAL CONDIITONS, TYPE=STRESS, USER

(iv) the FORTRAN script file (FORTRAN.for) is linked to the previously modified input file (INPUT.inp). This is achieved by submitting the Abaqus "job" for analysis using the command line as follows:

Abaqus job=INPUT user=FORTRAN interactive

The self-weight of the plate is neglected and a 1000 x 1000 x 5 mm, soda lime silica (E=70 GPa and v=0.23), glass plate is considered for this investigation.

The following stress fields are investigated:

(i) *AN*: annealed glass with a zero residual stress profile $\sigma_r(Z) = 0$ for $0 \le Z \le 5mm$.

(ii) *FT-SCALP*: Fully toughened glass with a residual surface compression of $\sigma_{r,surf}$=-85.1 MPa; the parabolic stress profile was obtained by SCALP-05, GlasStress Ltd. for the toughened glass plates of Section 3.2 and is described by Eq. 3.1. The obtained stress profile shows a slight deviation from equilibrium over the plate's thickness.

$$\sigma_r(Z) = -20.59 \cdot (Z - 2.5)^2 + 43.58 \text{ for } 0 \le Z \le 5mm \text{ and } \left(\int_0^h \sigma_r(Z) dZ = 3.43 \right) \quad \text{(Eq. 3.1)}$$

(iii) *FT_eq*: Fully toughened glass with a residual surface compression of $\sigma_{r,surf}$=-85.1 MPa; the parabolic stress profile is given by Eq. 3.2 and was obtained numerically in MATLAB to satisfy internal stress equilibrium.

$$\sigma_r(Z) = -20.42 \cdot (Z - 2.5)^2 + 42.55 \text{ for } 0 \le Z \le 5mm \text{ and } \left(\int_0^h \sigma_r(Z) dZ = 0 \right) \quad \text{(Eq. 3.2)}$$

(iv) *CT*: Chemically toughened glass with surface compression of $\sigma_{r,surf}$=-370 MPa, a core tension of $\sigma_{r,core}$=7.7 MPa and a case depth of d_c=70 µm. The stress profile was again obtained numerically in MATLAB to satisfy internal stress equilibrium i.e. $\left(\int_0^h \sigma_r(Z) dZ = 0 \right)$.

The results show that the Load *P*, vs. applied displacement δ_{AC}, path is identical for all types of glass. The same applies for the central deflection δ_E vs. applied load *P* path except for *FT-SCALP*; the change in the deformation mode occurred for *FT-SCALP* at smaller central deflections ($\delta_{E,FT\text{-}SCALP}$=2.75 mm) than the other glass plates (δ_E=3.00 mm). However, this cannot be attributed to the influence of the residual stress profile, because the mechanical response of the other glasses (*CT*, fully toughened *FT-eq* and annealed *AN*) were identical but had different levels of surface compression. This is instead attributed to the non-equilibrated residual stress in the *FT-SCALP* model $\left(\int_0^h \sigma_r(Z) dZ = 3.43 \right)$.

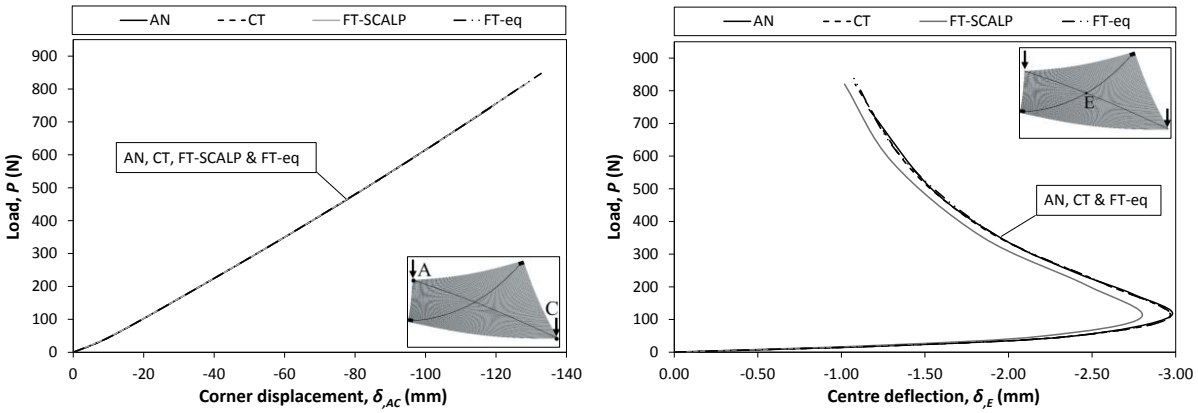

(a) (b)

Fig. 3.25: Residual stress influence: (a) Load vs. applied displacement and; (b) Load vs. centre deflection.

Therefore, no change in the mechanical response of the glass plate occurs during the bending process as a result of its residual stress profile. Deviations from the annealed response occur only

for non-equilibrated residual stress profiles: such a stress profile was obtained by SCALP-05, possibly due to accuracy/averaging errors. However, non-equilibrated stress profiles are not expected in reality without associated deviations from flatness.

Therefore, the high residual surface stress in chemically toughened glass plates does not influence its mechanical response and thus, the divergence between the experimental and the numerical results found in Fig. 3.24 can be attributed to deviations between the experimental set-up and the numerical model and / or inaccurate material properties as indicated previously. However, due to these inaccuracies the numerical model was not extended further for thinner plates $h < 2$ mm.

3.3.4 Conclusions on the cold bending of thin chemically toughened glass

The mechanical response of chemically toughened glass plates during the cold bending was investigated in Section 3.3 and was found to be similar to that of fully toughened glass. The change in the deformation mode during which one diagonal straightens while the other increases in curvature and the subsequent local instability along the support axis that is manifested as a cold bending distortion were also observed during the cold bending of the chemically toughened glass plates.

Additional numerical investigation on the influence of the residual stress profile on the mechanical response of toughened glass plates during the cold bending process, revealed that non-equilibrated residual stress profiles can change the load / applied displacement limits at which the change in the deformation mode and the resulting cold bending distortion occur; however, no change is observed for residual stress profiles that are in equilibrium. Stress profiles in flat toughened glass plates are expected to be in equilibrium or that, equilibrium would be naturally obtained though permanent deformations in the glass surface and consequent deviations from flatness / initial imperfections.

3.4 Conclusions

The aim of this Chapter was to investigate and characterise the mechanical response of monolithic glass plates when subjected to cold bending into anticlastic shapes. Numerical modelling validated by experimental testing revealed that chemically toughened and fully toughened glass plates exhibit a similar response while their difference in the levels of residual surface compression does not affect their bending response. The investigation showed that, three phenomena of interest may occur during the cold bending process: a change in the deformation mode, a local instability associated with a cold bending distortion and a global instability phenomenon (snap through buckling).

These phenomena are associated to the parameters chosen during the bending process and although they do not cause failure of the cold bent glass, they could exceed serviceability limits. In particular, the change in the deformation mode and the local instability are related to the boundary conditions at the corners of the plate; the former appears first during the cold bending process as significant deflections are confined in the load axis while the support axis decreases in curvature. Increasing the applied displacement on the plate further triggers a local instability across the support axis which is attributed to a build-up of axial compression. This instability manifests itself as a cold bending distortion and could in turn exceed optical quality serviceability limits for high distortion amplitudes. This poses questions on the optical quality of cold bent surfaces which prior to this study was considered to be significantly superior to conventional hot bent glass surfaces. To address these questions a user-friendly method was developed for achieving high optical quality for cold bent glass by choosing appropriate geometrical characteristics for the plate and bending radii.

Global instabilities can also occur during the cold bending process. These depend on the direction of the load during the cold bending process and initial imperfections associated with gravity, and appear as a sudden change from a double curved anticlastic shape to a double curved synclastic shape.

Unsurprisingly, the slender nature of toughened glass plates used in cold bending applications makes them prone to instabilities. However, high quality cold bent glass plates can be achieved with careful selection of the bending parameters (boundary conditions, geometrical characteristics and orientation of the plate, load locations and bending radii) that are able to eliminate or minimize the influence of instability phenomena identified in this research and the associated serviceability limits.

Further research should include the use of thin plate theory as a third means of validating the experimental and numerical results obtained in this study. Finally, safety reasons, often dictate that monolithic glass should not be used for structural applications, therefore, future investigations should focus on cold bent laminated glass, where the polymer interlayer between the two glass plates is expected to influence the mechanical response during the cold bending as a function of temperature and strain-rate.

4. Glass Strength Estimation

4.1 Introduction

Chapter 3 indicates that cold bending is an advantageous method for creating curved glass surfaces meeting stability and optical quality criteria within certain applied displacement limits. However, the cold bent glass plate is in a permanent state of stress throughout its service life and therefore, its strength after exposure to ageing conditions, must be quantified carefully. The assessment of the strength of aged glass is performed in this thesis and described in Chapter 6, but this involves a broad range of relatively advanced methods and implicit assumptions which are reviewed and assessed in Chapter 4.

The aim of Chapter 4 (Fig. 4.1) is therefore to identify the most reliable approach for estimating glass strength. This involves numerical modelling and analytical investigations of experimental glass strength data, obtained for the purpose of Chapter 5. In particular, Section 4.2 describes the destructive testing of glass and the numerical models used for the conversion of failure load to failure stress. The influence of sub-critical crack growth during the destructive testing is investigated in Section 4.3 by fractographic analysis and linear elastic fracture mechanics. A brief investigation on the effectiveness of existing fractographic models on the geometry factor of critical flaws is also provided. Section 4.4 aims to identify the most effective approach for statistically analysing glass strength data with a Weibull distribution. The number of samples needed for reliable statistical analysis of glass strength, is investigated in Section 4.5. Finally, Section 4.6 summarizes important findings that will form the basis of Chapters 5 & 6.

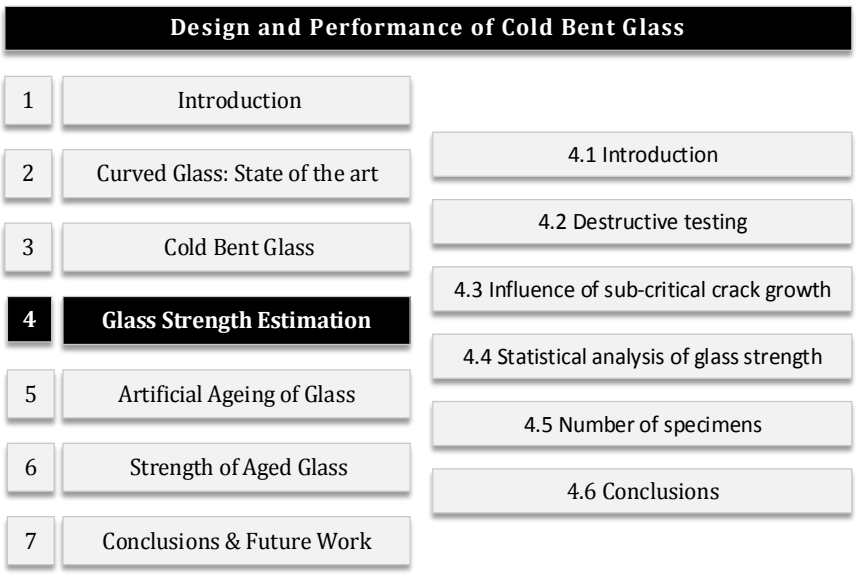

Fig. 4.1: Contents of Chapter 4.

4.2 Destructive testing

Coaxial double ring [133,134] and 4 point bending [135] tests are typically used for assessing glass strength. Coaxial double ring (CDR) tests are preferred in this study. The reason is that CDR tests: eliminate edge failures that can be potentially triggered during 4-point bending tests, and that; surface strength is investigated in this study.

4.2.1 Destructive testing for annealed glass

The diameters of the loading and the reaction ring are: D_L=51 mm and D_R=127 mm, respectively (Fig. 4.2b) and comply with ASTM C1499-03 [134] for specimens of 150 x 150 x 3 mm. The loading ring is connected to a 2 kN load cell Instron machine with an articulated joint to ensure uniform contact between the loading ring and the surface of the specimen.

Sub-critical crack growth is supressed when tests are performed in inert conditions (Section 2.5.2); this can be achieved by testing in vacuum or environmental conditions of RH=0%. However, inert conditions are hard to achieve in practice. High stress rates of 20 MPa/sec (corresponding to a displacement rate of 13.6 mm/min) are chosen instead in this study to induce fracture within a few seconds (1-7 sec) and therefore, minimize the influence of sub-critical crack growth. These conditions are known as quasi-inert and will be further investigated in Section 4.3.

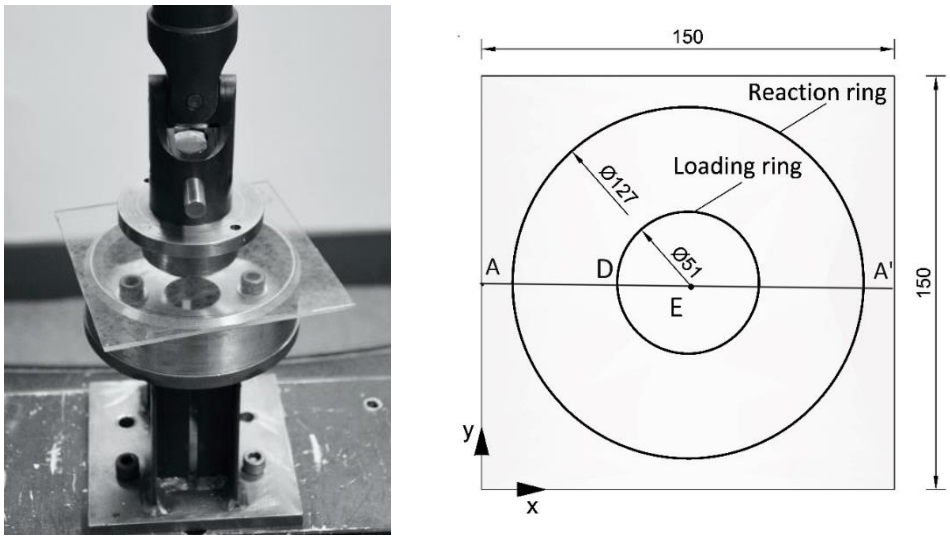

(a) (b)

Fig. 4.2: (a) Coaxial double ring set-up and; (b) Top view of specimen.

To assist the experimental destructive testing two FEA models (Fig. 4.3) were constructed in Abaqus - SIMULIA v6.12 [131] to simulate the destructive testing (CDR) of the glass (Poisson's ratio v=0.23 and Young's modulus E=70 GPa). Each of them consisted of 6,774 quadratic quadrilateral shell elements (S8R). The first model considered friction between the loading / reaction ring and the glass specimen while the other neglected it. Experimental strain gauge data

showed that the full friction FEA model was more representative than the null-friction model. Additionally, the full friction model was found to be more accurate than the analytical formula in Eq. 4.1 (ASTM C1499-03 [134] based on Timoshenko plate theory [136]); this is especially true for loads and centre displacements exceeding P >700 N and δ_E > 0.55 mm respectively when non-linear (membrane) effects become significant (Fig. 4.3b). Therefore, the full friction model was used to derive failure stress in this study.

$$\sigma_f = \frac{3 \cdot P}{2 \cdot \pi \cdot h^2} \cdot \left[(1-\nu) \cdot \frac{D_R^2 - D_L^2}{2 \cdot D^2} + (1+\nu) \cdot \ln\left(\frac{D_R}{D_L}\right) \right] \qquad \text{(Eq. 4.1)}$$

where: P: the failure load, h: the thickness of the specimen, D_R and D_L: the diameters of the reaction and the loading ring respectively, ν=0.23: Poisson's ratio and

$$D = \frac{l}{0.90961 + 0.12652\frac{h}{D_R} + 0.00168 \cdot \ln\left(\frac{l - D_R}{h}\right)} \quad \text{and} \quad l = 0.5 \cdot (l_x + l_y) \qquad \text{(Eq. 4.2a-b)}$$

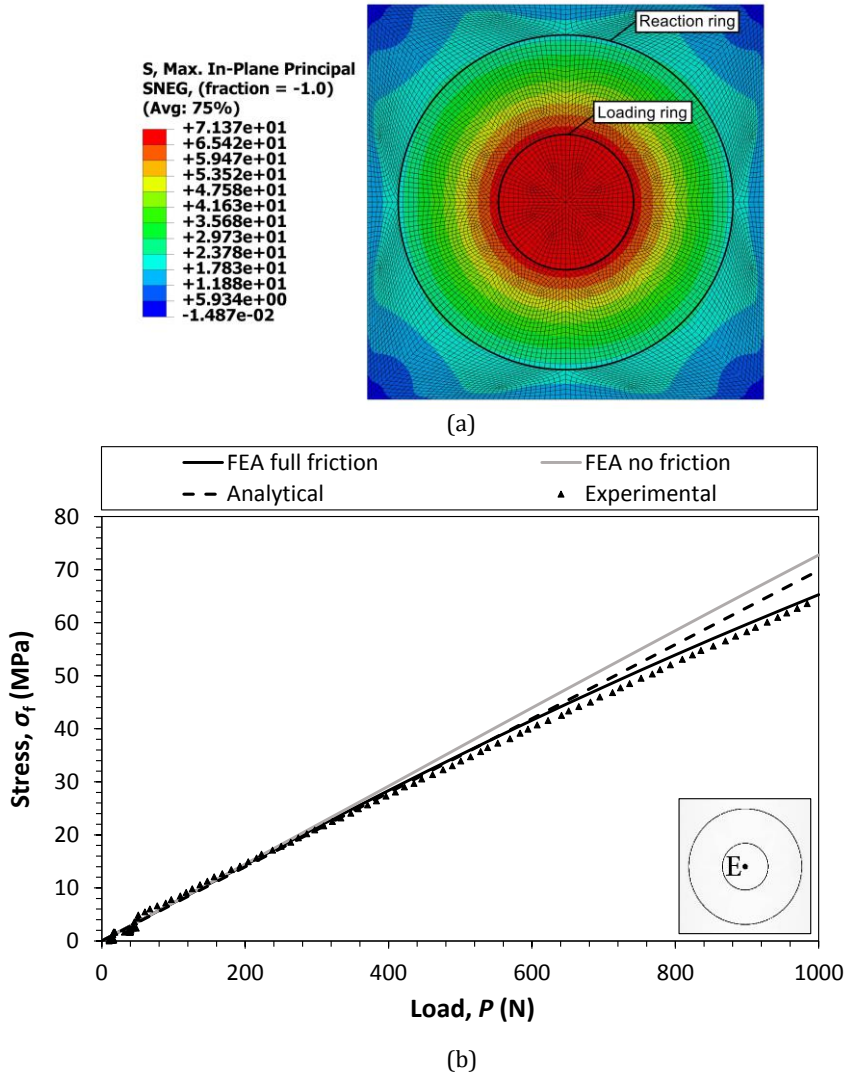

Fig. 4.3: Max. principal tensile stress: (a) FEM (P=1000N) and; (b) exp., num. and an. results at E (Fig. 4.2).

4.2.2 Destructive testing for fully toughened glass

The numerical model developed in Section 4.2.1 for annealed glass, was modified to suit the dimensions of the fully toughened glass (150 x 150 x 5.95 mm) that will be tested in Chapter 6. The applied displacement was also modified to incrementally reach $\delta_{applied}$=1.5 mm at the loading ring. The numerical model showed good agreement with the analytical formulae of Timoshenko plate theory [136]; small deviations appear only for loads exceeding P > 17 kN (Fig. 4.4). Therefore, a CDR set-up (D_L=51 mm and D_R=127 mm) is also used for fully toughened glass.

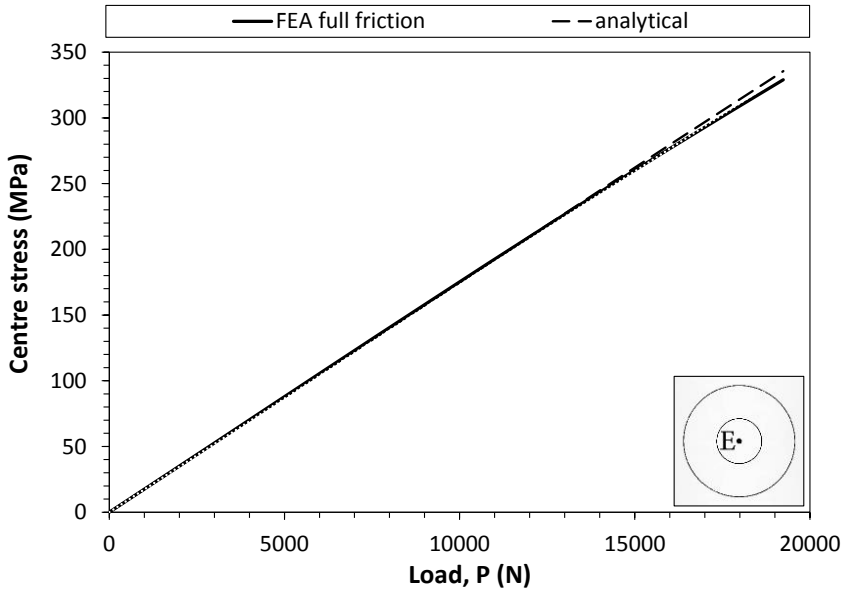

Fig. 4.4: Numerical and analytical max principal stress at point E for fully toughened glass.

4.2.3 Destructive testing for thin chemically toughened glass

The numerical model for CDR tests on annealed glass (Section 4.2.1) was also modified to suit the dimensions of chemically toughened glass (180 x 180 x 2 mm) that will be tested in Chapter 6. The applied displacement / load limits were also modified to incrementally reach $\delta_{applied}$=5.5 mm / P=24.8 kN. The numerical model was compared with analytical (Timoshenko [136]) and experimental strain gauge data at the centre of the specimen, point E, and at the proximity of the Loading Ring boundary, point D (Fig. 4.2b). Experimental stress data showed good agreement with the numerical model (Fig. 4.5). However, deviations from the linear analytical formulae [136] are noticed as a result of the significant non-linear/membrane effects that develop due to the small thickness of the glass plate and the high displacements required to induce fracture.

A corollary of this non-linearity is that the expected uniform equibiaxial state of stress within the area of the loading ring is not achieved for thin chemically toughened glass and a Coaxial Double Ring set-up. High radial stress concentrations that increase with increasing load, appear at the boundaries of the loading ring (Fig. 4.8a). This is attributed to the large ratio of applied

displacement to the thickness of the glass ($\delta_{applied}/h$) that causes the development of unequal radial and tangential stresses below the boundaries of the loading ring [137,138]. Stress concentrations (Fig. 4.8a) and the non-biaxial stress state in the loading ring make this set-up unreliable for thin high strength glass as the fracture strength obtained from the test is sensitive to the location and orientation of flaws within the loading ring [105,139].

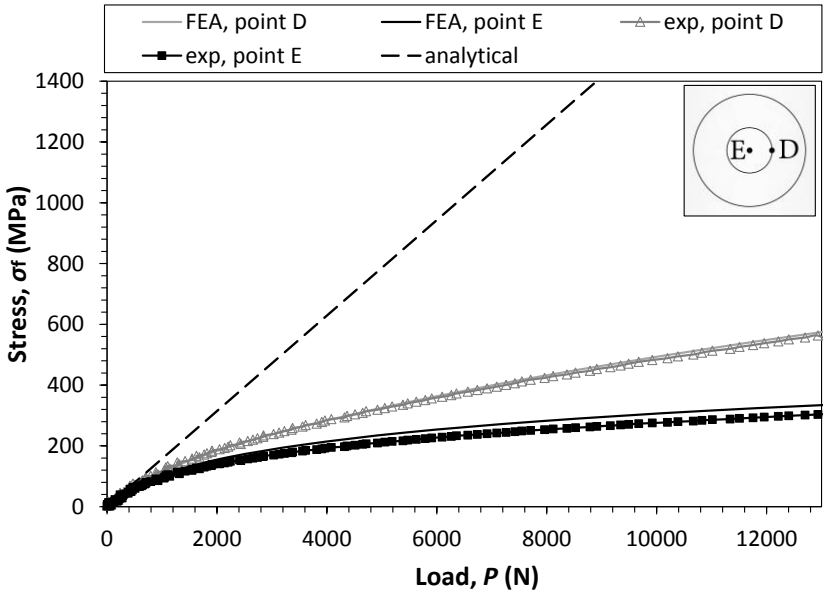

Fig. 4.5: Max principal stress at E and D for chemically toughened glass (exp., analyt. and num.).

It is therefore necessary to modify the coaxial double ring set-up to destructively test thin, high-strength glass in a reliable and reproducible manner. EN 1288-1:2000 [137] proposes the application of gas pressure within the volume confined by the loading ring which increases as a function of the applied ring load to create a uniform stress state within the loading ring area. However, this method is complicated to control experimentally because the gas pressure needs to be varied in real time during the test as a function of the applied load / displacement, to normalise the excessive development of radial stresses at the boundaries of the loading ring. This method is therefore, disregarded.

The following variations to the CDR set-up are investigated numerically to identify an effective destructive test for thin glass: *Set-up A* (Fig. 4.6a): application of uniformly distributed load over the area of the loading ring with a rubber plunger; *Set-up B* (Fig. 4.6b)*:* use of spreader plate(s).

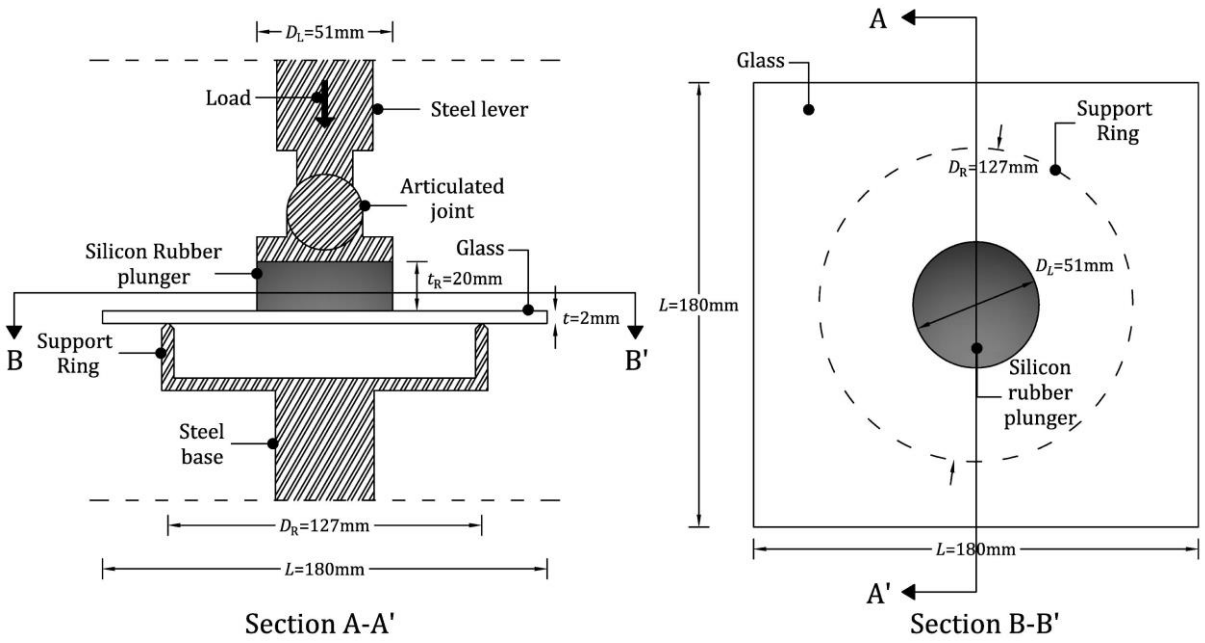

(a)

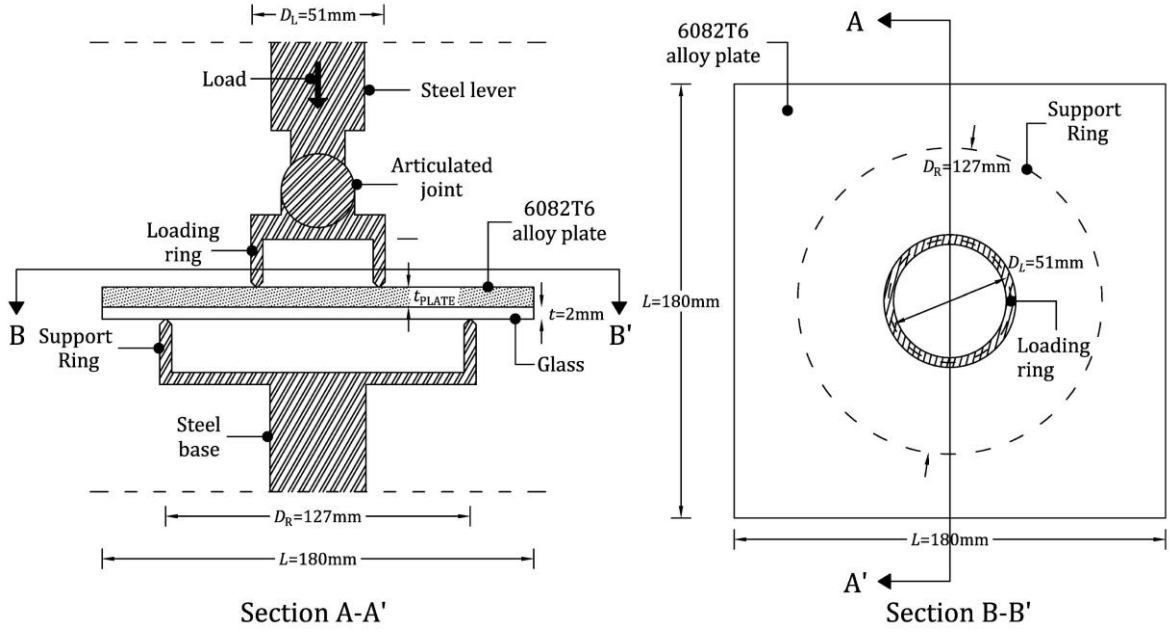

(b)

Fig. 4.6: Set-ups: (a) Set-up A: Rubber plunger and; (b) Set-up B: CDR with spreader plate.

Set-up A: Rubber plunger

Previous research suggests that application of a uniformly distributed load with a silicone rubber plunger over the loading ring area can be used to create a uniform equibiaxial stress field for the destructive testing of thin heat strengthened photovoltaic panels [140]. The deformable and incompressible properties of the silicone rubber are used in this set-up to follow the large deformation of the glass. However, the numerical validation of this set-up was only achieved for relatively low displacements corresponding to a maximum applied stress of 120 MPa. Therefore,

further investigation was undertaken to identify whether this method can be also implemented for high strength chemically toughened glass.

The numerical model was constructed in Abaqus - SIMULIA [131] for one quarter of this set-up employing symmetry conditions (Fig. 4.7a). A silicone rubber plunger with a diameter of Φ51 mm and a thickness of t_R=20 mm was used to apply the uniformly distributed load (Fig. 4.6a). The glass (E=70 GPa and v=0.23) was modelled with 1,662, 8-node, reduced integration shell elements (S8R) whilst the silicone rubber with 12,800, 8-node, reduced integration solid elements (C3D8R). A Shore hardness of 60° was used for the silicone rubber; uniaxial compression stress-strain data (Table 4.1) were included in Abaqus and were fitted to an Ogden material model (v=0.497). The contact between the two surfaces was frictionless in the tangential direction whilst hard contact was considered in the normal direction of their interface.

Table 4.1: Uniaxial compression data for silicone rubber (Shore Hardness of 60).

(1)		(2)		(3)		(4)	
Stress (MPa)	Strain	Stress (MPa)	Strain	Stress (MPa)	Strain	Stress (MPa)	Strain
0.0000	0.0000	-0.6907	-0.1144	-1.1041	-0.2284	-1.5379	-0.3425
-0.0204	-0.0076	-0.7213	-0.1220	-1.1302	-0.2361	-1.5747	-0.3500
-0.0625	-0.0152	-0.7527	-0.1296	-1.1571	-0.2437	-1.6125	-0.3577
-0.1122	-0.0229	-0.7904	-0.1373	-1.1785	-0.2513	-1.6543	-0.3653
-0.1932	-0.0305	-0.8164	-0.1448	-1.2082	-0.2589	-1.7011	-0.3728
-0.2528	-0.0381	-0.8416	-0.1525	-1.2311	-0.2666	-1.7428	-0.3803
-0.3131	-0.0457	-0.8711	-0.1602	-1.2605	-0.2741	-1.7901	-0.3880
-0.3614	-0.0534	-0.8983	-0.1677	-1.2890	-0.2817	-1.8441	-0.3956
-0.4145	-0.0610	-0.9313	-0.1754	-1.3165	-0.2893	-1.9003	-0.4031
-0.4622	-0.0686	-0.9566	-0.1829	-1.3445	-0.2969	-1.9570	-0.4107
-0.5047	-0.0762	-0.9829	-0.1905	-1.3743	-0.3045	-2.0200	-0.4182
-0.5539	-0.0839	-1.0067	-0.1981	-1.4032	-0.3121	-2.0844	-0.4258
-0.5862	-0.0914	-1.0297	-0.2058	-1.4366	-0.3196	-2.1599	-0.4334
-0.6233	-0.0992	-1.0553	-0.2133	-1.4714	-0.3273	-2.2410	-0.4410
-0.6575	-0.1068	-1.0816	-0.2209	-1.4999	-0.3349		

Fig. 4.8b shows that an almost uniform surface stress is achieved within the loading ring area for relatively low applied displacements, $\delta_{applied} < 0.75$ mm (corresponding to a stress of $\sigma < 100$ MPa) but as the applied displacement increases further the curvature of the stress profile becomes larger and leads in deviations from the uniform equibiaxial stress state. Other limitations of Set-up A are: (a) excessive distortion of the rubber elements causing numerical convergence problems; this is because of the rubber's high Poisson ratio that leads to excessive bulging and therefore, large distortions (Fig. 4.7b); (b) defining the rubber material properties is not trivial

and requires very careful material characterization to obtain accurate stress-strain data that describe the specific application and; (c) uncertainties associated with fitting a material model to describe the stress - strain data and accurately capture the response of the material (Ogden, Yeoh, Mooney Rivlin, etc.).

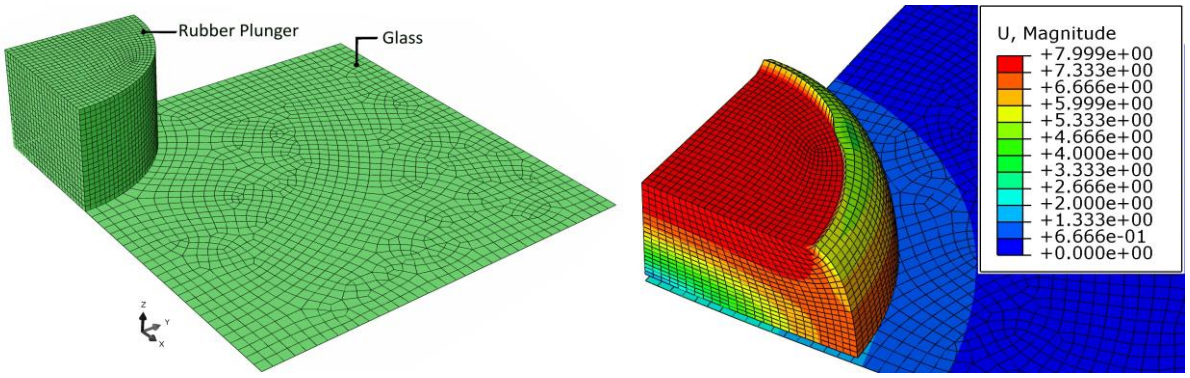

(a) (b)

Fig. 4.7: Set-up A; (a) FEM and; (b) deformed shape at $\delta_{applied}$= 2.5mm.

Set-up B: use of spreader plates

An alternative variation of a CDR set-up is investigated here. This uses spreader plate(s) above the glass specimen in the Coaxial Double Ring set-up (Fig. 4.6b). The plates have the same in-plane dimensions as the chemically toughened glass specimens (180 x 180 mm). The spreader plate(s) increase the bending stiffness of the un-bonded unit and reduce the ratio of applied displacement over the specimen's thickness, $\delta_{\text{applied}}/h$. This is expected to reduce excessive development of radial stress concentrations below the boundaries of the loading ring.

The number of additional plates was reduced to one to minimize the number of interfaces and consequently, to minimize the impact of numerical uncertainties related to contact and alignment issues during the experimental procedure.

Aluminium (E_A=70 GPa and ν_A=0.30) was chosen for the additional plate to suit the material properties of glass (E_G=70 GPa and ν_G=0.23). Similar material properties lead to similar load sharing factors and reduce failure load requirements. Aluminium alloys were chosen because of their higher yield strength than pure aluminium. In particular, a general purpose, medium strength alloy and a high strength aluminium alloy conforming to Grades 6082T6 and 7075T6 respectively (BS EN 485-2:2013 [141] and BS EN 573-3:2013 [142]) were chosen (Table 4.2).

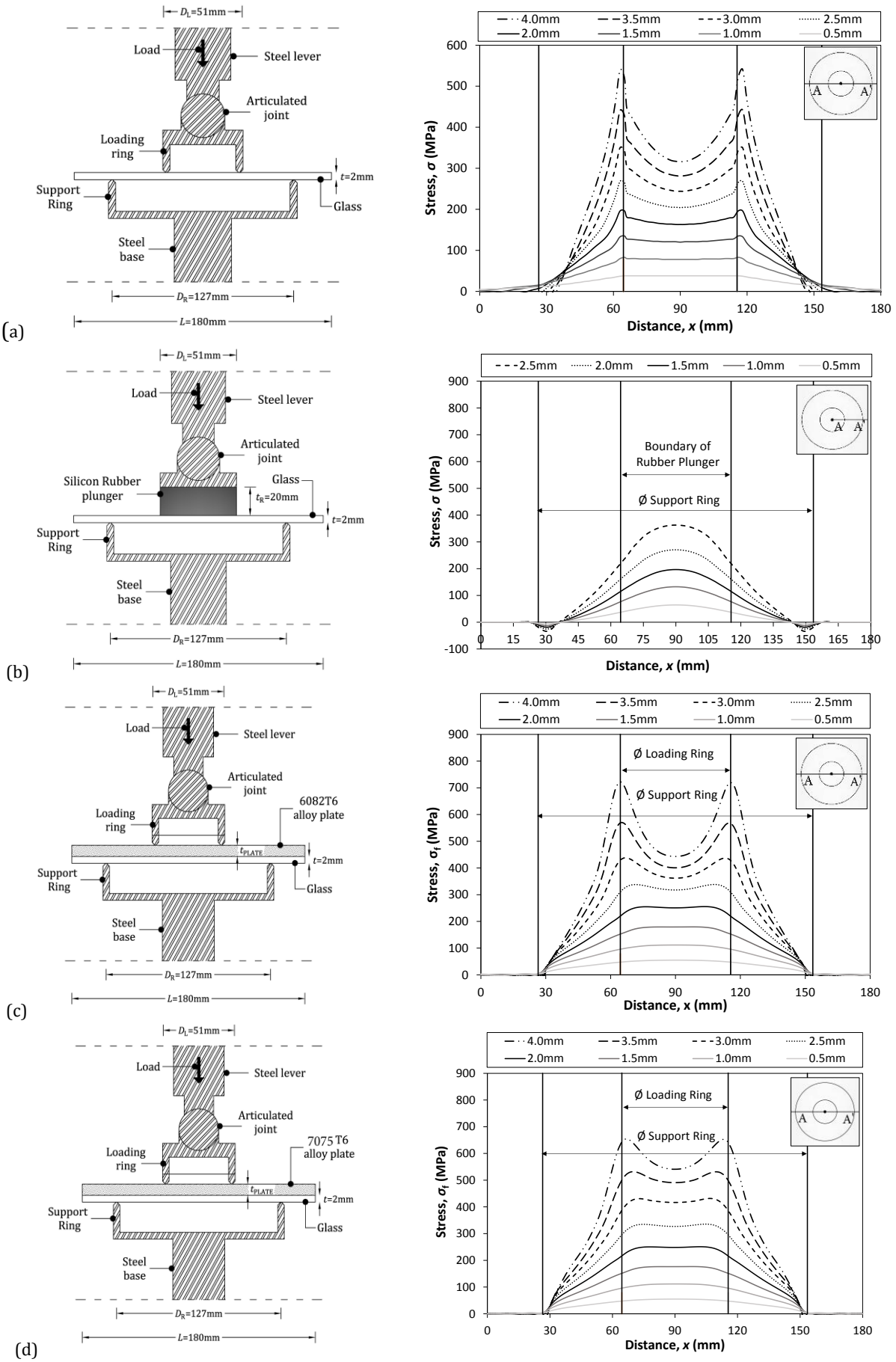

Fig. 4.8: Max. principal stress along A-A' for: (a) CDR; (b) Set-up A; (c-d) Set-up B: 6082T6 & 7075T6 alloy.

Table 4.2: Stress-strain data for Aluminium Grades: 6082 and 7075T6 [143].

Grade 6082T6 Aluminium			Grade 7075T6 Aluminium		
Stress	Strain	Plastic strain	Stress	Strain	Plastic strain
σ_{al} (MPa)	ε (%)	ε_{pl} (%)	σ_{al} (MPa)	ε (%)	ε_{pl} (%)
0.0	0.000	0.000	0.0	0.000	0.000
120.2	0.202	0.000	211.0	0.300	0.000
160.1	0.253	0.000	229.3	0.330	0.000
179.2	0.281	0.000	248.2	0.360	0.000
194.5	0.304	0.000	274.6	0.400	0.000
227.8	0.356	0.000	290.6	0.400	0.000
260.0	0.455	0.099	321.7	0.450	0.000
289.2	0.553	0.197	422.9	0.600	0.000
290.0	1.004	0.648	497.7	0.800	0.000
311.6	0.800	0.444	503.4	1.000	0.000
			522.7	1.300	0.300
			556.8	1.500	0.500

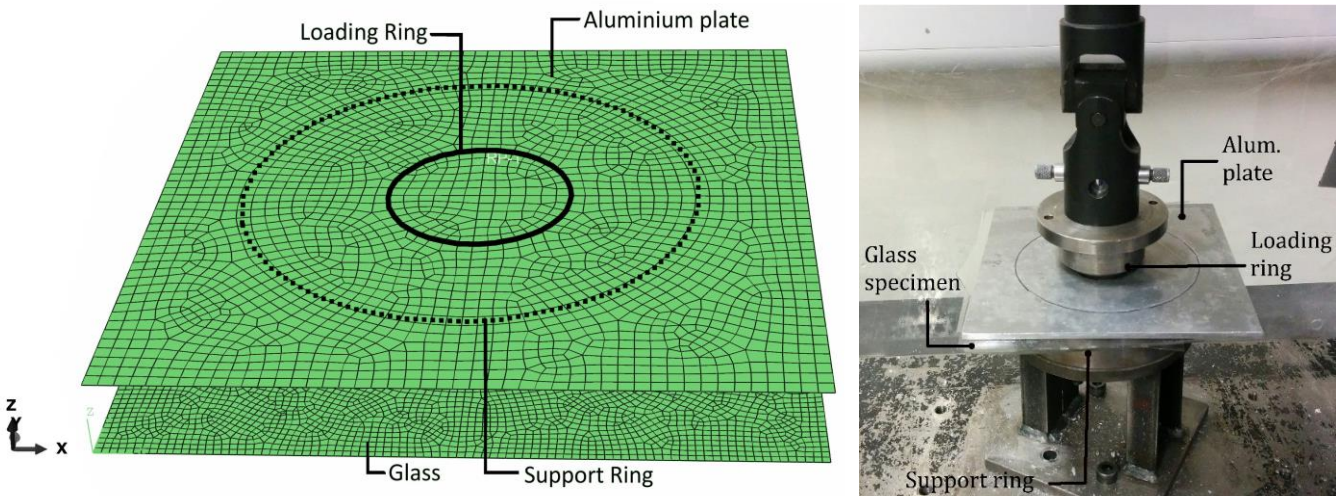

(a) (b)

Fig. 4.9: Set-up B: Introduction of aluminium plate over glass: (FEA) and; (b) experimental set-up.

A numerical model of a Coaxial Double Ring set-up for a glass plate (180 x 180 x 2 mm) and a Grade 6082T6 spreader plate (180 x 180 x 4.75 mm) was constructed in Abaqus, - SIMULIA (Fig. 4.9a). Linear elastic material properties (E_G=70 GPa and ν_G=0.23) were used for the glass and elastoplastic material properties for the aluminium (E_A=70 GPa and ν_A=0.30 were used for the elastic region & stress vs. plastic strain data, shown in Table 4.2, [143] were used for the plastic region). 9,595 and 2,432 linear reduced integration shell elements (S4R) were used for the glass and the aluminium plates respectively, with aluminium being the master surface and glass the slave surface in the contact. The interface between the glass and the aluminium was frictionless

in the tangential direction whilst exponential contact was chosen in the normal direction. The contact parameters (p=3 MPa and c_0=0.1 mm) were chosen to avoid opening or excessive overclosure between the two surfaces.

The model was subsequently validated with experimental (Fig. 4.9b) strain gauge data acquired from the tensile surface of the glass at points E and D in Fig. 4.2b which correspond to the centre of the plate and to the proximity of the Loading ring, respectively. Adequate agreement is found between the numerical and experimental results (Fig. 4.10) which also validates the initial assumption that an equibiaxial stress field can be created within the loading ring area. This is valid up to a total load of P=36 kN (Fig. 4.10 and a corresponding displacement of δ_{applied}≈2.2 mm at point D) for the 6082T6 alloy. However, for loads exceeding P > 36 kN, the aluminium plate reaches its ultimate tensile strength (Fig. 4.11). This increases the load sharing factor of glass and results in stress concentrations below the boundaries of the loading ring (Fig. 4.8c). The Grade 7075T6 spreader plate reaches its ultimate tensile strength at a higher applied displacement, δ_{applied}≈3.1 mm and thereby, suppresses significant stress concentrations ($(\sigma_{max} - \sigma_E)/\sigma_E$>10%) up to an applied displacement of δ_{applied}=3.5 mm (Fig. 4.8d).

The above investigation indicates that the introduction of a Grade of 6082T6 spreader plate with a thickness of 4.75 mm in the CDR set-up is able to suppress the development of significant radial stress concentrations ($(\sigma_{max} - \sigma_E)/\sigma_E$>10% and produce an almost equibiaxial stress field up to an applied displacement of δ_{applied}=2.6 mm / load of P=41 kN. Whereas when a Grade 7075T6 aluminium alloy is used instead, these limits are pushed to δ_{applied}=3.5 mm / P=80 kN.

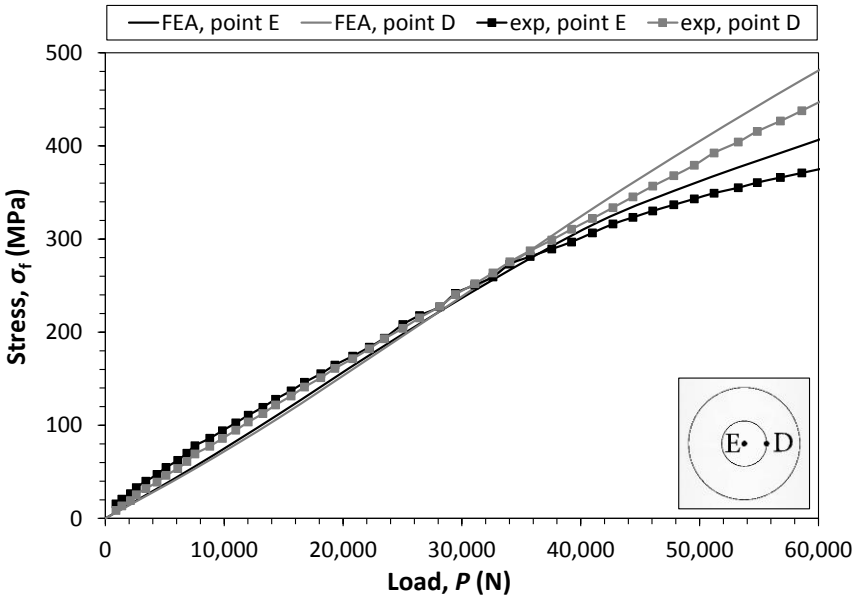

Fig. 4.10: Max. principal stress (exp. and num.) at points E and D of the glass (Fig. 4.2b) for Set-up B.

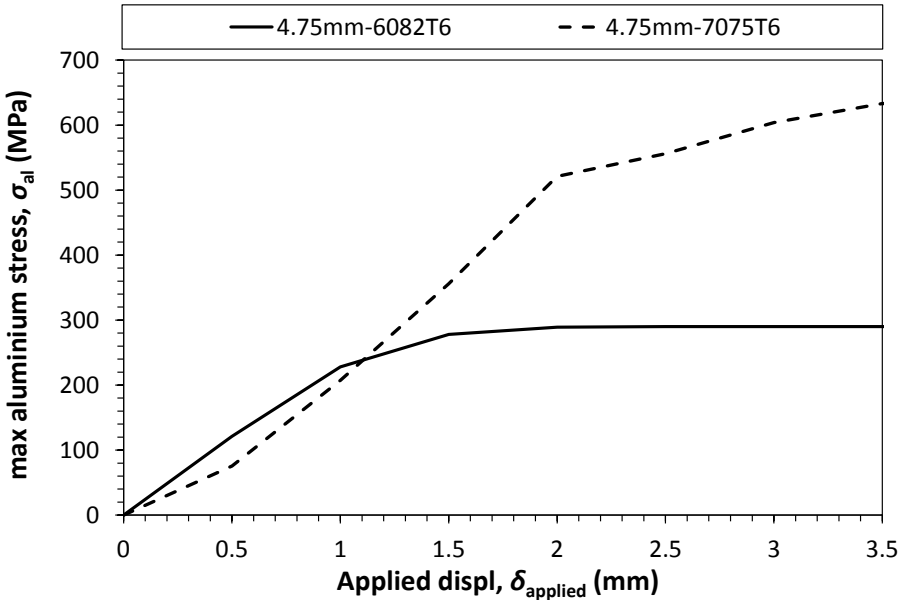

Fig. 4.11: Max. von Mises stress for 6082T6 and 7075T6 alloy plates in Set-up B.

4.3 Influence of sub-critical crack growth

The influence of sub-critical crack growth is investigated in this section to determine whether a high stress rate of 20 MPa/sec exerted during the destructive testing is sufficient to achieve inert conditions. Two of the series (SA4 and SA21), that were tested for the purposes of Chapter 5, are selected for this investigation. SA4 was artificially aged with sand abrasion which introduced some of the shallower flaws among the series tested within Chapter 5 whilst SA21 was artificially aged with sand and gravel abrasion and had some of the largest flaws among the series tested within Chapter 5 (detailed description of artificial ageing methods shown in Section 5.2.2).

4.3.1 Fractographic analysis

Fractographic analysis followed the destructive testing of the glass specimens for SA4 and SA21 to determine their critical flaw size with an optical microscope. The procedure is described below:

(i) the fracture pattern of the whole specimen is carefully observed to identify the approximate origin of the fracture (Fig. 4.12a);

(ii) the appropriate fragment is removed carefully to avoid the induction of additional flaws on the cross-section of the fragment;

(iii) the fragment is reduced in size, if needed, with a hand-held diamond cutter, to fit under an optical Leica DM ML microscope;

(iv) the lateral face of the fragment containing the critical flaw is investigated under the optical microscope. Wallner lines propagate from the critical flaw and are very useful for identifying the general location of the critical flaw while the mirror, mist and

hackle (Fig. 4.12b) reveal its precise location (Fig. 4.12c) [144].

(v) the dimensions (final depth, a_f and width $2c$) and the shape of the critical flaw are reported (Table 4.3). When radial/median cracks are present, depths are reported for: the radial/median crack depth, $\alpha_{r,f}$ and the effective flaw depth, $a_{ef,f}$ (Fig. 4.13).

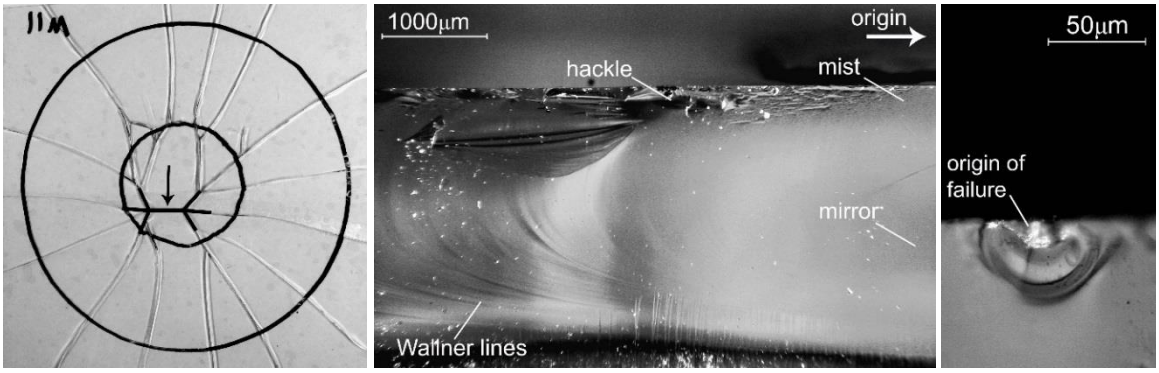

(a) (b) (c)

Fig. 4.12: (a) Approximate location of the origin of failure; (b) Mirror, mist and hackle and; (c) critical flaw.

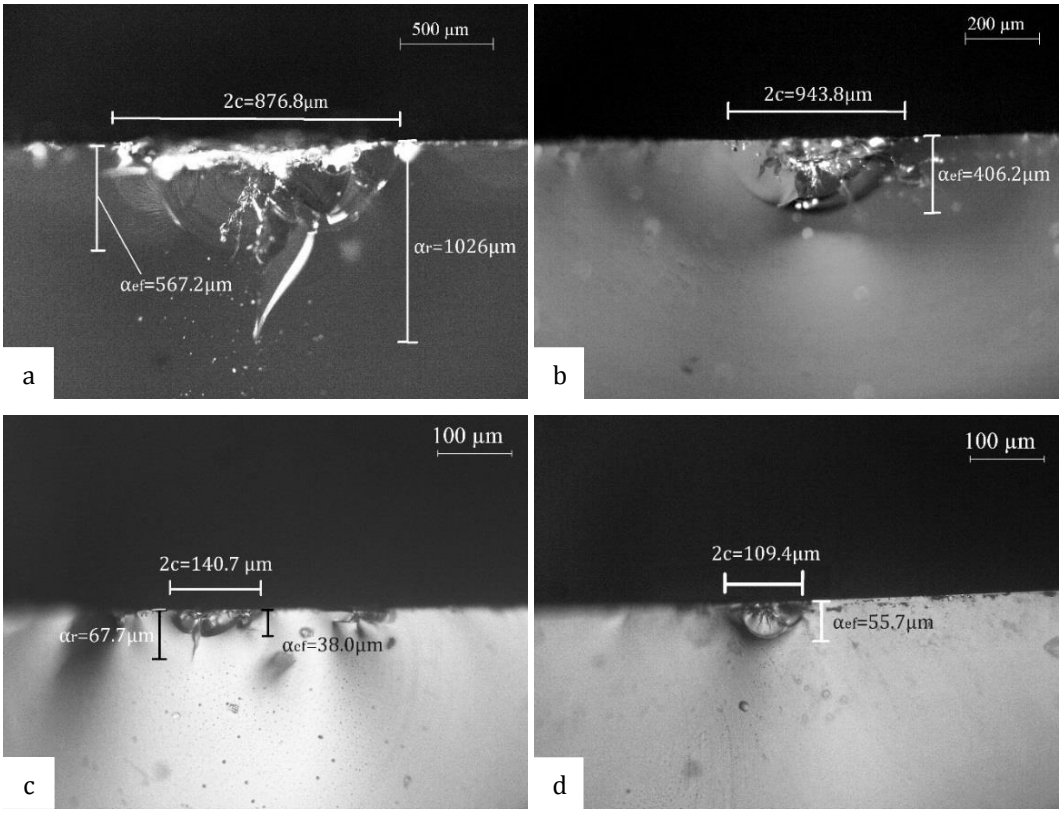

Fig. 4.13: Critical flaws (with and w/o radial/median cracks) revealed through optical microscopy after impact with: (a-b) gravel and; (c-d) sand.

Table 4.3: Geometrical characteristics of critical flaws for: (a) SA21 and; (b) SA4.

(a)

SA21							
Specimen	**Morphology**	a_{ef}	a_r	$2c$	A	σ_f	t_f
SA21-1	NA	NA	NA	NA	NA	32.27	1.56
SA21-2	trapezoidal	267.3	775.5	954.0	192134.4	41.23	1.99
SA21-3	semi elliptical	208.8	310.6	451.6	83909.0	41.23	2.03
SA21-4	irregular	332.4	483.3	649.4	147035.6	40.84	1.93
SA21-5	trapezoidal	326.1	548.3	1141.1	300615.7	45.62	2.18
SA21-6	semi elliptical	567.2	1026.0	876.8	601475.0	24.82	1.21
SA21-7	semi elliptical	270.4	328.2	1396.9	344319.6	44.53	2.10
SA21-8	semi elliptical	406.2	NA	943.8	272861.5	31.26	1.50
SA21-9	semi elliptical	334.3	435.8	859.0	188287.7	27.22	1.30
SA21-10	semi elliptical	167.2	NA	494.9	35456.5	48.73	2.32
SA21-11	semi elliptical	457.0	NA	1081.0	268095.9	39.97	1.92
SA21-12	triangular	632.4	859.1	2328.5	695346.6	39.69	1.91
SA21-13	triangular/irregular	299.2	615.7	1240.8	150783.3	41.29	1.99
SA21-14	trapezoidal	189.5	NA	792.2	106197.6	36.78	1.78
SA21-15	semi elliptical	172.8	NA	1692.3	181226.6	35.66	1.71

(b)

SA4							
Specimen	**Morphology**	$a_{ef,f}$	$a_{r,f}$	$2c$	A	σ_f	t_f
SA4-1	2 flaws connected	53.4	130.5	235.5	10578.9	47.751	2.73
SA4-2	semi elliptical	44.0	67.4	104.9	3444.7	51.926	2.76
SA4-3	semi elliptical	55.9	NA	148.7	5802.8	48.170	2.85
SA4-4	semi elliptical	59.7	105.2	232.3	10921.8	47.722	2.58
SA4-5	semi elliptical	57.4	NA	117.2	4514.3	44.319	2.43
SA4-6	semi elliptical	56.4	NA	217.7	7735.9	46.721	2.59
SA4-7	semi-circle	45.7	NA	84.2	2704.0	44.970	2.60
SA4-8	2 flaws connected	74.1	85.1	250.9	12179.8	49.275	2.67
SA4-9	semi elliptical	55.1	NA	149.4	5750.2	54.242	2.77
SA4-10	semi elliptical	51.5	NA	135.7	4818.3	52.317	2.78
SA4-11	semi elliptical	44.8	264.5	264.5	4005.5	52.683	2.72
SA4-12	irregular	67.3	93.9	328.6	10780.2	50.702	2.66
SA4-13	semi elliptical	65.1	NA	140.0	5678.9	49.828	2.59
SA4-14	semi elliptical	38.0	67.7	140.7	4083.1	51.839	2.99
SA4-15	semi elliptical	55.7	NA	109.4	4357.2	53.104	2.84

4.3.2 Linear elastic fracture mechanics investigation

Method

This section investigates whether sub-critical crack growth occurs during the destructive testing for the chosen stress rate. To assess this, the t_{IN} (Eq. 4.3a) i.e. the inert time limit that signifies the end of inert conditions (curve A in Fig. 2.23a-b) and therefore, the commencement of sub-critical crack growth (curve B in Fig. 2.23a-b) and the t_{TH} (Eq. 4.3b) i.e. the crack growth threshold time limit (curve C in Fig. 2.23a-b) need to be determined for each critical flaw. These time limits are subsequently compared to the experimental time to failure, t_f: (a) for $t_{IN} \geq t_f$: testing conditions are inert i.e. flaws did not grow under the influence of the load exerted during the destructive test; (b) for $t_{IN} < t_f < t_{TH}$: sub-critical crack growth occurred during the destructive test i.e. flaws have grown sub-critically within $t_{IN} < t < t_f$ and; (c) for $t_f > t_{TH}$: sub-critical crack growth occurred during the destructive test for $t_{IN} > t > t_{TH}$ but was suppressed after $t \geq t_{TH}$.

$$t_{IN} = \frac{2 \cdot a_i}{(n-2) \cdot v_0} \text{ and } t_{TH} = \frac{2 \cdot a_i}{(n-2) \cdot v_0} \cdot \left(\frac{K_{IC}}{K_{TH}} \right)^n \qquad \text{(Eq. 4.3a-b)}$$

where: a_i: the initial flaw size, n: static fatigue constant and; v_0: the crack velocity.

The initial flaw depth, α_i needs to be determined for the estimation of the inert time limit t_{IN} and the crack growth threshold time limit t_{TH}. However, fractographic analysis can only reveal the final flaw depth, α_f. The following steps can be taken to determine the initial flaw depth, α_i and consequently, the inert time limit, t_{IN}:

Step 1 - Description of the stress history: One can assume that sub-critical crack growth occurs at some point in time during the destructive testing i.e. that testing conditions correspond to curve B in Fig. 2.23a-b. Therefore, Eq. 4.4 can be used to describe the known stress history (ramp stress in this case) that was exerted experimentally. The complete form of Eq. 4.4 is used here to set the two limits for Curve B in Fig. 2.23 i.e. the inert limit (t_{IN}, end of Curve A in Fig. 2.23) and the threshold limit (t_{TH}, start of Curved C in Fig. 2.23) between which flaws can grow sub-critically.

$$\int_0^{t_f - t_r} \left[(\sigma + \sigma_r)(t) \right]^n dt = \left\{ \left[\frac{2}{(n-2) v_0 K_{IC}^{-n} (Y\sqrt{\pi})^n a_i^{(n-2)/2}} \right] \cdot \left[\frac{1 - \left(\frac{a_i}{a_f} \right)^{(n-2)/2}}{1 - \left(\frac{a_{TH}}{a_i} \right)^{(n-2)/2}} \right] \right\}^{1/n} \Rightarrow$$

$$\frac{\left(\sigma_f+\sigma_r\right)^n\cdot\left(t_f-t_r\right)}{(n+1)}=\left\{\left[\frac{2}{(n-2)v_0K_{IC}^{-n}(Y\sqrt{\pi})^n a_i^{(n-2)/2}}\right]\cdot\left[\frac{1-\left(\frac{a_i}{a_f}\right)^{(n-2)/2}}{1-\left(\frac{a_{TH}}{a_i}\right)^{(n-2)/2}}\right]\right\}^{1/n} \quad \text{(Eq. 4.4)}$$

where: a_f: the final flaw size (obtained by post-fracture microscopy: $a_f=a_r$ when radial/median cracks are present and $a_f=a_{ef}$ in any other case); a_i: the initial flaw depth; a_{TH}: the threshold flaw depth; K_{IC}: the fracture toughness; σ_f: the failure stress; σ_r: the residual surface stress, t_f: the time to failure; t_r: the time for the tensile stress to exceed the residual surface compression and; Y: the geometry factor.

Step 2 – Substitution of unknowns: The initial flaw depth α_i and the threshold flaw depth α_{TH} can be substituted in Eq. 4.4 with Eq. 4.5a and Eq. 4.5b respectively.

$$a_i=\left(\frac{K_{IC}}{\sigma_f\cdot \mathrm{Y}\cdot\sqrt{\pi}}\right)^2 \text{ and } a_{TH}=\left(\frac{K_{TH}}{\sigma_f\cdot \mathrm{Y}\cdot\sqrt{\pi}}\right)^2 \quad \text{(Eq. 4.5a-b)}$$

where K_{TH}: the crack growth threshold.

Step 3 – Determination of the geometry factor: At this point, the only unknown in Eq. 4.4 is the geometry factor, Y. Eq. 4.4 can be solved with respect to Y to obtain a 16th order polynomial (Eq. 4.6). The roots of Eq. 4.6 can be subsequently found using MATLAB or any other mathematical tool. The minimum real, positive root of Eq. 4.6 denotes the linear elastic fracture mechanics (LEFM) geometry factor, Y_{SCG}.

$$c_1\cdot Y^{16}-Y^{14}+c_2=0 \quad \text{(Eq. 4.6)}$$

where $c_1=\left(\frac{\left(\sigma_f-\sigma_r\right)^n\cdot\left(t_f-t_r\right)\cdot(n-2)\cdot v_0\cdot K_{IC}^{-2}\cdot\pi}{2(n+1)}\right)\cdot\left(1-\left(\frac{K_{TH}}{K_{IC}}\right)^{(n-2)}\right)$ and;

$$c_2=\frac{K_{IC}^{n-2}}{a_f{}^{(n-2)/2}\cdot\left(\sigma_f-\sigma_r\right)^{n-2}\cdot\pi^{(n-2)/2}}=0$$

Step 4 – Determination of initial flaw depth and the inert time limit: The LEFM geometry factor, Y_{SCG} can now be used to determine the initial flaw size using Eq. 4.5 and subsequently the inert time limit, t_{IN} using Eq. 4.3a.

Step 5 – Determination of the crack growth threshold time limit: The crack growth threshold time limit can also be determined using Eq. 4.3b. This time limit is worth noting for completeness sake

but experimental failure times are almost never expected to exceed this time limit as its values are typically significantly large (e.g. Fig. 2.23).

Implementation

This procedure was implemented in the annealed glass series SA4 and SA21 (data shown in Table 4.3). The residual surface compression was determined with SCALP-05 (GlasStress, Ltd.) and was found to be $\sigma_{r,mean}$=2.31±0.65 MPa while the failure stress, σ_f was determined experimentally with CDR tests (Section 4.2) and a stress rate of 20 MPa/sec. Even though some uncertainty exists on the crack velocity, v_0=0.01 mm/sec was chosen in this study based on Haldimann's recommendations [97] for laboratory conditions. The fracture toughness and the crack growth threshold for soda-lime-silica glass were K_{IC}=0.75 MPa $m^{1/2}$ (Table 2.1) and K_{TH}=0.25 MPa $m^{1/2}$ [97] respectively. The lack of research on the crack growth threshold in soda lime silica glass, suggests that there is some uncertainty on its value, but this is not expected to cause any significant change when determining the time limit regardless of small changes in the values of K_{TH} as $\left(1-\left(\frac{K_{TH}}{K_{IC}}\right)^{(n-2)}\right)$=1 in Eq. 4.6. The static fatigue constant n=16 was selected for normal environmental conditions as is commonly used in glass studies [62,97].

Results

Table 4.4 shows that deeper flaws lead to larger time limits (t_{IN}) below which testing conditions are inert. In particular, the time to failure never exceeded the time limit for SA21 ($t_{IN} > t_f$). Therefore, a high stress rate of 20 MPa/sec is sufficient for suppressing sub-critical crack growth for gravel impacts and ensures inert testing conditions. The initial assumption that some sub-critical crack growth occurs during the course of the experiment is therefore false; the geometry factor now becomes $Y_{LEFM}=Y_{IN}$ (Table 4.4) and a new value can be calculated for t_{IN_new} and $a_i=a_f$.

However, it was found that the time to failure exceeded the time limit for SA4 ($t_{IN} < t_f$); this indicates that sub-critical crack growth occurred during the destructive testing and thus, the initial assumption that sub-critical crack growth occurs is true ($Y_{LEFM}=Y_{SCG}$). However, the sub-critical increase in flaw depth was small; 4% was the maximum crack growth reported between initial and final flaw depth (Table 4.4) while 2% was the maximum difference in failure stress between inert and sub-critical crack growth calculations for SA4. Nevertheless, the testing conditions cannot be considered inert.

Table 4.4: Linear elastic fracture mechanics results on the occurrence of sub-critical crack growth.

(a)

SA21											
Specimen	Y_{SCG}	Y_{IN}	t_{IN}	t_f	***SCG***	$a_f=a_i$	t_{IN_new}	$(a_f-a_i)/a_i$ %	$Y_{LEFM}=Y_{IN}$	Y_{MUR}	Y_{NR}
SA21-1	NA	NA	NA	1.56	-	NA	NA	0	NA	NA	NA
SA21-2	0.392	0.390	10.98	1.99	-	775.49	11.08	0	0.390	0.826	0.764
SA21-3	0.618	0.617	4.42	2.03	-	310.55	4.44	0	0.617	0.760	0.711
SA21-4	0.500	0.500	6.89	1.93	-	483.30	6.90	0	0.500	0.693	0.695
SA21-5	0.419	0.417	7.77	2.18	-	548.33	7.83	0	0.417	0.836	0.737
SA21-6	0.587	0.587	14.66	1.21	-	1025.96	14.66	0	0.587	0.754	0.668
SA21-7	0.554	0.553	4.67	2.10	-	328.24	4.69	0	0.553	0.950	0.851
SA21-8	0.726	0.725	5.79	1.50	-	406.21	5.80	0	0.725	0.731	0.697
SA21-9	0.814	0.814	6.22	1.30	-	435.81	6.23	0	0.814	0.735	0.703
SA21-10	0.712	0.705	2.34	2.32	-	167.24	2.39	0	0.705	0.684	0.744
SA21-11	0.526	0.526	6.52	1.92	-	457.03	6.53	0	0.526	0.687	0.694
SA21-12	0.391	0.386	11.97	1.91	-	859.13	12.27	0	0.386	0.741	0.674
SA21-13	0.438	0.438	8.80	1.99	-	615.69	8.80	0	0.438	0.735	0.791
SA21-14	0.894	0.892	2.69	1.78	-	189.50	2.71	0	0.892	0.846	0.834
SA21-15	0.968	0.965	2.46	1.71	-	172.80	2.47	0	0.965	1.012	0.983

(b)

SA4											
Specimen	Y_{SCG}	Y_{IN}	t_{IN}	t_f	***SCG***	a_i	a_f	$(a_f-a_i)/a_i$ %	$Y_{LEFM}=Y_{SCG}$	Y_{MUR}	Y_{NR}
SA4-1	0.820	0.815	1.84	2.73	✓	128.92	130.52	1.24	0.820	0.896	0.900
SA4-2	1.052	1.039	0.94	2.76	✓	65.72	67.43	2.60	1.052	0.745	0.729
SA4-3	1.255	1.234	0.77	2.85	✓	54.05	55.89	3.40	1.255	0.753	0.748
SA4-4	0.915	0.909	1.48	2.58	✓	103.70	105.15	1.40	0.915	0.854	0.865
SA4-5	1.347	1.329	0.80	2.43	✓	55.92	57.42	2.68	1.347	0.698	0.723
SA4-6	1.287	1.269	0.78	2.59	✓	54.81	56.42	2.94	1.287	0.805	0.864
SA4-7	1.495	1.467	0.63	2.60	✓	44.02	45.71	3.84	1.495	0.688	0.720
SA4-8	0.986	0.976	1.19	2.67	✓	83.50	85.14	1.97	0.986	0.787	0.820
SA4-9	1.116	1.097	0.76	2.77	✓	53.31	55.12	3.40	1.116	0.757	0.755
SA4-10	1.200	1.179	0.71	2.78	✓	49.72	51.53	3.63	1.200	0.749	0.746
SA4-11	0.519	0.516	3.74	2.72	-	261.96	264.54	0.98	0.519	0.767	0.966
SA4-12	0.910	0.902	1.32	2.66	✓	92.33	93.93	1.73	0.910	0.801	0.918
SA4-13	1.117	1.103	0.91	2.59	✓	63.56	65.14	2.49	1.117	0.694	0.725
SA4-14	1.053	1.038	0.94	2.99	✓	65.83	67.68	2.82	1.053	0.837	0.860
SA4-15	1.135	1.116	0.77	2.84	✓	53.87	55.71	3.41	1.135	0.702	0.722

Y_{SCG}: sub-critical crack growth, Y_{IN}: inert, Y_{LEFM}: linear elastic fracture mechanics ($Y_{LEFM}=Y_{SCG}$ / Y_{IN} depending on testing conditions, Y_{MUR}: Murakami and; Y_{NR}: Newman-Raju and; SCG: sub-critical crack growth (✓occurrence, - suppression).

Conclusions and Discussion

Despite the very high stress rate (20 MPa/sec) during the destructive test, sub-critical crack growth can still occur and depends on the initial flaw depth and time to failure. The testing conditions can be therefore, considered quasi-inert which indicates that sub-critical crack growth is minimized but is not eliminated for all series. The influence of sub-critical crack growth becomes significantly larger for lower stress rates and larger failure times, and increases as the stress rates decrease. Therefore, the need to normalise its effect for specimens that failed at different times and that were consequently exposed to different levels of sub-critical crack growth, becomes urgent when direct comparison is needed among them.

One of the following approaches can be used to treat failure stress data to normalise the influence of sub-critical crack growth, depending on the amount of information that is available and the level of accuracy that one aspires to achieve:

Level I - Known fractographic and failure stress data for all specimens: An explicit approach similar to the one described in Section 4.3 can be used to determine the initial flaw size (α_i) and consequently the inert time limit (t_{IN}) in the ideal case when fractographic data (α_f) and failure stress data (σ_f and t_f) are available for each specimen. In this case three scenarios may appear:

(i) $t_f \leq t_{IN}$ for all specimens within the specific study: Sub-critical crack growth does not commence along the experimental ramp stress path and conversion to an equivalent stress is not necessary.

(ii) $t_f > t_{IN}$ for all specimens within a specific study: Sub-critical crack growth occurs along the experimental stress path for all specimens and therefore, the ramp failure stress needs to be converted to an equivalent constant failure stress for a reference time, t_{ref}. However, sub-critical crack growth occurs only when $t > t_{IN}$ and therefore Eq. 2.7 is transformed to Eq. 4.7 as follows:

- Annealed glass: $\int_0^{t_f - t_{IN}} \left[\frac{\left(\sigma_f - \sigma_{t_{IN}}\right) \cdot t}{t_f - t_{IN}} \right]^n dt = \int_0^{t_{ref} - t_{IN}} \left(\sigma_{f,eq} - \sigma_{t_{IN}}\right)^n dt \Rightarrow$

$$\sigma_{f,eq} = \sigma_{t_{IN}} + \left(\sigma_f - \sigma_{t_{IN}}\right) \cdot \left[\frac{t_f - t_{IN}}{\left(t_{ref} - t_{IN}\right) \cdot (n+1)} \right]^{1/n} \qquad \text{(Eq. 4.7)}$$

  where t_{ref}: the equivalent reference time; t_{IN}: the time at the commencement of sub-critical crack growth; $\sigma_{f,eq}$: the equivalent uniform failure stress for the reference time and; σ_{tIN}: the stress when t=t_{IN}.

- Toughened glass: As indicated in Section 2.5.3 sub-critical crack growth does not commence when the level of applied stress does not exceed the residual surface compression (i.e. $|\sigma_{app}| \leq |\sigma_r|$ and $t < t_r$). Therefore, in this case it should be determined whether $t_{IN} \geq t_r$ or $t_{IN} < t_r$. If the former applies, t_{IN} is more critical and therefore, Eq. 4.7 should be used to convert the

experimental failure stress to an equivalent, whereas if the latter is true, t_r is more critical than t_{IN} and Eq. 4.8 should be used instead.

$$\int_0^{t_f - t_r} \left[\frac{\left(\sigma_f + \sigma_r\right) \cdot t}{t_f - t_r} \right]^n dt = \int_0^{t_{ref} - t_r} \left(\sigma_{f,eq} + \sigma_r\right)^n dt \Rightarrow$$

$$\sigma_{f,eq} = -\sigma_r + \left(\sigma_f + \sigma_r\right) \cdot \left[\frac{t_f - t_r}{\left(t_{ref} - t_r\right) \cdot \left(n+1\right)} \right]^{1/n} \qquad \text{(Eq. 4.8)}$$

where σ_r: the residual surface compression and; t_r: the time for the applied stress to exceed the residual surface compression.

(iii) for incompatible modes among different specimens within a specific study i.e. $t_f > t_{IN}$ applies to some specimens (group 1) which indicates that sub-critical crack growth commenced for these specimens but $t_f < t_{IN}$ applies to the rest (group 2) which indicates that inert conditions were achieved for the rest of the specimens, it is necessary to convert the ramp failure stress to an equivalent constant failure stress for a reference time, t_{ref} in order to allow comparison across different specimens belonging to groups 1 & 2. In this case t_{ref} can be selected to be larger or smaller than t_{IN}.

- For $t_{ref} > t_{IN}$: sub-critical crack growth will occur for all specimens (groups 1 & 2) for the equivalent time and therefore, Eq. 4.7 and Eq. 4.8 should be used to obtain the equivalent failure stress for all specimens.
- For $t_{ref} \leq t_{IN}$: sub-critical crack growth will not commence for all specimens (groups 1 & 2) for the equivalent time. Therefore, the failure stress of specimens that did not exceed the inert limit t_{IN} (group 2) does not require any treatment but the failure stress of specimens that exceeded the inert limit t_{IN} (group 1) needs to be converted to its inert equivalent. To do so, the stress at the intersection point between curves A and B in Fig. 2.23 has to be determined using Eq. 4.9 a-b for annealed and toughened glass respectively.

$$\sigma_{f,eq} = \frac{K_{IC}}{\mathrm{Y} \cdot \sqrt{\pi \cdot a_i}} \text{ and } \sigma_{f,eq} = -\sigma_r + \frac{K_{IC}}{\mathrm{Y} \cdot \sqrt{\pi \cdot a_i}} \qquad \text{(Eq. 4.9a-b)}$$

Level II – Unknown fractographic data: Fractographic data are usually not available and fractographic analysis is time consuming to undertake for all specimens within a specific study. Therefore, the time limit between inert conditions and the commencement of sub-critical crack growth, t_{IN} cannot be determined. Consequently the *Level I* approach can no longer be used and additionally, the commencement or the influence of sub-critical crack growth for the specific destructive test cannot be evaluated. In this case, the more reliable approach involves converting the failure stress data to an equivalent constant failure stress for a reference time t_{ref} which is

significantly high (e.g. t_{ref}=60 sec) to ensure that sub-critical crack growth commences before t_{ref} is exceeded (i.e. $t_{IN} < t_{ref}$).

For annealed glass specimens this is achieved by using Eq. 4.10 whilst for toughened glass Eq. 4.8 should be used instead. This approach neglects the inert limit, however, this is safer / more reliable than completely neglecting the influence of sub-critical crack growth (especially for destructive tests with low stress rates).

$$\int_0^{t_f}\left(\frac{\sigma_f \cdot t}{t_f}\right)^n dt = \int_0^{t_{ref}} \sigma_{f,eq}^n dt \Rightarrow \sigma_{f,eq} = \sigma_f \cdot \left[\frac{t_f}{t_{ref} \cdot (n+1)}\right]^{1/n} \quad \text{(Eq. 4.10)}$$

This approach will be used throughout Chapter 5 for naturally aged, as-received, scratched and sand abraded annealed glass specimens as fractographic analysis data were not available for all specimens. However, uncertainties appear when this method is applied to toughened glass e.g. when the residual surface stress is unknown or the residual stress at the critical flaw depth is unknown; these will be discussed in detail in Section 6.3.3 of Chapter 6.

4.3.3 Geometry factors for critical flaws

The aim of this additional investigation is to compare the geometry factor obtained using the linear elastic fracture mechanics approach in Section 4.3.2 (Y_{LEFM}, Table 4.4) with geometry factors obtained using a fractographic approach which combines existing analytical models and the fractographic analysis data of Section 4.3.1.

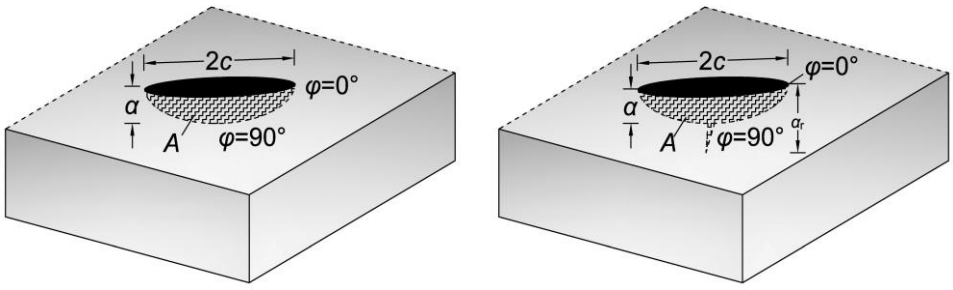

(a) (b)

Fig. 4.14: Flaw characteristics: (a) absence of radial-median cracks; (b) with radial median cracks.

A) Newman and Raju [145]: This model considers the geometry of elliptical surface flaws as well as the dimensions of the specimen and the loading conditions to obtain the geometry factor (Eq. 4.11) at the depth of the flaw (i.e. for $\varphi=\pi/2$ where φ is the parametric angle measured from the surface to the point of interest).

$$Y_{NR} = \frac{F_s \cdot H_s}{\sqrt{Q}} \quad \text{(Eq. 4.11)}$$

where F_s: boundary correction factor for surface flaws away from edges and under tension H_S: bending multiplier for flaws under flexure and; Q: shape factor for elliptical flaws. Detailed formulae for these are available in [145] for $a/c > 1$ and $a/c \leq 1$ (Fig. 4.14).

B) Murakami [146,147]: This method takes into account the area of the critical flaw perpendicular to the tensile opening stress, A (Fig. 4.14) and can be applied to irregularly shaped flaws. The geometry factor is given by Eq. 4.12a for a Poisson's ratio of v=0 [146] and Eq. 4.12b for v=0.3 [147]. These formulae are only valid for $a/c \geq 5$. For any other case a/c=5 should be used instead. A linear approximation was obtained in this study for soda lime silica glass and v=0.23 as shown in Eq. 4.13. This equation additionally incorporates the bending multiplier, H_s, of the Newman-Raju method to account for the bending:

$$Y = \frac{0.629 \cdot A^{1/4}}{\sqrt{a}} \text{ for } v=0 \text{ and } Y = \frac{0.650 \cdot A^{1/4}}{\sqrt{a}} \quad \text{for } v=0.3 \qquad \text{(Eq. 4.12a \& b)}$$

$$Y_{MUR} = \frac{0.645 \cdot A^{1/4}}{\sqrt{a}} \cdot H_s \qquad \text{(Eq. 4.13)}$$

The geometry factor was calculated with the above fractographic models for all specimens in the SA21 and the SA4 series. The flaw depth, α, was taken equal to α_r when radial/median flaws were present and α_{ef} in any other case (Table 4.4).

The geometry factors obtained from the above fractographic models and the linear elastic fracture mechanics approach in Section 4.3.2 are compared in Fig. 4.15 for each specimen in the SA21 and SA4 series; mean values are also reported.

It was found that the mean Murakami geometry factor is in good agreement with the mean Newman-Raju geometry factor for series SA21 (Fig. 4.15a) and series SA4 (Fig. 4.15b). Moreover, the mean values of the Murakami and the Newman-Raju models do not differ significantly between flaws induced by sand grains (SA4) and flaws induced by gravel (SA21) (Fig. 4.15a-b). This suggests that the above fractographic models are insensitive to the flaw size and predict a general mean geometry factor of Y_{mean}=0.7 for morphologically similar flaws induced by erosive action. This value is in close agreement with the geometry factor for half-penny shaped flaws subjected to bending which is Y=0.713 [148,149] (other typical geometry factors can be found in [97,124,150]).

The LEFM investigation in Section 4.3.2 however, indicates that the geometry factor is sensitive to the flaw size in this approach; flaws induced by gravel impact have a lower geometry factor ($Y_{LEFM,gravel}$=0.610) than flaws induced by sand impact ($Y_{LEFM,sand}$=1.080). Additionally, discrepancies were found between the linear elastic fracture mechanics calculations and the existing fractographic models (Fig. 4.15) for: (a) SA21: the LEFM mean geometry factor is 11%

and 17% smaller than that reported with the Murakami and the Newman-Raju model respectively and; (b) SA4: the LEFM mean geometry factor is 60% and 45% larger than that reported with the Murakami and the Newman-Raju model respectively.

Overall, a mean geometry factor of Y_{LEFM}=0.845 was found for all specimens with the LEFM approach (SA21 & SA4). This value is 14 and 26% higher than the mean factors reported by the Newman-Raju (Y_{NR}=0.728) and the Murakami (Y_{MUR}=0.673) models.

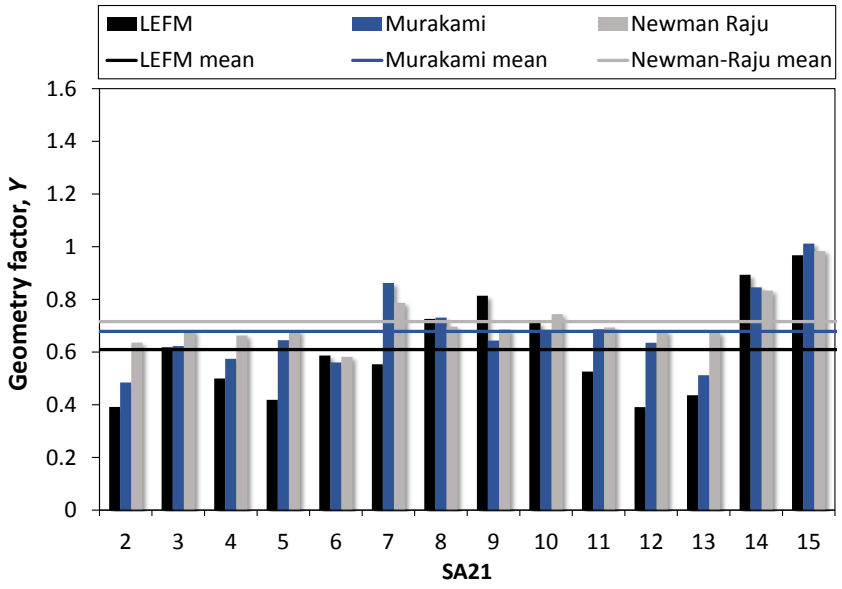

(a)

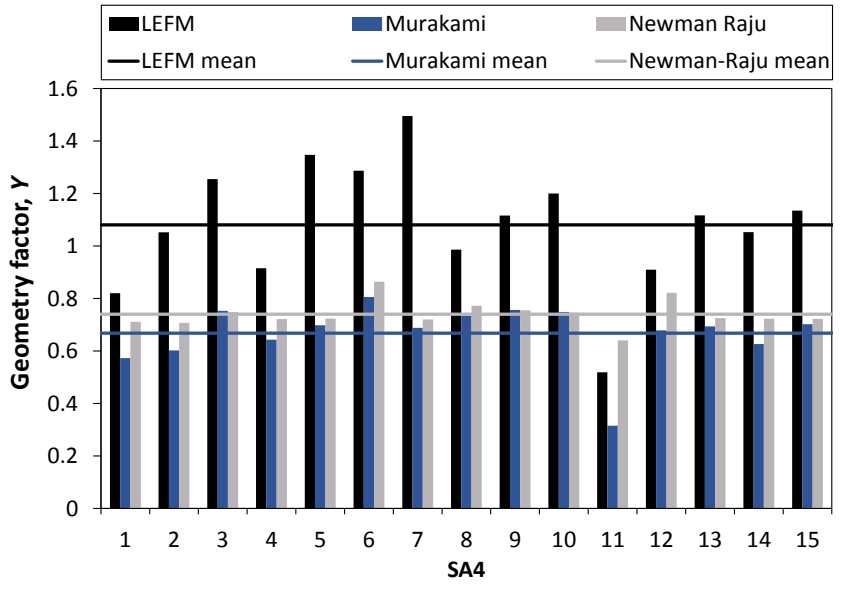

(b)

Fig. 4.15: Geometry factors (LEFM calculation, Newman Raju and Murakami) for SA4 & SA21.

The discrepancy between the LEFM investigation and the fractographic models could be attributed to one of the following reasons:

(a) fractographic models are designed for specific flaw morphologies e.g. Newman-Raju for elliptical flaws. However, flaws are usually irregularly shaped and therefore, difficult to apply to fractographic models. Although Murakami's model is designed for irregularly shaped flaws, uncertainties exist on the approximation made to suit the Poisson ratio of glass and the bending multiplier. Additionally, no information could be found on the modifications that are needed in these models, in addition to the half penny flaws, when radial/median flaws are present.

(b) uncertainties are associated with the LEFM investigation and particularly with the selection of input parameters (n, v_0, K_{IC} and K_{TH}). However, one would expect that such uncertainties would have a similar impact on both SA21 and SA4 series; however, this is not true in this case as the LEFM geometry factor is found to be larger than the fractographic ones, in SA21 whereas the opposite applies to SA4.

(c) a limitation of the LEFM approach is that only the flaw depth is taken into consideration with Eq. 4.4 for the estimation of the geometry factor, neglecting the flaw width or its area.

Further investigation is therefore, needed to address these issues. However, as this is not closely related to the main aims of this thesis, it is suggested for future work. Geometry factors are subsequently used only in Section 6.4.4 in Chapter 6 for gravel abraded fully toughened glass. A geometry factor of $Y_{LEFM,gravel}$=0.610 is adopted in that Section based on the findings of the linear elastic fracture mechanics approach shown in Section 4.3.2 for the gravel abraded series SA21. The LEFM approach is preferred for that case in order to account for the radial/median cracks arising from gravel impacts that the fractographic models fail to consider.

4.4 Statistical analysis of small samples of glass strength data

Strength data from macroscopically identical glass specimens is commonly described by a two-parameter Weibull distribution, as discussed in Section 2.5.3, but very little attention is given to the method that is used for fitting the strength data to the Weibull distribution.

There are various approaches for estimating the Weibull parameters from a given set of strength data. They can be classified either as manual or computational methods. Manual calculations can be performed by: (a) least square regression (*LR*); (b) weighted least square regression (*WLR*) and; (c) a linear approach based on good linear unbiased estimators (*GLUEs*); while computational (computer-based) methods are: (a) the maximum likelihood estimation (*MLE*) and; (b) the method of moments estimation (*MME*).

The aim of this Section is to review these different estimation methods for Weibull parameters and to propose the most effective method for the statistical analysis of small sized samples of glass strength. An overview of the existing methods for estimating the Weibull parameters and

goodness-of-fit for glass strength data are first reviewed in Section 4.4.1. The existing methods (*LR*, *WLR*, *GLUEs* and *MLE*) are then implemented on 30 real data sets, obtained from destructive tests on naturally aged, as-received and artificially aged glass obtained for the purpose of Chapter 5. The goodness-of-fit and strength estimations of each method are presented and discussed in Section 4.4.3 and the conclusions are provided in Section 4.4.4.

4.4.1 Review of Weibull statistics methods

The two principal steps when performing a statistical analysis are: estimating the statistical parameters and evaluating the goodness-of-fit. These are reviewed in this section in the context of a Weibull distribution for glass strength data.

Parameter estimation

The most commonly used approaches, within the Weibull statistics community, for the estimation of the shape and scale parameters of the Weibull distribution are described below.

Manual calculation methods

Equivalent strength data are ranked in ascending order (i=1 to k) for the manual calculation methods. Equal probabilities of failure, P_f, are assigned to each data point in cumulative form with functions called probability estimators, E_i. The simplest forms of probability estimators are $E=i/k$ or $E=(i-1)/k$ but these estimators eliminate the highest or lowest data point of the sample in the CDF graph for $P_f=1$ or $P_f=0$ respectively; the highest/lowest strength point are therefore, also eliminated during the estimation of the Weibull parameters so that instead of k specimens, only (k-1) would be considered. Therefore, these estimators are avoided and probability estimators of the following form are preferred instead:

$$E_j = \frac{i - C_j}{k + 1 - 2C_j} \qquad \text{(Eq. 4.14)}$$

where C_j is a constant $0 \le C_j < 1$, i is the index of the ascending order and k is the sample size. The following four probability estimators (E_j, j=1 to 4, [151–153]) are most commonly used in Weibull statistics:

- E_1 (mean rank estimator): $C_1 = 0 \rightarrow E_1 = \frac{i}{k+1}$ (Eq. 4.15a)
- E_2: (Hazen's estimator): $C_2 = 0.5 \rightarrow E_2 = \frac{i-0.5}{k}$ (Eq. 4.15b)
- E_3: (median rank estimator): $C_3 = 0.3 \rightarrow E_3 = \frac{i-0.3}{k+0.4}$ (Eq. 4.15c)

- E_4: (small sample estimator): $C_4 = 0.375 \rightarrow E_3 = \dfrac{i - 0.375}{k + 0.25}$ (Eq. 4.15d)

Least Squares Regression (LR)

The Weibull parameters are determined using a least squares approach (*LR*), minimizing the sum of squared residuals of the *x* values about Eq. 2.9:

$$\beta = \frac{k \cdot \sum_{i=1}^{k} \left[\ln(\sigma_i) \cdot y_i\right] - \sum_{i=1}^{k} (\ln \sigma_i) \cdot \sum_{i=1}^{k} (y_i)}{k \cdot \sum_{i=1}^{k} \left[(\ln \sigma_i)^2\right] - \left[\sum_{i=1}^{k} (\ln \sigma_i)\right]^2} \quad \text{(Eq. 4.16a)}$$

$$-\beta \cdot \ln \theta = \frac{\sum_{i=1}^{k} (y_i) - \beta \times \sum_{i=1}^{k} (\ln \sigma_i)}{k} \quad \text{(Eq. 4.16b)}$$

However, *LR* implicitly applies the same unit weight to each data point without accounting for the uncertainty of $y = \ln\left(\ln\left(\frac{1}{1-E}\right)\right)$ or E_i. and thus, provide biased estimates.

Weighted Least Squares Regression (WLR)

Weibull parameters with smaller bias can be obtained (Eq. 4.17a & b) when weight functions based on the uncertainty of *y* and *E* are introduced within the *LR* method leading to a Weighted Least Squares Regression, *WLR* [154].

$$\beta = \frac{\sum_{i=1}^{k} W_i \cdot \sum_{i=1}^{k} \left[\ln(\sigma_i) \cdot y_i \cdot W_i\right] - \sum_{i=1}^{k} \left[\ln(\sigma_i) \cdot W_i\right] \cdot \sum_{i=1}^{k} (y_i \cdot W_i)}{\sum_{i=1}^{k} W_i \cdot \sum_{i=1}^{k} \left[(\ln \sigma_i)^2 \cdot W_i\right] - \left[\sum_{i=1}^{k} (\ln \sigma_i) \cdot W_i\right]^2} \quad \text{(Eq. 4.17a)}$$

$$-\beta \cdot \ln \theta = \frac{\sum_{i=1}^{k} (y_i \cdot W_i) - \beta \cdot \sum_{i=1}^{k} \left[\ln(\sigma_i) \cdot W_i\right]}{\sum_{i=1}^{k} W_i} \quad \text{(Eq. 4.17b)}$$

where W_i is the weight applied to each data point.

Various weight functions have been proposed over the years [154–156] with Bergman's (Eq. 4.18a, [154]) and Faucher & Tyson's weight function (Eq. 4.18b, [155]) being mostly used. Faucher and Tyson's (*F&T*) was found to produce the most accurate estimates for data sets produced with Monte Carlo simulation [156–158]. However, these studies disagree on the choice of estimator used in conjunction with the *F&T* function; the two most accurate probability

estimators for small sized samples (k=10-20) were found to be the mean and median rank estimators (Eq. 4.15a & c, [156–158]).

$$W_i = \left[\left(1-P_i\right)\cdot\ln\left(1-P_i\right)\right]^2 \quad and; \quad W_i = 3.3\cdot P_i - 27.5\cdot\left[1-\left(1-P_f\right)^{0.025}\right] \qquad \text{(Eq. 4.18a-b)}$$

Good Linear Unbiased Estimators (GLUEs)

Simple unbiased estimators for the shape and the scale factor known as good linear unbiased estimators (*GLUEs*, Eq. 4.19a & b for complete / uncensored samples) were proposed by Bain [159,160]. This method uses an un-biasing constant, k_n and an integer number, s, to minimize the variance of the *GLUEs* (details given in [159–161]). Probability estimators, E_i, (Eq. 4.15a-d) are solely used in this method to assign a probability of failure to each equivalent strength data point whilst plotting the CDF (Eq. 2.9) and are not considered during the computation of the Weibull parameters; a median rank estimator (Eq. 4.15c) is proposed in EN 12603:2002 [162].

$$\beta = \frac{k\cdot k_n}{\frac{s}{k-s}\sum_{i=s+1}^{k}\left(\ln\sigma_i\right)-\sum_{i=1}^{s}\left(\ln\sigma_i\right)} \quad and; \quad \theta = \exp\left(\frac{1}{k}\sum_{i=1}^{k}\left(\ln\sigma_i\right)+0.5772\frac{1}{\beta}\right) \qquad \text{(Eq. 4.19a-b)}$$

where k_n is an un-biasing constant, values provided in Tables for k=2 to 60 [159,162] and s is the largest integer for the product of $0.84\cdot k$.

Computational methods

Maximum likelihood estimation (MLE)

The maximum likelihood estimation (*MLE*) is the method prescribed in ASTM C1239-13 [163] and DIN EN 843-5 [164]. This method computes a set of shape and scale factor that maximizes the likelihood / provides the highest probability of producing the data obtained from the destructive testing. The likelihood function (Eq. 4.20) is defined as the product, Π, of function, f, which associates the strength data, the shape and the scale parameters. The logarithm of the likelihood function is maximized by differentiating ln$L$ over each of the unknown parameters (β, θ) and subsequently setting each of the partial derivatives to 0 (Eq. 4.21a-b, likelihood equations). ln$L$ is preferred in this step to reduce the complexity of calculations (i.e. the logarithm of the product Π(f) is now converted in sums Σf). Analytical calculations lead to Eq. 4.22a-b (details shown in [165]). A closed form solution of Eq. 4.22a-b is not available; therefore, iterative numerical methods (e.g. gradient method) are used to obtain estimates for β and θ. A MATLAB script is used in this study.

$$L = \prod_{i=1}^{k} f\left(\sigma_i;\beta,\theta\right) \qquad \text{(Eq. 4.20)}$$

$$\frac{\partial \sum_{i=1}^{k} \ln L}{\partial \beta} = 0 \quad and; \quad \frac{\partial \sum_{i=1}^{k} \ln L}{\partial \theta} = 0 \qquad \text{(Eq. 4.21a-b)}$$

$$\frac{k}{\beta} - k \frac{\sum_{i=1}^{k} \left[\sigma_i^{\beta} \cdot \ln(\sigma_i)\right]}{\sum_{i=1}^{k} \sigma_i^{\beta}} + \sum_{i=1}^{k} \sigma_i = 0 \quad and; \quad \theta = \left(\frac{\sum_{i=1}^{k} \sigma_i^{\beta}}{k} \right)^{1/\beta} \qquad \text{(Eq. 4.22a-b)}$$

Method of moments estimation (MME)

Moments are quantitative characteristics that describe a distribution and can be taken about the origin of the distribution (raw moments, μ', Eq. 4.23a) or the mean (central moments, μ, Eq. 4.23b).

$$\mu'_r = \int_0^{\infty} \sigma^r \cdot P(\sigma) d\sigma \qquad \text{(Eq. 4.23a)}$$

$$\mu_r = \int_0^{\infty} \left(\sigma - \bar{\mu}\right)^r \cdot P(\sigma) d\sigma \qquad \text{(Eq. 4.23b)}$$

where r is the order of the moment; $P(\sigma)$ is the probability density function; σ is the strength of glass and $\bar{\mu}$ is the mean of the distribution.

For example, the 0th raw moment describes the total probability of failure $\left(\mu'_0 = 1\right)$ and the 1st raw moment describes the mean of the distribution $\left(\mu'_1 = \bar{\mu}\right)$. Additionally, the second, third and fourth central moments describe the variance $\left(\mu_2 = s^2\right)$, the skewness and the kurtosis of the distribution, respectively. For the Weibull distribution, the formula for the theoretical distributional moments is given by Eq. 4.23c (analytical calculations shown in [165]).

$$\mu_r = \theta^r \int_0^{\infty} y^{r/\beta} \cdot e^{-y} dy \qquad \text{(Eq. 4.23c)}$$

where $y = \left(\frac{\sigma}{\theta}\right)^{\beta}$.

Moments are used in the method of moments (*MME*) to calculate the shape and the scale factor of the Weibull distribution by extending the known characteristics/moments of the sample to the corresponding characteristics/moments of the population. The number of moments that are needed is defined by the number of unknowns; two moments are therefore, needed for the estimation of the shape, β, and scale, θ, factor. In particular, the known sample moments which can be obtained from strength data (Eq. 4.24), are equated to the corresponding raw theoretical distributional moments (Eq. 4.25a-b, [166]), as shown in Eq. 4.26a. Subsequently, their members are divided by parts as shown in Eq. 4.26b wherein β is the sole unknown. β can be computed

with numerical processes or tables provided in literature (e.g. in [166]). θ is then easily computed by substituting β in Eq. 4.25a.

$$\mathrm{M}_r = \frac{1}{k} \cdot \sum_{i=1}^{k} x_i^r \rightarrow \mathrm{M}_1 = \frac{1}{k} \cdot \sum_{i=1}^{k} x_i \quad and; \quad \mathrm{M}_2 = \frac{1}{k} \cdot \sum_{i=1}^{k} x_i^2 \qquad \text{(Eq. 4.24)}$$

$$\mu'_1 = \bar{\mu} = \theta \cdot \Gamma\left(1 + \frac{1}{\beta}\right) \qquad \text{(Eq. 4.25a)}$$

$$\mu'_2 = s^2 + \mu'^2_1 = \theta^2 \cdot \left[\Gamma\left(1 + \frac{2}{\beta}\right) - \Gamma^2\left(1 + \frac{1}{\beta}\right)\right] + \theta^2 \cdot \Gamma^2\left(1 + \frac{1}{\beta}\right) = \theta^2 \cdot \Gamma\left(1 + \frac{2}{\beta}\right) \qquad \text{(Eq. 4.25b)}$$

$$\mu'_1 = M_1 \quad \& \quad \mu'_2 = M_2 \qquad \text{(Eq. 4.26a)}$$

$$\frac{\mu'^2_1}{\mu'_2} = \frac{M_1^2}{M_2} \Rightarrow \frac{\theta^2 \cdot \Gamma^2\left(1 + \frac{1}{\beta}\right)}{\theta^2 \cdot \Gamma\left(1 + \frac{2}{\beta}\right)} = \frac{\left(\frac{1}{k} \cdot \sum_{i=1}^{k} x_i\right)^2}{\frac{1}{k} \cdot \sum_{i=1}^{k} x_i^2} \Rightarrow \frac{\Gamma^2\left(1 + \frac{1}{\beta}\right)}{\Gamma\left(1 + \frac{2}{\beta}\right)} = \frac{\left(\frac{1}{k} \cdot \sum_{i=1}^{k} x_i\right)^2}{\frac{1}{k} \cdot \sum_{i=1}^{k} x_i^2} \qquad \text{(Eq. 4.26b)}$$

where $\Gamma(n) = \int_0^\infty e^{-x} \cdot x^{k-1} dx$.

Comparison of methods

Previous research involving data generated numerically by Monte Carlo simulations, show contradictory results when comparing different Weibull parameter estimation methods. Computational methods (*MLE* and *MME*) are identified as more efficient in [167–169]. However, manual calculations and *WLS* in particular, produced the smallest standard deviation, *s*, for the shape parameter and was therefore found to be more accurate than computational methods [157]. In other studies, the accuracy of estimation methods was found to vary with the size of the sample, *k* [158,170]; computational methods performed better for medium or large size samples ($k > 52$) whilst manual calculations for small samples ($k < 52$). More specifically, the following were concluded for:

(a) manual calculations:

- *WLR* outperforms *LR* [155,158,170].
- Faucher and Tyson's (*F&T*) weight function provides the most accurate estimates (for $k \geq 7$ [156–158]).
- No clear conclusion has been reached on the choice of probability estimators; E_1 (Eq. 4.15a) is considered the most conservative estimator and is suggested for engineering purposes in [151]. E_1 is also preferred in Makkonen [171] because it is considered independent of any particular distribution; the mean of the cumulative distribution function converges to the

Weibull estimator when multiple samples are sourced from the same population. This was however, rebutted in Cook [172] pointing out that Makkonen fails to consider sampling errors and that the above would only be valid for an infinite number of samples; however, extreme value analysis is typically based on a limited number of samples and therefore, this suggestion is not valid. Among other probability estimators, E_2 (Eq. 4.15b) was found to provide the least biased estimations [99,169] and; E_3 (Eq. 4.15c) produced the smallest coefficient of variation of Weibull parameters [167].

- the bias of estimation is a function of sample size, *k*, and linear regression method [158].

(b) *computational methods*:

- Estimates for *MLE* are very similar to *MME* [170,173].
- *MLE* provides the least dispersion (narrower confidence intervals for *LR* methods) [158,173].
- The probability of overestimating strength is high (P=60%) for *MLE* [169].

A significant gap in the studies to-date is that the European standard EN12603 [162] on Weibull distributed glass strength data prescribes a *GLUEs* method, the effectiveness of which does not appear to have been investigated or compared in any of these studies. Another limitation of the above studies is that Weibull parameters were estimated for "artificial" data sets that were randomly generated with Monte Carlo simulations for a given shape and scale factor (β_{true} and θ_{true}). These data sets were then evaluated based on their accuracy i.e. the discrepancy between the true shape factor that was initially chosen, β_{true}, and the estimated shape factor obtained for a specific estimation method. This is a valid approach for artificially generated data sets, but this evaluation method cannot be used for real data sets since the true value of the shape factor of the population is unknown. Therefore, based on the knowledge that glass strength can be described with a 2-parameter, an alternative procedure that employs a goodness-of-fit test is used to assess the effectiveness of each Weibull parameter estimation method. Effectiveness in this paper is a measure of the goodness of fit i.e. the higher the goodness-of-fit the more effective the method.

Goodness-of-fit

The methods for estimating the Weibull parameters are based on the null hypothesis (H_0) that the equivalent strength data follow a Weibull distribution. Goodness-of-fit methods are used to evaluate whether H_0 needs to be rejected, which would indicate that the Weibull distribution does not provide a good fit to the data under consideration. A significance level, λ, is therefore, chosen prior to the statistical analysis (λ=0.05 in this study); λ represents the probability of rejecting a good fit i.e. it defines the confidence level that the data do not follow a Weibull distribution. The observed significance level p, that describes the specific data set is then compared to the chosen significance level, λ. If:

- $p \leq \lambda$: the data do not follow a Weibull distribution (H_0 rejected);
- $p > \lambda$: there is lack of evidence that data do not follow a Weibull distribution and therefore, H_0 cannot be rejected;

This study uses goodness-of-fit methods based on the empirical distribution function (EDF) statistics. EDF statistics are used in various goodness-of-fit methods (Kolmogorov-Smirnov, Cramer-von Mises, Chi-squared, Anderson Darling etc. [174]); these methods depend on the distance, *D*, between the EDF (Eq. 4.27) and the theoretical distribution function (TDF) i.e. the assumed CDF for the estimated shape and scale factor as shown in Fig. 4.16. EDF statistics are therefore, independent of the choice of probability estimator, *E* (Eq. 4.15). TDF should follow closely the EDF when the assumed distribution is a good fit for the particular data set.

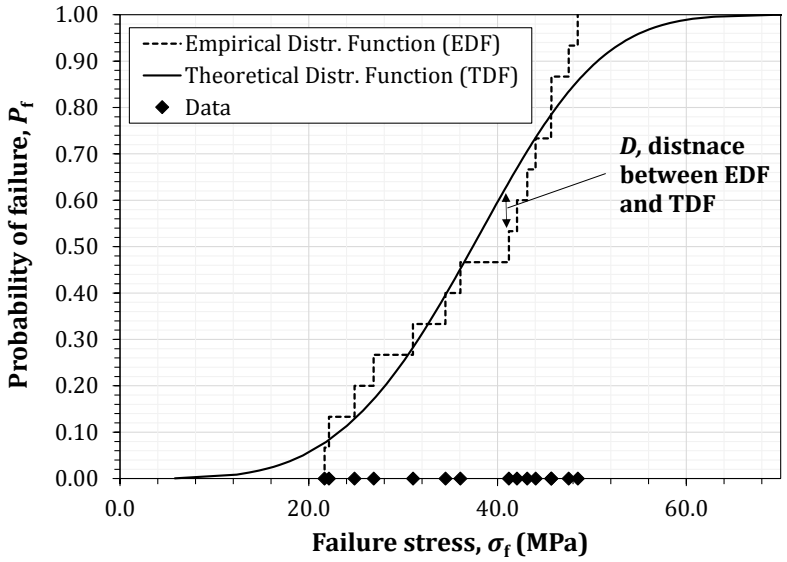

Fig. 4.16: Empirical distribution function and theoretical cumulative distribution function for glass strength.

$$F_k = \frac{1}{k}\sum_{i}^{k} 1\{\sigma_i \leq \sigma\} \qquad \text{(Eq. 4.27)}$$

where $1\{\sigma_i \leq \sigma\}$ is the indicator function that counts the number of observations that are equal to or smaller to a fixed σ which each time represents a particular data point of the set i.e.:

$$1\{\sigma_i \leq \sigma\} = \begin{cases} 1 & \sigma_i \leq \sigma \\ 0 & \sigma_i > \sigma \end{cases}$$

The Anderson Darling (*AD*) goodness-of-fit is typically used during the assessment of glass strength data [13,94,97]. *AD* belongs to the group of quadratic EDF statistics as it is a function of the squared distance, D^2, between the EDF and TDF. Additionally, this method employs a weight function, w_{AD} (Eq. 4.28) in order to apply more weight to the upper and lower tail of the CDF. This is essential for the statistical analysis of glass strength data as strengths at low probabilities of

failure (i.e. at the lower tail of CDF) are typically used in engineering design. Therefore, the AD goodness-of-fit will be used in this study. The observed significance level, p_{AD}, for the *AD* goodness-of-fit is given by Eq. 4.29.

$$AD = k\int_0^1 \frac{\left[F_k(\sigma) - P_f(\sigma)\right]^2}{w_{AD}} dP_f(\sigma) = k\int_0^1 \frac{\left[F_k(\sigma) - P_f(\sigma)\right]^2}{P_f(\sigma)\cdot\left[1 - P_f(\sigma)\right]} dP_f(\sigma) \qquad \text{(Eq. 4.28)}$$

$$p_{AD} = \frac{1}{1+\exp\left(-0.1+1.24\cdot\ln(AD^*)+4.48\cdot AD^*\right)} \qquad \text{(Eq. 4.29)}$$

where $AD^* = \left(1+\frac{0.2}{\sqrt{k}}\right)\cdot AD^2$ and $AD^2 = -k - \sum_{i=1}^{k}\frac{(2i-1)}{k}\cdot\left[\ln\left(P_f(\sigma_i)\right)+\ln\left(1-P_f(\sigma_{k+1-i})\right)\right]$

A unimodal Weibull distribution is typically sufficient to describe failures in glass. However, poor goodness of fit could potentially denote bi-modal distributions. Bi-modal distributions can occur due to different causes of failure/morphologies of critical flaws in different specimens in the same series. These data series are more faithfully described by mixed Weibull distributions (Appendix F, Eq. F1).

4.4.2 Method

Glass specimens and destructive tests

30 real data sets ($10 \le k \le 18$) of glass surface strength data, were obtained from as-received, naturally aged and artificially aged annealed glass specimens tested for the purpose of Chapter 5. The naturally aged glass (NA-AN$_a$-NA-AN$_b$) used in this study was obtained from a façade in Norfolk, UK after 20 year of exposure. The artificially aged glass was either sand abraded (SA1 - SA24) or scratched (SC1 - SC2).

Table 4.5 provides an overview of the series. In total 418 specimens, grouped in 30 series each consisting of between 10 and 18 specimens, were tested destructively. The destructive tests were performed in a coaxial double ring set-up complying with ASTM C1499-3 [134] to obtain glass surface strength data as already described in Section 4.2. Strength data were excluded from further consideration for specimens whose origin of failure was located outside the boundaries of the loading ring. A stress rate of 20 MPa/sec was chosen in order to minimize the influence of sub-critical crack (Section 4.3). Variations in sub-critical crack growth were normalised by converting strength results into equivalent strengths for a constant load of t_{ref}=60 sec (Section 4.3, raw data are shown in Table B1a-b, Appendix B).

Table 4.5: Specimens.

Abbr.	Glass type	Processing	Dimensions (mm)	No of data sets
NA-AN	annealed	Natural	150x150x3	2
AR-AN	annealed	As-received	150x150x3	1
SA-AN	annealed	Sand abraded	150x150x3	25
SC-AN	annealed	Scratched	150x150x3	2
Total				**30**

Estimation methods

The following estimation methods are implemented in this study on each set of glass strength data to determine its Weibull parameters: (a) *LR*; (b) *WLS* using Faucher & Tyson's (F&T) and Bergman's (B) weight function; (c) *GLUEs* and; (d) *MLE*. In total, 14 combinations of estimation methods, probability estimators and weight functions are used (Table 4.6). The Anderson Darling goodness-of-fit (p_{AD}) was the main criterion for evaluating the effectiveness of each method. The relative conservativeness of strength for each estimation method is also provided as supplementary material.

Table 4.6: Combinations of estimation methods, estimators and weight functions.

a/a	Method	Abbr.	Estimator	Abbr.	Weight Function
1	Least squares regression	*LR*	Mean rank (Eq. 4.15a)	E_1	-
2			Hazen's (Eq. 4.15b)	E_2	-
3			Median rank (Eq. 4.15c)	E_3	-
4			Small sample (Eq. 4.15d)	E_4	-
5	Weighted least squares regression	*WLR-F&T*	Mean rank (Eq. 4.15a)	E_1	Faucher and Tyson (Eq. 4.18b)
6			Hazen's (Eq. 4.15b)	E_2	
7			Median rank (Eq. 4.15c)	E_3	
8			Small sample (Eq. 4.15d)	E_4	
9	Weighted least squares regression	*WLR-B*	Mean rank (Eq. 4.15a)	E_1	Bergman (Eq. 4.18a)
10			Hazen's (Eq. 4.15b)	E_2	
11			Median rank (Eq. 4.15c)	E_3	
12			Small sample (Eq. 4.15d)	E_4	
13	Good linear unbiased estimator	*GLUEs*	Hazen's (Eq. 4.15b)	E_2	-
14	Maximum likelihood estimation	*MLE*	Hazen's (Eq. 4.15b)	E_2	-

To reduce the number of possible permutations the assessment is divided in two steps:

1st step: the performance (goodness-of-fit and conservativeness of strength estimates) of probability estimators (E_1-E_4) is assessed for the *LR*, *WLR-F&T* and *WLR-B* estimation methods.

The *GLUEs* and *MLE* are excluded from this assessment, because as explained in Section 4.4.1, the probability estimators do not influence the Weibull parameters.

2nd step: the best performing probability estimators from the 1st step is used to assess the performance of the five different Weibull parameter estimation methods (*LR-*E_2, *WLR-F&T-*E_2 and *WLR-B-*E_2, *GLUEs* and *MLE*).

4.4.3 Results and Discussion

Step 1: Performance of probability estimators

Probability estimators are ranked in ascending order (1-4) in Table 4.7 for methods *LR*, *WLR-F&T* and *WLR-B* based on their goodness-of-fit, p_{AD}, and strength estimates, $\sigma_{0.001}$. *1* denotes the probability estimator with the highest goodness of fit, p_{AD} and the highest strength estimate of $\sigma_{0.001}$ whilst *4* denotes the probability estimator with the lowest goodness of fit, p_{AD} and the lowest strength estimate of $\sigma_{0.001}$. True values for all methods are shown in Appendix C, Table C1-C3.

The following can be observed for E_1-E_4 in terms of:

Goodness-of-fit (p_{AD}): The ranking of probability estimators is consistent for all data sets of *WLR-F&T* and is therefore, independent of the sample size considered in this study. Hazen's estimator, E_2, delivers the best goodness-of-fit for *WLR-F&T*, followed by the small sample estimator E_4, the median rank estimator E_3 and finally the mean estimator E_1. The difference in goodness-of-fit between E_2 and E_1 is between $12.5\% \leq \Delta p_{AD,E2\text{-}E1}/p_{AD,E2} \leq 51.8\%$. Additionally, Hazen's estimator E_2 provided the best fit for 70% of the *WLR-B* data sets and for 43.3% of the *LR* data sets. The low percentage of effectiveness of E_2 in the *LR* data sets is not essential as the *LR* goodness-of-fit is largely poorer with respect to that of the *WLR-F&T* method (Table 4.8). Therefore, *LR* will be omitted for the rest of this study.

Strength estimates ($\sigma_{0.001}$): the ranking of probability estimators is identical for all data sets and methods of Table 4.7 and it is therefore, independent of the sample size or the estimation method considered in this study. Hazen's estimator, E_2, provides the highest strength estimates, followed by the small size estimator, E_4, the median rank estimator, E_3, and finally the mean estimator, E_1. Therefore, the mean estimator E_1 provides the most conservative strength estimates. The difference in strength at low probabilities of failure between E_2 and E_1 is $1.8\ \% \leq \Delta\sigma_{0.001,E2\text{-}E1}/\sigma_{0.001,E2} \leq 25.6\%$.

Conservative strength estimates are traditionally preferred for engineering purposes. However, the most conservative strength estimates for the data sets used in this study were produced by E_1 i.e. the probability estimator with the poorest goodness-of-fit. Therefore, this probability estimator is not deemed effective enough and is therefore, not recommended. Overall, E_2 is the best performing estimator and will be subsequently used for the rest of this study.

Table 4.7: Best performing estimator for data sets of different size.

		LR								WLR-F&T								WLR-B							
		p_{AD}				$\sigma_{0.001}$				p_{AD}				$\sigma_{0.001}$				p_{AD}				$\sigma_{0.001}$			
k	**Series**	**E1**	**E2**	**E3**	**E4**	**E1**	**E2**	**E3**	**E4**	**E1**	**E2**	**E3**	**E4**	**E1**	**E2**	**E3**	**E4**	**E1**	**E2**	**E3**	**E4**	**E1**	**E2**	**E3**	**E4**
10	AR	2	4	1	3	4	1	3	2	4	1	3	2	4	1	3	2	4	1	3	2	4	1	3	2
11	SA8	4	2	3	1	4	1	3	2	4	1	3	2	4	1	3	2	2	4	1	3	4	1	3	2
	SA25	4	1	3	2	4	1	3	2	4	1	3	2	4	1	3	2	4	1	3	2	4	1	3	2
12	SA6	4	1	3	2	4	1	3	2	4	1	3	2	4	1	3	2	4	2	3	1	4	1	3	2
	SA11	4	1	3	2	4	1	3	2	4	1	3	2	4	1	3	2	4	3	1	2	4	1	3	2
13	NA_b	4	2	3	1	4	1	3	2	4	1	3	2	4	1	3	2	4	1	3	2	4	1	3	2
	SA9	1	4	2	3	4	1	3	2	4	1	3	2	4	1	3	2	4	1	3	2	4	1	3	2
14	SA2	1	4	2	3	4	1	3	2	4	1	3	2	4	1	3	2	4	1	3	2	4	1	3	2
	SA5	4	1	3	2	4	1	3	2	4	1	3	2	4	1	3	2	4	1	3	2	4	1	3	2
	SA7	4	1	3	2	4	1	3	2	4	1	3	2	4	1	3	2	4	1	3	2	4	1	3	2
	SA12	4	1	3	2	4	1	3	2	4	1	3	2	4	1	3	2	4	1	3	2	4	1	3	2
	SA13	4	1	3	2	4	1	3	2	4	1	3	2	4	1	3	2	4	1	3	2	4	1	3	2
	SA16	4	1	3	2	4	1	3	2	4	1	3	2	4	1	3	2	4	2	3	1	4	1	3	2
	SA18	4	1	3	2	4	1	3	2	4	1	3	2	4	1	3	2	4	1	3	2	4	1	3	2
	SA19	4	3	2	1	4	1	3	2	4	1	3	2	4	1	3	2	4	1	3	2	4	1	3	2
	SA22	4	3	1	2	4	1	3	2	4	1	3	2	4	1	3	2	4	1	3	2	4	1	3	2
	SA23	2	4	1	3	4	1	3	2	4	1	3	2	4	1	3	2	4	1	3	2	4	1	3	2
	SA24	1	4	2	3	4	1	3	2	4	1	3	2	4	1	3	2	3	4	1	2	4	1	3	2
	SC2	4	1	3	2	4	1	3	2	4	1	3	2	4	1	3	2	4	1	3	2	4	1	3	2
15	SA1	1	4	2	3	4	1	3	2	4	1	3	2	4	1	3	2	4	2	3	1	4	1	3	2
	SA3	4	1	3	2	4	1	3	2	4	1	3	2	4	1	3	2	4	1	3	2	4	1	3	2
	SA4	3	4	1	2	4	1	3	2	4	1	3	2	4	1	3	2	4	1	3	2	4	1	3	2
	SA10	4	2	3	1	4	1	3	2	4	1	3	2	4	1	3	2	4	1	3	2	4	1	3	2
	SA14	1	4	2	3	4	1	3	2	4	1	3	2	4	1	3	2	4	1	3	2	4	1	3	2
	SA15	4	2	3	1	4	1	3	2	4	1	3	2	4	1	3	2	4	3	1	2	4	1	3	2
	SA17	4	1	3	2	4	1	3	2	4	1	3	2	4	1	3	2	2	4	1	3	4	1	3	2
	SA20	4	3	1	2	4	1	3	2	4	1	3	2	4	1	3	2	4	3	2	1	4	1	3	2
	SA21	4	1	3	2	4	1	3	2	4	1	3	2	4	1	3	2	4	1	3	2	4	1	3	2
	SC1	1	4	2	3	4	1	3	2	4	1	3	2	4	1	3	2	4	1	3	2	4	1	3	2
18	NA_a	1	4	2	3	4	1	3	2	4	1	3	2	4	1	3	2	4	1	3	2	4	1	3	2

Table 4.8: Goodness-of-fit of LR (LR-E1, LR-E2, LR-E3 and LR-E4) vs. WLR-F&T-E2 methods.

k	**Series**	**WLR-F&T-E2 p_{AD}**	**max LR p_{AD}**
10	AR	**0.666**	0.633
11	SA8	**0.117**	0.102
	SA25	**0.623**	0.577
12	SA6	**0.686**	0.685
	SA11	**0.599**	0.592
13	NA_b	**0.796**	0.796
	SA9	**0.194**	0.188
14	SA2	0.359	**0.360**
	SA5	**0.172**	0.118
	SA7	**0.784**	0.776
	SA12	**0.189**	0.127
	SA13	**0.507**	0.500
	SA16	**0.569**	0.198
	SA18	**0.800**	0.800
	SA19	**0.672**	0.668
	SA22	**0.482**	0.482
	SA23	**0.575**	0.535
	SA24	**0.151**	0.130
	SC2	0.238	**0.244**
15	SA1	**0.489**	0.460
	SA3	**0.641**	0.357
	SA4	**0.729**	0.729
	SA10	**0.212**	0.212
	SA14	**0.728**	0.715
	SA15	**0.324**	0.295
	SA17	**0.173**	0.150
	SA20	**0.148**	0.126
	SA21	**0.580**	0.570
	SC1	**0.178**	0.151
18	NA_a	**0.097**	0.085

***Step 2*: Performance of estimation methods for the Weibull parameters**

Similarly to Step 1, the different estimation methods (*WLR-F&T*, *WLR-B*, *GLUEs* and *MLE*) are ranked in ascending order (Table 4.9) based on their Anderson Darling goodness of fit, p_{AD}, and their strength estimates, $\sigma_{0,001}$. Again number *1* denotes the method with the highest goodness of fit, p_{AD} / the highest strength estimate of $\sigma_{0.001}$ and number *4* the lowest goodness of fit, p_{AD} / the lowest strength estimate of $\sigma_{0.001}$. True values are shown in Table C4, Appendix C. The following can be concluded on the effectiveness of the different estimation methods (Table 4.9) in terms of their:

Goodness-of-fit: *WLR-F&T-*E_2 provides the best fit amongst the rest of the manual and computational methods for 83.3% of the 30 data sets. Similarly, *WLR-B-*E_2 is the most effective method for 10% of the data sets whilst *GLUEs* and *MLE* are most effective only for 3.3% of the data sets each. The difference in goodness-of-fit between *WLR-F&T* and *GLUEs* is $0.4\ \% \leq \Delta p_{AD,WLPR\text{-}F\&T\text{-}GLUEs}/p_{AD,E2} \leq 80.3\%$.

Strength estimates: *WLR-B-*E_2 provided the most conservative estimates for strengths at low probabilities of failure, $\sigma_{0.001}$ for 46.7% of the data sets, followed by *WLR-F&T-*E_2 for 26.7% of the data sets, *GLUEs* for 20% of the data sets and finally *MLE* for 6.7% of the data sets. However, *WLR-B-*E_2 provided a lower goodness-of-fit than *WLR-F&T-*E_2 and therefore, is considered inferior as its results are less reliable.

Overall, *WLR-F&T-*E_2 was found to be the most effective method for the small sized samples investigated in this study because it provided the best goodness-of-fit. *GLUE*s proposed for the statistical analysis of glass in EN 12603 [162], was one of the least effective estimation methods. In particular, the difference between *WLR-F&T-*E_2 and *GLUEs* can be as high as 80% for p_{AD} (SA10, Fig. 4.17a-b) and 65% for $\sigma_{0.001}$ estimates (SC2, Fig. 4.17c-d) (true values shown in Table C4, Appendix C). *MLE*, proposed for the statistical analysis of glass in ASTM C1239-1[163] and DIN843-5 [164], was found to perform better than *GLUEs* for the majority of series. However, *WLR-F&T-*E_2 is superior to *MLE*. *WLR-F&T-*E_2 improved the goodness-of-fit up to 63% (SA10, Fig. 4.17a-b) and provided up to 73% more conservative strength estimates for $\sigma_{0.001}$ with respect to *MLE* (SC2, Fig. 4.17c-d).

The difference in p_{AD} and $\sigma_{0.001}$ between *WLR-F&T-*E_2 and *GLUE*s / *MLE* increases as the shape factor of the Weibull distribution decreases (Table C4, Appendix C). Low shape factors are typical of naturally aged glass and therefore, the selection of estimation method becomes even more important.

Table 4.9: Ranking of estimation methods in terms of p_{AD} and $\sigma_{0.001}$.

		p_{AD}				$\sigma_{0.001}$			
k	**Series**	**WLR-F&T-E2**	**WLR-B-E2**	**GLUEs**	**MLE**	**WLR-F&T-E2**	**WLR-B-E2**	**GLUEs**	**MLE**
10	AR	1	2	4	3	2	3	1	4
11	SA8	1	4	3	2	1	4	3	2
	SA25	1	2	4	3	2	1	3	4
12	SA6	1	2	4	3	2	3	1	4
	SA11	1	4	3	2	1	4	3	2
13	NA_b	1	2	3	4	2	1	3	4
	SA9	1	3	4	2	2	1	4	3
14	SA2	1	4	3	2	2	1	3	4
	SA5	4	1	3	2	2	3	1	4
	SA7	1	3	2	4	2	1	3	4
	SA12	2	3	4	1	2	3	1	4
	SA13	1	2	3	4	2	1	3	4
	SA16	3	1	4	2	2	4	1	2
	SA18	1	2	3	4	3	1	2	4
	SA19	1	3	4	2	2	1	3	4
	SA22	1	2	3	4	2	1	3	4
	SA23	1	3	4	2	1	2	3	4
	SA24	1	3	4	2	2	4	1	3
	SC2	1	2	4	3	2	1	3	4
15	SA1	1	2	4	3	1	3	2	4
	SA3	2	1	4	3	1	3	2	4
	SA4	1	3	2	4	2	1	3	4
	SA10	1	2	4	3	2	1	4	3
	SA14	1	2	3	4	2	1	3	4
	SA15	1	2	4	3	2	4	3	1
	SA17	1	3	4	2	2	4	3	1
	SA20	1	2	4	3	1	3	4	2
	SA21	2	3	1	4	1	2	3	4
	SC1	1	2	4	3	1	2	4	3
18	NA_a	1	3	4	2	2	1	3	4

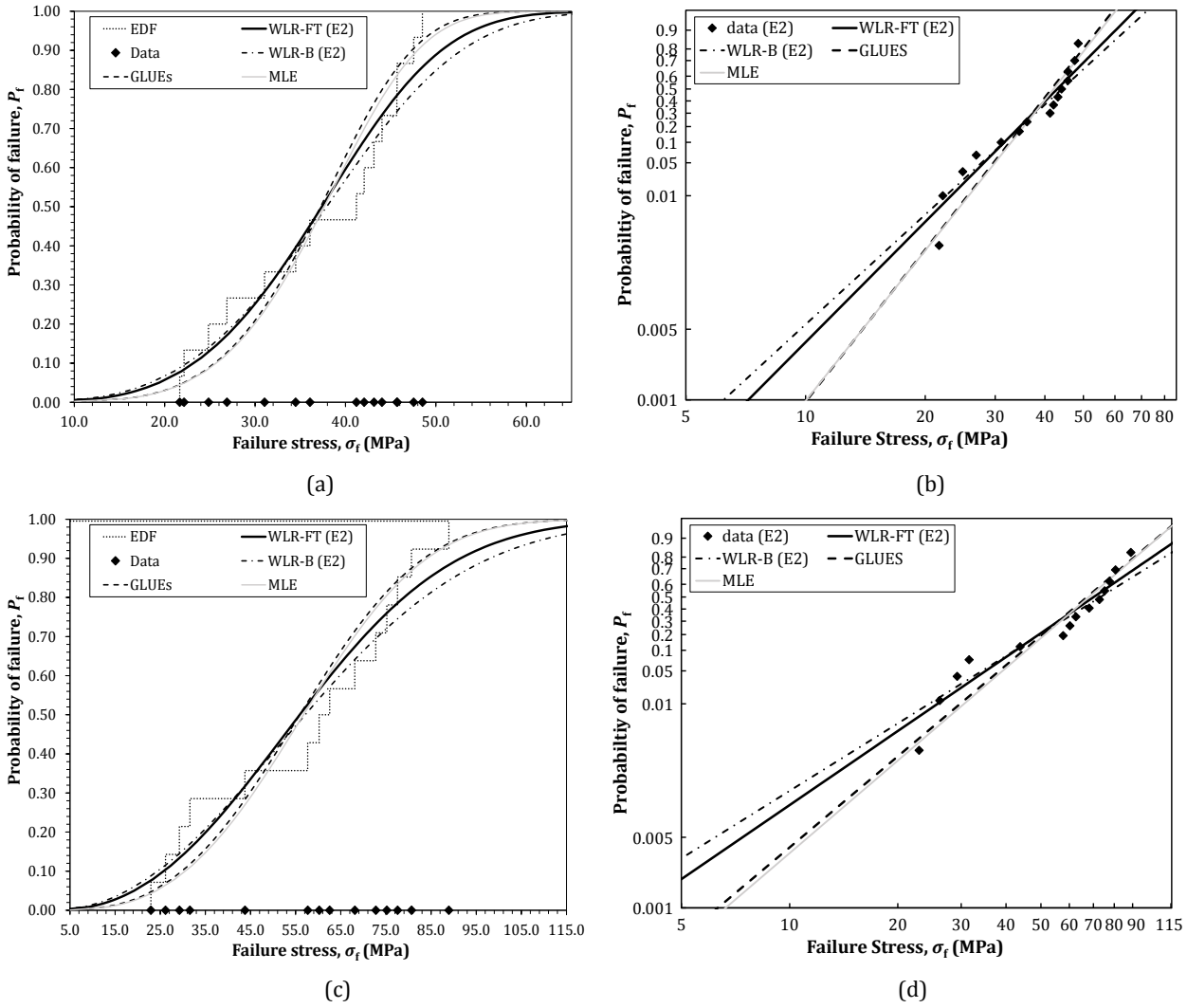

Fig. 4.17: CDFs vs EDF (left) and; logarithmic CDFs (right) for: (a-b) SA10 and (c-d) SC2.

4.4.4 Statistical analysis conclusions

This study reviewed the statistical analysis of glass strength data with a Weibull distribution. The following methods were considered for the estimation of the Weibull parameters: (a) Unweighted least squares regression (*LR*) using 4 probability estimators namely, mean rank (E_1), Hazen's (E_2), median rank (E_3) and small sample (E_4) estimators; (b) Weighted Least Squares Regression (*WLR*) using Bergman's (*B*) and Faucher and Tyson's (*F&T*) weight functions and 4 probability estimators namely, mean rank (E_1), Hazen's (E_2), median rank (E_3) and small sample (E_4) estimators; (c) Good Linear Unbiased Estimators (*GLUEs*); (d) Maximum Likelihood Estimation (*MLE*) and; (e) Method of Moments Estimation (*MME*). A total of 14 combinations of estimation methods, probability estimators and weight functions were subsequently implemented for the statistical analysis of small sized data sets of glass strength. The effectiveness of these combinations were evaluated based on their goodness-of-fit. The Anderson Darling goodness-of-fit is used in this study because is more sensitive to the lower parts of the CDF which correspond

to low probabilities of failure that are typically used for engineering design and was therefore, preferred over other goodness-of-fit tests for glass strength.

The analysis of the 30 series of real strength data used in this study shows that glass strength data can be successfully described with a 2-parameter Weibull distribution. This concurs with the widely established approach adopted within the glass engineering community.

The Weighted Least Squares Regression (*WLR*) in conjunction with Faucher and Tyson's weight function (*F&T*) and Hazen's probability estimator (E_2) were identified as the most effective estimation method. *WLR-F&T-*E_2 outperformed the Good Linear Unbiased Estimators (*GLUE*s) and the Maximum Likelihood Estimation (*MLE*) prescribed in EN 12603 [162] and ASTM C1239-13 [163] and DIN843-5 [164] respectively for the analysis of glass strength data. In fact, for the glass strength data considered in this study, *WLR-F&T-*E_2 provided up to 80% and 63% improvement in the goodness-of-fit with respect to the *GLUEs* and *MLE*, respectively, and up to 65% and 73% more conservative estimates of strength with respect to *GLUEs* and *MLE*, respectively.

Therefore, *WLR-F&T-*E_2 is recommended for small sized samples of glass strength data firstly because it produces a better goodness-of-fit than other manual calculations and computational methods, and secondly because it is simpler to implement.

4.5 Number of specimens

The number of specimens, k that are needed per series in order to obtain reliable glass strength data is investigated in this section. Groups with different number of as-received glass specimens were tested destructively to obtain their strength data which were subsequently statistically analysed to identify the required number of specimens.

4.5.1 Method

Six series of k= 5, 10, 15, 20, 25 and 30 specimens of as-received annealed glass were tested in a Coaxial Double Ring set-up (Table 4.10). The tin side was always placed on the tension face of the CDR set-up for consistency. Specimens with origins of failure outside the boundaries of the loading ring were excluded from further analysis. The strength data were subsequently fitted to a 2-parameter Weibull distribution following the *WLR-FT-*E_2 method which was identified as the most effective method for fitting glass strength data to a 2-parameter Weibull distribution in Section 4.4.

Table 4.10: Specimens.

Series	Type of glass	No of specimens, *k*	No of valid specimens*
5-sp	As-received SLS glass	5	3
10-sp	As-received SLS glass	10	8
15-sp	As-received SLS glass	15	13
20-sp	As-received SLS glass	20	15
25-sp	As-received SLS glass	25	18
30-sp	As-received SLS glass	30	26
Total-sp	As-received SLS glass	105	83

*excluding origins of failure outside of the loading ring.

The following were used to evaluate the results:

confidence intervals: Confidence intervals were computed for each series as prescribed in EN 12603 [162] for a 90% confidence level. Confidence intervals are sometimes erroneously used to set the limits for the true population. However, a confidence level of 90% means, that if the population is sampled multiple times, e.g. 10 times in Fig. 4.18, and interval estimations are made in each case, 90% of the resulting intervals would bracket the true value of the population [165] whereas 10% would not, e.g. confidence intervals for sample 5 in Fig. 4.18 do not bracket the true value.

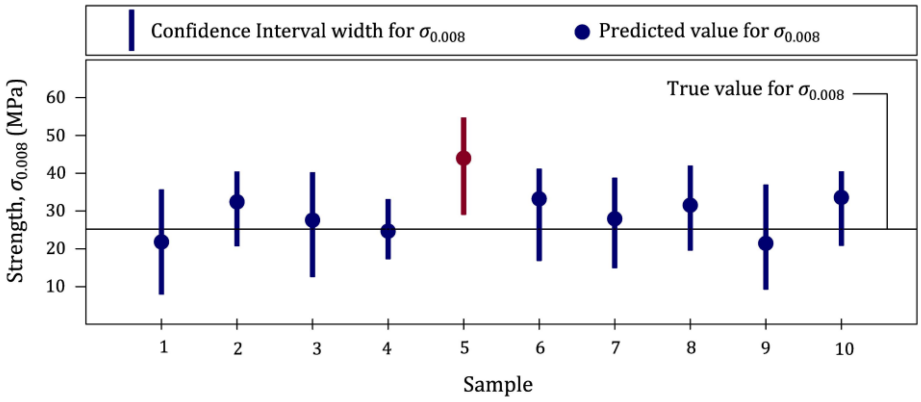

Fig. 4.18: Example for a confidence level of 90%.

However, confidence intervals can be used to describe the level of uncertainty in the obtained data as a function of the width between the upper and the lower bound of each cumulative distribution function, e.g. there is larger uncertainty associated with the strength prediction of sample 1 than sample 4 in Fig. 4.18. This is true only when a good fit to a distribution is achieved and fixed errors are small. The width of the confidence intervals can be used in this study to assess the uncertainty in the data because fixed errors are small and constant; (a) glass was obtained

from a single supplier and; (b) destructive tests were performed by the same researcher in the same set-up.

strength estimates of complete sample: all results of the complete sample were combined in a single series of k=105 specimens in total to provide a more representative picture of the population. These strength estimates were then compared to the strength estimates of each individual series. Strengths were evaluated at design level P_f=0.008 complying with ASTM E1300-12a [33] and mean probabilities of failure P_f=0.50.

4.5.2 Results and Discussion

Comparison to the results of the total sample

The cumulative distribution function (Fig. 4.19) was found to be in close agreement for series that had 15 or more specimens ($k \geq 15$). In particular, their difference in strength estimates from the complete sample ranged between $1.0\% \leq \left|\left(\Delta\sigma_{0.008,\max/\min}\right)\right| / \sigma_{0.008,105} \leq 5.3\%$ for P_f=0.008 and between $1.3\% \leq \left|\left(\Delta\sigma_{0.50,\max/\min}\right)\right| / \sigma_{0.50,105} \leq 5.3\%$ for P_f=0.50 (Fig. 4.20a, Table 4.11). Series with fewer specimens (k=5 or k=10) showed poor agreement to the complete sample (k=105) especially at the low probabilities of failure (Fig. 4.19 and Fig. 4.20a).

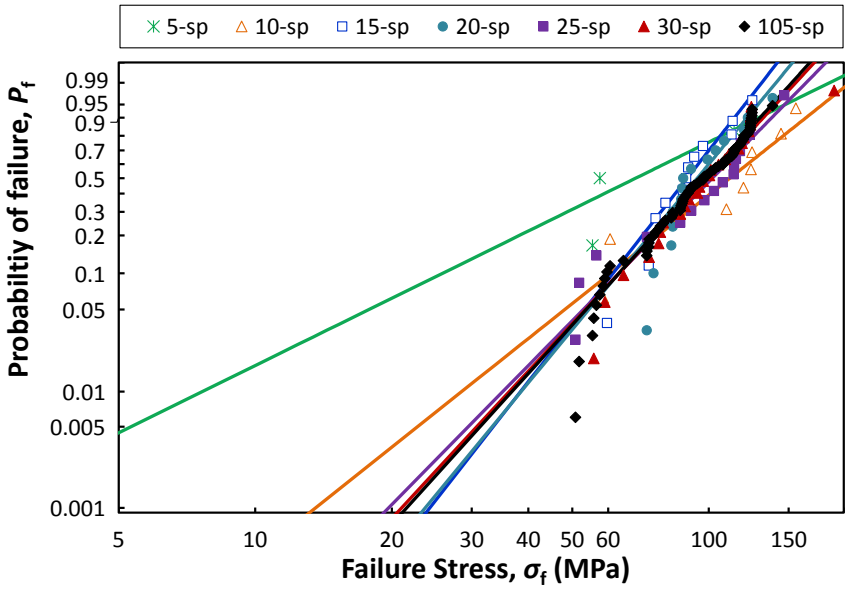

Fig. 4.19: CDF for series with different specimen numbers (failures outside the load. ring are excluded).

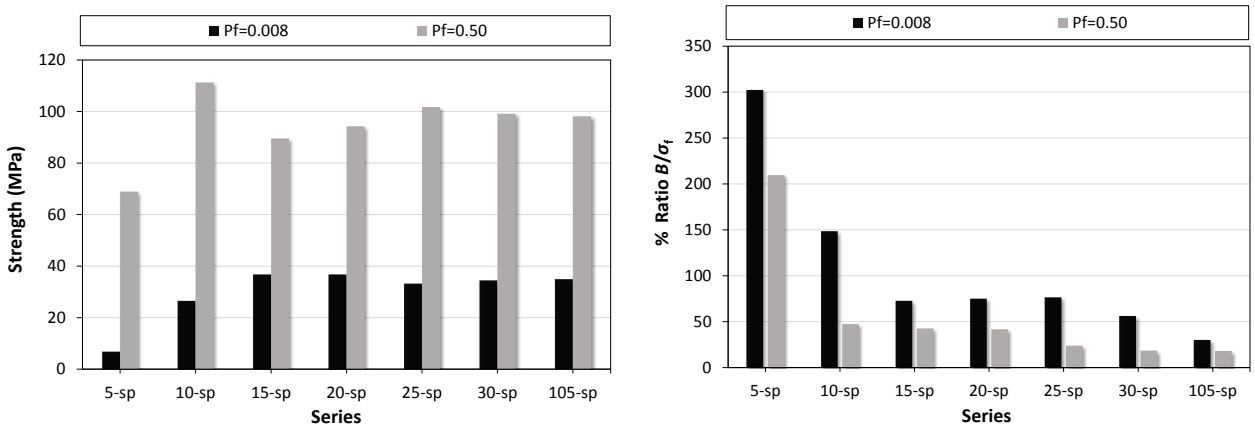

Fig. 4.20: Strength estimates and confidence interval widths for series with different number of specimens.

Confidence intervals

All series provided acceptable goodness of fit (i.e. $p_{AD} > 5\%$) and therefore, the width of confidence intervals, B, can be used to assess the uncertainty in strength estimates. This is evaluated at design (P_f=0.008) and mean (P_f=0.50) level. The dimensionless ratio of B/σ_f (Table 4.11 & Fig. 4.20b) which represents the uncertainty in strength estimates, follows a descending trend as the number of specimens increases. The highest values of B/σ_f occurred for series with k=5 or k=10 specimens. Very similar values of B/σ_f were reported for series 15-sp, 20-sp and 25-sp which were significantly lower with respect to those of 5-sp and 10-sp. The uncertainty decreased further as the number of specimens increased to k=30 for both P_f=0.008 and P_f=0.50 and even further for k=105 and P_f=0.008. The difference between the CDF and the confidence intervals of 15-sp, 30-sp and 105-sp is also shown graphically in Fig. 4.21.

Table 4.11: Fractile values and confidence intervals for series with different numbers of specimens.

Series	Weibull parameters				Fractile values		Confidence Intervals					
	β	θ	p_{AD}	CV	$\sigma_{f,0.5}$	$\sigma_{f,0.008}$	$\sigma_{f,0.008,up.}$	$\sigma_{f,0.008,lo.}$	$B_{0.008}$*	$\sigma_{f,0.5,up.}$	$\sigma_{f,0.5,lo.}$	$B_{0.50}$*
		MPa	%	%	MPa	MPa	MPa	MPa	MPa	MPa	MPa	MPa
5-sp	1.92	83.38	23.7	54.1	68.92	6.80	22.53	1.99	20.5	173.31	28.95	144.4
10-sp	3.11	125.17	22.4	35.2	111.25	26.52	47.76	8.37	39.4	137.45	84.70	52.7
15-sp	5.01	96.38	44.1	22.9	89.58	36.76	51.27	24.53	26.7	116.96	78.82	38.1
20-sp	4.74	101.83	6.06	24.1	94.24	36.77	52.26	24.67	27.6	116.96	77.66	39.3
25-sp	3.98	111.58	11.0	28.2	101.76	33.19	47.87	22.46	25.4	113.31	88.95	24.4
30-sp	4.22	108.16	17.9	26.8	99.15	34.44	45.92	26.55	19.4	108.00	89.65	18.4
total	4.31	106.86	96.70	26.20	98.15	34.92	41.25	30.71	10.54	106.70	88.95	17.75

*$B_{0.008}=\sigma_{f,0.008,\,up.}-\sigma_{f,0.008,\,lo.}$ & $B_{0.008}=\sigma_{f,0.50,\,up.}-\sigma_{f,0.50,\,lo.}$

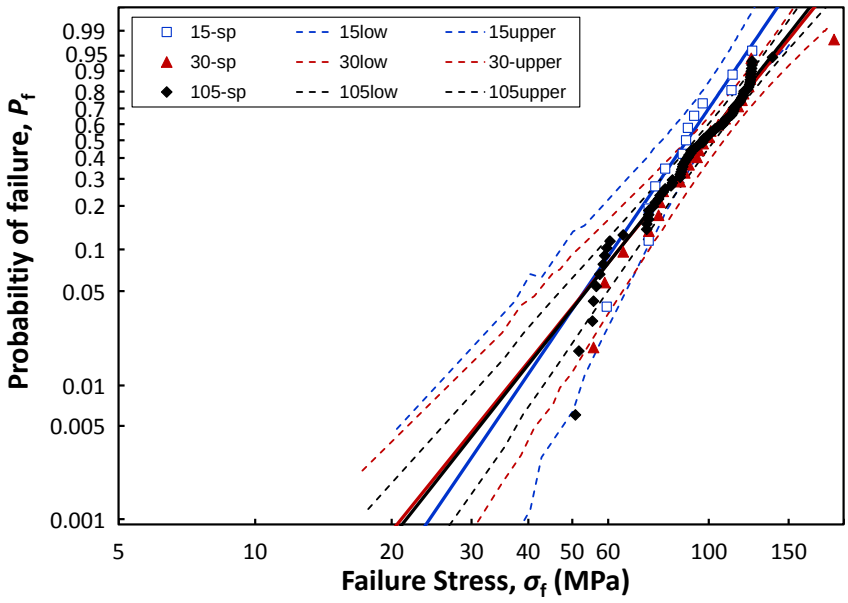

Fig. 4.21: CDF and confidence intervals for n=15, 30 and 105 specimens.

4.5.4 Conclusions on the number of specimens

The above results indicate that k=15 is the smallest number of specimens that produces strength estimates that closely represent the strength estimates of the complete sample, k=105, and that simultaneously yields relatively small uncertainty in strength estimates. It is true that the uncertainty decreases further as the number of specimens increases beyond $k \geq 30$. However, 15 specimens provide a good balance between cost, experimental labour and reliability in strength estimates and so k=15 specimens are chosen for all series in Chapter 5 and Chapter 6.

4.6 Conclusions

The aim of Chapter 4 was to identify the most accurate / reliable approach for the estimation of glass strength that will be implemented in Chapters 5 & 6 for the evaluation of the strength of different types of aged glass.

Coaxial double ring tests are confirmed to be the most suitable method of destructive testing when surface strength is under investigation. Coaxial double ring tests will therefore, be used in subsequent Chapters for annealed and fully toughened glass. However, the small thickness of some chemically toughened glasses ($h \leq 2$ mm) in combination with their high strength lead to undesirable stress concentrations when a conventional Coaxial Double Ring test set-up is used. This means that the uniform equibiaxial stress state within the loading ring is not maintained and the Coaxial Double Ring test is no longer appropriate. Investigation of different set-ups was undertaken in this Chapter to propose an alternative set-up for the destructive testing of thin chemically toughened glass that creates a uniform equibiaxial stress within the loading ring area.

Of the alternative set-ups investigated, the best results were obtained with a 4.75 mm thick, Grade7075T6 aluminium, spreader plate that was placed between the top of the glass specimen and the loading ring in the CDR set-up.

Additionally, a high stress rate of 20 MPa/sec (corresponding to 13.6 mm/min for a 150 x 150 x 3 mm specimen) was found to eliminate or minimize the effects of sub-critical crack growth for annealed glass specimens that were abraded with gravel or sand respectively. Consequently, the testing conditions of the coaxial double ring test are considered quasi-inert. In order to eliminate the small influence of sub-critical crack growth, the strength data need to be converted to an equivalent uniform stress (t_{ref}=60 sec) prior to their statistical analysis to normalise the small influence of sub-critical crack growth and allow comparison across specimens that failed at different times and that were therefore, subjected to different levels of sub-critical crack growth.

Additionally, a Weighted Least Squares Regression (*WLR*) in conjunction with Faucher and Tyson's weight function (*F&T*) and Hazen's probability estimator (E_2) were identified as the most effective method for statistically analysing small samples of glass strength data with a Weibull distribution. This method provided better goodness-of-fit and more conservative strength estimates than the Maximum Likelihood Estimation (*MLE*) proposed in ASTM C1239-13 [163] and DIN843-5 [164]or the Good Linear Unbiased Estimator method proposed in EN 12603 [162] Therefore, WLR-FT-E2 will be implemented in Chapter 5 and Chapter 6 for the statistical analysis of glass strength data.

Finally, statistical analysis of different sizes of small samples of glass strength data ranging between $5 \leq k \leq 30$ specimens showed that k=15 samples are sufficient for the purpose of this study providing a close agreement to the strength estimates of the complete sample and significantly reducing uncertainty in strength-estimates when compared to series of fewer specimens.

5. Artificial Ageing of Glass

5.1 Introduction

Exposed glass surfaces will accumulate damage during their service life. It is therefore, essential to predict glass strength when glass is used in load bearing applications. Artificial ageing tests can be very useful in this regard, to simulate natural ageing mechanisms and permit the evaluation of the mechanical performance of aged glass. However, artificial ageing methods have traditionally focused on degradation of the light transmittance properties of glass rather than its strength. Experimental testing is undertaken in this Chapter (Fig. 5.1) to investigate the effectiveness of a falling abrasive and a linear scratching method for the artificial ageing of glass. The former involves free falling of abrasive medium on the surface of monolithic glass and thus induces a random surface flaw population whilst the latter employs a scratching device to induce a single linear flaw on the glass surface. Section 5.2 describes the procedure used to artificially age 420 annealed glass specimens grouped in 28 series using different combinations of ageing parameters. The specimens were subsequently subjected to destructive and non-destructive tests to determine the effect of each ageing method and its corresponding parameters. The aim is to establish a combination of ageing test parameters that produces strength characteristics equivalent to those of naturally aged glass. The results are presented and discussed in Section 5.3. These results are subsequently condensed in a set of guidelines for the assessment of the strength of aged glass in Section 5.4. Finally, Section 5.5 summarizes important conclusions.

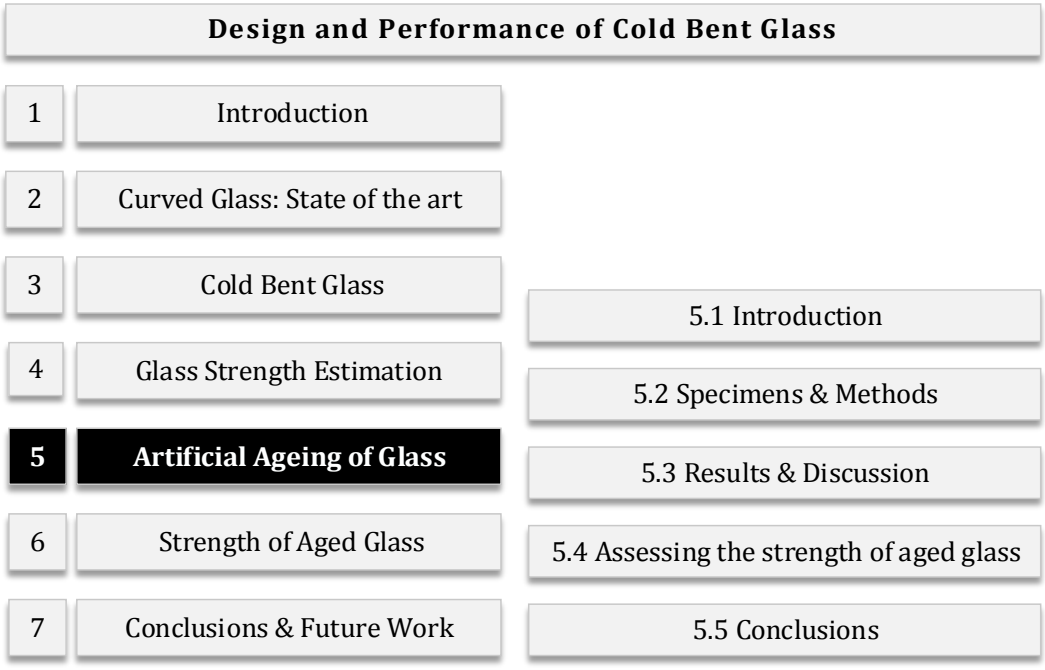

Fig. 5.1: Contents of Chapter 5.

5.2 Specimens and Methods

5.2.1 Specimens

Monolithic annealed soda–lime–silica glass in the form of naturally aged (NA) and as-received glass (AR) was used to investigate the effectiveness of a falling abrasive and a scratching method for the artificial ageing of glass. Naturally aged glass was used as a reference for the artificially aged series. The naturally aged glass was obtained from a low rise building in Norfolk, UK, situated at a distance greater than 10 km from the coast, that was exposed to natural ageing mechanisms for 20 years as part of the façade. This was a low rise building in a rural location with a distance greater than 10 km from the coast. The glass was cleaned with warm soapy water to remove the organic residue that had accumulated on its surface during its service life and was then cut to size with a hand-held diamond cutter. Two series of naturally aged (NA-AN_a & NA-AN_b) were tested; specimens for these series were obtained from the same façade but different panels.

AR-AN is new as-received annealed glass, obtained from a single supplier and cut to size with a hand-held diamond cutter. One series of this glass was tested in its as-received state (AR-AN) while the rest were either subjected to abrasion with a falling abrasive method (SA) or scratched with a scratching device (SC).

Table 5.1 summarizes the types of annealed glass and the number of specimens used in this study. The chemical composition of the naturally aged and the as-received annealed glass used in this study was found to be similar (Table 5.2 a-b, [95]). The surface residual stress of the naturally aged and the as-received glass was also found to be similar. This was measured through the thickness of the glass with a scattered light polariscope (SCALP-05, GlasStress Ltd. [175]). The stress profile was obtained at the centre of each specimen in the *x* and *y* directions. The mean surface compression for the naturally aged and the as-received annealed glass was 3.7±1.0MPa and 2.31±0.65 MPa respectively.

Table 5.1: Specimen overview.

Abbr.	Glass type	Ageing	Dimensions (mm)	Nominal thickness (mm)	No. of Series	Specimens/ series
NA-AN	Float SLS annealed	Natural	150x150	2.83±0.08	2	15
AR-AN	Float SLS annealed	As-received	150x150	2.85±0.03	1	15
SA-AN	Float SLS annealed	Sand abraded	150x150	2.85±0.04	26	15

*SLS: soda lime silica

Table 5.2: Chemical composition by weight from electron microscopy (mean and standard deviation) for: (a) elements and; (b) oxides [95].

Specimens	(a) Elements															
	Na		Si		Al		K		Ca		Fe		Mg		O	
	%	SD	%	SD	%	SD	%	SD	%	SD	%	SD	%	SD	%	SD
AR-AN, air side	8.77	0.25	33.88	0.10	0.51	0.01	0.31	0.03	7.07	0.07	0.08	0.03	2.51	0.02	46.68	0.20
AR-AN, tin side	8.77	0.25	33.88	0.10	0.51	0.01	0.31	0.03	7.07	0.07	0.08	0.03	2.51	0.02	46.68	0.20
NA-AN, exposed side	8.75	0.25	33.99	0.14	0.53	0.01	0.29	0.03	6.74	0.05	0.06	0.03	2.78	0.03	46.85	0.19
NA-AN, protected side	8.95	0.25	33.60	0.35	0.53	0.01	0.30	0.03	6.66	0.08	0.09	0.03	2.73	0.03	46.41	0.34

Specimens	(b) Oxides													
	Na_2O_2		SiO_2		Al_2O_3		K_2O		CaO		FeO		MgO	
	%	SD	%	SD	%	SD	%	SD	%	SD	%	SD	%	SD
AR-AN, air side	12.07	0.42	71.97	0.41	0.95	0.01	0.37	0.04	9.94	0.14	0.10	0.03	4.19	0.04
AR-AN, tin side	11.82	0.34	72.48	0.21	0.97	0.01	0.38	0.03	9.89	0.10	0.10	0.04	4.16	0.04
NA-AN, exposed side	11.80	0.46	72.71	0.30	1.00	0.02	0.35	0.04	9.43	0.08	0.08	0.04	4.61	0.05
NA-AN, protected side	12.06	0.47	71.88	0.75	1.00	0.02	0.36	0.04	9.31	0.11	0.11	0.04	4.52	0.06

5.2.2 Experimental methods

The artificial ageing method and the evaluation tests used in this study are described in turn in this section. Experimental tests were always performed on the weaker surface of the specimens; for the naturally aged glass this is the "external" surface i.e. the surface that was exposed to weathering action during its service life whereas for the as-received annealed glass this corresponds to the tin side (identified with a UV-light). It was not possible to distinguish between tin side and air side for the naturally aged glass, because unlike the as-received glass, the reflection of the two surfaces on exposure to UV light was indistinguishable. However, this is not expected to affect the fracture strength data because the critical flaw depths found in naturally aged glass as a result of natural weathering (micrographs shown in Fig. 5.9), are larger than those induced on the tin side during the float process ($\alpha \approx 28.9$ μm [176]).

Artificial ageing with falling abrasive

Part of the as-received annealed glass was artificially aged with the falling abrasive method (Fig. 5.2a). This method is intended to induce a random flaw population on the surface of the glass and is based on the methods proposed in DIN52348 [129] and ASTM D968-05 [130]. The artificial ageing procedure was performed as follows:

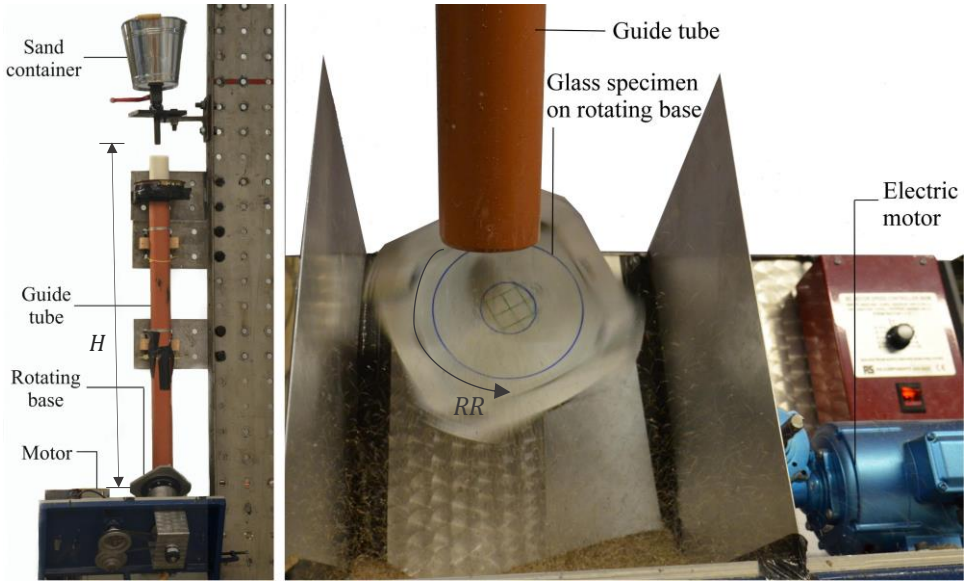

(a) (b)

Fig. 5.2: Falling abrasive test: (a) Set-up (rear view) and; (b) Rotating specimen base (front view).

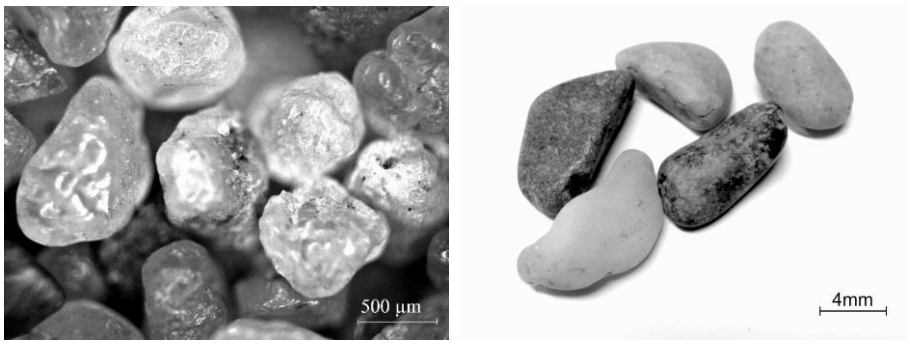

(a) (b)

Fig. 5.3: Morphology of: (a) silica sand grains (0.5≤GSR≤0.7mm) and; (b) riverside gravel (8.0≤GSR≤9.5mm).

Table 5.3: Range of artificial ageing parameters.

Parameter	**Abbr.**		**Values investigated**
Drop Height	H	(m)	3.0, 2.3, 1.65, 1.2
Abrasive medium			Silica sand & river gravel
Mass of abrasive	m	(kg)	1.0, 1.5, 2.0, 3.0, 4.0, 5.0
Maximum grain size range	MGS	(mm)	0.7, 1.0, 5.6, 9.5
Gravel %	p		0, 0.1, 10
Rotation rate	RR	(rpm)	0, 125, 250
Curing time	t_c	(hrs)	2, 168
Environmental conditions during curing			ambient, immersed in water

i. The abrasive medium is loaded in a sand container. Silica sand and riverside gravel (Fig. 5.3a-b) with different grain sizes ranging between $0.5 \leq GSR \leq 1.0$ mm and $1.0 \leq GSR \leq 9.5$ mm respectively were used in this study (grain size curves are shown in D1 in Appendix D) The morphology of the silica sand is mostly rounded with few angular edges while riverside gravel is rounded with smooth edges (Fig. 5.3a-b);
ii. The glass specimen is clamped to a steel base with the tin side facing upwards. This is the side that will be subjected to artificially ageing. The base is inclined at an angle of 45° to the ground and rotates with the aid of an electrical motor (Fig. 5.2b);
iii. As the specimen rotates at full speed, the abrasive material is allowed to trickle on the surface of the glass under the effect of gravity. The rate of the abrasive flow is controlled with a manually operated steel valve that is fitted below the sand container; when the valve is fully open the flow rate is 100 g/sec; a guide tube (Ø82mm) prevents the abrasive material from dispersing over a wide area as it falls.
iv. The artificial ageing process ends when the whole mass of the abrasive material impacts the surface of the specimen.
v. The specimens are subsequently stored / "cured" for a set time duration and environmental conditions prior to any evaluation test.

Table 5.3 summarizes the different values for artificial ageing parameters (drop height, rotation rate of the base, mass and grain size range of abrasive material) that were tested in this study for the sand abraded series (SA).

Artificial ageing with a scratching device

Two series of specimens (SC) were scratched with the use of a custom-made scratching device similar to those used in other studies [95,97]. The scratching device (Fig. 5.4a) consists of a 90° tungsten carbide tip which is attached to the stem of the device incorporating dampers to allow the adjustment of the tip on the glass surface. The specimen is clamped along two edges with two steel plates while the device is dragged manually at a speed of approximately 4 mm/sec on the tin side of the glass specimen inducing a single flaw on its surface. PTFE tape is used to cover the supporting legs of the scratching device to reduce friction when in contact with the glass and avoid the induction of additional flaws. The length of the flaw, induced by the tungsten carbide tip, is controlled by the steel clamping plates, is kept constant for both sets of specimens and is 20 mm. A mass of 1.0 kg was placed on the platform, resulting in a total weight of 1.6 kg when the self-weight of the platen and the stem of the device are also considered. The difference between the two sets (SC_1 and SC_2) is the sharpness of the indenter. A sharp 90° tip angle indenter (infinitesimally small radius of curvature, Eq. 2.2a) was used for SC_1 while a blunt 90° tip angle indenter (radius of curvature R=0.17 mm, Eq. 2.2a) was used for SC_2. (Fig. 5.4b). The blunt tip of

the indenter was a natural result of wear due to the extensive use of the scratching device. The blunt indenter was tested to evaluate the need for inspecting the condition of the tip of the indenter after using the scratching device and replacing the tip.

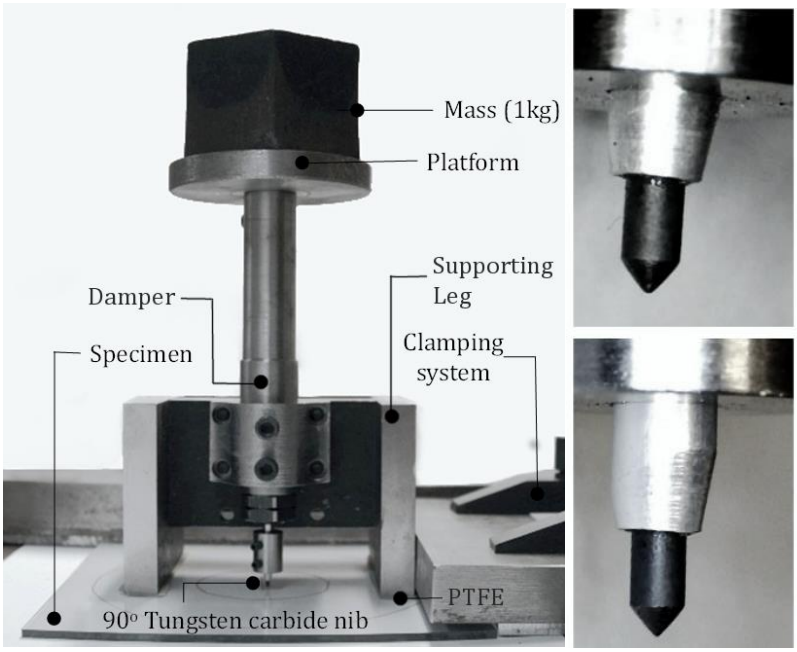

(a) (b)

Fig. 5.4: (a) Scratching device and; (b): Blunt (top) and sharp (bottom) 90° indenter tip.

Surface roughness characterisation

The average surface roughness (Eq. 5.1) was determined individually for each specimen for 15 as-received, 33 naturally aged, 30 scratched and 30 sand abraded glass specimens using a Form Talysurf PGI 820 surface profilometer (Taylor and Hobson Ltd, Fig. 5.5a). The profilometer uses a 2 μm radius stylus to obtain the profile of the surface along the evaluation length (Fig. 5.5b-c). Six evaluation lengths (each of 50 mm) were obtained for each scanned specimen along the *x* and the *y* direction on the surface of the specimens. These six lengths were spaced 15 mm apart to obtain a representative value of the area that coincides with the area of the loading ring where the fracture stress will be assessed (Fig. 5.5 b).

$$R_a = \frac{\sum_{i=1}^{n} |z_i|}{n} \qquad \text{(Eq. 5.1)}$$

where *n*: the number of measured points within the evaluation length and *z*: the vertical distance of each measured point from the mean line of the profile.

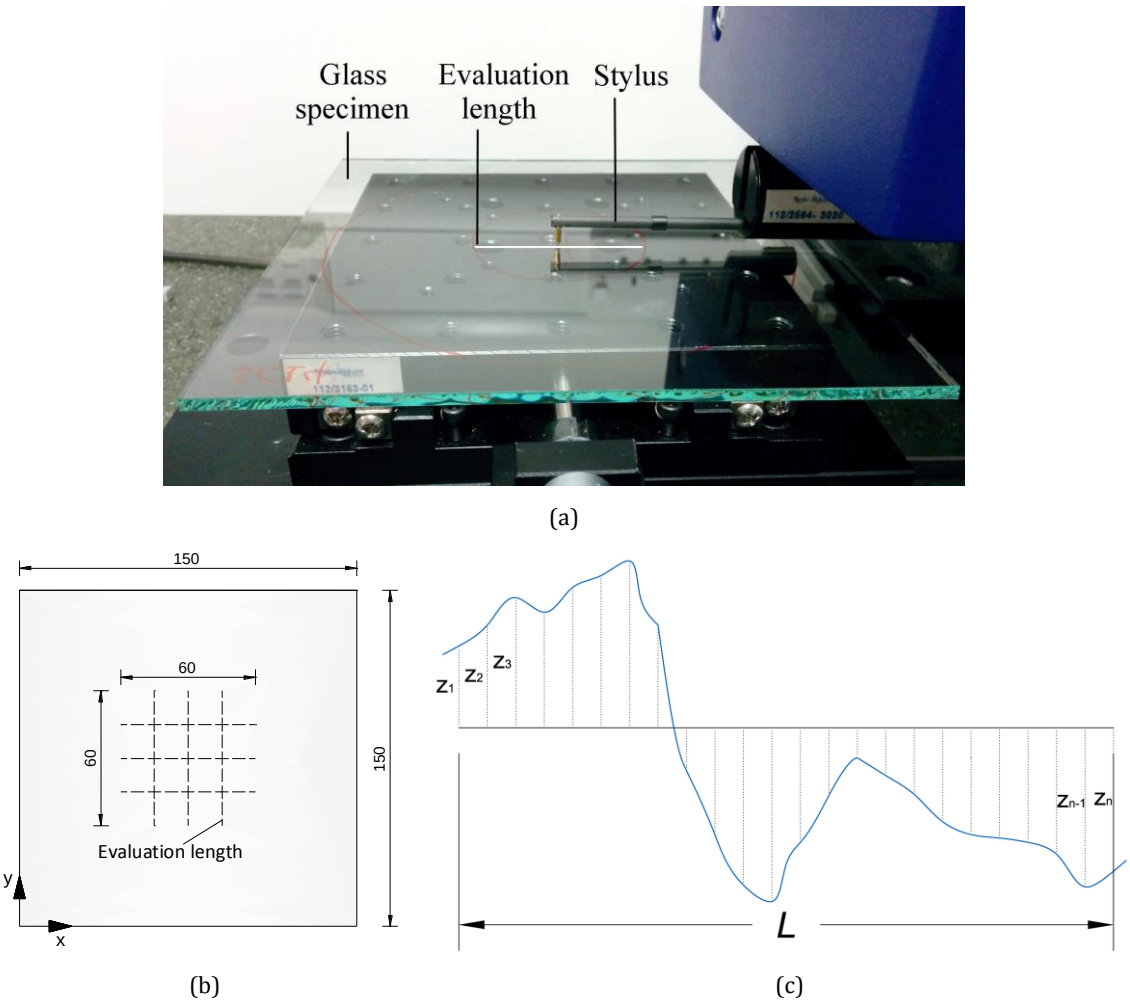

Fig. 5.5: Surface roughness: (a) surface profilometer; (b) Evaluation lengths; (c) Sketch of obtained profile.

Optical microscopy and coaxial double ring tests

Qualitative micrographs of the surface of the glass specimens were obtained with a Leica DM ML optical microscope. Prior to the destructive testing, a clear self-adhesive film was applied on the non-aged surface of the specimen to allow fractographic analysis. Destructive testing was performed approximately 2 hrs after the artificial ageing, in a coaxial double ring set-up (Section 4.2, Fig. 4.2a-b) with a stress rate of 20 MPa/sec (displacement rate of 13.6 mm/min) to minimize the influence of sub-critical crack growth (Section 4.3). The specimens were oriented so that the tin side of the as-received annealed glass specimens and the external side of the naturally aged glass specimens were in tension during the destructive test while the self-adhesive film was on the compressive surface.

The self-adhesive film was successful in holding the fragments together after fracture of the specimen. This enabled fractographic analysis following the procedure described in Section 4.3.1 in order to locate and measure the critical flaw.

Data processing methods

Specimens with origins of failure located outside the loading ring were excluded from further analysis of glass strength. The failure load was converted to failure stress using the full friction numerical model that was developed in Section 4.2. Sub-critical crack growth occurred in some series for the chosen stress rate (20 MPa/sec) as shown in Section 4.3. The uneven effect of sub-critical crack growth was therefore, normalised by converting the failure stress of each specimen to an equivalent strength for a load duration of 60 sec using Eq. 4.7.

The experimental equivalent strength data were fitted to a 2-parameter Weibull distribution (Eq. 2.9) with the *WLR-FT-E_2* approach (a weighted least square regression method using Faucher and Tyson's weight function, Eq. 4.18b and Hazen's probability estimator, E_2, Eq. 4.15b). This method was found to be the most effective (Section 4.4) for fitting glass strength data to a 2-parameter Weibull distribution. The resulting distribution was then evaluated using the Anderson Darling goodness of fit, p_{AD}, considering a 95% confidence level.

Strength data were subsequently evaluated for the design and mean probabilities of failure i.e. P_f=0.008 and P_f=0.50, respectively. A probability of failure of 0.008 for the design strength follows the recommendations of ASTM E1300-09 [33], but any other suitably low probability of failure could be selected for comparing across the tests performed in this study. Additionally, confidence intervals were estimated following the procedure described in EN 12603 [162] (Table E1, Appendix E).

5.3 Results and Discussion

As received and naturally aged annealed glass

Surface roughness: Table 5.4 and Fig. 5.6 summarize the average surface roughness, R_a, results for naturally aged, as-received, scratched and sand abraded specimens.

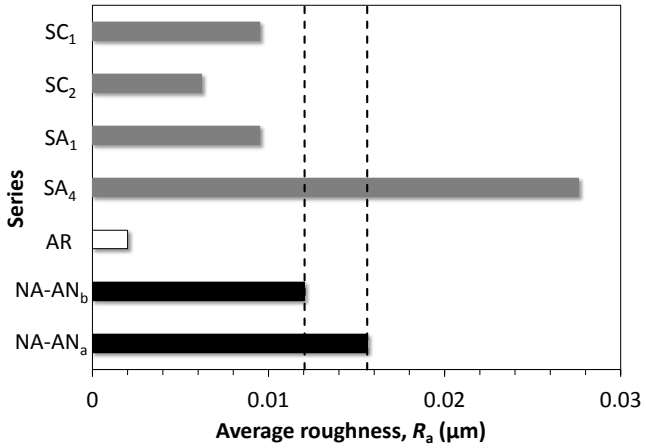

Fig. 5.6: Average surface roughness for AR, NA-AN_a-NA-AN_b, SC1-SC2 and SA1-SA4.

Table 5.4: Roughness results.

Series	$R_{a,av}$ (µm)	% roughness increase $R_{a,av}$
NA-AN$_a$	0.0156	680
NA-AN$_b$	0.0121	505
AR-AN	0.002	0
SA4	0.0276	1280
SA1	0.0093	375
SC1	0.0095	375
SC2	0.0062	210

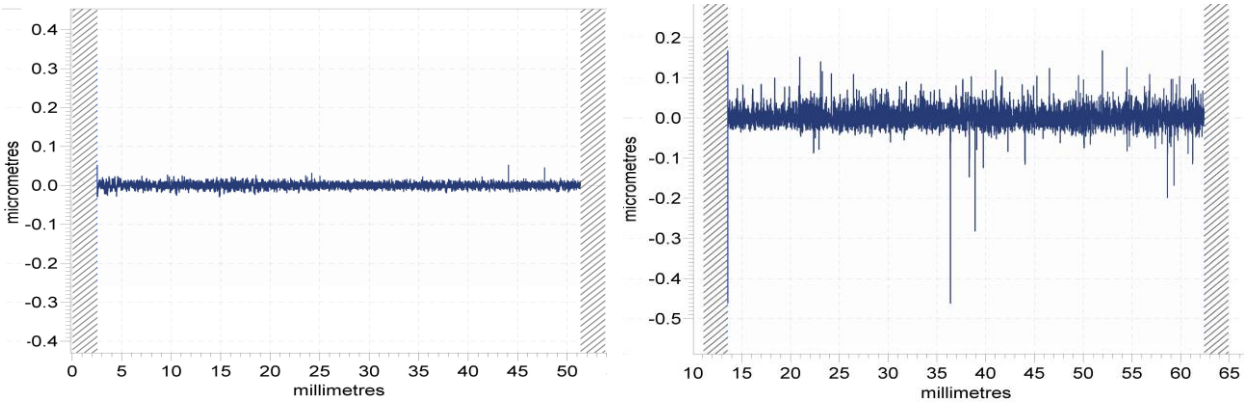

(a) (b)

Fig. 5.7: Surface profile of: (a) as received (AR) and; (b) naturally aged (NA) annealed glass.

Unsurprisingly, as-received annealed glass had the lowest R_a while naturally aged glass showed a high average surface roughness (increase of 505% for NA-AN$_b$ and 680% for NA-AN$_a$ with respect to as-received glass). Indeed, this difference can be seen qualitatively in Fig. 5.7a & b which depict the surface profiles of as-received and naturally aged glass as obtained by the surface profilometer along one of the evaluation lengths on the glass specimens.

Microscopy: Micrographs of the surfaces of as-received and naturally aged are shown in Fig. 5.8. As-received annealed glass is almost defect free at a magnification level of 100x (Fig. 5.8a). However, the surface of the naturally aged glass (Fig. 5.8b-c) shows signs of moderate to extensive ageing. NA-AN$_a$ (Fig. 5.8b) is more severely damaged when compared to NA-AN$_b$ (Fig. 5.8c). Additionally, digs are more frequently encountered than scratches [177]). This supports the initial assumption that the naturally aged glass of this study was mostly exposed to erosive action.

Two types of critical flaws were distinguished for naturally aged glass as was expected based on Section 2.5.2: (a) digs induced by impact potentially by flying projectiles or objects forced on the surface of glass during its service life of the glass or; (b) scratches that were potentially induced during transportation, installation and / or cleaning of the glass (Fig. 5.9).

The flaw depths captured by the surface profilometer (Fig. 5.7) are orders of magnitude smaller than the flaw depths revealed by the fractographic analysis; this is attributed to the relatively thick (compared to the dimensions of the flaw) stylus of the surface profilometer that prohibits full characterisation of the flaw profile and thus, estimation of its depth. Therefore, surface profilometry can be used qualitatively to obtain the average surface roughness of the glass specimens but cannot be used to evaluate the flaw depths with a stylus radius of 2 μm.

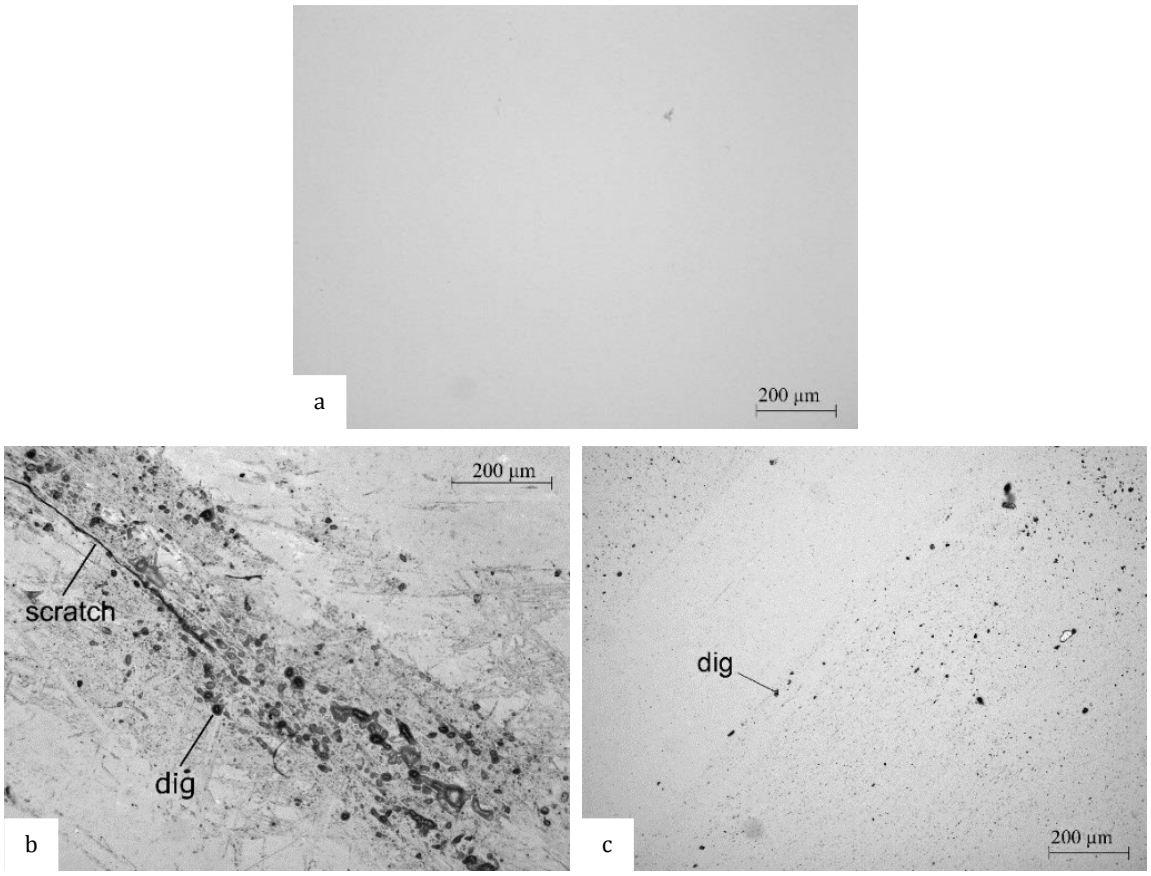

Fig. 5.8: Micrographs of the surface of: (a) AR-AN; (b) NA-AN$_a$ and; (c) NA-AN$_b$.

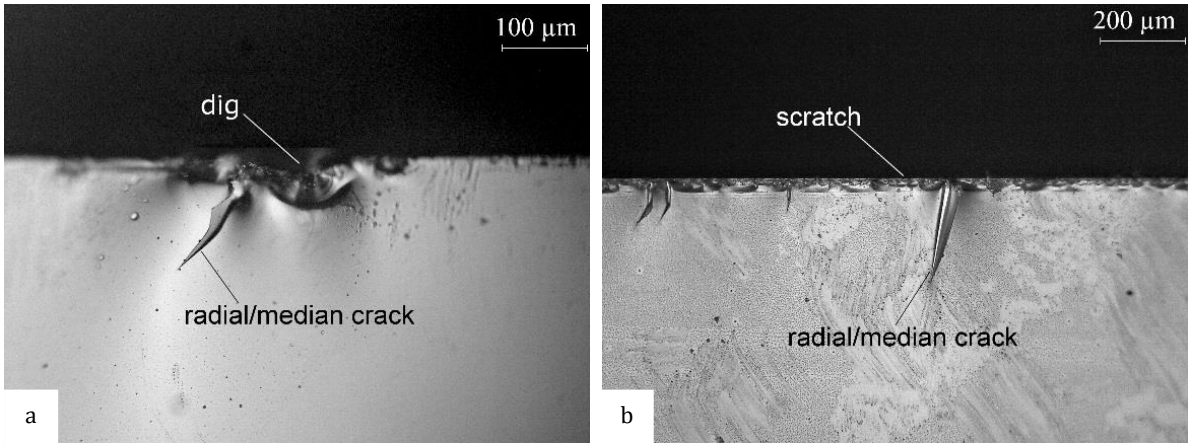

Fig. 5.9: Critical flaws in naturally aged glass: (a) dig and; (b) scratch.

Fracture strength: The differences in size and quantity of the flaws observed at microscopic level on NA-AN_a and NA-AN_b on naturally aged glass are also evident in the fracture strength of the respective glass specimens (Fig. 5.10); the design (P_f=0.008) and mean (P_f=0.50) strengths of NA-AN_a were 46% and 29% lower than the those of NA-AN_b. A reduction in fracture strength was expected as the surface damage on the NA-AN_a glass was more extensive. More importantly, naturally aged glass suffered 73-85% and 51-66% reduction in design and mean strength ($\Delta\sigma_{NA,AR}/\sigma_{NA}\%$) respectively with respect to as-received glass.

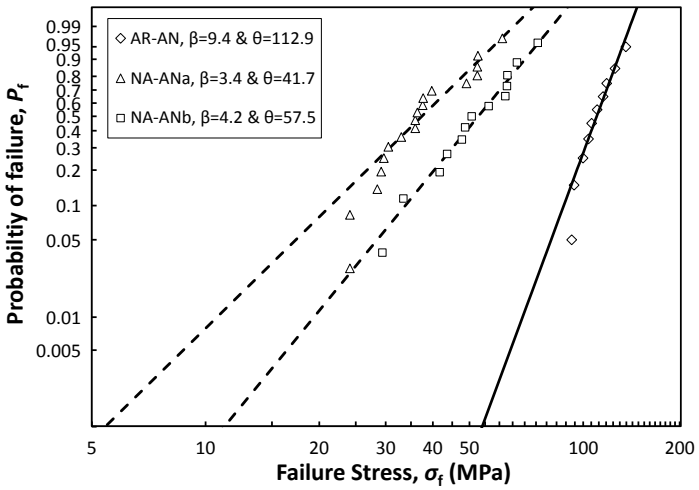

Fig. 5.10: CDFs for naturally aged (NA), as-received (AR) annealed glass.

Scratched annealed glass

Surface roughness: The average surface roughness of scratched specimens increases when a sharper indenter is used ($R_{a,SC1}$>$R_{a,SC2}$, Table 5.4, Fig. 5.7).

Microscopy: The damage regime of the scratch depends on the sharpness of the indenter; Micro-cracking is induced by the sharp indenter as radial/median cracks and chips are formed along the length of the scratch (Fig. 5.11a, Fig. 2.26). The increased average surface roughness of the SC1 series is attributed to the occurrence of chips with the sharp intender. On the other hand, scratches induced with the blunt indenter belong to the micro ductile regime (Fig. 5.11c).

Additionally, the formation of radial/median cracks is a function of the sharpness of the indenter; sharp indenters introduce numerous radial/median cracks along the length of the crack which are larger in depth and therefore, more severe (Fig. 5.11b) than the few radial/median cracks introduced by the blunt indenter (Fig. 5.11d).

Fracture strength: The fracture strength of scratched glass was found to be a function of the sharpness of the indenter (Fig. 5.12). To support the microscopic and average surface roughness observations (Fig. 5.6 and Fig. 5.11), the fracture strength of each specimen scratched with a sharp indenter (SC1) was lower than those scratched with a blunt indenter (SC2). However, the

reverse is observed for strengths at lower probabilities of failure (e.g. P_f=0.008); series scratched with a sharp indenter have a higher design strength with respect to those scratched with a blunt indenter. This is attributed to the higher scatter in the fracture strength data of the blunt indenter (SC2), (coefficient of variation of CV=17.1% for SC1 and CV=43.8 % for SC2). Higher coefficients of variation lead to lower values of shape factor, β, of the Weibull distribution and thus lower gradients of the CDF resulting in significant rotation of the distribution. Therefore, the condition of the tip of the indenter needs to be evaluated frequently to determine whether replacement is necessary during scratching.

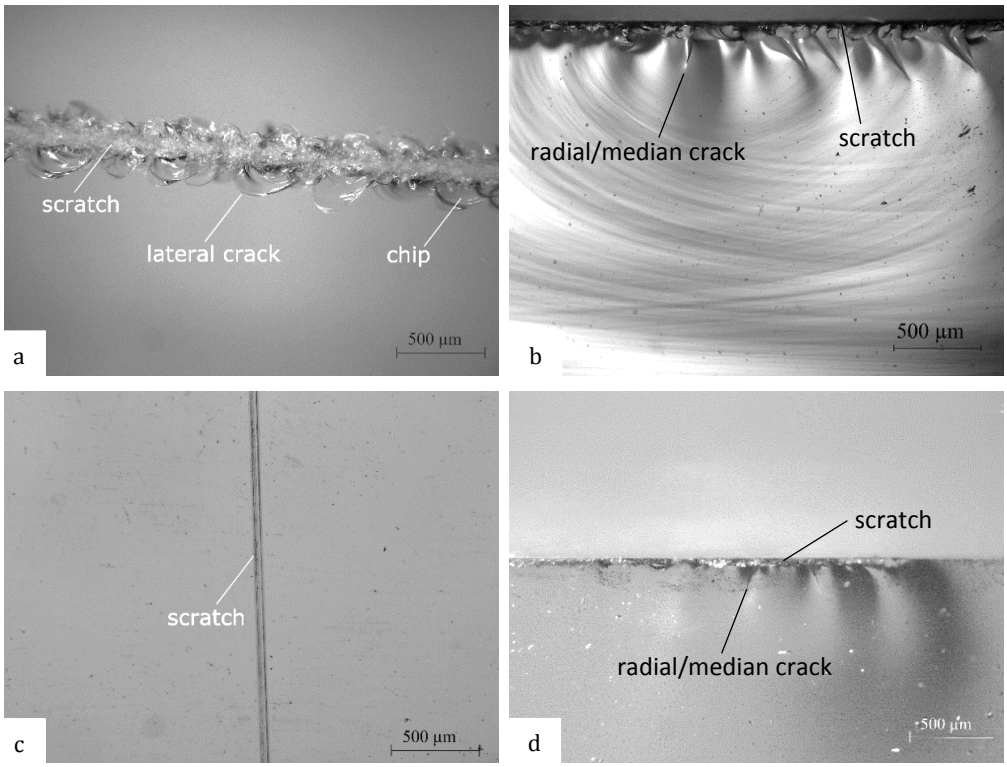

Fig. 5.11: Surface micrograph and critical flaws of (a-b) SC1 (sharp indenter) and; (c-d) SC2 (blunt indenter).

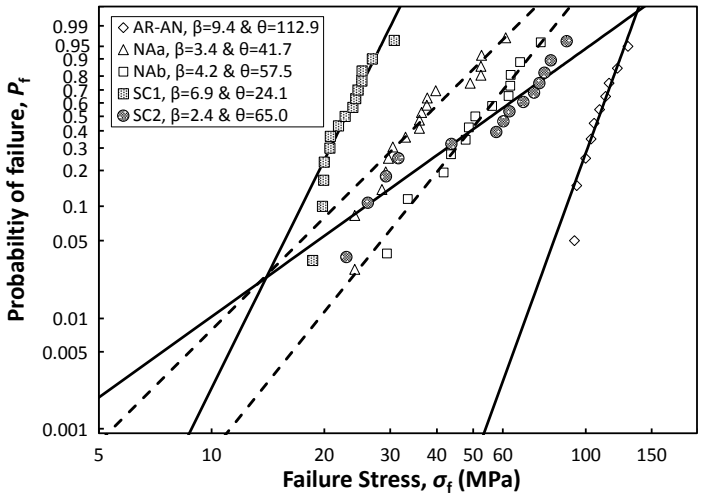

Fig. 5.12: CDFs for naturally aged (NA), as-received (AR) and scratched (SC) annealed glass.

Correlation to naturally aged glass: Naturally aged glass has a large coefficient of variation. Therefore, the CDF of the glass scratched with the blunt indenter (SC2) was found to be a good match to the CDF of the naturally aged glass (Fig. 5.12). However, its design strength (P_f=0.008) though was lower than that reported for naturally aged glass (reduction of $\Delta\sigma_{NA,SC}/\sigma_{NA}$ =10% and 51% with respect to NA-AN_a and NA-AN_b respectively). On the other hand, the design strength of the glass scratched with the sharp indenter (SC1) was found to be within the range of design strengths obtained for the naturally aged glass (Fig. 5.12).

However, the average surface roughness of the scratched glass was lower than that of naturally aged glass (Table 5.4, Fig. 5.7). Therefore, inducing a single flaw on the glass surface is not equivalent to the damage found in naturally aged glass which comprised multiple flaws. Moreover, microscopic observations reveal that the naturally aged glass used in this study, was mostly exposed to erosive action during its service life with little exposure to linear scratching. Therefore, the induction of linear scratches on the glass surface is not representative of the naturally aged glass of this study as the underlying ageing mechanisms are largely different.

Sand abraded annealed glass

Surface roughness: Table 5.4 and Fig. 5.7 show that increasing the drop height of the falling abrasive method from 1.2 m (SA1) to 3.1 m (SA4) leads to a corresponding increase in the average surface roughness of the sand abraded glass. Even though only two of the sand abraded series were evaluated in terms of their surface roughness, the results are promising when compared to the average surface roughness of the naturally aged glass ($R_{a,SA4}$>$R_{a.NAa}$, $R_{a,Nab}$> $R_{a,SA1}$).

Microscopy: Micrographs of the SA series (Fig. 5.13 a, d & f) show that the damage regime depends on the maximum grain size (*MGS*) of the abrasive medium; micro-ductile and occasionally micro-cracking regimes are noted when the abrasive medium is silica sand (0.5 ≤ *GSR* ≤ 0.7 mm, Fig. 5.13a). However, as the *MGS* increases beyond 5.6 mm and riverside gravel are also included in the medium, the flaw size also increases (Fig. 5.13 c & f). The damage in these cases belongs to the micro-cracking or the micro-abrasive regime as the lateral cracks caused by the impact, extend to the surface and in some cases create debris.

The size of the critical flaws in sand abraded series is proportional to the maximum grain size of the abrasive medium (Fig. 5.13 b, c, e & g). Additionally, the formation of radial/median cracks depends on the type of the abrasive medium; radial/median cracks were typically induced when gravel (MSG > 2.0 mm) was included in the abrasive medium (Fig. 5.13 e & g). However, radial/median cracks were rarely found when only silica sand is used (micro-ductile regime shown in Fig. 5.13b and micro-cracking regime shown in Fig. 5.13c).

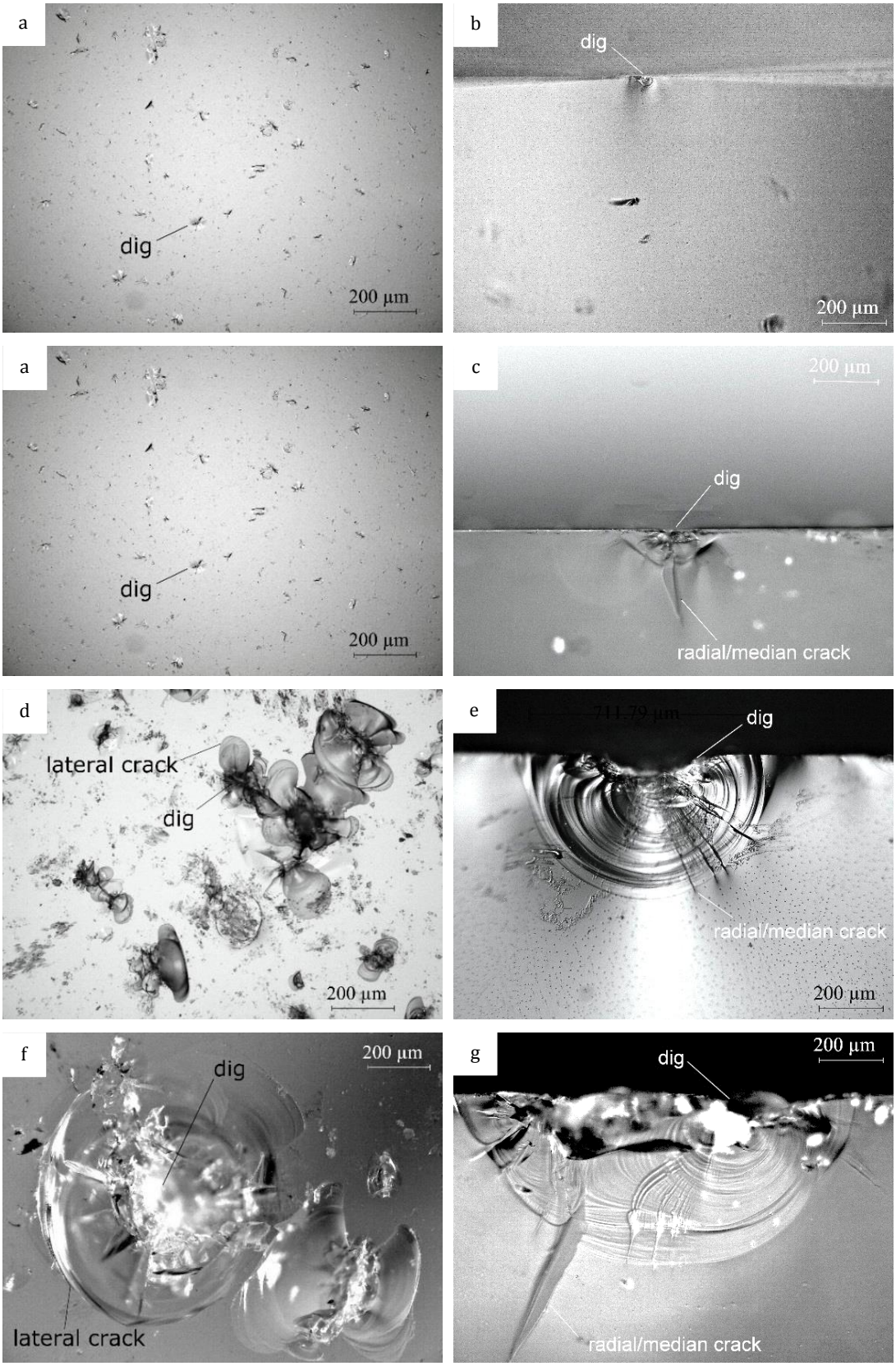

Fig. 5.13: Surface and critical flaws for SA glass: (a-c) MGS=0.7mm; (d-e) MGS= 5.6mm and; (f-g) MGS= 9.5mm

Fracture strength: DIN52348 [129] prescribes a drop height H=1.65 m, a mass of abrasive medium m=3.0 kg, a grain size range of silica sand of $0.5 \leq GSR \leq 0.7$ mm and a rotation rate of the base RR=250 rpm. The fracture strength data of the sand abraded series using these artificial ageing parameters (SA2) produce a good correlation with the mean strength (P_f=0.50) of naturally aged glass (Fig. 5.14). However, they significantly overestimate strengths at low probabilities of failure; $92 \leq \Delta\sigma_{SA,NA}/\sigma_{NA} \leq 253\%$ overestimation of strength was found for P_f=0.008 (Table 5.5). Therefore, DIN 52348 [129] does not reproduce surface damage that is representative of the natural ageing processes that the glass (used in this study) underwent during its service life.

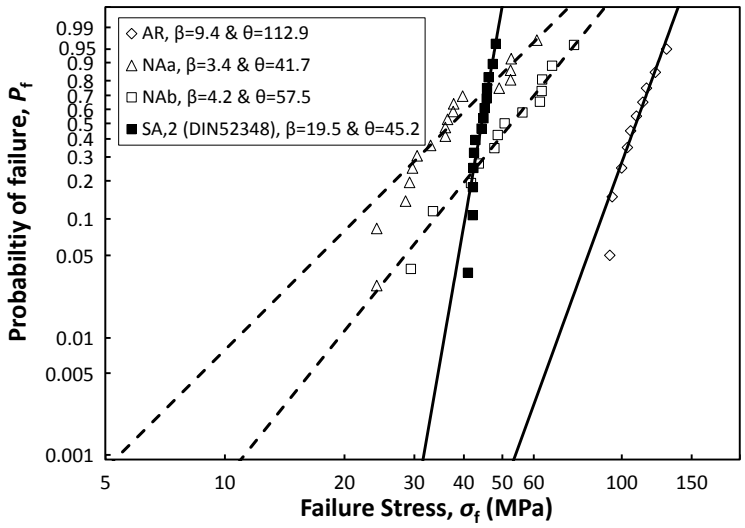

Fig. 5.14: CDFs of naturally aged (NA), as-received (AR) and sand abraded (SA2 DIN 52348) annealed glass.

Therefore, it is pertinent to identify a combination of artificial ageing parameters that would produce a representative cumulative distribution function to those reported for naturally aged glass. For this reason, the influence of each artificial ageing parameter (drop height - H, mass of abrasive medium - m, maximum grain size of abrasive medium - MGS, gravel percentage in the abrasive medium - p, rotation rate of the base - RR, curing time of the specimens - t_c and environmental conditions during curing) on the strength of the sand abraded glass is discussed in turn in this section.

Table 5.5: Salient results of the Weibull statistics analysis for fracture strength data of all series.

Series	Artificial ageing parameters						Weibull parameters				Fractile values			
	H	***m***	***GSR***	***p***	***RR***	t_c	β	θ	p_{AD}	***CV***	$\sigma_{f,0.008}$	***max σ***	***min σ***	$\sigma_{f,0.5}$
	m	kg	mm	%	rpm	hrs		MPa	%	%	MPa	MPa	MPa	MPa
NA-AN$_a$	-	-	-	-	-	-	3.39	41.68	9.69	32.58	10.00	61.06	24.12	37.41
NA-AN$_b$	-	-	-	-	-	-	4.22	57.54	79.58	26.70	18.36	75.80	29.41	52.76
AR-AN	-	-	-	-	-	-	9.36	112.92	66.63	12.81	67.44	129.67	93.243	108.58
SA1	1.20	3.0	0.5-0.7	0*	250	2	34.66	47.24	48.86	3.63	41.10	49.11	44.61	46.74
SA2	1.65	3.0	0.5-0.7	0*	250	2	19.47	45.20	35.86	6.36	35.28	48.14	40.96	44.36
SA3	2.30	3.0	0.5-0.7	0*	250	2	15.76	41.55	64.12	7.80	30.59	44.25	30.96	40.59
SA4	3.00	3.0	0.5-0.7	0*	250	2	17.29	35.28	72.92	7.13	26.69	37.50	30.38	34.54
SA5	1.20	1.0	0.5-0.7	0*	250	2	14.78	49.28	17.16	8.29	35.56	52.88	38.87	48.08
SA6	1.20	1.5	0.5-0.7	0*	250	2	13.99	48.84	68.62	8.74	34.59	53.58	39.22	47.57
SA7	1.20	2.0	0.5-0.7	0*	250	2	15.32	48.17	78.44	8.01	35.16	51.26	38.54	47.03
SA8	1.65	1.0	0.5-0.7	0*	250	2	20.86	51.30	11.70	5.95	40.70	55.51	44.89	50.41
SA9	1.65	1.5	0.5-0.7	0*	250	2	16.70	47.57	19.35	7.38	35.63	51.61	43.10	46.53
SA10	1.65	2.0	0.5-0.7	0*	250	2	17.69	45.83	71.81	6.98	34.89	48.51	41.21	44.89
SA11	3.00	1.0	0.5-0.7	0*	250	2	22.35	45.52	59.91	5.57	36.68	48.61	39.44	44.78
SA12	3.00	1.5	0.5-0.7	0*	250	2	22.66	38.22	18.87	5.49	30.89	40.11	31.80	37.61
SA13	3.00	2.0	0.5-0.7	0*	250	2	15.13	43.30	50.66	8.11	31.48	45.67	35.72	42.26
SA14	3.00	4.0	0.5-0.7	0*	250	2	18.38	37.43	72.82	6.73	28.79	39.48	33.22	36.69
SA15	3.00	5.0	0.5-0.7	0*	250	2	41.05	38.91	32.41	3.07	34.59	40.61	36.54	38.56
SA16	3.00	3.0	0.5-1.0	0*	250	2	19.93	36.42	56.89	6.22	28.59	38.45	28.54	35.76
SA17	3.00	3.0	0.5-5.6	45*	250	2	21.17	18.87	17.33	5.87	15.02	20.53	16.65	18.54
SA18	3.00	3.0	0.5-0.7 & 8.0-9.5	0.1	250	2	9.94	28.51	79.98	12.10	17.55	32.03	20.12	27.48
SA19	3.00	3.0	0.5-1.0	0*	0	2	16.22	32.25	67.24	7.59	23.96	34.90	26.57	31.53
SA20	3.00	3.0	0.5-1.0	0*	125	2	13.82	33.86	14.81	8.84	25.52	38.48	27.84	32.97
SA21	3.00	3.0	0.5-0.7 & 8.0-9.5	0.1	250	168	6.20	27.63	58.04	18.81	12.68	33.31	16.29	26.05
SA22	3.00	3.0	0.5-9.5	55*	250	2	15.05	15.22	48.23	8.15	11.04	16.10	12.81	14.85
SA23	3.00	3.0	0.5-0.7 & 8.0-9.5	10	250	2	8.44	17.56	57.53	14.11	9.91	20.91	13.02	16.81
SA24	3.00	3.0	0.5-0.7 & 8.0-9.5	10	250	168	11.55	19.75	15.06	10.50	13.01	22.57	16.16	19.13
SA25	3.00	3.0	0.5-0.7 & 8.0-9.5	10	250	168	11.85	19.21	62.33	10.24	12.78	20.97	14.20	18.62
SA26	3.00	3.0	0.5-0.7 & 8.0-9.5	0.05	250	2	11.90	38.26	19.06	10.21	25.51	43.45	28.37	37.07

*Well graded distributions, *H*= Drop Height, *m*=mass of abrasive medium, *GSR*=grain size range, *p*=percentage of gravel, *RR*=rotation rate, t_c=curing time, β=shape factor, θ= scale factor, *CV*= coefficient of variation, $\sigma_{0.008}$=design strength, $\sigma_{0.5}$=mean strength.

Drop height

Drop heights, H, of 1.2, 1.65 (prescribed in DIN52348 [129]), 2.3 and 3.0 m were considered to investigate the influence of the drop height on the strength of the artificially aged glass. All other artificial ageing parameters were kept constant at m=3 kg, 0.5 ≤ GSR ≤ 0.7 mm, RR=250 rpm and t_c=2 hrs. As expected, glass strength reduces as the drop height increases (Fig. 5.15).

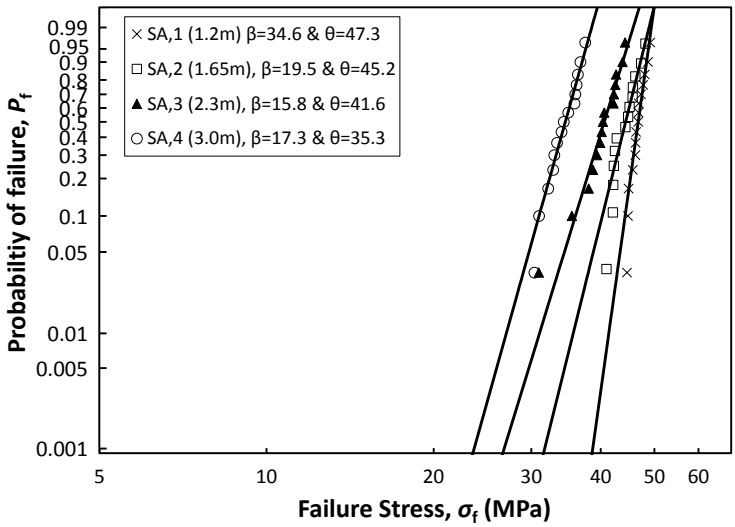

Fig. 5.15: CDFs of SA strength for various drop heights and m=3.0kg, 0.5≤GSR≤0.7mm, RR=250rpm & t_c=2hrs

Mass of abrasive medium

In addition to the mass of 3 kg prescribed in DIN 52348 [129], the following masses were also investigated: 1.0, 1.5, 2.0, 4.0 and 5.0 kg. All other artificial ageing parameters were kept constant at H=3.0 m, 0.5 ≤ GSR ≤ 0.7 mm, RR=250 rpm and t_c=2 hrs.

The results show that the failure mode of the artificially aged glass depends on the mass of the abrasive medium; unimodal Weibull distributions were found for masses m ≥ 3.0 kg (Fig. 5.16a) and bi-modal Weibull distributions were found for masses m < 3.0 kg (Fig. 5.16b). A bi-modal Weibull distribution signifies that the fracture data can be divided in two groups and suggests that the critical flaws on either side of the bi-modal discontinuity are morphologically different (Appendix F).

<u>m ≥ 3 kg</u>: The increase in the mass of the abrasive medium did not result, in the expected decrease in strength (Fig. 5.16a). As the mass increased above 3 kg, the strength of the specimens also increased at low probabilities of failure and converged at very high probabilities of failure. This increase in strength can potentially be attributed to the extended sand abrasion; as the mass of the abrasive medium increases, material can be uniformly removed from the surface reducing the overall thickness of the glass and smoothing out flaws induced by the sand abrasion. The depth of the flaws is thereby reduced making the flaws less severe.

m < 3 kg: Unsurprisingly, the unimodal Weibull distributions commonly used in glass strength statistics [162], provided a poor fit (p_{AD} <0.05) to the bi-modal data from the experiments; these series can therefore, be more accurately described by mixed Weibull distributions (Eq. F1, Appendix F) providing acceptable goodness of fit.

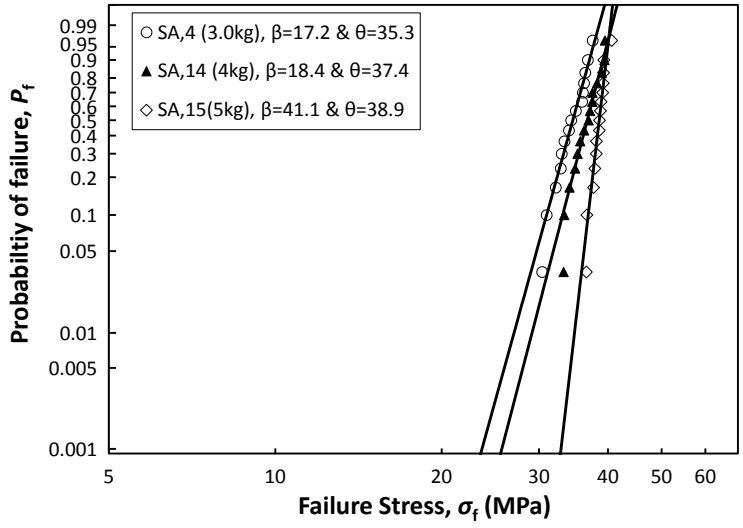

(a)

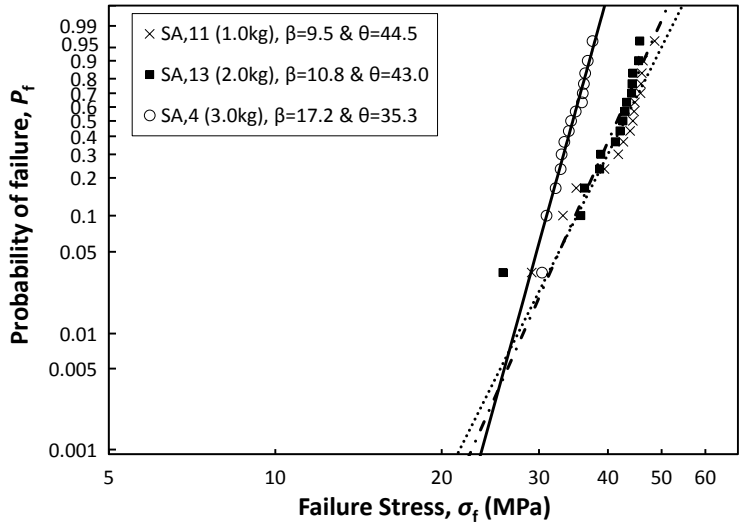

(b)

Fig. 5.16: CDFs of SA strength for H=3m, 0.5≤GSR≤0.7mm, RR=250rpm & t_c=2hrs: (a) m≤3.0kg; (b) m≥3.0kg.

Fractographic microscopy validates the initial assumption that the critical flaws belonging to the first mode of the bi-modal distribution i.e. the group of points characterised by lower failure stresses, are scratches of different morphology (Fig. 5.17a) than the flaws induced by sand impact (second mode of the distribution, Fig. 5.17b). These scratches were potentially introduced during transportation and handling of the glass. The flaw depth of these scratches was larger than the depth of flaws introduced by the artificial ageing (Fig. 5.17a-b) and were therefore, more critical. The mixed Weibull distribution is therefore, not used further in this study since pre-existing flaws

and the uncertainties associated with their formation, are excluded from the analysis of the artificial ageing parameters. In fact, unimodal failures with acceptable goodness of fit can be achieved for masses m < 3 kg when the data points that correspond to the first mode of failure (scratches) are excluded (Table 5.5). In general, masses m < 3.0 kg should be avoided in order to eliminate the influence of flaws created during handling and transportation of the glass.

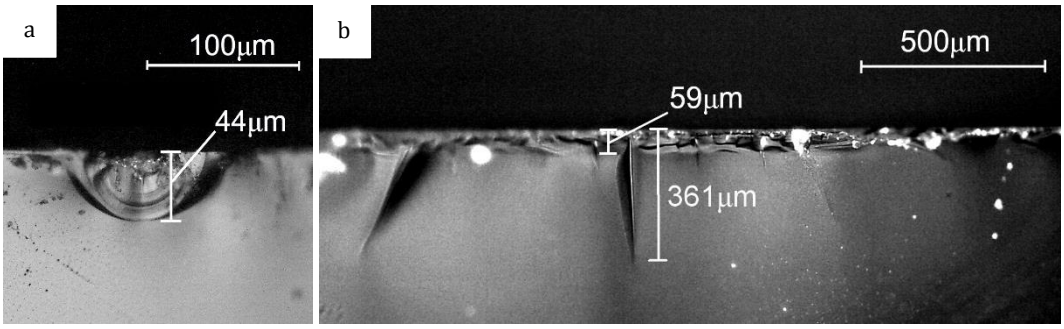

Fig. 5.17: Critical flaw of: (a) 2nd failure mode: elliptical flaw and; (b) 1st failure mode: scratch.

Maximum grain size of the abrasive medium

Well graded ranges of abrasive medium, namely 0.5 ≤ *GSR* ≤ 0.7 mm, 0.5 ≤ *GSR* ≤ 1.0 mm, 0.5 ≤ *GSR* ≤ 5.6 mm and 0.5 ≤ *GSR* ≤ 9.5 mm (grain size distribution curves shown in Appendix D, Fig. D1), were used to study the influence of the maximum grain size, *MGS*, on the strength of the artificially aged glass while all other artificial ageing parameters were kept constant at H=3.0 m, m=3 kg, RR=250 rpm and t_c=2 hrs. A small increase in *MGS* from 0.7 to 1.0 mm produces negligible differences in strength (7% and 3% increase for the design and mean strength respectively with respect to SA4, Fig. 5.18). However, significant strength reduction was noted when the maximum grain size increased considerably (44% & 46% reduction in design & mean strength for *MGS*=5.6 mm and 59% & 57% reduction in design & mean strength for *MGS*=9.5 mm with respect to SA4).

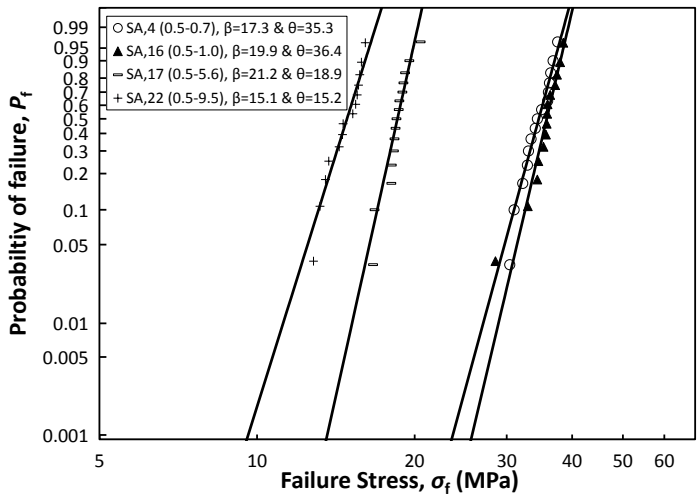

Fig. 5.18: CDFs of SA strength for various max grain sizes and H=3.0m, m=3kg, RR=250rpm & t_c=2hrs.

Percentage of gravel

The influence of the percentage of gravel, p, of the abrasive medium on the strength of glass was also investigated. In particular, abrasive medium of m=3 kg was used which predominantly consisted of a grain size range of 0.5 ≤ GSR ≤ 0.7 mm and small percentages of gravel (8.0 ≤ GSR ≤ 9.5 mm) namely 0%, 0.05%, 0.1% and 10%. All other artificial ageing parameters were kept constant at H=3.0 m, RR=250 rpm and t_c=2 hrs. The integration of a very small percentage of gravel in the abrasive mixture (p=0.05% which corresponds to 1 gravel) leads to wider distribution of strength data (Fig. 5.19, CV=10.21% for p=0.05% and CV=7.13% for p=0, Table 5.5) seen as a clockwise rotation of the distribution. Increasing the percentage of gravel further (p=0.1% and 10%) leads to the expected strength reduction (Fig. 5.19) and a clockwise rotation of the distribution as seen for p=0.05% (CV=12.10% for p=0.1% and CV=14.11% for p=10%). This clockwise rotation is represented by the decrease in shape factor, β, (Table 5.5); a reduction of 31%, 43% and 51% was reported for p=0.05%, 0.1% and 10% respectively with respect to p=0%. This is an important finding as the shape factor of naturally aged glass is typically low (3.4 ≤ β ≤ 4.2 in this study) and therefore, these series are more representative of the naturally aged glass investigated in this study.

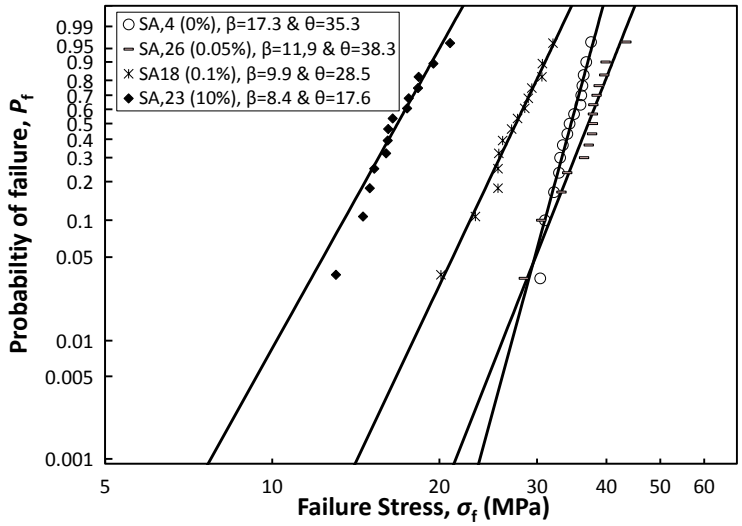

Fig. 5.19: CDFs of SA strength for various gravel % and H=3.0m, m=3kg, RR=250rpm & t_c=2hrs.

Base rotation rate

The effect of the base rotation rate on the strength of the artificially aged glass was investigated for RR=0, 125 and 250 rpm. All other artificial ageing parameters were kept constant at H= 3.0 m, m=3.0 kg, 0.5 ≤ GSR ≤ 1.0 mm and t_c=2 hrs. The results show that increasing the rotation rate leads to an increase in strength (Fig. 5.20). This is expected because a stationary base results in concentrating damage to the confined area directly under the guide pipe, thereby, leading to more severe flaws and thus, lower strengths.

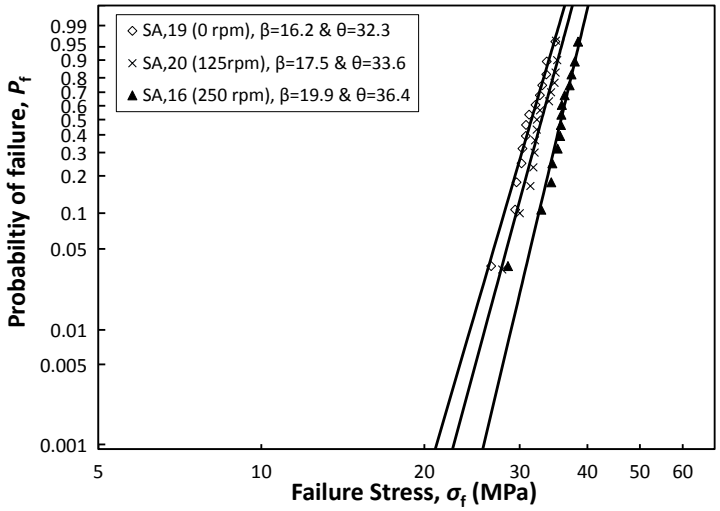

Fig. 5.20: CDFs of SA strength for various rotation rates and H=3.0 m, m=3 kg, 0.7≤GSR≤1.00 mm & t_c=2hrs.

Curing time and environmental conditions

The influence of the curing time and environmental conditions during curing were also investigated in this study. Curing time, t_c, is the time between the artificial ageing process and the CDR tests. Two cases were considered for the curing time: (a) destructive testing shortly after the sand abrasion (t_c≈2 hrs) and; (b) destructive testing after storing the sand abraded specimens for 1 week (t_c=7 days). Two storing conditions were investigated: (a) ambient lab conditions (T=22±3°C and RH=42±8%) and; (b) storing under potable tap water (T=22±3°C and RH=100%).

Influence of curing time at ambient conditions: The following artificial ageing parameters were used: H=3.0 m, m=3.0 kg, RR=250 rpm 0.5 ≤ GSR ≤ 0.7 mm (99.9%) & 8.0 ≤ GSR ≤ 9.5 mm (p=0.1%) and t_c=2 hrs or t_c=7 d. The influence of curing time on the strength of glass was different, leading to strength reduction in SA21 and strength increase in SA24 (Fig. 5.21a & b).

Two distinct phenomena can occur in parallel but on different extents during curing: (a) changes in the chemical composition at the crack tip due to leaching of alkali [90] leading in strength increase and; (b) sub-critical crack growth, triggered by residual surface stresses induced during impact [178] leading to strength reduction.

p=0.1% of gravel: The results show that the influence of the curing time is negligible on the mean strength (4% reduction for t_c=7 d, Fig. 5.21a). However, the influence at lower probabilities of failure is significant (38% reduction for the design strength for t_c=7 d, Fig. 5.21). The increase in curing time therefore, produces a wider distribution of strength data, manifested as a change in the gradient of the Weibull distribution (Fig. 5.21a) and correspondingly smaller values of the shape factor, β (Table 5.5). The underlying physical reasons for this response have not been investigated further, but it could be attributed to the sub-critical crack growth that occurs during the curing period of the specimens as a result of the local residual stresses that are generated

during impact with sand/gravel grains. This could cause flaws to grow and therefore, specimens to fail at lower stresses.

p=10% of gravel: The results show that with a higher percentage of gravel, increasing the curing time does lead to an increase in strength (Fig. 5.21b, 31% and 14% for design, P_f=0.008 and mean, P_f=0.50 strength respectively). It therefore, appears that the strength gains associated with curing are a function of the flaw size and the water tightness of the flaw. In particular, larger flaws (α > 400 μm) produce a net strengthening after curing whereas smaller flaws produce a net weakening after curing. However, further investigation is needed to verify this.

Influence of environmental conditions during storage: The influence of the environmental conditions (ambient or under water) during storage was found to be negligible and to produce almost identical strength results (Fig. 5.21b) and is in agreement with [179].

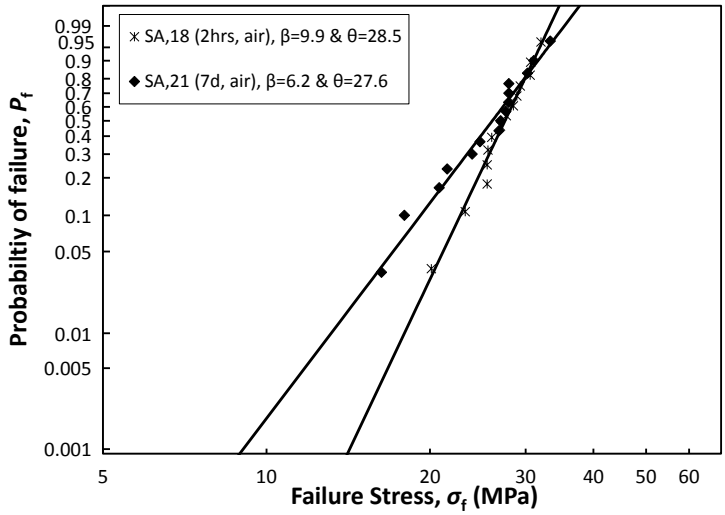

(a)

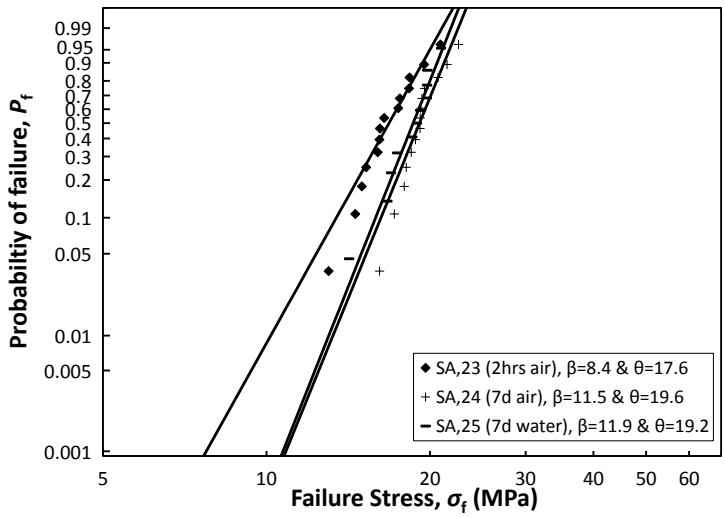

(b)

Fig. 5.21: CDFs of SA strength for various curing times and H=3.0m, m=3.0kg, RR=250rpm and; (a) 0.5≤GSR≤0.7mm (99.9%) & 8.0≤GSR≤9.5mm (0.1%); (b) 0.5≤GSR≤0.7mm (90%) & 8.0≤GSR≤9.5mm (10%).

Correlation to naturally *aged* glass:

Fig. 5.22a-d shows a detailed comparison across all the series (AR, NA and SA) that were tested in this study. Good agreement was found for the mean strength between most of the SA series and the NA glass (Fig. 5.22a), but there was generally poor agreement at the lower probabilities of failure commonly used in engineering design. In fact, most of the SA series overestimated the design strength by a very significant margin (Fig. 5.22b). Statistically, this is evidenced by the lower shape factor, β in naturally aged glass than most of the SA series (Fig. 5.22c); the shape factor represents the gradient of the distribution and therefore has a larger influence on the lower (and higher) fractile values away from the mean. Low shape factors, closer to the values found in naturally aged glass, were found for SA series with small percentages of gravel (p=0.1% in SA18 & p=10% in SA23) and longer curing times (t_c=7 days in SA21). Additionally, NA glass had significantly larger coefficients of variation ($30 \leq CV \leq 33\%$) than most of the SA series ($4 \leq CV \leq 19\%$) that generally provided fairly consistent results with low scatter (Fig. 5.22d).

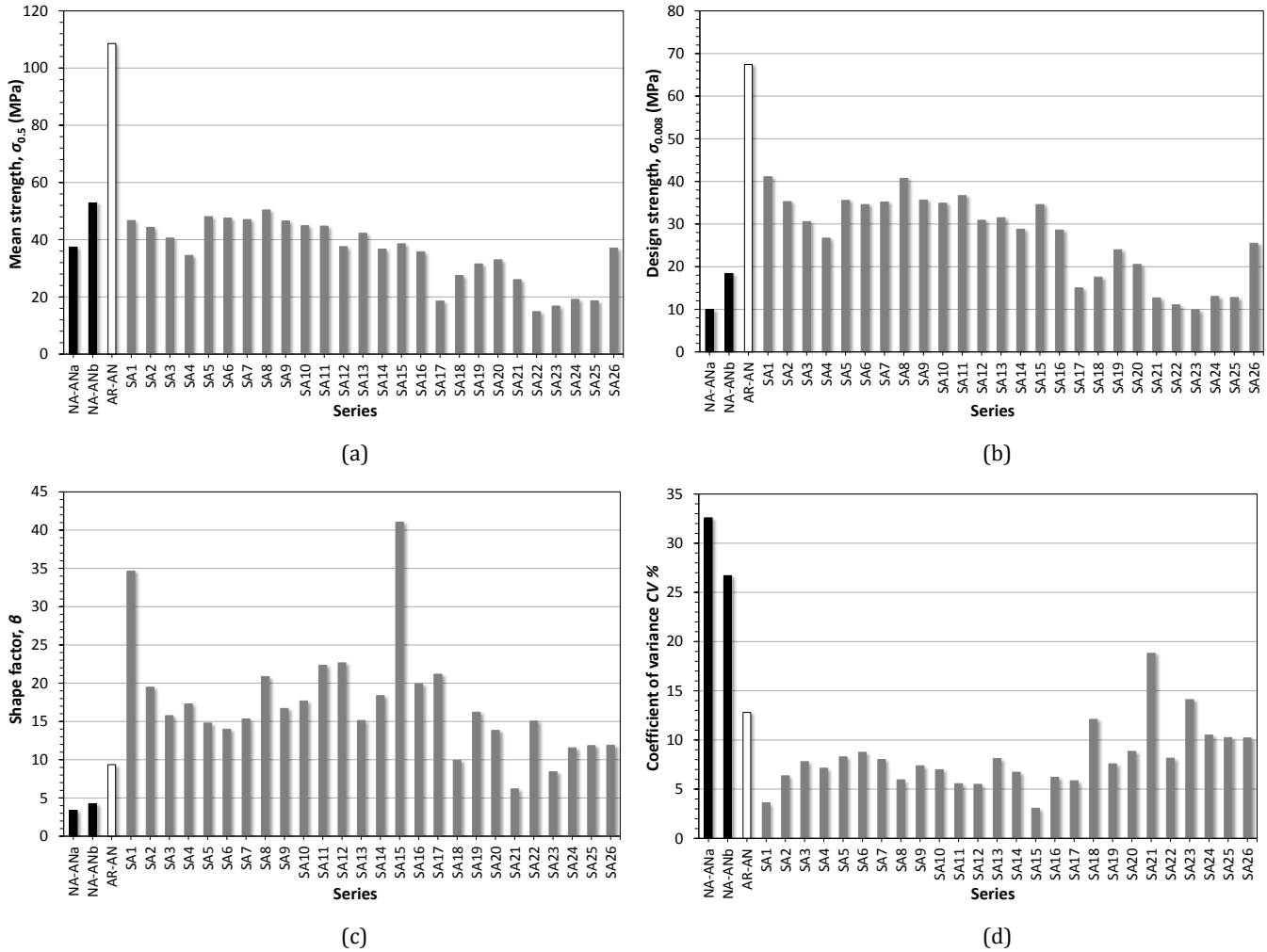

Fig. 5.22: AR, NA & SA comparison: (a) mean strength; (b) design strength; (c) shape factor and; (d) coefficient of variance.

The ageing parameters prescribed in DIN 52348 [129] and adopted in SA2, provide a good estimate of the mean strength of naturally aged glass but significantly overestimate design strength ($92\% \leq \Delta\sigma_{NA,SA2}/\sigma_{NA} \leq 253\%$ for the 0.008 probability of failure). Therefore, this method is not suitable for assessing the strengths at low probabilities of failure.

A close correlation at all probabilities of failure between the strength of naturally aged and sand abraded glass is very difficult to obtain. However, strengths at low probabilities govern engineering design and on this basis, SA21 can be considered the best performing among the SA series (Fig. 5.22, Fig. 5.23 and Table 5.5).

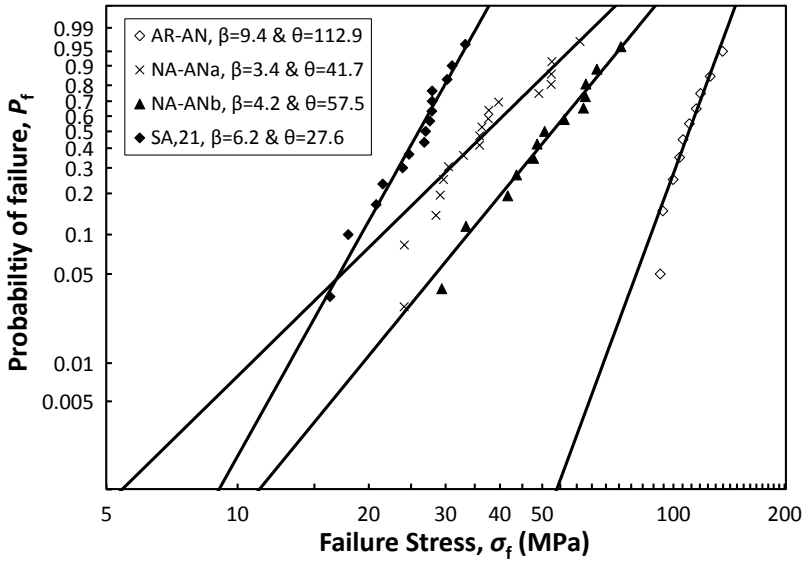

Fig. 5.23: CDF for NA-AN, AR-AN and best performing of SA series (SA21).

5.4 Procedure for assessing the strength of aged glass

Section 5.3 shows that artificial ageing with the falling abrasive method has the potential to produce similar Weibull parameters and therefore, equivalent levels of damage to those found in the naturally aged glass of this study that was exposed to erosive action. These results are condensed here into a procedure for the assessment of the strength of aged glass (Fig. 5.24):

<u>Step 1</u>: *Destructive testing of as-received glass:* Perform Coaxial Double Ring (CDR) tests to obtain fracture strength data of the as-received glass. Fit a 2-parameter Weibull distribution to the data to obtain strength results at low, P_f=0.008 or mean, P_f=0.50 probability of failure.

<u>Step 2</u>: *Establish the target level of erosion to which the glass will be exposed during the intended application*: Damage accumulation varies and is a function of the level of exposure (location and type of application). Therefore, the target level of damage needs to be adapted accordingly.

(2a) *Known erosion level:* If reliable CDR data on naturally aged glass exposed to the target

erosion level are available, proceed to step 3. If not, source, test destructively and obtain design and mean strength predictions for such naturally aged glass.

(2b) *Unknown erosion level*: Assume a general erosion level e.g. the erosion level of the naturally aged glass NA-AN_{a-b} of this study (design strength of $10.0 \leq \sigma_{f,0.008} \leq 18.36$ MPa and mean strength of $37.41 \leq \sigma_{f,0.50} \leq 52.76$ MPa).

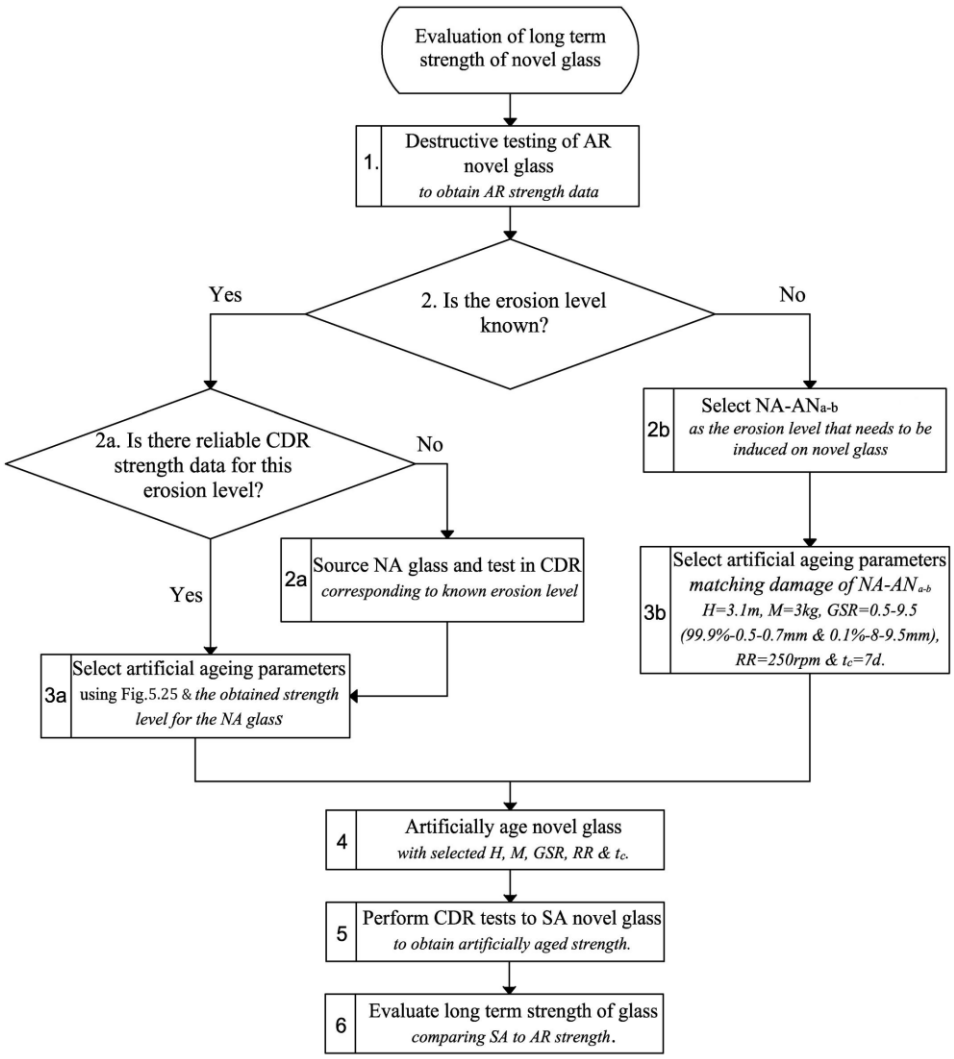

Fig. 5.24: Procedure for artificial ageing and evaluation of strength for aged glass.

<u>Step 3</u>: *Selection of artificial ageing parameters:* Select artificial ageing parameters (H, m, *GSR*, *RR* & t_c) of the falling abrasive method for the target level of erosion.

(3a) *Known erosion level*: Refer to Fig. 5.25a-b to match the shape factor and the design or the mean strength of naturally aged glass obtained in step 2 with the strength of one of the artificially aged series. Subsequently, refer to Table 5.6 to obtain the artificial ageing parameters that were used for the selected artificially aged series.

(3b) *Unknown erosion level:* Select the artificial ageing parameters of SA21 i.e. H=3.1 m, m=3.0

kg, 0.5 ≤ *GSR* ≤ 9.5 mm (99.9% of 0.5 ≤ *GSR* ≤ 0.7mm & *p*=0.1% of 8.0 ≤ *GSR* ≤ 9.5 mm), *RR*=250 rpm and t_c=7 days to replicate the damage found in NA-$AN_{a\text{-}b}$ of this study.

Step 4: Artificial ageing: Artificially age the as-received glass in a falling abrasive set-up with the ageing parameters selected in step 3.

Step 5: Destructive testing of artificially aged glass: Perform CDR tests on the artificially aged glass and fit data to a 2-parameter Weibull distribution.

Step 6: Evaluation of strength after ageing: Compare the strength of artificially aged with that of as-received glass to assess its strength degradation.

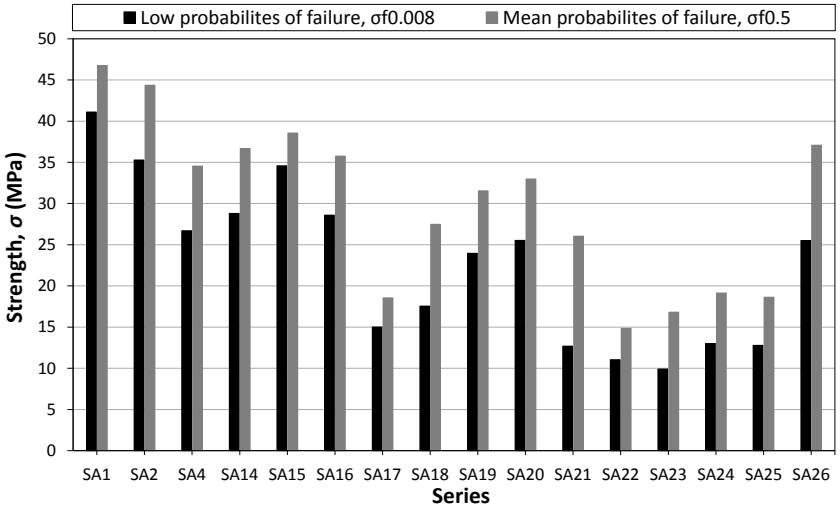

(a)

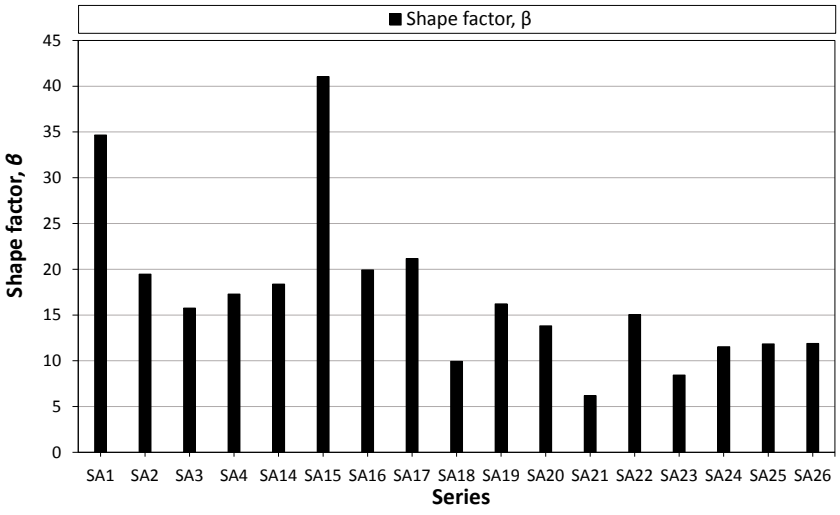

(b)

Fig. 5.25: (a) Strength at P_f=0.008 and P_f=0.50 and; (b) shape factor for artificially aged series of annealed glass (Table 5.6).

Table 5.6: Ageing parameters and salient Weibull results for fracture strength data of SA series.

Series	Artificial ageing parameters						Fractile values	
	H	m	GSR	p	RR	t_c	$\sigma_{f,0.008}$	$\sigma_{f,0.5}$
	m	kg	mm	%	rpm	hrs	MPa	MPa
SA1	1.20	3.0	0.5-0.7	0*	250	2	41.10	46.74
SA2	1.65	3.0	0.5-0.7	0*	250	2	35.28	44.36
SA3	2.30	3.0	0.5-0.7	0*	250	2	30.59	40.59
SA4	3.00	3.0	0.5-0.7	0*	250	2	26.69	34.54
SA14	3.00	4.0	0.5-0.7	0*	250	2	28.79	36.69
SA15	3.00	5.0	0.5-0.7	0*	250	2	34.59	38.56
SA16	3.00	3.0	0.5-1.0	0*	250	2	28.59	35.76
SA17	3.00	3.0	0.5-5.6	45*	250	2	15.02	18.54
SA18	3.00	3.0	0.5-0.7 & 8.0-9.5	0.1	250	2	17.55	27.48
SA19	3.00	3.0	0.5-1.0	0*	0	2	23.96	31.53
SA20	3.00	3.0	0.5-1.0	0*	125	2	25.52	32.97
SA21	3.00	3.0	0.5-0.7 & 8.0-9.5	0.1	250	168	12.68	26.05
SA22	3.00	3.0	0.5-9.5	55*	250	2	11.04	14.85
SA23	3.00	3.0	0.5-0.7 & 8.0-9.5	10	250	2	9.91	16.81
SA24	3.00	3.0	0.5-0.7 & 8.0-9.5	10	250	168	13.01	19.13
SA25	3.00	3.0	0.5-0.7 & 8.0-9.5	10	250	168	12.78	18.62
SA26	3.00	3.0	0.5-0.7 & 8.0-9.5	0.05	250	2	25.51	37.07

*Well graded distributions

H= Drop Height, m=mass of abrasive medium, GSR=grain size range, p=percentage of gravel, RR=rotation rate, t_c=curing time, β=shape factor, θ= scale factor, CV= coefficient of variation, $\sigma_{0.008}$=design strength, $\sigma_{0.5}$=mean strength.

5.5 Conclusions

The study described in this Chapter showed that annealed glass suffered a significant reduction in its extrinsic as-received strength during its 20-year service life; an 85% reduction in strength was found for the lower probabilities of failure, commonly used for determining the design strength of naturally aged glass. Therefore, the evaluation of the performance of aged glass (annealed, heat treated and chemically toughened) is essential, particularly if glass is used in demanding load bearing applications. The first step in this evaluation is to establish a reliable artificial ageing method that produces equivalent damage to that found in naturally aged glasses. For this reason, a scratching and a falling abrasive method were used to replicate natural ageing phenomena in annealed glass.

Even though scratching produced a fairly good correlation to the strength of naturally aged glass, it failed to replicate the surface roughness. Furthermore, microscopic qualitative observations

revealed that the naturally aged glass of this study was mainly exposed to erosive action and therefore scratching was not a faithful representation of the ageing mechanisms.

DIN 52348 [129] proposes a falling abrasive method to replicate ageing phenomena on glass. However, the level of damage induced by this method seems to be arbitrary and is not correlated with the strength of naturally aged glass. This study showed that the artificial ageing recommendations in DIN 52348 lead to a good estimation of the mean strength (P_f=0.5) but a significant overestimation of strength at the lower probabilities of failure which ranges between 92% ≤ $\Delta\sigma_{NA,SA2}/\sigma_{NA}$ ≤ 253% with respect to the 2 series of naturally aged glass of this study, and is therefore unsafe.

Further investigations in this study showed that the falling abrasive method can induce equivalent levels of damage to that found in naturally aged glass but this requires careful selection of artificial ageing parameters (drop height, mass and grain size of abrasive medium, rotation rate, curing time and curing conditions). Investigation of each artificial ageing parameter in turn, showed that drop height and maximum grain size of the abrasive medium are inversely proportional to the strength of the sand-abraded glass. The opposite applies to the rotation rate of the specimen base. Masses of abrasive medium smaller than 3 kg lead to bi-modal Weibull distributions triggered by pre-existing flaws and should therefore, be avoided while masses larger than 3 kg lead to an increase in strength attributed to surface material removal. Therefore, a mass of 3 kg is generally recommended. Additionally, the integration of a small percentage of gravel (0.1 ≤ p ≤ 10% of 8.0 ≤ GSR ≤ 9.5 mm) and longer curing times results in larger scatter of strength data; this leads to lower estimates for $\sigma_{f,0.008}$ and lower shape factors, β, thereby providing a better correlation with the naturally aged glass. The following artificial ageing parameters: H=3.0 m, m=3.0 kg, 0.5 ≤ GSR ≤ 9.5 mm (99.9% of 0.5 ≤ GSR ≤ 0.7 mm & p=0.1% of 8.0 ≤ GSR ≤ 9.5 mm), RR=250 rpm and t_c=7 d were found to more closely reproduce the strength characteristics of the naturally aged glass investigated in this study, at low probabilities of failure.

The results were then summarized in a user-friendly set of guidelines that allows the selection of ageing parameters for the artificial ageing of novel glass and therefore, the evaluation of its strength after ageing. These guidelines can be implemented for a known target level of exposure by selecting artificial ageing parameters to suit this exposure level. However, they can also be applied for a general case scenario of exposure when specific details are not available; in this case the naturally aged glass of this Chapter or any other suitable naturally aged glass can be used to set the target level of exposure in order to select artificial ageing parameters.

6. Strength of Aged Glass

6.1 Introduction

As discussed in previous Chapters, the strength of aged glass is not well documented. In particular, there is a lack of knowledge on the strength of aged toughened glass. The guidelines on the assessment of the strength of aged glass that were formulated in Chapter 5, will be implemented in this Chapter on annealed, fully toughened and chemically toughened glass.

The aim of this Chapter (Fig. 6.1) is to evaluate the strength of aged glass when subjected to erosive action during its service life. This will enable the assessment of the safe use of glass in load bearing applications including cold bent glass applications where the glass is subjected to the permanent cold bending stress. Section 6.2 describes the specimens and the methods used for the artificial ageing and the evaluation of glass. Section 6.3 presents the results whilst Section 6.4 summarizes salient results and conclusions.

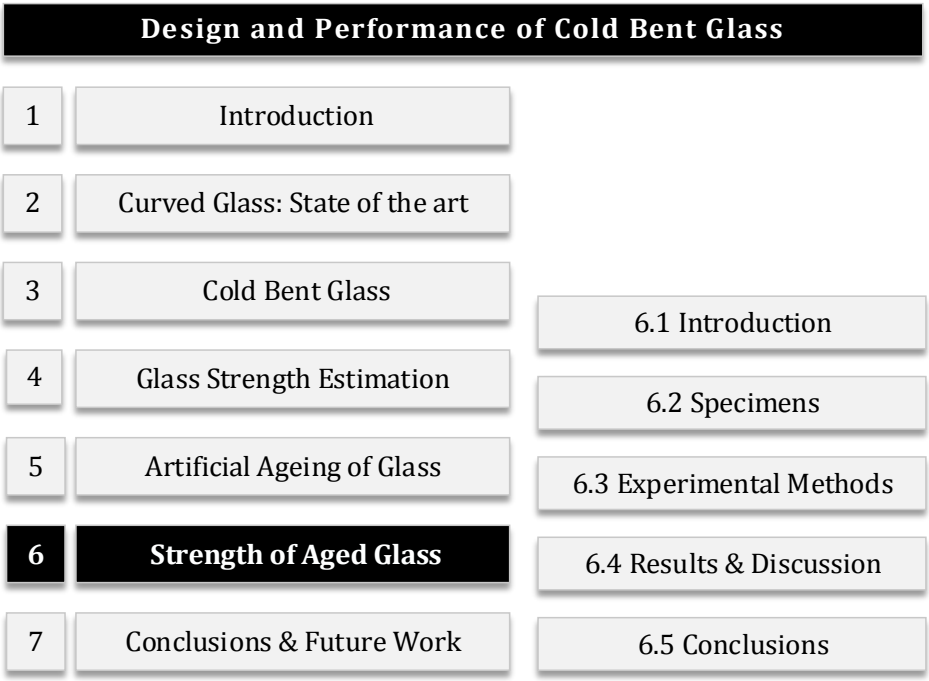

Fig. 6.1: Contents of Chapter 6.

6.2 Specimens

The strength of aged chemically toughened glass (CTG), fully toughened glass (FTG) and annealed glass are evaluated in this section after exposure to erosive action using the procedure described in Section 5.4. Fifteen specimens were used per series (Table 6.1). Annealed glass was soda lime silica glass of 150 x 150 x 3 mm and a residual surface stress of σ_r=-2.31±0.6 MPa. The fully

toughened glass was soda-lime-silica glass, toughened in accordance with EN12150-1 [16] and was supplied in individual specimens of 150 x 150 x 6 mm. An average residual surface compression σ_r=-89 MPa and an average case depth d_c=1.21mm was measured by SCALP-05, GlasStress Ltd [175]. The residual surface stress profile is described as a function of the depth by:

$$\sigma_r = \frac{4(\sigma_r - \sigma_t)}{h^2} \cdot z + \sigma_t \Rightarrow \sigma_r = -14.67 \cdot z^2 + 43.02\,, \qquad \text{for -3.0} \le z \le \text{3.0 mm} \qquad \text{(Eq. 6.1)}$$

The chemically toughened glass was alumino-silicate glass and was supplied in plates of 1000 x 1000 x 2 mm. Specimens of 180 x 180 x 2 mm were manually cut with a diamond cutter; the 20% increase in the in-plane dimensions compared to the annealed and fully toughened specimens accounted for the stress relaxation that was expected near the edges as a result of the cutting process. The residual surface stress could not be measured reliably with SCALP-05, GlasStress Ltd [175] for chemically toughened glass as the measurement errors (percentage of excluded pixels and fitting errors) were significantly high.

Table 6.1: Overview of glass specimens.

Abbr.	Glass type	Processing	Residual surface stress (MPa)	Dimensions (mm)	Nom. thickness (mm)	No of data sets
AN-AR	Annealed	As-received	2.31±0.65	150x150x3	2.85±0.03	1
SA21	Annealed	Sand abraded	2.31±0.65	150x150x3	2.86±0.02	1
FT-AR	Fully toughened	As-received	89.03±8.57	150x150x6	5.96±0.03	1
FT-SA	Fully toughened	Sand abraded	89.03±8.57*	150x150x6	5.95±0.02	1
CT-AR	Chemically toughened	As-received	NA**	180x180x2	2.00±0.01	1
CT-SA	Chemically toughened	Sand abraded	NA**	180x180x2	1.99±0.01	1
Total						**6**

*before artificial ageing ** could not be measured reliably with SCALP-05, GlasStress Ltd.

6.3 Experimental methods

Annealed, fully toughened glass and chemically toughened glass were examined under an optical microscope and tested to destruction in their as-received and artificially aged state to evaluate their strength. For consistency, artificial ageing and destructive tests were always performed on the tin side for the annealed and fully toughened glass specimens which was identified with a UV light. Distinction between the two external surfaces of chemically toughened glass was not important because the surface quality of both surfaces is expected to be identical as a result of the Fusion Downdraw process during its production (Section 2.2.2).

6.3.1 Artificial ageing

The artificial ageing parameters were selected using the procedure for assessing the strength of aged glass that was developed in Section 5.4. The damage found in the naturally aged glass of this study ($10.0 \leq \sigma_{f,0.008} \leq 18.36$ MPa) was used as the target level of damage to be introduced in the fully toughened and chemically toughened glass specimens.

The strength of this naturally aged glass ($10.0 \leq \sigma_{f,0.008} \leq 18.36$ MPa) was subsequently mapped onto Fig. 5.25 to identify the artificial ageing parameters to be used in the sand abrasion to induce the target level of damage. Series SA21 provides the best correlation to the damage of the naturally aged glass (Section 5.2.3), and therefore, the artificial ageing parameters used in this series were obtained from Table 5.6 : H=3.1 m, m=3.0 kg, $0.5 \leq GSR \leq 9.5$ mm (99.9% of 0.5-0.7 mm & p=0.1% of 8.0-9.5 mm), RR=250 rpm and t_c=7 d. The glass specimens were abraded, stored for 7 days at ambient laboratory conditions (T=22±3°C and RH=42±8%) and tested to destruction.

6.3.2 Destructive testing

The destructive tests used for annealed, fully toughened and chemically toughened glass are described in this section.

Annealed Glass

Section 4.2 confirms that the Coaxial Double Ring (CDR) set-up is a suitable method for the destructive testing of annealed glass. An identical set-up (D_L=51 mm and D_R=127 mm) to that used in Section 5.2.2 and a stress rate of 20 MPa/sec (13.6 mm/min), are also used for the annealed glass in this Chapter. The failure load was converted to failure stress with Eq. 6.2 based on the full friction numerical model developed in Section 4.2.1 for annealed glass of a thickness h_{AN}=2.85mm:

$$\sigma = 0.0674 \cdot P \qquad \text{(Eq. 6.2)}$$

Fully toughened glass

The same Coaxial Double Ring set-up is also used for the fully toughened glass (Section 4.2.2). Additionally, a stress rate of 70 MPa/sec (20 mm/min) is selected to induce fracture within a few seconds while the failure stress within the loading ring for the 150 x 150 x 5.95 mm fully toughened glass specimens is given by Eq. 6.3 based on the results of the numerical model that was developed in Section 4.2.2:

$$\sigma = 0.0173 \cdot P \qquad \text{(Eq. 6.3)}$$

Chemically toughened glass

Section 4.2.3 confirms that the Coaxial Double Ring set-up is not suitable for thin high strength glass as stress concentrations appear underneath the boundaries of the loading ring when certain displacement limits are exceeded. A variation of the Coaxial Double Ring set-up which involves the introduction of a spreader plate above the glass specimens was therefore, proposed to create an almost equibiaxial stress within the loading ring area in Section 4.2.3.

The 4.75 mm thick, aluminium, spreader plates of Grade 6082T6 and 7075T6, which were proposed in Section 4.2.3, are sufficient for the destructive testing of the sand abraded chemically toughened glass (CT-SA) and as-received chemically toughened glass (CT-AR) respectively in this study; failure loads below $P < 20$ kN and $P < 60$ kN are expected for the former and the latter respectively. The high stress rate chosen to induce fast fracture is 50 MPa/sec (30 mm/min) for CT-SA and 90 MPa/sec (45mm/min) for CT-AR. The mean failure stress within the loading ring is given by Eq. 6.4a for CT-SA up to $P \approx 20$ kN / $\delta_{applied} \approx 1.4$ mm, and Eq. 6.4b for CT-AR up to $P \approx 60$ kN and $\delta_{applied} \approx 3$ mm. These equations are based on the numerical models which were developed in Section 4.2.3 for Set-up B.

$$\sigma = 0.0075 \cdot P \text{ and } \sigma = 0.0068 \cdot P \qquad \text{(Eq. 6.4a-b)}$$

6.3.3 Data processing methods

The experimental failure load was converted to failure stress using Eq. 6.2 – Eq. 6.4 depending on the type of glass. High stress rates induce fracture within a few seconds, thereby minimizing the influence of sub-critical crack growth as shown in Section 4.3. Nevertheless, sub-critical crack growth can occur. This can be normalised as follows converting failure stress to a 60 sec equivalent stress (Fig. 2.24):

$$\sigma_{f,eq} = -\sigma_r + \left(\sigma_f + \sigma_r\right) \cdot \left[\frac{t_f - t_r}{\left(t_{ref} - t_r\right) \cdot \left(n+1\right)}\right]^{1/n} \qquad \text{(Eq. 6.5)}$$

where: σ_f: the failure stress, σ_r: the residual surface compression, $\sigma_{f,eq:}$ the equivalent stress for the reference time period of 60 sec, t_f: the time to failure during testing, t_r: the time when tensile stresses exceeds the residual surface compression, t_{ref}: the equivalent time of 60 sec and n: the static fatigue constant.

However, it is not possible to apply Eq, 6.5 to chemically toughened glass because its residual surface stress is unknown. Additionally, there are some uncertainties in applying Eq. 6.5 to sand abraded fully toughened glass because the residual stress at the flaw tips (which were induced by the sand abrasion) is not known. The latter applies, even when fractographic analysis data are

obtained, as the critical flaw depth is expected to have grown under the influence of sub-critical crack growth.

Therefore, the failure stress data for all specimens in this Chapter is not converted to an equivalent stress to remove the above mentioned uncertainties. Even though this means that sub-critical crack growth has been neglected in this Chapter, it is not expected to cause any significant change in the results; this is true if one considers that the difference in failure strength after accounting for sub-critical crack growth was similar in all specimens for as-received annealed glass (Fig. 6.2) and ranged between $24.8\% \le \left(\sigma_f - \sigma_{f,60}\right)/\sigma_f \le 26.6\%$. Errors incurred by neglecting sub-critical crack growth in the other test series of this Chapter are expected to be similar to that in annealed as-received glass and are therefore, considered negligible for the given stress rates. However, when lower stress rates are used during the destructive tests these errors are expected to increase and therefore, this approach would no longer be valid.

The fracture stress data were subsequently fitted to a 2-parameter Weibull distribution with a weighted least squares regression method (details shown in Chapter 4). The goodness-of-fit was evaluated with the Anderson Darling method and a confidence level of 95%.

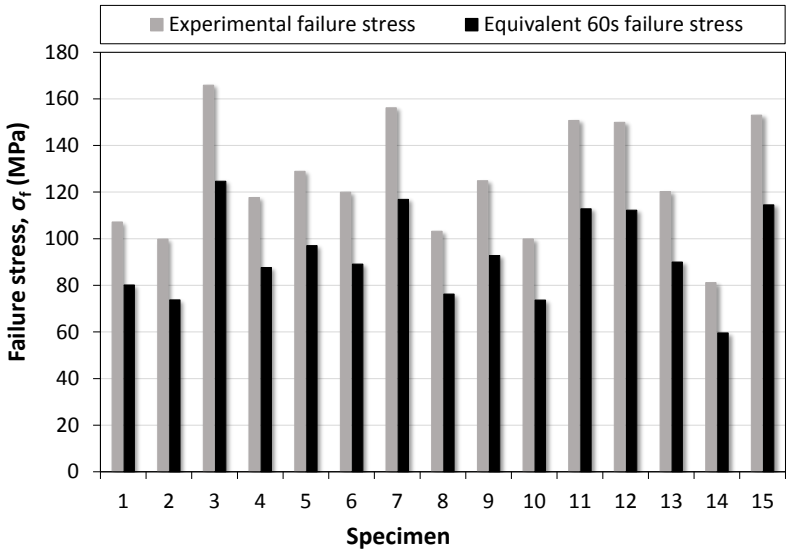

Fig. 6.2: Experimental and 6s equivalent failure stress for annealed as-received glass.

6.4 Results and Discussion

6.4.1 Microscopy

Micrographs of the surface were obtained prior and after the artificial ageing for all three types of glass (Fig. 6.3). The surface of as-received annealed (Fig. 6.3a) and chemically toughened glass (Fig. 6.3g) are almost defect free at a magnification of 100x whilst as-received fully toughened glass has multiple digs on its surface (Fig. 6.3d).

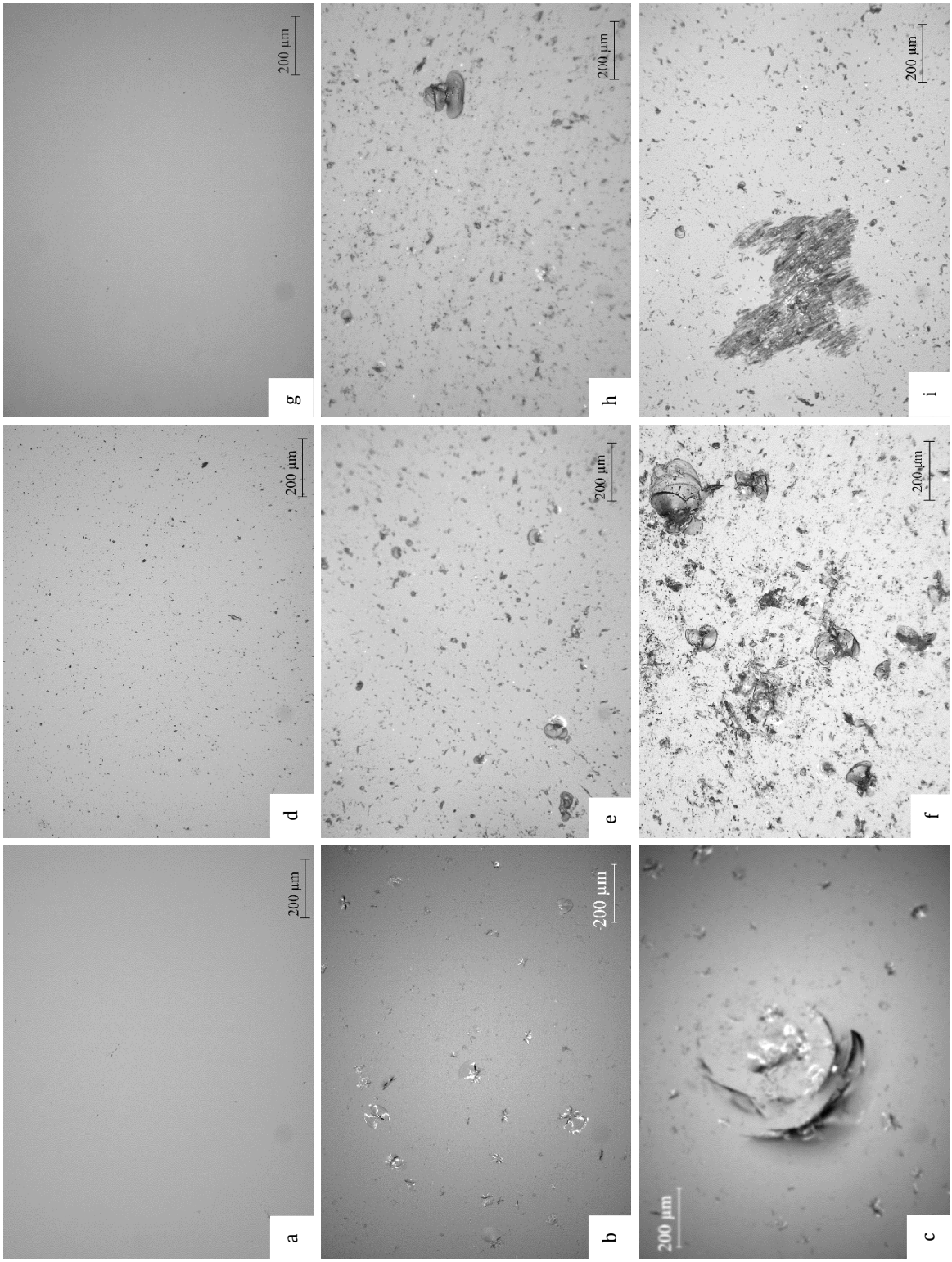

Fig. 6.3: Micrographs of as-received surface, sand impacts and gravel impacts in: (a-c) annealed; (d-f) fully toughened and; (g-i) chemically toughened glass.

Artificial ageing with sand abrasion results in digs and some lateral cracks in annealed (Fig. 6.3b), fully toughened (Fig. 6.3e) and chemically toughened (Fig. 6.3h) glass and therefore, their surface damage belongs to the micro-ductile or the micro-cracking regime. Flaws induced by impact of sand grains are similar in all types of glass (Fig. 6.3b, e & h). However, the flaws induced by the larger gravel particularly on the annealed and fully toughened glass differ from those in the chemically toughened glass: (a) digs surrounded by lateral cracks that intersect with the glass surface are found in annealed and fully toughened glass; these flaws are larger in annealed (Fig. 6.3c) than fully toughened glass (Fig. 6.3f), and; (b) gravel impacts do not form digs in chemically toughened glass but result in abrasive damage (Fig. 6.3i).

6.4.2 Fracture strength

Table 6.2 shows the fracture strength statistics for annealed, fully toughened and chemically toughened glass in as-received and artificially aged form. All series showed acceptable goodness-of-fit and therefore, the Weibull distribution is successful in describing the strength data. Unsurprisingly, as-received chemically toughened glass is the strongest, followed by fully toughened glass and subsequently annealed glass; the strength of as-received fully toughened glass (FT-AR) and chemically toughened glass is 191% and 321% respectively larger than annealed glass (AN-AR) at mean probabilities of failure (P_f=0.50, Table 6.2). This could be attributed to the combined effect of the residual surface compression and the thermal healing of flaws during the toughening process of toughened glasses [13].

Table 6.2: Salient results of the Weibull statistics analysis for fracture strength data of all series.

Glass	Weibull parameters				Fractile values			
	β	θ	p_{AD}	CV	$\sigma_{f,0.008}$	$max\ \sigma$	$min\ \sigma$	$\sigma_{f,0.5}$
		MPa	%	%	MPa	MPa	MPa	MPa
NA-AN$_a$	3.4	41.7	9.7	32.6	10.0	61.1	24.1	37.4
NA-AN$_b$	4.2	57.5	79.6	26.7	18.4	75.8	29.4	52.8
AN-AR	5.0	96.4	44.1	22.9	36.8	124.6	59.6	89.6
AN-SA	6.2	27.6	58.0	18.8	12.7	33.3	16.3	26.1
FT-AR	7.6	241.0	57.8	15.5	128.0	272.3	167.0	229.7
FT-SA	15.8	141.7	66.7	7.8	104.3	150.6	122.9	138.4
CT-AR	6.3	408.9	6.0	18.6	189.6	454.4	242.4	385.7
CT-SA	1.6	80.4	59.6	65.14	3.7	126.1	6.3	63.7

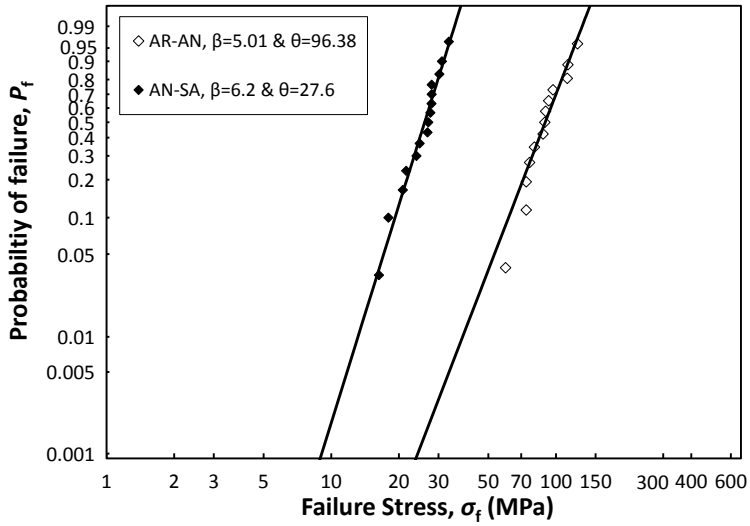

(a)

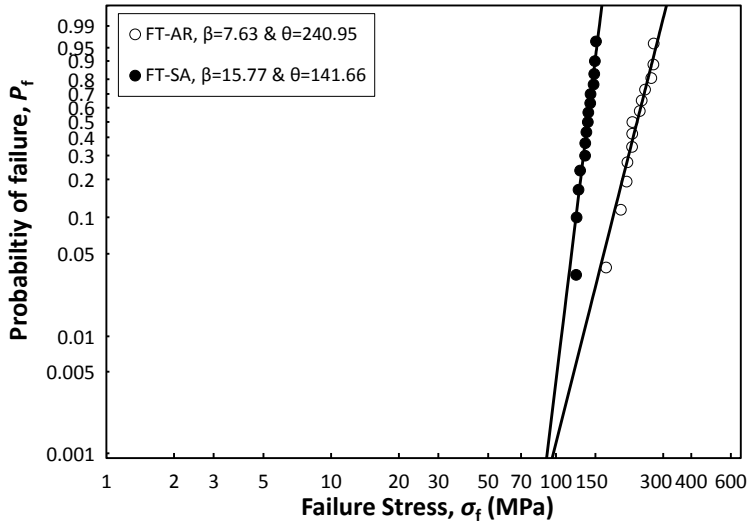

(b)

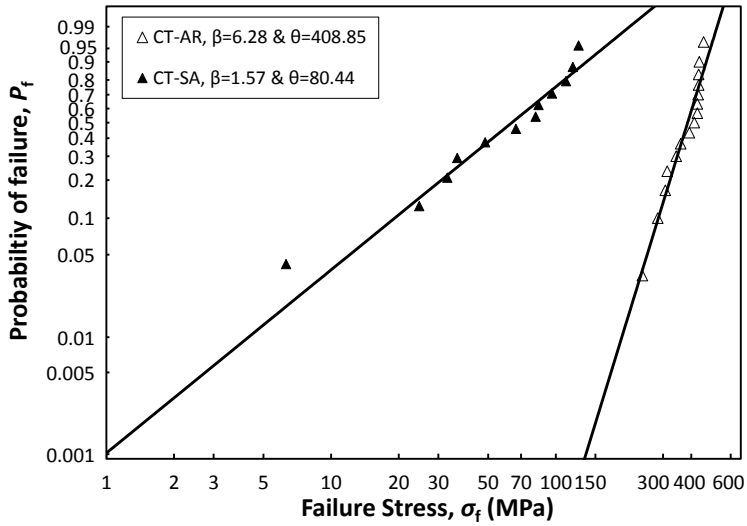

(c)

Fig. 6.4: CDF for as-received & abraded: (a) annealed; (b) fully toughened and; (c) chemically toughened glass.

Strength reduction is evident in all types of glass after sand abrasion. In particular, annealed glass suffers a 61% and 68% reduction in strength for P_f=0.008 and P_f=0.50 respectively after artificial ageing (Fig. 6.4a). Fully toughened glass had a better response than annealed glass after artificial ageing showing a reduction of 19% and 40% in as-received strength for P_f=0.008 and P_f=0.50 respectively (FT-SA, Fig. 6.4b). This better performance is a result of the residual surface stress and the large case depth of fully toughened glass. Whereas, chemically toughened glass had the worst performance among all types of glass despite its high degree of toughening. In particular, it suffered a 98% and 83% reduction in as-received strength for P_f=0.008 and P_f=0.50 respectively (CT-SA, Fig. 6.4c). Additionally, the strength of sand abraded chemically toughened glass (CT-SA) at low probabilities of failure (P_f=0.008) is even lower than that of annealed sand abraded glass (AN-SA).

It is noteworthy to mention that all chemically toughened as-received specimens failed at loads below P < 67 kN and that all chemically toughened sand abraded specimens at loads below P < 19 kN; this validates the initial assumption in Section 6.3.2 that an almost uniform equibiaxial stress field can achieved during the destructive testing of the chemically toughened glass specimens for the selected set-ups.

6.4.3 Post fracture optical microscopy

Post-fracture optical microscopy was successfully performed for all of the annealed and fully toughened artificially aged glass specimens but only on a small percentage of the sand abraded chemically toughened glass. In general, chemically toughened glass is expected to fail in fairly large fragments, typically larger than fully toughened glass (Fig. 6.5a). However, the high loads, that were required for the thin chemically toughened glass in this study, to overcome the residual surface compression, increase the elastic energy that is stored within the specimen. This energy is released upon fracture and is dissipated in opening new crack surfaces, resulting in a very dense fragmentation pattern (Fig. 6.5b).

Therefore, post-fracture microscopy was only possible for the few chemically toughened glass specimens that failed at the “lower” stress tail of the Weibull distribution and thereby resulted in “larger” fragments. Specimens that fail at the lower stresses do so, because they have relatively deeper flaws on their surface. Therefore, post-fracture microscopy in those specimens is biased because it will only reveal the upper range (maximum depth) of critical flaws.

Results reveal average critical flaw depths after sand abrasion of 472 μm (132 ≤ α ≤ 1370 μm) in annealed glass, 127 μm (72 ≤ α ≤ 218 μm) for fully toughened glass and 96 μm (71 ≤ α ≤ 132 μm) for chemically toughened. Typical micrographs of the critical flaws are shown in Fig. 6.6a-i, representing the largest, average and smallest flaw for each type of glass.

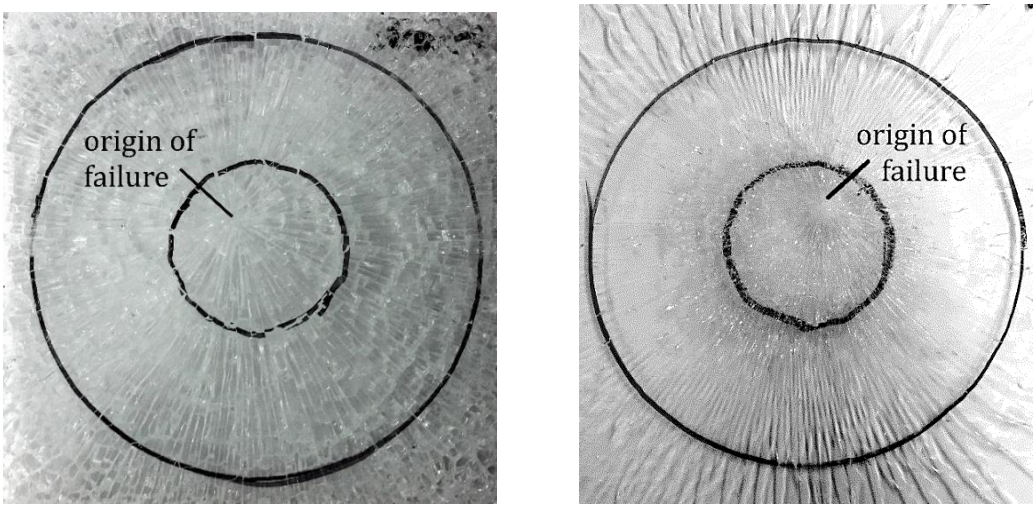

(a) (b)

Fig. 6.5: Fragmentation of sand abraded: (a) fully toughened and; (b) chemically toughened glass.

Statistical analysis of the flaw depths followed by fitting the data to a two–parameter Weibull distribution (Fig. 6.7) producing acceptable goodness-of-fit (data shown in Appendix B, Table B3b). Larger critical flaws were therefore, found for annealed, followed by fully toughened and then chemically toughened glass. This implies that the degree of toughening/amount of residual surface stress affects the critical flaw depth for the same artificial ageing procedure and thereby, the abrasive resistance of glass. In particular, higher residual surface stress results in smaller flaw depths under the same ageing conditions.

Critical flaws of 95 μm (P_o=0.50), are expected to eliminate the beneficial effects of the surface compression for chemically toughened glasses whose case depths typically range between 40 ≤ d_c ≤ 90 μm [21,26,27]. However, the statistical analysis for chemically toughened glass involved only the largest critical flaws, because the fragmentation pattern in the specimens that failed at higher loads was too dense to permit fractographic analysis, and is therefore, conservative. Therefore, flaws could, but are not always expected to, completely remove the favourable effect of the residual surface stress. Fully toughened glass showed a better response than chemically toughened glass; its residual surface stress was only reduced by 11% using Eq. 6.1 at the flaw tip for the mean flaw depth of z=0.122 mm (P_o=0.50). This smaller reduction in residual stress is a result of the larger case depth of the fully toughened glass (d_c=1.21 mm).

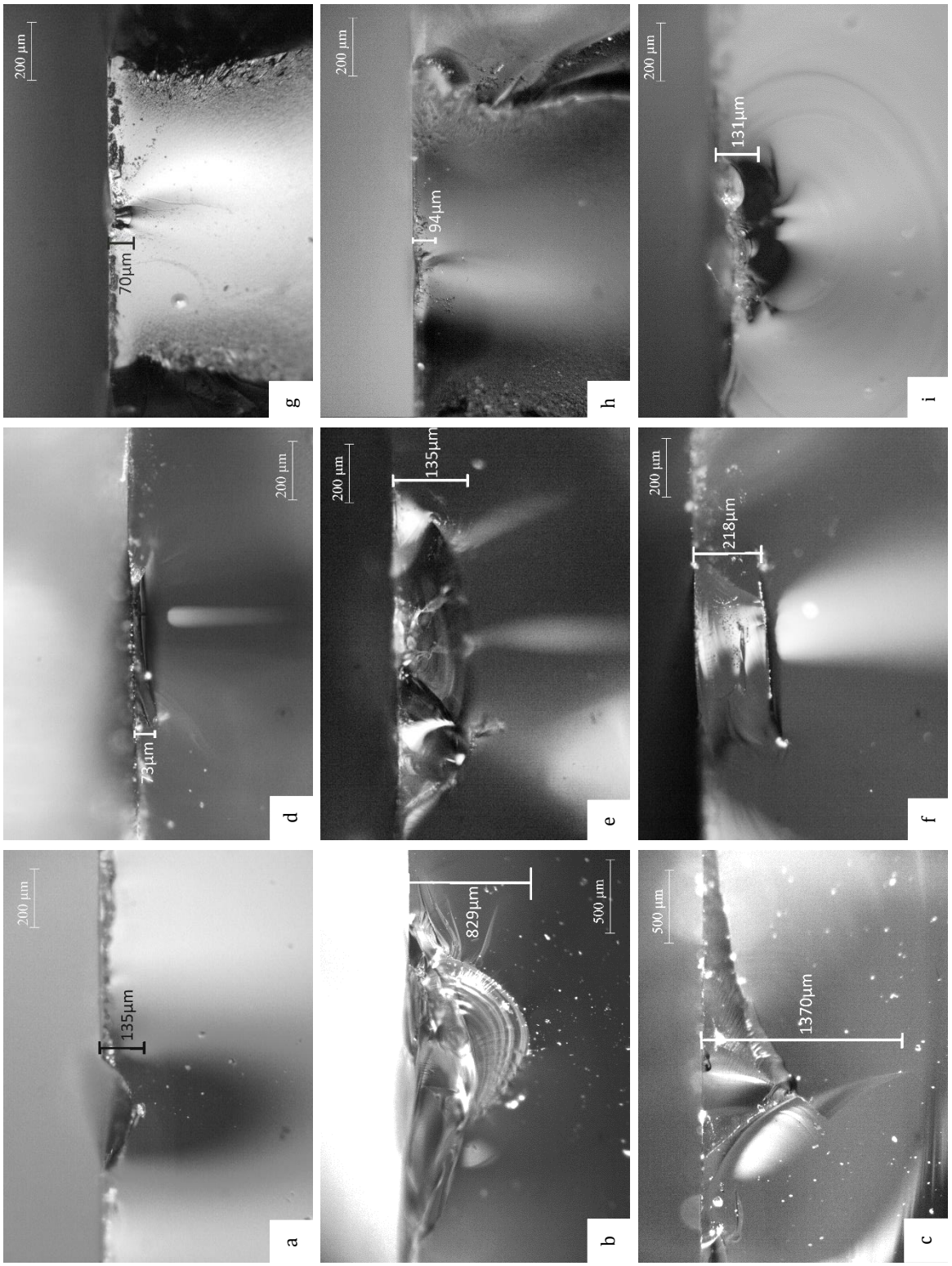

Fig. 6.6: Critical flaws in abraded: (a-c) annealed; (d-f) fully toughened and; (g-i) chemically toughened glass (max., mean and min. depth).

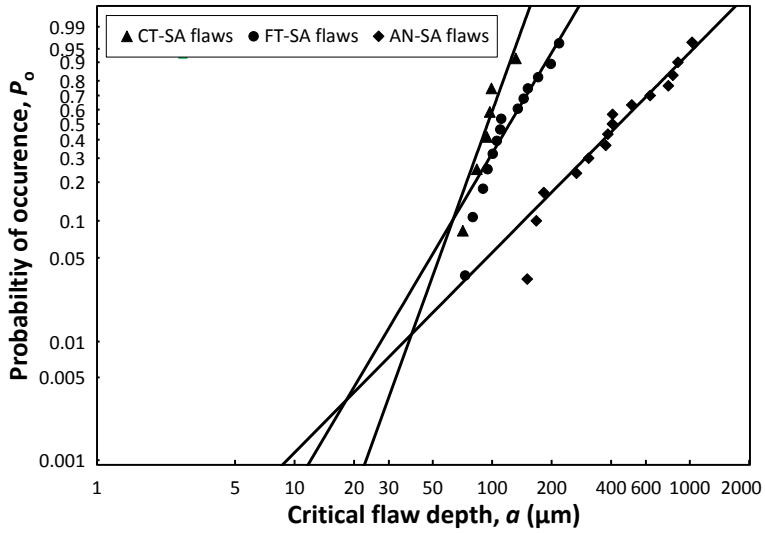

Fig. 6.7: CDF of flaw depths for annealed, fully toughened and chemically toughened, sand abraded glass.

The mean flaw depths (P_o=0.50) of fully toughened ($\alpha_{mean,FT}$=122 µm) and annealed glass ($\alpha_{mean,AN}$=439 µm) can be further used to predict the difference in strength between annealed and fully toughened sand abraded glass as follows:

$$\frac{\sigma_{f,FT-SA}}{\sigma_{f,AN-SA}} = \frac{\sigma_r + \dfrac{K_{IC}}{Y \cdot \sqrt{\pi \cdot a_{FT}}}}{\dfrac{K_{IC}}{Y \cdot \sqrt{\pi \cdot a_{AN}}}} = 4.63 \qquad \text{(Eq. 6.6a)}$$

where K_{IC}=0.75MPa m$^{1/2}$: the fracture toughness; Y=0.61: the geometry factor for gravel induced flaws (Section 4.3.3) and; σ_r=89.03 MPa: the residual surface stress for fully toughened glass.

This adequately (12% difference) tallies with the ratio of the mean strengths (P_f=0.50) of the statistical analysis (Table 6.2) after abrasion for fully toughened and annealed glass as shown in Eq. 6.6b. Mean values are selected in this case to exclude any sensitivities of the Weibull distribution to its tails.

$$\frac{\sigma_{f,0.50,FT-SA}}{\sigma_{f,0.50,AN-SA}} = \frac{138.4}{26.1} = 5.30 \qquad \text{(Eq. 6.6b)}$$

The residual surface compression in toughened glass has a two-fold effect: (a) increase of glass strength as a result of the surface compression that prevents flaws from growing when $\alpha < d_c$, (Fig. 2.27); (b) increase in the abrasive resistance of the glass; as indicated above, flaw depths induced with an identical ageing method are smaller for higher levels of residual surface compression.

The influence of these effects (a and b) is quantified below for fully toughened glass. The ratio of the expected strength for fully toughened abraded glass (i.e. the mean strength of annealed

abraded glass plus the residual surface compression of fully toughened glass at a flaw depth $\alpha_{mean,FT}$=122 μm) over the obtained mean strength for fully toughened abraded glass (Eq. 6.7) is used to indicate the contribution of the residual surface compression on the increased strength of fully toughened glass.

$$\frac{\sigma_{f,FT,expected}}{\sigma_{f,obtained}} = \frac{\sigma_{f,0.50,FT-AN} + \sigma_r(\alpha)}{\sigma_{f,0.50,FT-SA}} = 0.76 \quad \text{(Eq. 6.7)}$$

Therefore, the increased strength of fully toughened glass can be attributed by 76% to its residual surface compression (effect a) while the remaining 24% can attributed to its higher abrasive resistance (effect b).

Some further glass strength prediction calculations are shown in Section 6.4.4 linking strength results with residual surface stress measurements and fractographic analysis for each specimen.

6.4.4 Toughened glass strength prediction

The fractographic data and the residual surface compression of fully toughened glass are used in this section to predict the strength of fully toughened glass. Even though this investigation is not the main aim of this Chapter, it is of high importance because it provides a means of evaluating the strength of damaged glass panels in terms of their safe use / need for replacement. Analytical research is therefore, undertaken here to evaluate whether flaws of known depth and residual stress profiles are adequate to accurately predict glass strength for fully toughened glass using Eq. 6.8:

$$\sigma_f + \sigma_r(a) = \frac{K_{IC}}{Y \cdot \sqrt{\alpha\pi}} \quad \text{(Eq. 6.8)}$$

where K_{IC}=0.75 MPa m$^{1/2}$: the fracture toughness for soda lime silica glass, σ_f: the failure stress; Y=0.610: the geometry factor for the gravel induced flaws shown in Fig. 6.6 (this value is selected based on the linear elastic fracture mechanics approach for gravel impacts in SA21, shown in Section 4.3.2 and discussed in Section 4.3.3); α: the depth of the critical flaw (obtained for each specimen through fractographic analysis in Section 6.4.3) and; σ_r=-89 MPa: the residual surface compression (this value was adjusted individually at the measured flaw depth for each specimen using Eq. 6.1 and a depth z equal to the flaw depth α from the fractographic data, values shown in Table 6.3).

Fig. 6.8 shows that the analytical prediction for the average strength of fully toughened glass is in agreement with the average failure stress that was reported experimentally (3.7% difference). The highest difference between these values range individually for every specimen between

$-18.4\% \le \left(\sigma_{f,\exp} - \sigma_{f,an.}\right) / \sigma_{f,\exp} \le 9.8\%$. The difference between analytical and experimental results could be potentially attributed to the small influence of sub-critical crack growth which has been discussed previously in Section 6.3.3 and/or rounding errors during the fractographic analysis for the determination of the critical flaw depths.

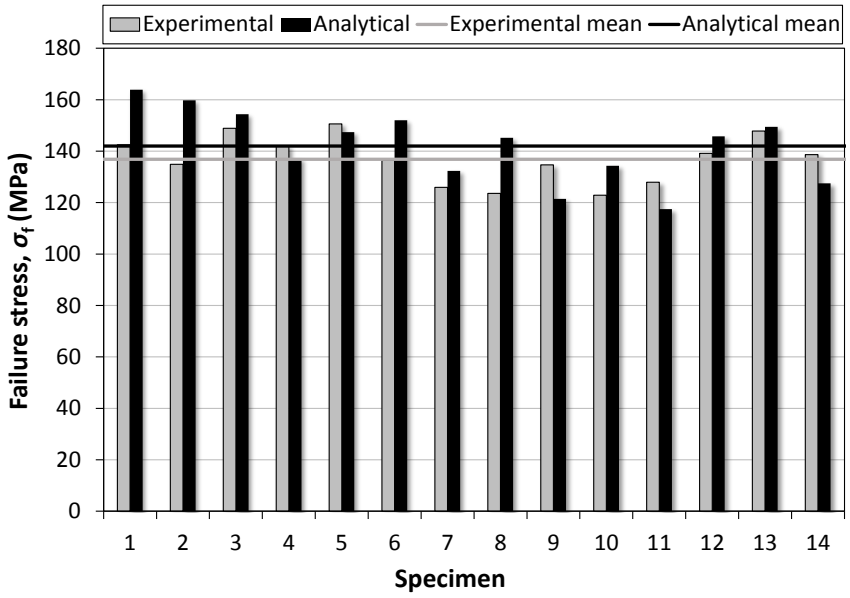

Fig. 6.8: Experimental and analytical results for strength of fully toughened glass.

Table 6.3: Toughened glass strength prediction: input data and results.

Specimen	$\sigma_{f,exp}$	K_{IC}	Y	$\sigma_{r,z=0}$	$\sigma_{r,z=ai}$	$\sigma_{f,an.}$
FT-SA1	142.52	0.75	0.610	-89	-82.67	163.88
FT-SA2	134.90	0.75	0.610	-89	-82.09	159.77
FT-SA3	148.88	0.75	0.610	-89	-81.21	154.37
FT-SA4	141.97	0.75	0.610	-89	-77.41	137.16
FT-SA5	150.60	0.75	0.610	-89	-79.88	147.37
FT-SA6	136.43	0.75	0.610	-89	-80.80	152.03
FT-SA7	125.91	0.75	0.610	-89	-76.00	132.34
FT-SA8	123.56	0.75	0.610	-89	-79.41	145.22
FT-SA9	134.67	0.75	0.610	-89	-72.16	121.46
FT-SA10	122.86	0.75	0.610	-89	-76.60	134.33
FT-SA11	127.93	0.75	0.610	-89	-70.51	117.47
FT-SA12	139.12	0.75	0.610	-89	-79.53	145.74
FT-SA13	147.84	0.75	0.610	-89	-80.30	149.45
FT-SA14	138.63	0.75	0.610	-89	-74.40	127.48

The analysis presented in this section indicates that if non-destructive evaluation means to determine the flaw depth of installed / as-received glass were to be produced, the prediction of glass strength would be possible. This would eventually allow the evaluation of installed damaged glass panels and potentially reduce costs in cases where replacement is currently the only option.

6.5 Conclusions

The aim of this chapter was to investigate the strength of aged annealed, fully toughened and chemically toughened glass. This investigation involved pre- and post-fracture optical microscopy and destructive tests in a Coaxial Double Ring (CDR) set-up for annealed and fully toughened glass and a variation of the Coaxial Double Ring set-up, including a spreader plate above the glass specimen, for chemically toughened glass.

Unsurprisingly, the evaluation of the 3 types of glass in their as-received form showed that chemically toughened glass is the strongest, followed by fully toughened glass and annealed glass. However, the favourable effect of the residual surface compression of toughened glass was reduced after abrasion which was equivalent to 20-year erosive action. In particular, the beneficial surface compression can be completely eliminated in chemically toughened glass as the flaws that are introduced by the artificial ageing, can be significantly deeper than its case depth. In fact, chemically toughened glass suffered a 98% reduction in as-received strength at low probabilities of failure (P_f=0.008). Additionally, a 61% reduction in as–received strength was reported for annealed glass (P_f=0.008) whilst fully toughened glass had the best strength performance after ageing as it only suffered a 19% reduction in as-received strength at low probabilities of failure (P_f=0.008). This is due to the larger case depth that is typical in fully toughened glasses; the case depth of fully toughened glass in this study was an order of magnitude larger than the depth of the surface flaws.

However, despite its very high reduction in strength, chemically toughened glass showed the largest resistance to surface abrasion during the artificial ageing; flaws introduced by gravel ($8.0 \leq GSR \leq 9.5$ mm) resulted in deeper flaws in annealed glass, followed by fully toughened glass and finally, chemically toughened glass. This suggests that the level of residual surface compression affects the depth of critical flaws introduced by erosive ageing and therefore, the erosive resistance of the glass.

The findings of this Chapter indicate that fully (thermally) toughened glass could be safely used for load bearing applications such as cold bent applications, even when exposed to ageing. However, the reduction in strength after ageing should be carefully considered during the design process. On the other hand, the significant strength degradation in chemically toughened glass suggests that it should be used with caution in load bearing applications exposed to ageing

mechanisms. The limitations of chemically toughened glass could be potentially addressed with bi-tempered glass [28] whose enhanced properties of high residual surface compression and relatively large case depth could potentially outperform other toughened glasses. Alternatively, chemically toughened glass could be used in load bearing applications if the glass surfaces are not directly exposed to erosive / scratching action, e.g. by means of a protective surface. Further investigation is however, needed to evaluate the performance of bi-tempered glass and to identify safe service life limits for all types of glass exposed to different levels of exposure.

7. CONCLUSIONS AND FUTURE WORK

7.1 Summary & Conclusions

Cold bending has recently emerged as an alternative method for creating curvilinear glass forms by bending toughened glass plates at ambient conditions. The method is largely thought to produce curved glass surfaces with significantly better optical quality than heat bending methods and to minimize the high energy requirements and costs that are typically associated with the latter. The aim of this thesis was to develop the understanding of cold bent glass plates and in particular, to investigate their potential to fulfil stability and serviceability criteria during the cold bending process and strength criteria after exposure to ageing mechanisms. Several outcomes and conclusions have been reached through the experimental, numerical and analytical investigations carried out in this thesis to achieve this aim. These are briefly discussed in the following paragraphs.

The stability/serviceability of monolithic toughened glass plates during the cold bending process were investigated in Chapter 3, in which plates were experimentally and numerically bent at ambient conditions in double curved anticlastic shapes with out-of-plane forced displacements and corner supports. A parametric analysis involving boundary conditions, geometrical characteristics of the glass plate, orientation / initial imperfections of the plate and load locations revealed that local and global instabilities could be triggered during the cold bending process. Even though these instabilities do not trigger fracture / safety issues, they could result in serviceability limits. Indeed, local instabilities, attributed to membrane effects and boundary conditions, result in a previously unreported, sinusoidal distortion along the support axis that has now been termed “cold bending distortion”. The amplitude of the cold bending distortion defines the optical quality of cold bent glass. This indicates that the optical quality of cold bent glass is not necessarily superior to that achieved with conventional heat bending methods, as is commonly thought. However, cold bending distortions are not triggered or are not perceptible when certain displacement limits are respected. For this reason, a user-friendly set of guidelines was developed in this thesis for plates of different geometrical characteristics to assist designers and manufacturers in achieving an acceptable optical quality for cold bent glass plates. Deviations from the desired curved shape can be also caused by global instabilities, attributed to the combined effect of loading direction and initial imperfections due to self-weight. These instabilities trigger a sudden change of curvature as the plate buckles from a double curved anticlastic configuration to a double curved synclastic configuration. However, such instabilities can be avoided when initial imperfections are negligible.

It was also found that these phenomena equally apply to fully toughened and chemically toughened monolithic glass plates; the level of residual surface compression does not influence the mechanical response of the plate but only permits a higher level of cold bending i.e. smaller radii of curvature, prior to fracture.

Cold bent glass plates are subjected to permanent bending moments; the ability to preserve their strength after exposure to ageing mechanisms is therefore, an essential requirement to establish their safe use in the façade industry. To investigate this, research was undertaken at a material level to characterise the strength of aged glass. In order to perform these glass strength investigations in a systematic manner, it was necessary to address uncertainties associated with glass strength and artificial ageing techniques in Chapter 4 and Chapter 5 respectively, before establishing the strength of aged annealed and aged toughened glass in Chapter 6.

Chapter 4 aimed to address uncertainties that could arise on the estimation of glass strength and involve investigations on the method of destructive testing, the influence of sub-critical crack growth during the destructive tests, the required number of specimens and the method for the statistical analysis of glass strength data that are needed in order to obtain reliable strength predictions. This was achieved through numerical analysis, statistical analysis, linear elastic fracture mechanics and fractographic investigations. The findings confirmed that a Coaxial Double ring set-up is suitable for annealed and fully toughened glass but it can lead to stress concentrations in thin chemically toughened glass. For this reason, an optimised Coaxial Double Ring set-up was developed in Chapter 4 by introducing a spreader plate between the chemically toughened glass specimen and the loading ring to eliminate these stress concentrations. Additionally, it was shown that using a high stress rate (20 MPa/sec for annealed glass) during the destructive testing can minimize or even eliminate the influence of sub-critical crack growth; this circumvents the need to test in a vacuum or dry nitrogen chamber and thereby reduces experimental complexity to achieve the same result. Additionally, 15 glass specimens were found to be sufficient for glass strength analysis; this number represents a balance between accuracy / width of confidence intervals at low probabilities of failure (typically associated with design values) and time / cost related matters. Finally, it was shown that the selected statistical estimation method affects the accuracy of the cumulative distribution function when fitting glass strength data to a 2-parameter Weibull distribution; a weighted least squares regression method using Faucher and Tyson's weight function and Hazen's estimator was found to improve goodness-of-fit compared to commonly used methods like the Good Linear Unbiased Estimators prescribed in EN12603-2002 [162] and the Maximum Likelihood Estimation prescribed in ASTM C1239-13 [163].

Chapter 5 in turn aimed to identify an artificial ageing method that introduces equivalent levels of damage to those found in naturally aged glass because a reliable ageing standard has yet to be established. An abrasion method adopted from that described in DIN 52348 was found to be more representative than scratching for the naturally aged glass used in this thesis. The investigation revealed that even though the parameters in DIN 52348 greatly overestimate strengths at design level, careful selection of artificial ageing parameters in the falling abrasive set-up can achieve similar damage on the surface of as-received glass with that found in naturally aged glasses. These results were subsequently condensed into a user-friendly procedure that permits the selection of artificial ageing parameters to represent different levels of exposure to erosive action. The significance of this is that a more efficient use of glass and more effective glass treatments could eventually be achieved by selecting the glass and glass treatment that are tailored for the specific application and the corresponding surface damage expected during its service life.

Finally, Chapter 6 aimed to evaluate the strength of aged glass with different treatments and therefore, different levels of residual surface compression; these are: soda lime silica annealed, soda lime silica fully toughened and alumino-silicate chemically toughened glass. The glass specimens were evaluated in their as-received and artificially aged states with microscopy, destructive tests (Coaxial Double Ring set-up for annealed and fully toughened glass and the optimised Coaxial Double Ring set-up of Chapter 4 for chemically toughened glass) and fractographic analysis to evaluate strength degradation. The artificial ageing parameters were selected based on the procedure that was developed in Chapter 5 for the artificial ageing of glass.

The findings suggest that the level of residual surface compression in glass is proportional to its erosive resistance; smaller critical flaw depths were found for chemically toughened glass, followed by fully toughened and subsequently annealed glass under the same ageing procedure. However, the strength of toughened glass is not only related to the depth of critical flaws, but is also associated with its case depth (i.e. the depth of residual surface compression). The superficial case depth of chemically toughened glass results in elimination of its high residual surface compression and therefore, exhibits similar, if not lower, strength than annealed glass with a 20-year equivalent of erosive action. This raises questions on the safe use of chemically toughened glass in load bearing applications when the installed glass is exposed to ageing mechanisms (erosive and / or scratching action). The limitation of chemically toughened glass could be potentially addressed if chemically toughened glass is not directly exposed to ageing mechanisms in load bearing applications (e.g. by using a protective layer on the surface of chemically toughened glass) or by substituting chemically toughened glass with bi-tempered glass that has a similar residual surface compression but a larger case depth. Fully toughened glass exhibits a significantly smaller reduction in strength (19%) than chemically toughened glass as a result of

its larger case depth. This level of strength reduction can be taken into account with careful planning and design strategies without creating safety concerns.

Overall, the research undertaken in this PhD thesis, has developed the understanding of cold bent glass surfaces showing that **high quality cold bent glass is feasible within certain applied displacement limits, but glass strength degradation, after exposure to ageing mechanisms, is not trivial and should not be neglected;** cold bending can be successfully implemented in fully toughened glass and chemically toughened glass during the production process. However, due to the limitations associated with the strength of chemically toughened glass under exposure to ageing mechanisms, cold bending should be best limited to fully toughened glass. This applies until careful replacement strategies / strict service life limits are developed to suit the level of exposure for chemically toughened glass.

7.2 Future work

The following are identified as potential areas of research that require further investigation:

A) Cold bending of glass

Bending process: A detailed investigation of the mechanical performance of monolithic cold bent glass during the bending process was performed in this thesis however, further research should be undertaken at a fundamental level to investigate the mechanical performance of laminated cold bent glass. This would involve characterisation of its optical quality and stability during the bending process as was done in Chapter 3 for monolithic glass and additionally investigation of the viscoelastic time/temperature dependent behaviour of the interlayer and the associated creep. Research should also focus on the cold bending of insulated glass units to identify the most effective method of bending i.e. bending of the glass prior or following its bonding to the frame and potential issues associated with the curvature in the plate's edges and their bonding to the frame.

Service life: Despite the characterisation of the stability of cold bent glass during the bending process and their strength degradation after ageing, research should also cover its strength and stability during its service life. This involves investigation of the influence of: (a) long term loads on the sub-critical crack growth of flaws in monolithic glass and; (b) time dependent loading and temperature loads on creep and stress relaxation phenomena in laminated glass due to the viscoelastic response of the interlayer. Uncertainties associated with the mechanical performance of adhesives and the integrity of the edge seal in cold bent insulated glass units under temperature cycling and weathering, as well as the energy performance of the unit should be also addressed.

Cold bent glass guidelines: Research from a more applied point of view should be also undertaken on monolithic and laminated cold bent glass plates to form a set of guidelines (to extend those developed in Chapter 3 for the optical quality of cold bent glass), for their stability during service life and ultimate limit state. These guidelines would set: maximum service life loads that the cold bent plates can successfully withstand without stability issues and; maximum limits of curvature/applied displacement for Ultimate limit state analysis. These would be calibrated for glass plates of different treatment/toughening, geometrical characteristics and desired curved shape. The guidelines would also ideally involve different interlayers for cold bent laminated glass to predict maximum temperature loads that the glass can undergo during their service life to successfully maintain its curved shape.

B) Strength of aged glass

Natural ageing of glass: One source of naturally aged annealed glass was investigated in this thesis. However, further fundamental research should be undertaken at a material level to deepen the available knowledge on natural ageing mechanisms of glass and to determine their influence on the strength of glass. This would be achieved by performing similar investigations to those described in Chapter 5, on multiple sources of naturally aged glass, including glass that is exposed to a broad range of erosive and/or scratching action. This would allow extension of the procedure described in Chapter 5 for the artificial ageing of glass, to cover exposure to erosive or scratching action and their possible combinations.

Bi-tempered glass: Further research similar to that described in Chapter 6, should be undertaken to evaluate the performance of bi-tempered glass after ageing. Its advanced properties of high residual surface compression and its large case depth could lead to a superior performance than other toughened glasses and could therefore, prove to be a better choice for load bearing applications that are exposed to ageing mechanisms.

Non-destructive testing and repair of glass: The need for developing reliable non-destructive and repair techniques for glass is a corollary of the significant strength degradation revealed in Chapter 6 for some types of aged glass. Fundamental research is therefore needed in this regard to identify potential non-destructive and repair techniques that can be applied on glass accounting for different types of flaws and / or applications. Non-destructive techniques would allow the assessment of damaged, installed or as-received glass to determine whether replacement is needed whilst repair techniques would permit strength recovery or a halt to strength degradation as a possible alternative to costly replacement.

APPENDICES

Appendix A: Modelling of residual surface stress

Two FORTRAN scripts for incorporating residual stress in an Abaqus numerical model using the SIGINI subroutine for: (a) fully toughened and; (b) chemically toughened glass follow below.

```
A) Subroutine SIGINI(SIGMA,COORDS,NTENS,NCRDS,NOEL,NPT,LAYER,
       KSPT,LREBAR,NAMES)
!-------------------------------------------------------------------------
---
! Subroutine used to define initial stress state.
!
! INPUT
!     COORDS(ncrds)     Array for the initial coordinates of this point
!     NTENS             Number of stresses to be defined (depends on
element type)
!     NCRDS             Number of coordinates
!     NOEL              Element number
!     NPT               Integration point number in the element
!     LAYER             Layer number (for composite shells and layered
solids)
!     KSPT              Section point number within the current layer.
!     LREBAR            Rebar flag. If LREBAR=1, the current integration
point is associated with element rebar. Otherwise, LREBAR=0.
!     NAMES(1)          Name of the rebar to which the current integration
point belongs, which is the name given in the rebar or rebar layer

      INCLUDE 'ABA_PARAM.INC'

      DIMENSION SIGMA(NTENS),COORDS(NCRDS)

      CHARACTER NAMES(2)*80

!     Sigma(1)=σxx, Sigma(2)=σyy, Sigma(3)=σzz, Sigma(4)=τxy, Sigma(5)=τzx,
Sigma(6)=τyz

      Sigma(1) =-28.8*((Coords(3)-2.5)**2)+60
      Sigma(2) = -28.8*((Coords(3)-2.5)**2)+60
      Sigma(3) = 0
      Sigma(4) = 0
      Sigma(5) = 0
      Sigma(6) = 0

      RETURN
      END !subroutine sigini
```

```
B) Subroutine SIGINI(SIGMA,COORDS,NTENS,NCRDS,NOEL,NPT,LAYER,
       KSPT,LREBAR,NAMES)
!-------------------------------------------------------------------------
---
! Subroutine used to define initial stress state.
!
! INPUT
!     COORDS(ncrds)     Array for the initial coordinates of this point
!     NTENS             Number of stresses to be defined (depends on
element type)
!     NCRDS             Number of coordinates
!     NOEL              Element number
!     NPT               Integration point number in the element
!     LAYER             Layer number (for composite shells and layered
solids)
!     KSPT              Section point number within the current layer.
!     LREBAR            Rebar flag. If LREBAR=1, the current integration
point is associated with element rebar. Otherwise, LREBAR=0.
!     NAMES(1)          Name of the rebar to which the current integration
point belongs, which is the name given in the rebar or rebar layer
definition.

      INCLUDE 'ABA_PARAM.INC'

      DIMENSION SIGMA(NTENS),COORDS(NCRDS)

      CHARACTER NAMES(2)*80

!     Sigma(1)=σxx, Sigma(2)=σyy, Sigma(3)=σzz, Sigma(4)=τxy, Sigma(5)=τzx,
Sigma(6)=τyz

      IF (Coords(3) .GT. 0.0 .AND. Coords(3) .LT. 0.1) Then
      Sigma(1)=3700*Coords(3)-370

      Else IF (Coords(3) .GT. 4.9 .AND. Coords(3) .LT. 5.) Then
      Sigma(1)=-3700*Coords(3)+18130

      Else IF (Coords(3) .GT. 0.1 .AND. Coords(3) .LT. 4.9) Then
      Sigma(1)=7.7

      END IF

      IF (Coords(3) .GT. 0.0 .AND. Coords(3) .LT. 0.1) Then
      Sigma(2)=3700*Coords(3)-370

      Else IF (Coords(3) .GT. 4.9 .AND. Coords(3) .LT. 5.) Then
      Sigma(2)=-3700*Coords(3)+18130

      Else IF (Coords(3) .GT. 0.1 .AND. Coords(3) .LT. 4.9) Then
      Sigma(2)=7.7

      END IF

      Sigma(3)=0
      Sigma(4)=0
      Sigma(5)=0
      Sigma(6)=0

      RETURN
      END !subroutine sigini
```

Appendix B: Raw strength data

The raw strength, time to failure and critical flaw depth data used in: (B1) Section 4.4 and Chapter 5; (B2) Section 4.5 and; (B3) Chapter 6, follow below.

Table B1a: Raw strength data for annealed glass (as-received, sand abraded, scratched and naturally aged used in Section 4.4 & Chapter 5).

k	***k*=10**	***k*=11**		***k*=12**		***k*=13**		***k*=14**							
a/a	**AR**	**SA8**	**SA25**	**SA6**	**SA11**	**NA-b**	**SA9**	**SA2**	**SA5**	**SA7**	**SA12**	**SA13**	**SA16**	**SA18**	**SA19**
1	128.3	72.0	29.0	60.4	68.6	62.9	66.4	60.7	57.7	73.1	55.0	52.8	51.0	45.0	50.3
2	141.4	74.6	30.0	68.9	64.1	60.3	62.2	64.8	73.7	63.3	54.2	61.0	54.1	42.7	47.5
3	129.7	70.5	30.1	76.2	63.8	88.7	62.2	65.6	73.4	71.6	55.3	55.9	52.0	38.7	42.9
4	136.8	64.6	31.8	72.6	64.9	88.0	69.8	69.0	68.7	65.7	54.0	56.2	53.7	38.0	48.7
5	154.4	79.0	30.0	70.7	65.7	80.0	63.2	66.2	56.1	68.3	53.4	64.4	54.1	40.0	44.8
6	165.5	70.5	21.4	69.6	65.1	93.9	73.9	61.2	70.2	66.4	57.4	59.5	52.6	41.0	46.6
7	158.6	68.7	26.6	65.3	59.3	43.1	69.6	65.5	68.5	65.1	53.2	63.5	50.1	42.0	48.7
8	150.0	72.8	25.7	70.5	63.3	71.9	65.1	60.5	70.4	72.0	54.3	63.4	53.9	37.9	44.9
9	177.5	72.9	29.4	69.1	61.5	106.3	70.4	63.6	68.3	63.8	46.6	64.2	52.1	46.9	45.5
10	145.4	72.5	26.1	56.7	66.4	48.7	66.0	61.5	67.3	69.7	58.1	59.6	51.2	34.7	43.1
11		73.3	28.9	67.4	57.1	69.7	65.7	67.6	65.6	69.7	54.1	62.1	47.9	30.3	47.9
12				62.2	62.1	68.6	64.6	58.9	75.1	69.8	57.6	61.3	41.9	43.3	43.9
13						88.5	70.2	64.2	69.4	59.0	52.6	51.9	49.9	38.0	44.1
14								60.7	69.0	55.8	55.8	63.7	51.7	45.2	38.9

k	***k*=14**				***k*=15**										***k*=18**
a/a	**SA22**	**SA23**	**SA24**	**SC2**	**SA1**	**SA3**	**SA4**	**SA10**	**SA14**	**SA15**	**SA17**	**SA20**	**SA21**	**SC1**	**NA-a**
1	24.1	26.6	28.9	101.2	66.3	57.9	47.8	63.5	51.3	50.0	27.7	50.8	32.3	37.3	86.8
2	22.4	25.1	22.1	84.6	67.0	44.6	51.9	32.6	48.5	55.3	27.3	46.5	41.2	30.9	69.7
3	19.8	23.0	30.9	45.9	69.6	56.2	48.2	65.8	51.8	57.0	28.8	47.1	41.2	29.5	47.8
4	20.3	26.7	27.8	62.6	65.5	55.2	47.7	39.8	53.7	56.7	25.4	50.0	40.8	35.9	43.3
5	23.9	29.5	33.7	38.3	70.1	57.3	44.3	68.3	53.5	56.0	25.2	50.6	45.6	36.3	54.4
6	21.1	24.7	29.1	81.2	67.7	58.7	46.7	60.8	54.3	56.8	27.6	41.0	24.8	39.6	56.8
7	23.3	24.6	28.9	104.6	64.2	62.1	45.0	50.4	49.7	56.3	28.6	47.1	44.5	35.2	52.4
8	24.6	24.5	32.0	95.1	66.3	60.3	49.3	52.6	48.6	56.4	27.8	49.5	31.3	37.2	54.0
9	22.1	27.8	28.2	87.8	66.2	60.6	54.2	36.8	54.5	54.8	31.2	45.9	27.2	44.9	74.1
10	23.6	23.4	24.5	111.9	64.5	62.8	52.3	45.7	50.7	53.2	27.2	46.7	48.7	30.8	44.3
11	24.0	20.1	27.2	107.8	68.7	60.1	52.7	69.6	52.6	56.1	28.5	51.2	40.0	33.6	42.7
12	23.8	27.8	29.2	122.8	66.9	57.2	50.7	59.6	56.4	55.1	27.5	55.7	39.7	27.9	52.0
13	20.8	31.5	28.8	32.9	68.3	51.7	49.8	62.4	54.3	58.9	28.2	47.8	41.3	32.4	35.5
14	22.3	22.4	26.0	41.4	67.1	58.1	51.8	65.6	57.1	57.0	28.1	46.0	36.8	29.7	51.8
15					64.0	59.8	53.1	32.5	57.0	55.4	29.3	44.1	35.7	29.8	41.7
16															74.0
17															35.5
18															81.5

Table B1b: Time to failure data for annealed glass (as-received, sand abraded, scratched and naturally aged used in Section 4.4 and Chapter 5).

k	***k*=10**	***k*=11**		***k*=12**		***k*=13**		***k*=14**							
a/a	**AR**	**SA8**	**SA25**	**SA6**	**SA11**	**NA_b**	**SA9**	**SA2**	**SA5**	**SA7**	**SA12**	**SA13**	**SA16**	**SA18**	**SA19**
1	6.2	3.3	1.6	3.0	4.1	2.9	3.0	2.9	2.8	3.5	2.6	2.6	3.4	2.2	2.9
2	6.7	3.3	1.8	3.4	3.1	2.8	2.9	3.1	3.7	3.1	2.6	3.7	4.3	2.0	2.6
3	6.6	3.4	1.7	3.6	3.1	4.2	2.9	3.1	3.6	3.4	2.6	2.8	2.6	1.8	2.4
4	6.6	3.0	1.8	3.5	4.1	3.9	3.1	3.2	3.4	3.1	2.6	2.8	2.7	1.8	2.7
5	6.8	3.6	1.7	3.4	3.2	3.6	2.9	3.2	2.9	3.3	2.6	4.1	2.7	1.9	2.5
6	7.2	3.4	1.9	3.4	4.1	4.3	3.3	2.9	3.4	3.2	2.7	2.9	2.7	1.9	2.6
7	6.3	3.3	1.5	3.2	3.8	2.3	3.2	3.3	3.3	3.1	2.5	3.1	2.6	2.0	2.7
8	6.0	3.3	1.4	3.4	4.0	3.8	3.0	3.1	3.4	3.5	2.6	3.1	3.6	1.8	2.5
9	6.7	3.3	1.6	3.4	3.0	4.5	3.2	3.2	3.3	3.1	2.2	4.1	2.6	2.2	2.5
10	5.8	3.3	1.4	2.8	3.2	2.5	3.0	3.0	3.3	3.3	2.7	3.9	2.6	1.7	2.5
11		3.3	1.6	3.3	2.7	3.3	3.1	3.4	3.3	3.4	2.5	3.1	2.5	1.4	2.7
12				3.1	3.9	3.1	2.9	3.0	3.7	3.4	2.7	3.0	2.2	2.0	2.6
13						4.3	3.2	3.3	3.4	2.9	2.5	2.6	2.5	1.8	2.6
14								3.1	3.4	2.8	2.6	3.1	2.7	2.1	2.3

n	***k*=14**				***k*=15**										***k*=18**
a/a	**SA22**	**SA23**	**SA24**	**SC2**	**SA1**	**SA3**	**SA4**	**SA10**	**SA14**	**SA15**	**SA17**	**SA20**	**SA21**	**SC1**	**NA_a**
1	1.2	1.2	1.5	5.1	3.2	2.7	2.7	2.9	2.5	2.5	1.4	2.6	1.6	2.0	4.4
2	1.1	1.2	1.9	4.4	3.3	2.9	2.8	2.1	2.4	2.6	1.4	2.4	2.0	1.7	3.8
3	1.0	1.1	1.7	2.6	3.4	2.7	2.8	3.0	2.6	2.7	1.5	2.4	2.0	1.7	2.7
4	1.0	1.3	1.5	3.3	3.2	2.6	2.6	1.9	2.7	2.7	1.3	2.5	1.9	1.9	2.4
5	1.2	1.4	1.7	2.3	3.4	3.7	2.4	3.1	2.7	2.7	1.3	2.5	2.2	2.0	2.9
6	1.0	1.2	1.5	4.3	3.3	2.8	2.6	2.8	2.7	2.7	1.4	2.1	1.2	2.1	3.4
7	1.1	1.2	1.5	5.2	3.2	3.8	2.6	2.3	2.5	2.6	1.5	2.4	2.1	2.0	3.0
8	1.2	1.2	1.8	4.9	3.3	3.8	2.7	2.4	2.4	2.6	1.5	2.5	1.5	2.0	3.2
9	1.0	1.3	1.5	4.5	3.2	3.7	2.8	1.9	3.5	2.6	2.4	3.1	1.3	2.4	4.1
10	1.1	1.1	1.3	5.4	3.1	3.8	2.8	2.1	2.5	2.5	1.4	2.4	2.3	1.7	2.6
11	1.2	1.0	1.5	5.3	3.3	3.7	2.7	3.2	2.6	2.6	1.5	2.6	1.9	1.9	2.3
12	1.1	1.3	1.6	5.9	3.3	2.6	2.7	2.8	2.8	2.5	1.5	2.7	1.9	1.6	2.8
13	1.0	1.4	1.5	3.2	3.3	2.5	2.6	2.8	2.7	2.6	1.5	2.4	2.0	1.8	2.1
14	1.1	1.1	1.4	3.9	3.3	2.8	3.0	3.1	2.8	2.6	1.5	2.3	1.8	1.7	2.9
15					3.1	3.8	2.8	1.6	2.8	2.5	1.5	2.2	1.7	1.7	2.4
16															4.1
17															2.1
18															0.9

Table B2: Strength and time to failure data for annealed as-received glass (used in Section 4.5).

k	**5-sp (*k*=5)**		**10-sp (*k*=10)**		**15-sp(*k*=15)**		**20-sp (*k*=20)**		**25-sp (*k*=25)**		**30-sp (*k*=30)**	
a/a	σ_f	t_f	σ_f	t_f	σ_f	t_f	σ_f	t_f	σ_f	t_f	σ_f	t_f
	(MPa)	(sec)	(MPa)	(sec)	(MPa)	(sec)	(MPa)	(sec)	(MPa)	(sec)	(MPa)	(sec)
1	151.8	10.0	146.5	9.5	81.2	9.8	122.8	9.0	153.1	10.0	132.2	7.4
2	75.5	7.1	194.2	8.8	99.9	8.0	144.4	9.8	78.1	5.7	118.2	6.9
3	79.5	5.7	165.3	10.1	99.9	10.5	102.0	8.3	156.2	10.2	123.6	6.9
4			209.5	8.7	103.2	9.1	162.4	10.3	137.4	9.6	81.8	5.4
5			165.9	10.4	107.2	10.8	133.3	9.2	107.1	8.4	134.4	9.3
6			82.4	7.3	117.7	8.8	159.6	10.1	157.4	9.8	155.1	10.1
7			79.7	7.3	119.9	8.0	186.1	8.7	98.8	8.1	76.0	7.1
8			158.8	10.3	120.3	8.9	111.4	8.6	70.7	6.9	99.8	8.1
9					124.9	7.8	98.7	8.2	143.4	9.8	88.0	7.6
10					128.9	10.0	118.0	8.9	164.6	10.2	119.2	8.8
11					149.9	9.9	117.5	8.8	165.8	10.3	126.7	9.0
12					150.7	9.8	117.2	8.4	166.8	7.9	105.5	8.4
13					165.9	7.3	138.7	9.3	123.0	8.9	165.1	10.6
14							112.2	8.5	151.5	9.9	145.2	9.8
15							113.8	6.8	69.4	6.9	128.0	9.1
16									132.1	8.3	140.5	9.7
17									117.8	7.2	163.1	10.4
18									151.6	10.1	104.7	8.3
19											135.3	9.6
20											159.0	10.4
21											107.1	8.4
22											164.6	10.3
23											164.9	10.3
24											252.1	10.0
25											151.2	7.0
26											157.9	10.0

Table B3a: Strength and time to failure data for annealed, fully toughened and chemically toughened glass (as-received and sand abraded used in Chapter 6).

k	**AN-AR**		**AN-SA**		**FT-AR**		**FT-SA**		**CT-AR**		**CT-SA**	
a/a	σ_f	t_f	σ_f	t_f	σ_f	t_f	σ_f	t_f	σ_f	t_f	σ_f	t_f
	(MPa)	(sec)	(MPa)	(sec)	(MPa)	(sec)	(MPa)	(sec)	(MPa)	(sec)	(MPa)	(sec)
1	81.2	9.8	32.3	1.6	218.8	4.5	122.9	3.3	431.4	10.7	6.3	1.6
2	99.9	8.0	41.2	2.0	284.1	5.4	123.6	3.1	359.3	9.4	83.7	5.7
3	99.9	10.5	41.2	2.0	249.1	4.9	125.9	3.4	426.2	9.5	96.1	6.2
4	103.2	9.1	40.8	1.9	218.3	4.5	127.9	3.5	426.2	9.8	66.4	5.1
5	107.2	10.8	45.6	2.2	265.4	5.2	134.7	3.4	283.8	7.4	32.8	5.1
6	117.7	8.8	24.8	1.2	167.0	3.7	134.9	3.2	392.3	9.2	119.0	6.0
7	119.9	8.0	44.5	2.1	217.9	4.4	136.4	2.4	413.2	9.5	81.2	4.7
8	120.3	8.9	31.3	1.5	320.6	6.0	138.6	3.1	242.4	7.3	24.7	3.0
9	124.9	7.8	27.2	1.3	207.9	4.5	139.1	3.2	312.9	8.2	48.4	3.5
10	128.9	10.0	48.7	2.3	240.6	4.9	142.0	3.0	429.3	10.6	126.1	7.0
11	149.9	9.9	40.0	1.9	206.1	4.4	142.5	3.1	307.0	7.9	110.8	7.2
12	150.7	9.8	39.7	1.9	194.2	4.2	147.1	3.3	434.5	9.4	140.3	6.4
13	165.9	7.3	41.3	2.0	235.8	4.8	147.8	3.4	454.4	9.7	36.4	4.2
14			36.8	1.8			148.9	3.2	343.1	8.3	45.9	5.9
15			35.7	1.7			150.6	3.3	431.6	11.7		

Table B3b: Critical flaw depths for annealed, fully toughened and chemically toughened sand abraded glass (used in Chapter 6).

Critical flaw depth					
Specimen	**Flaw depth**	**Specimen**	**Flaw depth**	**Specimen**	**Flaw depth**
	µm		µm		µm
AN-SA1	182.4	FT-SA1	73.0	CT-SA1	99.2
AN-SA2	263.5	FT-SA2	79.7	CT-SA2	97.3
AN-SA3	333.1	FT-SA3	89.9	CT-SA3	71.0
AN-SA4	484.7	FT-SA4	134.8	CT-SA5	83.6
AN-SA5	637.3	FT-SA5	105.6	CT-SA9	131.7
AN-SA6	991.7	FT-SA6	94.8	CT-SA10	94.1
AN-SA7	280.4	FT-SA7	151.6		
AN-SA8	208.8	FT-SA8	111.1		
AN-SA9	394.1	FT-SA9	198.0		
AN-SA10	132.4	FT-SA10	144.4		
AN-SA11	829.4	FT-SA11	218.2		
AN-SA12	1370.1	FT-SA12	109.8		
AN-SA13	612.8	FT-SA13	100.6		
AN-SA14	185.4	FT-SA14	170.8		
AN-SA15	179.8				

Appendix C: Weibull statistics results

The results of the various statistical analysis methods of Section 4.4, follow below (Tables C1-C4).

Table C1: Results of the LR method for different estimators.

LR																	
k	**Series**	**Shape factor, β**				**Scale factor, ϑ**				**Goodness of fit, P_{AD}**				**Des. Strength, $\sigma_{0.001}$ (MPa)**			
		E1	E2	E3	E4	E1	E2	E3	E4	E1	E2	E3	E4	E1	E2	E3	E4
10	AR	9.2	11.0	10.1	10.4	113.9	113.4	113.6	113.5	0.623	0.532	0.633	0.610	53.6	60.6	57.5	58.6
11	SA8	18.3	22.4	20.4	21.1	51.6	51.5	51.6	51.5	0.071	0.101	0.099	0.102	35.4	37.8	36.8	37.2
	SA25	9.0	10.9	10.0	10.3	19.3	19.2	19.3	19.3	0.268	0.577	0.456	0.505	8.9	10.2	9.7	9.9
12	SA6	11.5	13.8	12.7	13.1	49.1	48.9	49.0	48.9	0.456	0.685	0.622	0.653	26.9	29.6	28.4	28.9
	SA11	18.4	22.1	20.3	21.0	45.7	45.6	45.6	45.6	0.372	0.592	0.530	0.561	31.4	33.4	32.5	32.8
13	NA_b	3.7	4.4	4.1	4.2	58.1	57.6	57.8	57.7	0.683	0.787	0.787	0.796	9.1	12.0	10.6	11.1
	SA9	17.5	20.5	19.1	19.6	47.8	47.7	47.8	47.7	0.188	0.108	0.162	0.145	32.2	34.0	33.3	33.5
14	SA2	20.2	23.5	22.0	22.5	45.4	45.3	45.3	45.3	0.360	0.247	0.335	0.310	32.2	33.7	33.1	33.3
	SA5	11.2	13.3	12.3	12.7	49.7	49.5	49.6	49.5	0.033	0.118	0.072	0.087	26.8	29.5	28.3	28.7
	SA7	12.7	14.9	13.9	14.2	48.3	48.1	48.2	48.2	0.523	0.776	0.708	0.741	28.0	30.3	29.3	29.7
	SA12	17.1	20.6	18.9	19.5	38.5	38.4	38.4	38.4	0.030	0.127	0.072	0.090	25.7	27.4	26.7	26.9
	SA13	12.8	15.0	14.0	14.4	43.4	43.3	43.3	43.3	0.303	0.500	0.439	0.467	25.3	27.3	26.5	26.8
	SA16	13.2	15.9	14.6	15.1	36.7	36.6	36.6	36.6	0.032	0.198	0.092	0.123	21.8	23.7	22.8	23.1
	SA18	8.4	9.9	9.2	9.4	28.7	28.6	28.6	28.6	0.563	0.800	0.743	0.773	12.6	14.2	13.5	13.8
	SA19	14.6	17.3	16.0	16.5	32.4	32.3	32.3	32.3	0.544	0.652	0.659	0.668	20.2	21.7	21.0	21.3
	SA22	13.8	16.2	15.1	15.4	15.2	15.2	15.2	15.2	0.417	0.456	0.482	0.482	9.2	9.9	9.6	9.7
	SA23	8.3	9.7	9.0	9.2	17.7	17.6	17.7	17.7	0.523	0.441	0.535	0.513	7.7	8.6	8.2	8.4
	SA24	11.7	13.8	12.8	13.2	19.9	19.9	19.9	19.9	0.130	0.080	0.118	0.106	11.1	12.0	11.6	11.8
	SC2	2.2	2.6	2.4	2.4	65.8	64.8	65.2	65.0	0.174	0.244	0.232	0.241	2.8	4.4	3.6	3.9
15	SA1	35.3	40.8	38.3	39.1	47.3	47.3	47.3	47.3	0.460	0.313	0.423	0.391	38.9	39.9	39.5	39.6
	SA3	11.1	13.2	12.2	12.5	41.8	41.7	41.7	41.7	0.077	0.357	0.198	0.249	22.4	24.7	23.7	24.0
	SA4	16.3	19.0	17.7	18.2	35.3	35.3	35.3	35.3	0.693	0.665	0.729	0.717	23.2	24.5	23.9	24.1
	SA10	3.6	4.2	3.9	4.0	41.2	40.8	41.0	40.9	0.163	0.208	0.207	0.212	6.0	7.8	7.0	7.3
	SA14	18.1	20.9	19.6	20.0	37.5	37.4	37.5	37.4	0.715	0.616	0.713	0.689	25.6	26.9	26.3	26.5
	SA15	37.3	43.6	40.6	41.6	39.0	39.0	39.0	39.0	0.220	0.294	0.286	0.295	32.4	33.2	32.9	33.0
	SA17	19.2	22.5	20.9	21.4	19.0	18.9	19.0	18.9	0.098	0.150	0.139	0.146	13.2	13.9	13.6	13.7
	SA20	13.4	15.7	14.6	15.0	34.1	34.0	34.1	34.1	0.108	0.111	0.126	0.124	20.3	21.9	21.2	21.5
	SA21	5.1	6.0	5.6	5.7	27.9	27.7	27.7	27.7	0.333	0.570	0.493	0.527	7.3	8.8	8.1	8.3
	SC1	7.2	8.3	7.8	8.0	24.5	24.4	24.4	24.4	0.151	0.098	0.137	0.125	9.4	10.6	10.1	10.3
18	NA_a	3.7	4.2	4.0	4.1	42.5	42.2	42.3	42.3	0.085	0.028	0.054	0.044	6.7	8.3	7.5	7.8

Table C2: Results of the WLR-F&T method for different estimators.

		WLR-F&T															
k	**Series**	**Shape factor, β**				**Scale factor, ϑ**				**Goodness of fit, p_{AD}**				**Des. Strength, $\sigma_{0.001}$ (MPa)**			
		E1	E2	E3	E4	E1	E2	E3	E4	E1	E2	E3	E4	E1	E2	E3	E4
10	AR	8.2	9.4	8.8	9.0	113.7	112.9	113.2	113.1	0.505	0.666	0.623	0.644	48.8	54.0	51.8	52.6
11	SA8	17.5	20.9	19.2	19.8	51.5	51.3	51.4	51.3	0.066	0.117	0.099	0.107	34.7	36.8	35.9	36.2
	SA25	9.9	11.9	11.0	11.3	19.3	19.2	19.2	19.2	0.449	0.623	0.583	0.604	9.6	10.7	10.3	10.4
12	SA6	12.0	14.0	13.1	13.4	49.0	48.8	48.9	48.9	0.534	0.686	0.654	0.672	27.5	29.8	28.8	29.2
	SA11	18.9	22.3	20.8	21.3	45.6	45.5	45.6	45.5	0.437	0.599	0.563	0.583	31.7	33.4	32.7	32.9
13	NA_b	3.7	4.2	4.0	4.1	58.0	57.5	57.7	57.7	0.687	0.796	0.776	0.788	9.1	11.2	10.3	10.6
	SA9	15.1	16.7	16.0	16.2	47.7	47.6	47.6	47.6	0.135	0.194	0.176	0.184	30.2	31.5	30.9	31.1
14	SA2	17.7	19.5	18.7	19.0	45.3	45.2	45.2	45.2	0.258	0.359	0.328	0.341	30.7	31.7	31.3	31.4
	SA5	12.7	14.8	13.9	14.2	49.4	49.3	49.3	49.3	0.090	0.172	0.141	0.154	28.7	30.9	30.0	30.3
	SA7	13.5	15.3	14.5	14.8	48.3	48.2	48.2	48.2	0.663	0.784	0.761	0.774	28.9	30.7	30.0	30.2
	SA12	19.5	22.7	21.3	21.8	38.3	38.2	38.2	38.2	0.100	0.189	0.159	0.172	26.9	28.2	27.6	27.8
	SA13	13.5	15.1	14.4	14.7	43.4	43.3	43.3	43.3	0.381	0.507	0.473	0.489	25.9	27.4	26.8	27.1
	SA16	16.5	19.9	18.4	18.9	36.5	36.4	36.4	36.4	0.274	0.569	0.468	0.512	24.0	25.8	25.0	25.3
	SA18	8.8	9.9	9.4	9.6	28.6	28.5	28.6	28.5	0.669	0.800	0.774	0.788	13.0	14.2	13.7	13.9
	SA19	14.4	16.2	15.4	15.7	32.3	32.3	32.3	32.3	0.535	0.672	0.641	0.658	20.0	21.1	20.6	20.8
	SA22	13.6	15.1	14.5	14.7	15.2	15.2	15.2	15.2	0.394	0.482	0.462	0.473	9.2	9.6	9.4	9.5
	SA23	7.5	8.4	8.0	8.2	17.7	17.6	17.6	17.6	0.430	0.575	0.537	0.556	7.0	7.7	7.4	7.6
	SA24	10.3	11.5	11.0	11.2	19.8	19.8	19.8	19.8	0.098	0.151	0.134	0.142	10.1	10.9	10.5	10.7
	SC2	2.2	2.4	2.3	2.4	65.6	65.0	65.2	65.1	0.177	0.238	0.220	0.229	2.8	3.8	3.4	3.6
15	SA1	31.4	34.7	33.2	33.8	47.3	47.2	47.3	47.3	0.368	0.489	0.456	0.471	38.0	38.7	38.4	38.5
	SA3	13.4	15.8	14.7	15.1	41.6	41.5	41.6	41.6	0.399	0.641	0.572	0.605	24.9	26.8	26.0	26.3
	SA4	15.7	17.3	16.6	16.9	35.3	35.3	35.3	35.3	0.638	0.729	0.711	0.721	22.8	23.7	23.3	23.4
	SA10	3.6	4.0	3.8	3.9	41.2	41.0	41.1	41.0	0.164	0.212	0.199	0.205	6.1	7.2	6.7	6.9
	SA14	16.8	18.4	17.7	18.0	37.5	37.4	37.5	37.4	0.628	0.728	0.705	0.717	24.9	25.7	25.4	25.5
	SA15	35.8	41.0	38.6	39.4	39.0	38.9	38.9	38.9	0.199	0.324	0.283	0.301	32.1	32.9	32.5	32.7
	SA17	18.4	21.2	19.8	20.3	18.9	18.9	18.9	18.9	0.093	0.173	0.143	0.156	13.0	13.6	13.3	13.4
	SA20	12.1	13.8	13.0	13.3	34.0	33.9	33.9	33.9	0.083	0.148	0.124	0.134	19.2	20.5	20.0	20.2
	SA21	5.5	6.2	5.9	6.0	27.8	27.6	27.7	27.7	0.451	0.580	0.552	0.567	7.8	9.1	8.5	8.7
	SC1	6.2	6.9	6.6	6.7	24.3	24.1	24.2	24.2	0.104	0.178	0.150	0.161	7.9	8.8	8.4	8.6
18	NA_a	3.2	3.4	3.3	3.3	42.1	41.7	41.9	41.8	0.074	0.097	0.091	0.094	4.7	5.4	5.1	5.2

Table C3: Results of the WLR-B method for different estimators.

WLR-B																	
k	**Series**	**Shape factor, β**				**Scale factor, ϑ**				**Goodness of fit, p_{AD}**				**Des. Strength, $\sigma_{0.001}$ (MPa)**			
		E1	E2	E3	E4	E1	E2	E3	E4	E1	E2	E3	E4	E1	E2	E3	E4
10	AR	8.2	9.4	8.9	9.1	113.1	112.3	112.7	112.5	0.523	0.637	0.619	0.631	48.9	54.1	51.9	52.7
11	SA8	20.0	25.9	23.0	24.0	51.3	51.1	51.2	51.2	0.110	0.061	0.110	0.096	36.3	39.2	37.9	38.4
	SA25	10.1	11.6	11.0	11.2	19.3	19.3	19.3	19.3	0.456	0.607	0.566	0.585	9.8	10.6	10.3	10.4
12	SA6	12.5	14.6	13.7	14.0	49.0	48.9	48.9	48.9	0.596	0.681	0.679	0.686	28.2	30.4	29.5	29.9
	SA11	20.3	24.0	22.4	23.0	45.6	45.5	45.5	45.5	0.538	0.569	0.599	0.596	32.5	34.1	33.5	33.7
13	NA_b	3.7	4.0	3.9	3.9	58.2	57.8	58.0	57.9	0.654	0.779	0.745	0.760	8.9	10.4	9.8	10.0
	SA9	14.4	15.5	15.1	15.3	47.6	47.5	47.6	47.6	0.100	0.143	0.128	0.134	29.5	30.5	30.1	30.2
14	SA2	16.9	18.1	17.6	17.8	45.3	45.2	45.2	45.2	0.187	0.271	0.241	0.253	30.1	30.9	30.6	30.7
	SA5	13.5	15.8	14.8	15.2	49.4	49.3	49.4	49.3	0.129	0.191	0.178	0.185	29.7	31.8	31.0	31.3
	SA7	13.4	14.7	14.2	14.4	48.3	48.3	48.3	48.3	0.630	0.761	0.724	0.740	28.9	30.2	29.7	29.9
	SA12	20.4	23.1	22.0	22.4	38.2	38.2	38.2	38.2	0.129	0.174	0.167	0.172	27.3	28.3	27.9	28.1
	SA13	13.2	14.5	14.0	14.2	43.5	43.5	43.5	43.5	0.322	0.450	0.407	0.425	25.8	27.0	26.5	26.7
	SA16	18.3	21.7	20.2	20.8	36.5	36.4	36.4	36.4	0.462	0.591	0.583	0.594	25.0	26.5	25.9	26.1
	SA18	8.7	9.6	9.3	9.4	28.6	28.5	28.5	28.5	0.669	0.786	0.756	0.770	13.0	13.9	13.5	13.7
	SA19	14.2	15.5	15.0	15.1	32.3	32.2	32.2	32.2	0.508	0.629	0.596	0.611	19.9	20.6	20.3	20.4
	SA22	12.7	13.6	13.3	13.4	15.3	15.3	15.3	15.3	0.267	0.371	0.333	0.348	8.9	9.2	9.1	9.1
	SA23	7.7	8.5	8.2	8.3	17.6	17.5	17.5	17.5	0.463	0.540	0.532	0.539	7.1	7.8	7.5	7.6
	SA24	10.9	12.5	11.8	12.0	19.7	19.6	19.7	19.7	0.123	0.116	0.134	0.130	10.5	11.3	11.0	11.1
	SC2	2.1	2.2	2.2	2.2	67.6	67.3	67.4	67.4	0.111	0.164	0.144	0.152	2.4	3.0	2.8	2.8
15	SA1	31.9	35.1	33.7	34.3	47.2	47.2	47.2	47.2	0.387	0.452	0.446	0.452	38.0	38.8	38.5	38.6
	SA3	14.2	16.2	15.4	15.7	41.7	41.6	41.6	41.6	0.508	0.651	0.620	0.636	25.7	27.1	26.6	26.8
	SA4	14.9	15.8	15.5	15.6	35.4	35.3	35.4	35.4	0.517	0.652	0.607	0.625	22.2	22.9	22.6	22.7
	SA10	3.4	3.6	3.5	3.6	42.0	42.0	42.0	42.0	0.098	0.141	0.125	0.131	5.4	6.2	5.9	6.0
	SA14	16.3	17.5	17.0	17.2	37.5	37.4	37.5	37.4	0.561	0.691	0.650	0.668	24.5	25.2	25.0	25.1
	SA15	39.2	45.3	42.6	43.6	38.9	38.9	38.9	38.9	0.296	0.301	0.330	0.325	32.6	33.4	33.1	33.2
	SA17	20.8	24.7	22.9	23.6	18.9	18.8	18.8	18.8	0.164	0.124	0.168	0.156	13.5	14.2	13.9	14.0
	SA20	12.9	14.5	13.8	14.1	33.9	33.7	33.8	33.8	0.113	0.136	0.137	0.139	19.8	21.0	20.5	20.7
	SA21	5.6	6.2	5.9	6.1	27.9	27.8	27.8	27.8	0.469	0.577	0.553	0.565	8.1	9.2	8.7	8.9
	SC1	6.3	7.0	6.7	6.8	24.1	24.0	24.0	24.0	0.120	0.166	0.154	0.160	8.1	8.9	8.6	8.7
18	NA_a	3.0	3.2	3.1	3.1	41.7	41.3	41.5	41.4	0.049	0.064	0.059	0.061	4.2	4.7	4.5	4.6

Table C4: Results of different estimation methods.

k	Series	Shape factor, β					Scale factor, ϑ					Anderson Darling goodness of fit, p_{AD}					Design Strength, $\sigma_{0.001}$				
		a	b	c	d	e	a	b	c	d	e	a	b	c	d	e	a	b	c	d	e
10	**AR**	9.2	9.4	9.4	9.0	10.2	0.0	112.9	112.3	115.0	113.6	0.000	0.666	0.637	0.458	0.632	0.0	54.0	54.1	53.6	57.7
11	**SA8**	18.3	20.9	25.9	20.6	20.7	51.6	51.3	51.1	51.7	51.5	0.071	0.117	0.061	0.077	0.109	35.4	36.8	39.2	36.9	36.9
	SA25	9.0	11.9	11.6	13.1	13.1	19.3	19.2	19.3	19.1	19.2	0.268	0.623	0.607	0.529	0.563	8.9	10.7	10.6	11.3	11.3
12	**SA6**	11.5	14.0	14.6	13.6	14.7	49.1	48.8	48.9	49.0	48.8	0.456	0.686	0.681	0.669	0.679	26.9	29.8	30.4	29.5	30.5
	SA11	18.4	22.3	24.0	22.3	22.4	45.7	45.5	45.5	45.6	45.6	0.372	0.599	0.569	0.579	0.597	31.4	33.4	34.1	33.5	33.5
13	**NA_b**	3.7	4.2	4.0	4.5	4.6	58.1	57.5	57.8	57.7	57.5	0.683	0.796	0.779	0.776	0.748	9.1	11.2	10.4	12.4	12.8
	SA9	17.5	16.7	15.5	18.8	18.8	47.8	47.6	47.5	47.9	47.7	0.188	0.194	0.143	0.135	0.174	32.2	31.5	30.5	33.1	33.1
12	**SA2**	20.2	19.5	18.1	21.0	22.3	45.4	45.2	45.2	45.5	45.3	0.360	0.359	0.271	0.284	0.320	32.2	31.7	30.9	32.7	33.3
	SA5	11.2	14.8	15.8	14.7	16.7	49.7	49.3	49.3	49.4	49.2	0.033	0.172	0.191	0.175	0.176	26.8	30.9	31.8	30.9	32.6
	SA7	12.7	15.3	14.7	15.6	17.0	48.3	48.2	48.3	48.1	48.1	0.523	0.784	0.761	0.781	0.575	28.0	30.7	30.2	30.9	32.0
	SA12	17.1	22.7	23.1	21.4	24.9	38.5	38.2	38.2	38.4	38.2	0.030	0.189	0.174	0.149	0.193	25.7	28.2	28.3	27.8	29.0
	SA13	12.8	15.1	14.5	17.1	17.8	43.4	43.3	43.5	43.1	43.2	0.303	0.507	0.450	0.385	0.361	25.3	27.4	27.0	28.8	29.3
	SA16	13.2	19.9	21.7	19.3	21.2	36.7	36.4	36.4	36.4	36.4	0.032	0.569	0.591	0.523	0.577	21.8	25.8	26.5	25.4	26.3
	SA18	8.4	9.9	9.6	9.7	10.7	28.7	28.5	28.5	28.7	28.5	0.563	0.800	0.786	0.777	0.772	12.6	14.2	13.9	14.1	14.9
	SA19	14.6	16.2	15.5	16.2	17.5	32.4	32.3	32.2	32.4	32.3	0.544	0.672	0.629	0.616	0.646	20.2	21.1	20.6	21.2	21.7
	SA22	13.8	15.1	13.6	17.6	18.0	15.2	15.2	15.3	15.2	15.2	0.417	0.482	0.371	0.309	0.278	9.2	9.6	9.2	10.2	10.4
	SA23	8.3	8.4	8.5	8.5	8.8	17.7	17.6	17.5	17.8	17.7	0.523	0.575	0.540	0.425	0.548	7.7	7.7	7.8	7.9	8.1
	SA24	11.7	11.5	12.5	11.1	12.0	19.9	19.8	19.6	20.1	19.9	0.130	0.151	0.116	0.062	0.138	11.1	10.9	11.3	10.8	11.2
	SC2	2.2	2.4	2.2	3.0	3.0	65.8	65.0	67.3	63.2	64.0	0.174	0.238	0.164	0.098	0.111	2.8	3.8	3.0	6.3	6.6
15	**SA1**	35.3	34.7	35.1	34.1	37.3	47.3	47.2	47.2	47.4	47.3	0.460	0.489	0.452	0.290	0.450	38.9	38.7	38.8	38.7	39.3
	SA3	11.1	15.8	16.2	16.2	17.0	41.8	41.5	41.6	41.4	41.4	0.077	0.641	0.651	0.583	0.609	22.4	26.8	27.1	27.0	27.6
	SA4	16.3	17.3	15.8	18.9	19.6	35.3	35.3	35.3	35.3	35.3	0.693	0.729	0.652	0.674	0.600	23.2	23.7	22.9	24.5	24.8
	SA10	3.6	4.0	3.6	5.0	5.0	41.2	41.0	42.0	40.1	40.5	0.163	0.212	0.141	0.042	0.076	6.0	7.2	6.2	10.1	10.1
	SA14	18.1	18.4	17.5	18.7	20.9	37.5	37.4	37.4	37.6	37.4	0.715	0.728	0.691	0.661	0.620	25.6	25.7	25.2	26.0	26.9
	SA15	37.3	41.0	45.3	43.8	40.6	39.0	38.9	38.9	39.0	39.0	0.220	0.324	0.301	0.274	0.297	32.4	32.9	33.4	33.3	32.9
	SA17	19.2	21.2	24.7	21.2	20.5	19.0	18.9	18.8	19.0	18.9	0.098	0.173	0.124	0.112	0.145	13.2	13.6	14.2	13.7	13.5
	SA20	13.4	13.8	14.5	14.5	13.7	34.1	33.9	33.7	34.2	34.1	0.108	0.148	0.136	0.093	0.127	20.3	20.5	21.0	21.2	20.5
	SA21	5.1	6.2	6.2	6.3	6.7	27.9	27.6	27.8	27.6	27.6	0.333	0.580	0.577	0.583	0.535	7.3	9.1	9.2	9.2	9.9
	SC1	7.2	6.9	7.0	7.4	7.1	24.5	24.1	24.0	24.6	24.4	0.151	0.178	0.166	0.096	0.163	9.4	8.8	8.9	9.7	9.3
18	**NA_a**	3.7	3.4	3.2	3.7	3.9	42.5	41.7	41.3	43.3	42.4	0.085	0.097	0.064	0.057	0.072	6.7	5.4	4.7	6.5	7.1

*a=LR-E1, b=WLR-F&T-E2, c=WLR-B-E2, d=GLUES & e=MLE

Appendix D: Grain size distribution curves

The grain size distribution curves used in Chapter 5 for the sand abraded series, are presented below.

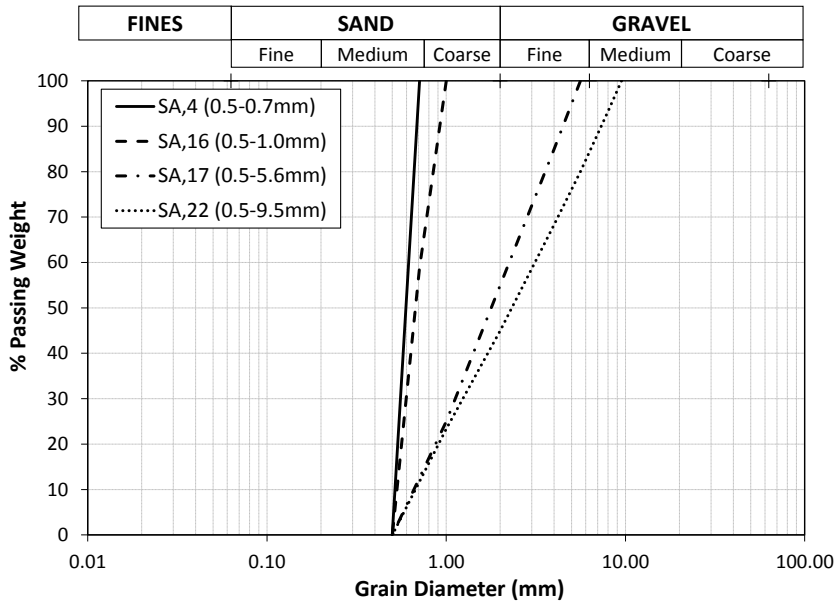

(a)

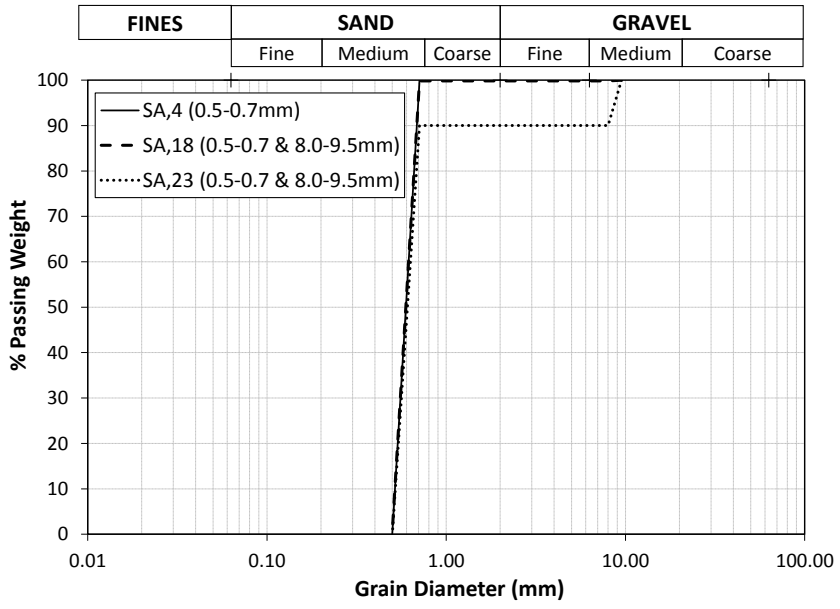

(b)

Fig. D1: Grain size distribution curves for: (a) well graded abrasive media and; (b) well sorted abrasive media.

Appendix E: Confidence intervals

Confidence intervals (90%) for the strength of the naturally aged and artificially aged series of Chapter 5, were computed based on EN 12603 [162]. The results are shown in Table E1 and Fig. E1a-b for design (P_f=0.008) and mean strength (P_f=0.50).

The width of the confidence intervals can be used to assess the uncertainty in the data for the sand abraded series because fixed errors are small and constant: (a) glass was provided by the same supplier; (b) artificial ageing and destructive tests were performed by the same researcher and; (c) the testing procedure was identical for all specimens in all series. The width of the intervals for SA series is small (5.9±2.8 MPa) for P_f=0.008 and negligible for P_f=0.50 (2.5±1.9 MPa). This indicates that 15 specimens per series is sufficient to derive reliable strength results. However, it is not possible to establish if the number of specimens is sufficient for naturally aged glass based on the width of their confidence intervals. This is because of the larger errors / uncertainties that are associated with naturally aged glass during its service life.

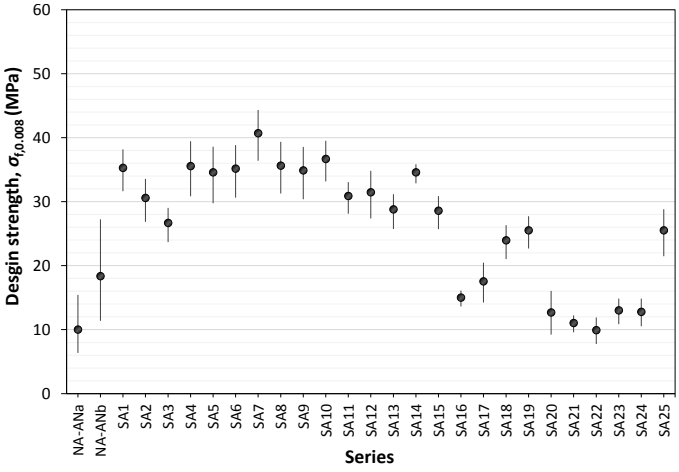

(a)

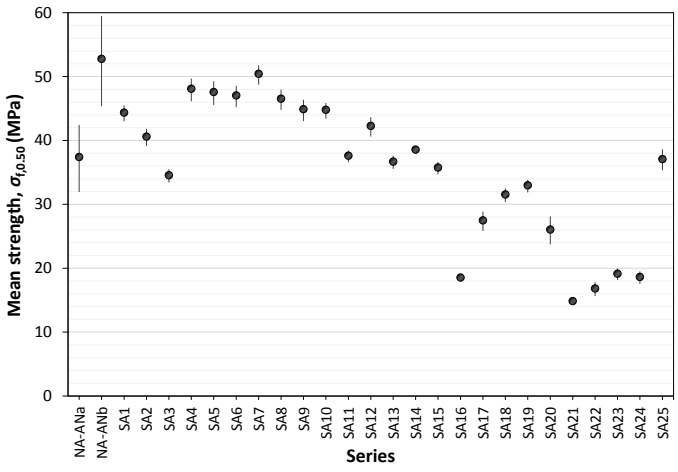

(b)

Fig. E1: Upper and lower bound (based on confidence intervals) and CDF strength (dot) for: (a) design strength P_f=0.008 and; (b) mean strength (P_f=0.50).

Table E1: Confidence interval upper and lower bounds for design (P_f=0.008) and mean (P_f=0.50) probabilities of failure.

Series	Fractile values							
	$\sigma_{f,0.008}$	$\sigma_{f,0.008,\,up.}$	$\sigma_{f,0.008,\,low.}$	$\sigma_{f,0.008,\,up.}$-$\sigma_{f,0.008,\,low.}$	$\sigma_{f,0.5}$	$\sigma_{f,0.5,\,up.}$	$\sigma_{f,0.5,\,low.}$	$\sigma_{f,0.50,\,up.}$-$\sigma_{f,0.50,\,low.}$
	MPa	MPa	MPa	MPa	MPa	MPa	MPa	MPa
NA_a	10.00	15.43	6.36	9.07	37.41	42.44	31.94	10.50
NA_b	18.36	27.24	11.39	15.84	52.76	59.49	45.34	14.16
SA1	41.10	43.12	38.69	4.43	46.74	48.14	45.52	2.62
SA2	35.28	38.17	31.64	6.53	44.36	45.48	43.00	2.48
SA3	30.59	33.55	26.84	6.71	40.59	41.82	39.13	2.69
SA4	26.69	29.04	23.68	5.35	34.54	35.49	33.40	2.09
SA5	35.56	39.44	30.84	8.61	48.08	49.68	46.14	3.54
SA6	34.59	38.59	29.76	8.83	47.57	49.26	45.55	3.70
SA7	35.16	38.85	30.64	8.22	47.03	48.54	45.20	3.34
SA8	40.70	44.32	36.40	7.92	50.41	51.74	48.72	3.02
SA9	35.63	39.36	31.28	8.08	46.53	47.97	44.78	3.19
SA10	34.89	38.57	30.38	8.19	44.89	46.38	43.03	3.34
SA11	36.68	39.51	33.16	6.35	44.78	45.85	43.43	2.43
SA12	30.89	33.05	28.12	4.93	37.61	38.43	36.62	1.81
SA13	31.48	34.83	27.38	7.45	42.26	43.64	40.60	3.04
SA14	28.79	31.16	25.72	5.44	36.69	37.64	35.55	2.09
SA15	34.59	35.84	32.87	2.97	38.56	39.00	38.02	0.98
SA16	28.59	30.88	25.70	5.17	35.76	36.64	34.69	1.96
SA17	15.02	16.09	13.62	2.47	18.54	18.96	18.04	0.92
SA18	17.55	20.47	14.24	6.23	27.48	28.86	25.85	3.00
SA19	23.96	26.33	21.03	5.30	31.53	32.49	30.37	2.12
SA20	25.52	27.74	22.68	5.06	32.97	33.82	31.85	1.97
SA21	12.68	16.05	9.23	6.82	26.05	28.10	23.72	4.37
SA22	11.04	12.23	9.60	2.63	14.85	15.34	14.26	1.07
SA23	9.91	11.89	7.77	4.12	16.81	17.81	15.65	2.16
SA24	13.01	14.85	10.85	4.00	19.13	19.96	18.15	1.80
SA25	12.78	14.85	10.52	4.33	18.62	19.50	17.54	1.96
SA26	25.51	28.83	21.48	7.35	37.07	38.59	35.34	3.26

Appendix F. Mixed Weibull distributions

Bi-modal distributions in glass strength data occur due to different underlying causes of failure/flaw morphologies within the same data set. These series are more faithfully described by mixed Weibull distributions (Eq. F1). The estimation of the mixed Weibull parameters is based on graphical approaches [180]. Even though computational methods (*MME* and *MLE*) exist for such cases [181,182], they can be time-consuming since there are 5 unknowns (β_1, β_2, θ_1, θ_2 & p).

$$P_f\left(\sigma_{f,60}\right) = p \cdot \left\{1 - \exp\left[-\left(\frac{\sigma_{f,60}}{\theta_1}\right)^{\beta_1}\right]\right\} + q \cdot \left\{1 - \exp\left[-\left(\frac{\sigma_{f,60}}{\theta_2}\right)^{\beta_2}\right]\right\} \qquad \text{(Eq. F1)}$$

where: p and q: the mixing weights for the two Weibull distributions $\left(p + q = 1\right)$.

An example of bi-modal failure is given in Fig. F1 for series SA10. The types of critical flaws were: (a) pre-existing linear scratches and; (b) digs induced during the artificial ageing process. It was found that a mixed Weibull distribution provides a better fit to the bi-modal data than a 2-parameter Weibull distribution (159% increase in goodness-of-fit).

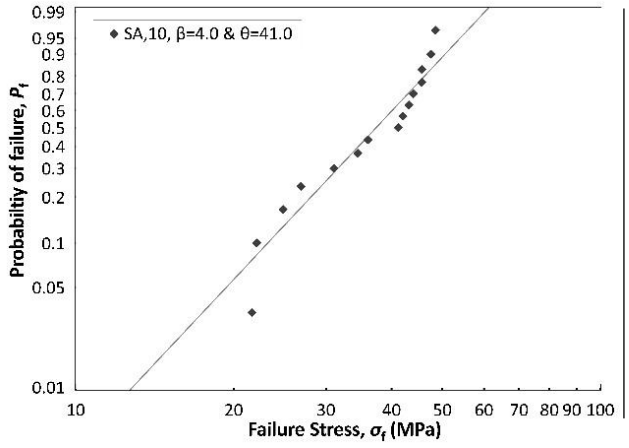

(a)

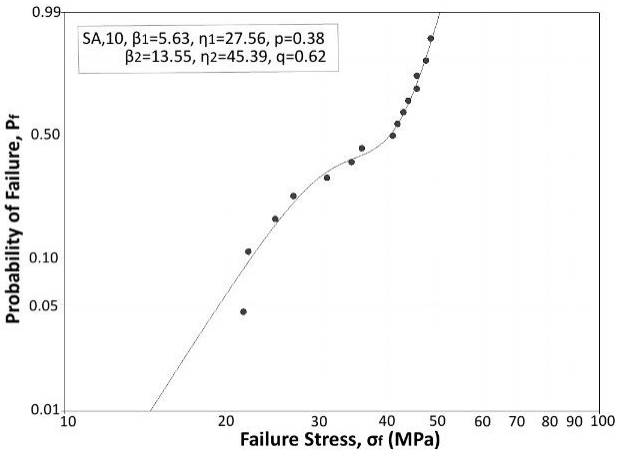

(b)

Fig. F1: CDF for bi-modal strength data described by: (a) 2 parameter Weibull and; (b) mixed Weibull distribution.

Appendix G. Outputs of this dissertation

Journal papers:

K. Datsiou and M. Overend, Artificial ageing of glass with sand abrasion, Journal of Construction and Building Materials, vol. 142, pp. 556–531, March 2017.

K. Datsiou and M. Overend, The mechanical response of cold bent monolithic glass plates during the bending process, Engineering Structures, vol. 117, pp. 575-590, March 2016.

K. Datsiou and M. Overend, Weibull statistics for glass strength, Journal of Structural Safety, pp. 1–29, December 2016 (under review).

K. Datsiou and M. Overend, The strength of aged glass, Glass Structures & Engineering, pp. 1–23, March 2017 (under review).

Conference papers:

K. Datsiou and M. Overend, Behaviour of cold bent glass plates during the shaping process, Engineered Transparency Conference at Glasstec, Dusseldorf, Germany, 2014, pp. 125–133.

K. Datsiou and M. Overend, Evaluation of Artificial Ageing Methods for Glass, Challenging Glass 5 Conference, Ghent, Belgium, 2016, pp. 581–591.

Participation in exhibitions:

Display: "Cold bending of glass: an innovative method of introducing curvature in façades", Ecobuild 2017, 7-9th March 2017, London, UK (Fig. F1).

Fig. F1: Interactive set-up of cold bending thin chemically toughened glass by mechanical means.

Awards & Distinctions:

Onassis Foundation Scholarship award on research project "Design and Performance of Cold Bent Glass", Onassis Foundation, Scholarship programmes for Hellenes, September 2016.

3rd joint award for oral presentation on "Design and Performance of cold bent glass", at 17th Young Researchers' Conference, Institution of Structural Engineers, London, UK, April 2015.

Distinction on 1st year PhD project report on "Buckling Behaviour of Cold bent glass plates", Structures Group, Department of Engineering, University of Cambridge, UK, October 2014.

REFERENCES

[1] NSG Group, Pilkington and the Flat Glass Industry: 2010, Tokyo, Japan, 2010.

[2] M. Eekhout, Design, Engineering, Production & Realisation of Glass Structures for "Free-Form" Architecture, Design, Engineering and Production, CWCT Meeting, pp. 1–18, 2004.

[3] J. E. Shelby, Introduction to Glass Science and Technology, 2nd ed., The Royal Society of Chemistry, 2005.

[4] A. K. Vashneya, Fundamentals of Inorganic Glasses, 2nd ed., The Society of Glass Technology, 2012.

[5] B. Mysen, P. Richet, Developments in Geochemistry 10: Silicate Glasses and Melts: Properties and Structure, Elsevier, 2005.

[6] EN 572-1:2012-11, Glass in building. Basic soda-lime silicate glass products. Definitions and general physical and mechanical properties, CEN European Committee for Standardization, 2016.

[7] EN 15681-1:2016, Glass in building. Basic alumino silicate glass products. Definitions and general physical and mechanical properties, CEN European Committee for Standardization, 2016.

[8] M. Haldimann, M. Overend, A. Luible, Structural use of glass, International Association for Bridge and Structural Engineering, IABSE Association, 2008.

[9] N.P. Bansal, R. Doremus, Handbook of Glass Properties, Harcourt Brace Jovanovich, 1986.

[10] B. Carter, G. Norton, Ceramic Materials: Science and Engineering, Springer, 2007.

[11] Pilkington L.A.B, The float glass process, The Royal Society: Series A, Mathematical and Physical Sciences, London, 1969.

[12] S. Dockerty, Sheet forming apparatus, Patent: US 3338696 A, 1967.

[13] M. Zaccaria, M. Overend, Thermal Healing of Realistic Flaws in Glass, Journal of Materials in Civil Engineering, vol. 4015127, pp. 1–9, 2015.

[14] E.H. Lee, T.G. Rogers, T.C. Woo, Residual Stresses in a Glass Plate Cooled Symmetrically from Both Surfaces, Journal of the American Ceramic Society, vol. 48, pp. 480–487, 1965.

[15] O.S. Narayanaswamy, Stress and Structural Relaxation in Tempering Glass, Journal of the American Ceramic Society, vol. 61, pp. 146–152, 1978.

[16] EN 12150-1:2004, Glass in building Thermally toughened soda lime silicate safety glass-Part 1: Definition and description, CEN European Committee for Standardization, 2000.

[17] ASTM C1048-12, Standard Specification for Heat-Strengthened and Fully Tempered Flat Glass, ASTM International, 2012.

[18] D. Bowman, T. Whitney, H. M., TCRP Report 15: Procurement Specification Guidelines for Mass Transit Vehicle Window Glazing, Transportation Research Board, National Research Council, Washington, 1996.

[19] EN 14179-1: Glass in building - Heat soaked thermally toughened soda lime silicate safety glass - Part 1: Definition and description, CEN European Committee for Standardization, 2005.

[20] S.S. Kistler, Stresses in Glass Produced by Nonuniform Exchange of Monovalent Ions, Journal of the American Ceramic Society, vol. 45, pp. 59–68, 1962.

[21] R. Gy, Ion exchange for glass strengthening, Materials Science and Engineering B, vol. 149, pp. 159–165, 2008.

[22] S. Karlsson, B. Jonson, C. Stålhandske, The Technology of Chemical Glass Strengthening - A review, Glass Technology:European Journal of Glass Science and Technology A, vol. 51, pp. 41–54, 2010.

[23] M.E. Nordberg, E.L. Mochel, H.M. Garfinkel, J.S. Olcott, Strengthening by Ion Exchange, Journal of the American Ceramic Society, vol. 47, pp. 215–219, 1964.

[24] A. J. Burggraaf, The strengthening of glass by ion exchange. Part 2. Stress formation and stress relaxation after ion exchange in alkali aluminosilicate glasses in connection with structural changes in the glass, Physics and Chemistry of Glasses, vol. 7, pp. 169–172, 1966.

[25] R. Bartholomew, H. Garfinkel, Chemical Strengthening of Glass. In: Elasticity and Strength in Glasses, Glass: Science and Technology, Elsevier, 1980.

[26] A. K. Varshneya, P. K. Kreski, The chemistry of chemical strengthening of glass in: Processing, Properties, and Applications of Glass and Optical Materials: Ceramic Transactions, vol. 231, The American Ceramic Society, 2012.

[27] A.L. Zijlstra, A.J. Burggraaf, Fracture phenomena and strength properties of chemically and phisically strengthened glass - I, Journal of Non-Crystalline Solids, vol. 1, pp. 49–68, 1968.

[28] M. Zaccaria, Bi-tempered glass, PhD thesis, University of Cambridge, 2016.

[29] S. Bennison, M. Qin, P. Davies, High-performance laminated glass for structurally efficient

glazing, Innovative Light-Weight Structures and Sustainable Facades, pp. 1–12, 2008.

[30] R.A. Behr, J.E. Minor, M.P. Linden, C.V.G. Vallabhan, Laminated glass units under uniform lateral pressure, Journal of Structural Engineering, vol. 111, pp. 1037–1050, 1985.

[31] R. A. Behr, J. E. Minor, H. S. Norville, Structural Behavior of Architectural Laminated Glass, Journal of Structural Engineering, vol. 119, pp. 202–222, 1993.

[32] H.S. Norville, K.W. King, J.L. Swofford, Behavior and Strength of Laminated Glass, Journal of Engineering Mechanics, vol. 124, pp. 46–53, 1998.

[33] ASTM E1300−12a, Standard Practice for Determining Load Resistance of Glass in Buildings, ASTM International, 2012.

[34] prEN 16612:2013, Glass in building: Determination of the load resistance of glass panes, European Committee for Standardization, 2013.

[35] L. Galuppi, G. Royer-Carfagni, The effective thickness of laminated glass plates, Journal of Mechanics of Materials and Structures, vol. 7, pp. 375–400, 2012.

[36] L. Galuppi, G. Royer-Carfagni, Laminated beams with viscoelastic interlayer, International Journal of Solids and Structures, vol. 49, pp. 2637–2645, 2012.

[37] L. Galuppi, G. Royer-Carfagni, The design of laminated glass under time-dependent loading, International Journal of Mechanical Sciences, vol. 68, pp. 67–75, 2013.

[38] P. Foraboschi, Behavior and Failure Strength of Laminated Glass Beams, Journal of Engineering Mechanics, vol. 133, pp. 1290–1301, 2007.

[39] M. Overend, C. Butchart, H. Lambert, M. Prassas, The mechanical performance of laminated hybrid-glass units, Composite Structures, vol. 110, pp. 163–173, 2014.

[40] I. V. Ivanov, Analysis, modelling, and optimization of laminated glasses as plane beam, International Journal of Solids and Structures, vol. 43, pp. 6887–6907, 2006.

[41] A. Van Duser, A. Jagota, J. Bennison, Analysis of glass/polyvinyl butyral laminates subjected to uniform pressure, Journal of Engineering Mechanics, vol. 125, pp. 435–442, 1999.

[42] P. D'Haene, G. Savineau, Mechanical properties of laminated safety glass - FEM Study, Glass Performance Days, pp. 594–598, 2007.

[43] I. V. Ivanov, D.S. Velchev, N.G. Georgiev, I.D. Ivanov, T. Sadowski, A plate finite element for modelling of triplex laminated glass and comparison with other computational models, Meccanica, vol. 51, pp. 341–358, 2016.

[44] G. Molnár, L.G. Vigh, G. Stocker, L. Dunai, Finite element analysis of laminated structural glass plates with polyvinyl butyral (PVB) interlayer, Periodica Polytechnica: Civil Engineering, vol. 56, pp. 35–42, 2012.

[45] G. Manara, C. Florian, L. Tonon, Cold Twisting in point fixed glass : a case study, XXV A.T.I.V. INTERNATIONAL CONFERENCE, pp. 1–8, 2010.

[46] H. Pottmann, A. Schiftner, P. Bo, H. Schmiedhofer, W. Wang, N. Baldassini, J. Wallner, Freeform surfaces from single curved panels, ACM Transactions on Graphics, vol. 27, pp. 1, 2008. doi:10.1145/1360612.1360675.

[47] ASTM C1651 – 11, Standard Test Method for Measurement of Roll Wave Optical Distortion in Heat- Treated Flat Glass, ASTM International, 2011.

[48] M. Abbott, J. Madocks, Roller Wave Distortion – Definition , Causes and a Novel Approach to Accurate , On-line Measurement, Glass Processing Days Conference, pp. 226–230, 2001.

[49] M. Eronen, Sag Bending Windshields – Intorduction of Key Process Parameters to Superior Optical Quality, Glass Perfomance Days Conference, pp. 2–5, 2012.

[50] J. Neugebauer, Applications for Curved Glass, Journal of Facade Design and Engineering, vol. 2, pp. 67–83, 2014.

[51] M. Teich, S. Kloker, H. Baumann, Curved glass: bending and applications., Engineered Transparency. International Conference, pp. 75–83, 2014.

[52] F. Weber, Curved glass structures, Glass Performance Days Conference, pp. 375–380, 2009.

[53] A. Von Starck, A. Muhlbauer, C. Kramer, Handbook of Thermoprocessing Technologies, Fundamentals, Processes, Components, Safety, Vulkan-Verlag GMbH edition, 2005.

[54] M. Saksala, Curved And Tempered Glass - Demand, Challenge And Opportunity For The Market-Driven Technology, Glass Processing Days Conference, pp. 63–65, 2003.

[55] B. Marradi, Function follows form. Strategies for integrated design of complex glass envelopes, Challenging Glass 3 & COST Action TU0905 Mid-Term Conference, pp. 61–68, 2013.

[56] L. Galuppi, G. Royer-Carfagni, Rheology of cold-lamination-bending for curved glazing, Engineering Structures, vol. 61, pp. 140–152, 2014.

[57] L. Galuppi, G. Royer-Carfagni, Cold-lamination-bending of glass: Sinusoidal is better than circular, Composites Part B, vol. 79, pp. 285–300, 2015.

[58] D. Dernie, J. Gaspari, Material Imagination in Architecture, Routledge, Taylor & Francis

Group, London and New York, 2016.

[59] N. Baldassini, Hidden and expressed geometry of glass, Challenging Glass 2 Conference, pp. 9–18, 2008.

[60] P.M. Eekhout, S. Niderehe, The New, Cold Bent Glass Roof of the Victoria & Albert Museum, London, Glass Performance Days Conference, pp. 408–412, 2009.

[61] M. Overend, Recent developments in design methods for glass structures, The Structural Engineer, vol. 88, pp. 18–26, 2010.

[62] M. Overend, K. Zammit, A computer algorithm for determining the tensile strength of float glass, Engineering Structures, vol. 45, pp. 68–77, 2012.

[63] M. Eekhout, W. Lockefeer, D. Staaks, Application of cold twisted tempered glass panels in double curved architectural designs, Glass Performance Days Conference, pp. 213–220, 2007.

[64] EN 1990:2002+A1, Eurocode - Basis of structural design, CEN European Committee for Standardization, 2010.

[65] E. van Herwijen, D. Staaks, E. M., Cold Bent Glass Sheets in Facade Structures, Structural Engineering International, vol. 2, pp. 98–101, 2004.

[66] M. Eekhout, D. Staaks, Cold Deformation of Glass, International Symposium on the Application of Architectural Glass, ISAAG, pp. 1–11, 2004.

[67] L. Galuppi, S. Massimiani, G. Royer-Carfagni, Large deformations and snapthrough instability of cold bent glass, Challenging Glass 4 & COST Action TU0905 Final Conference, pp. 681–690, 2014.

[68] L. Galuppi, S. Massimiani, G. Royer-Carfagni, Buckling phenomena in double curved cold-bent glass, International Journal of Non-Linear Mechanics, vol. 64, pp. 70–84, 2014.

[69] K. Datsiou, M. Overend, Behaviour of cold bent glass plates during the shaping process, Engineered Transparency. International Conference, pp. 125–133, 2014.

[70] B. Beer, Complex Geometry Facades – Introducing a New Design Concept for Cold-Bent Glass, Glass Performace Days Conference, pp. 516–522, 2013.

[71] J. Lagowski, H.C. Gatos, E.S. Sproles, Surface stress and the normal mode of vibration of thin crystals: GaAs, Applied Physics Letters, vol. 26, pp. 493–495, 1975.

[72] M.J. Lachut, J.E. Sader, Effect of Surface Stress on the Stiffness of Cantilever Plates, Physical Review Letters, vol. 99, pp. 1–4, 2007.

[73] M.J. Lachut, J.E. Sader, Effect of surface stress on the stiffness of cantilever plates: Influence of cantilever geometry, Applied Physics Letters, vol. 95, pp. 15–18, 2009.

[74] M.X. Shi, B. Liu, Z.Q. Zhang, Y.W. Zhang, H.J. Gao, Direct influence of residual stress on the bending stiffness of cantilever beams, Proceedings of the Royal Society A: Mathematical, Physical and Engineering Sciences, vol. 468, pp. 2595–2613, 2012.

[75] M.E. Gurtin, X. Markenscoff, R.N. Thurston, Effect of surface stress on the natural frequency of thin crystals, Applied Physics Letters, vol. 29, pp. 529–530, 1976.

[76] U. Breuninger, M. Stumpf, Cold bent Arches of laminated Glass, ISAAG 2004, International Symposium on the Application of Architectural Glass, 2004.

[77] T. Fildhuth, J. Knippers, F. Bindji-Odzili, N. Baldassini, S. Pennetier, Recovery Behaviour of Laminated Cold Bent Glass : Numerical Analysis and Testing, Challenging Glass 4 & COST Action TU0905 Final Conference, pp. 113–121, 2014.

[78] T. Fildhuth, J. Knippers, Double Curved Glass Shells from Cold Bent Glass Laminates, Glass Performance Days Conference, pp. 384–389, 2011.

[79] J. Belis, B. Inghelbrecht, R. Van Impe, D. Callewaert, Cold bending of laminated glass panels, Heron, vol. 52, pp. 123–146, 2007.

[80] J. Belis, B. Inghelbrecht, R. Van Impe, D. Callewaert, Experimental assessment of cold-bent glass panels, Glass Performance Days Conference, pp. 115–117, 2007.

[81] K. Besserud, M. Bergers, A.J. Black, L.D. Carbary, A. Mazurek, D. Misson, K. Rubis, Durability of Cold-Bent Insulating-Glass Units, Journal of ASTM International, vol. 9, 2012.

[82] B. Hoffmeister, P.. Di Biase, C.. Richter, M. Feldmann, Innovative steel-glass composite structures for high- performance building skins – testing of full-scale prototypes, Glass Structures & Engineering, pp. 1–22, 2016.

[83] A.A. Griffith, The Phenomena of Rupture and Flow in Solids, Philosophical Transactions of the Royal Society of London. Series A, vol. 221, pp. 163–198, 1921.

[84] G. R. Irwin, Analysis of Stresses and Strains Near the End of a Crack Traversing a Plate, Journal of Applied Mechanics, pp. 163–364, 1957.

[85] S. M. Wiederhorn, Influence of Water Vapor on Crack Propagation in Soda-Lime Glass, Journal of the American Ceramic Society, vol. 50, pp. 407–414, 1967.

[86] T. Michalske, S. Freiman, A Molecular Mechanism for Stress Corrosion in Vitreous Silica, Journal of the American Ceramic Society, vol. 66, pp. 284–288, 1983.

[87] S.M. Wiederhorn, L.H. Bolz, Stress Corrosion and Static Fatigue of Glass, Journal of the American Ceramic Society, vol. 53, pp. 543–548, 1970.

[88] R. Mould, Strength and static fatigue of abraded glass under controlled ambient conditions: IV, Effect of surrounding medium, Journal of the American Ceramic Society, vol. 44, pp. 481–491, 1961.

[89] S.M. Wiederhorn, S.W. Freiman, E.R. Fuller, C.J. Simmons, Effects of water and other dielectrics on crack growth, Journal of Materials Science, vol. 17, pp. 3460–3478, 1982.

[90] E. Gehrke, C. Ullner, M. Hähnert, Fatigue limit and crack arrest in alkali-containing silicate glasses, Journal of Materials Science, vol. 26, pp. 5445–5455, 1991.

[91] J. Watson, J. Nielsen, M. Overend, A critical flaw size approach for predicting the strength of bolted glass connections, Engineering Structures, vol. 57, pp. 87–99, 2013.

[92] R.A. Behr, M.J. Karson, J.E. Minor, Reliability analysis of window glass failure pressure data, Structural Safety, vol. 11, pp. 43–58, 1991.

[93] C.-C. Liu, A Comparison Between The Weibull And Lognormal Models Used To Analyse Reliability Data, PhD thesis, University of Nottingham, 1997.

[94] K. Zammit, M. Overend, Increasing the design strength of glass - fractography and stress testing, International Association for Shell and Spatial Structures (IASS) Symposium, 2009.

[95] M. Overend, C. Louter, The effectiveness of resin-based repairs on the inert strength recovery of glass, Construction and Building Materials, vol. 85, pp. 165–174, 2015.

[96] K.C. Datsiou, M. Overend, Evaluation of Artificial Ageing Methods for Glass, Challenging Glass 5 Conference, pp. 581–591, 2016.

[97] M. Haldimann, Fracture strength of structural glass elements - analytical and numerical modelling , testing and design, PhD Thesis, École Polytechnique Fédérale de Lausanne (EPFL), 2006.

[98] W. Weibull, A statistical distribution function of wide applicability, Journal of Applied Mechanics, vol. 18, pp. 293–297, 1951.

[99] K. Trustrum, A. De S. Jayatilaka, On estimating the Weibull modulus for a brittle material, Journal of Materials Science, vol. 14, pp. 1080–1084, 1979.

[100] prEN 13474, Glass in building - Determination of the strength of glass panes, CEN European Committee for Standardization, 2009.

[101] EN 1991-1-1, Actions on structures - Part 1-1: General actions - Densities, self-weight,

imposed loads for buildings, Eurocode 1, CEN European Committee for Standardization, 2002.

[102] H.S. Norville, J.E. Minor, Strength of weathered window glass, American Ceramic Society Bulletin, vol. 64, pp. 1467–1470, 1985.

[103] A. Fink, Ein Beitrag zum Einsatz von Floatglas als dauerhaft tragender Konstruktionswerkstoff im Bauwesen, PhD thesis, Technical University of Darmstadt, 2000.

[104] J. J. Abiassi, The Strength of Weathered Window Glass Using Surface Characteristics, PhD, thesis, Texas Tech University, 1981.

[105] W.L. Beason, J.R. Morgan, Glass Failure Prediction Model, Journal of Structural Engineering, vol. 110, pp. 197–212, 1984.

[106] B. Afolabi, H.S. Norville, S.M. Morse, Experimental Study of Weathered Tempered Glass Plates from the Northeastern United States, Journal of Architectural Engineering, vol. 22, pp. 1–8, 2016.

[107] C. Louter, J. Belis, F. Veer, J.P. Lebet, Durability of SG-laminated reinforced glass beams: Effects of temperature, thermal cycling, humidity and load-duration, Construction and Building Materials, vol. 27, pp. 280–292, 2012.

[108] L. Andreozzi, S. Briccoli Bati, M. Fagone, G. Ranocchiai, F. Zulli, Weathering action on thermo-viscoelastic properties of polymer interlayers for laminated glass, Construction and Building Materials, vol. 98, pp. 757–766, 2015.

[109] S.B. Bati, G. Ranocchiai, C. Reale, L. Rovero, Time-Dependent Behavior of Laminated Glass, Journal of Materials in Civil Engineering, vol. 22, pp. 389–396, 2010.

[110] C. Schuler, Ö. Bucak, V. Sackmann, H. Gräf, G. Albrecht, Time and temperature dependent mechanical behaviour and durability of laminated safety glass, Structural Engineering International: Journal of the International Association for Bridge and Structural Engineering (IABSE), vol. 14, pp. 80–83, 2004.

[111] C.P. Pantelides, A.D. Horst, J. E, Postbreakage bevavior of heat strengthened laminated glass under wind effect, Journal of Structural Engineering, vol. 119, pp. 454–467, 1993.

[112] C. Völker, D. Philipp, M. Masche, T. Kaltenbach, Development of a test method for the investigation of the abrasive effect of sand particles on components of solar energy systems, 29th European PV Solar Energy Conference, pp. 22–26, 2014.

[113] F. Roumili, S. Benbahouche, J.-C. Sangleboeuf, Mechanical strength of soda-lime glass

sandblasted by gravitation, Friction, vol. 3, pp. 65–71, 2015.

[114] S. Benbahouche, F. Roumili, R. Zegadi, Mechanical strength of tempered soda – lime – silica glass damaged by sand gravitation determined by bending with circular supports, XIX International Congress on Glass, pp. 286–289, 2001.

[115] N. Protopopescu, Sand Trickling Abrasion Testing of Float Glass . Some Methodological and Experimental Considerations, Glass Processing Days Conference, pp. 261–265, 2001.

[116] N. Adjouadi, N. Laouar, C. Bousbaa, N. Bouaouadja, G. Fantozzi, Study of light scattering on a soda lime glass eroded by sandblasting, Journal of the European Ceramic Society, vol. 27, pp. 3221–3229, 2007.

[117] S. Bouzid, N. Bouaouadja, Effect of impact angle on glass surfaces eroded by sand blasting, Journal of the European Ceramic Society, vol. 20, pp. 481–488, 2000.

[118] C. Bousbaa, A. Madjoubi, M. Hamidouche, N. Bouaouadja, Effect of annealing and chemical strengthening on soda lime glass erosion wear by sand blasting, Journal of the European Ceramic Society, vol. 23, pp. 331–343, 2003.

[119] A.J. Sparks, I.M. Hutchings, Transitions in the erosive wear behaviour of a glass ceramic, Wear, vol. 149, pp. 99–110, 1991.

[120] J. Schneider, S. Schula, W.P. Weinhold, Characterisation of the scratch resistance of annealed and tempered architectural glass, Thin Solid Films, vol. 520, pp. 4190–4198, 2012.

[121] J. Schneider, H. Techen, R. Stengler, Determination of the scratch resistance of annealed and tempered glasses by using UST (Universal Surface Tester), 53rd Internationales Wissenschaftliches Kolloquium, 2008.

[122] Y. Rodichev, Y. Yevplov, H. Soroka, F. Veer, Surface Cracked Layer and Damage Resistance of Glass under Contact Loading, Challenging Glass 3 Conference, 2012.

[123] V. Houerou, J. Sanglegoefu, S. Deriano, T. Rouxel, G. Duisit, Surface damage of soda – lime – silica glasses : indentation scratch behavior, Journal of Non-Crystalline Solids, vol. 316, pp. 54–63, 2003.

[124] S. Schula, Charakterisierung der Kratzanfälligkeit von Gläsern im Bauwesen, PhD thesis, Technical University of Darmstadt, 2014.

[125] G. S. Glaesemann, T. M. Gross, J. F. Bayne, J. J. Price, Fractography in the Development of Ion-Exchange Cover Glass In: Fractography of Glasses and Ceramics VI: Ceramic

Transactions, vol. 230, The American Ceramic Society, 2012.

[126] T. M. Gross, Scratch damage in ion-exchanged alkali aluminosilicate glass: Crack evolution and dependence of lateral cracking threshold on contact geometry In: Fractography of Glasses and Ceramics VI: Ceramin Transactions, vol. 230, The American Ceramic Society, 2012.

[127] J.J. Swab, S.R. Thies, J.C. Wright, J.A. Schoenstein, P.J. Patel, Influence of Surface Scratches on the Flexure Strength of Soda-Lime Silicate and Borosilicate Glass, Experimental Mechanics, vol. 53, pp. 91–96, 2013.

[128] A.M. Butaev, I.N. Vygorka, Effect of abrasive action on the mechanical strength of flat glass strengthened by ion exchange, Glass and Ceramics (English Translation of Steklo I Keramika), vol. 43, pp. 454–458, 1987.

[129] DIN 52348, Standard for Testing of Glass and Plastics; Abrasion Test; Sand Trickling Method, Deutsches Institut Fur Normung, 1985.

[130] ASTM D968-05, Standard Test Methods for Abrasion Resistance of Organic Coatings by Falling Abrasive, ASTM International, 1991.

[131] Abaqus 6.12 Documentation, Analysis User's Manual, SIMULIA, 2012.

[132] E. H. Mansfield, The bending and stretching of plates, 2nd ed., Cambridge University Press, 1989.

[133] EN 1288-5, Glass in building Coaxial double ring test on flat specimens with small test surface areas, CEN European Committee for Standardization, 2000.

[134] ASTM C1499-03, Standard Test Method for Monotonic Equibiaxial Flexural Strength of Advanced Ceramics at Ambient Temperature, ASTM International, 2009.

[135] EN 1288-3, Glass in building-Determination of the bending strength of glass- Part 3: Test with specimen supported at two points (four point bending), CEN European Committee for Standardization, 2008.

[136] S. Timoshenko, S. Woinowsky Krieger, Theory of plates and shells, 2nd ed., McGraw-Hill, 1987.

[137] EN 1288-1, Glass in building. Determination of the bending strength of glass; Part 1: Fundamentals of testing glass, CEN European Committee for Standardization, 2000.

[138] W. Adler, D. Mihora, Biaxial Flexure Testing: analysis and experimental results, Fracture Mechanics of Ceramics: Fracture Fundamentals, High-Temperature Deformation, Damage,

and Design, vol. vol.10, pp. 227–246, 1992.

[139] M. Overend, G. a. Parke, D. Buhagiar, Predicting Failure in Glass—A General Crack Growth Model, Journal of Structural Engineering, vol. 133, pp. 1146–1155, 2007.

[140] L. Blaumeiser, J. Schneider, Strength testing of thin glasses, Engineered Transparency Conference, pp. 459–468, 2016.

[141] BS EN 485-2:2013, Aluminium and aluminium alloys. Sheet, strip and plate. Mechanical properties, CEN European Committee for Standardization, 2013.

[142] BS EN 573-3:2013, Aluminium and aluminium alloys. Chemical composition and form of wrought products. Chemical composition and form of products, CEN European Committee for Standardization, 2013.

[143] C. Boller, T. Seeger, Materials Science Monographs: Materials data for cyclic loading, Part D: Aluminium and titanium alloys, Elsevier, 1987.

[144] G.D. Quinn, Fractography of Ceramics and Glasses, Office, U.S. Government Printing, Washington, 2007.

[145] J. C. Newman, I. S. Raju, Stress-intensity factor equations for cracks in three-dimensional finite bodies subjected to tension and bending loads, 1984.

[146] Y. Murakami, S. Nemat-Nasser, Growth and stability of interacting surface flaws of arbitrary shape, Engineering Fracture Mechanics, vol. 17, pp. 193–210, 1983.

[147] Y. Murakami, M. Ishida, Analysis of An Arbitrarily Shaped Surface Crack and Stress Field at Crack Front Near Surface, Trans. Jpn. Soc. Mech. Eng. A, vol. 51, pp. 1050–1056, 1985.

[148] P.D. Warren, Statistical determination of surface flaw distributions in brittle materials, Journal of the European Ceramic Society, vol. 15, pp. 385–394, 1995.

[149] M. Overend, The Appraisal of Structural Glass Assemblies, PhD Thesis, University of Surrey, 2002.

[150] M. Lindqvist, Structural Glass Strength Prediction Based on Edge Flaw Characterization, PhD thesis, École Polytechnique Fédérale de Lausanne (EPFL), 2013.

[151] B. Bergman, On the estimation of the Weibull modulus, Journal of Materials Science Letters, vol. 3, pp. 689–692, 1984.

[152] J. Sullivan, P. Lauzon, Experimental probability estimators for Weibull plots, Journal of Materials Science Letters, vol. 5, pp. 1245–1247, 1986.

[153] D. Stienstra, T. Anderson, L. Ringer, Statistical inferences on cleavage fracture-toughness data, Journal of Engineering Materials and Technology, vol. 112, pp. p.31-37, 1990.

[154] B. Bergman, Estimation of Weibull Parameters By Using a Weight Function, Journal of Material Science Letters, vol. 5, pp. 611–614, 1986.

[155] B. Faucher, W.R. Tyson, On the determination of Weibull parameters, Journal of Materials Science Letters, vol. 7, pp. 1199–1203, 1988.

[156] H.L. Lu, C.H. Chen, J.W. Wu, A note on weighted least-squares estimation of the shape parameter of the Weibull distribution, Quality and Reliability Engineering International, vol. 20, pp. 579–586, 2004.

[157] C.N. E. Barbero, J. Fernandez-Saez, On the estimation of percentiles of the Weibull distribution, Journal of Material Science Letters, vol. 18, pp. 1441–1443, 1999.

[158] D. Wu, J. Zhou, Y. Li, Methods for estimating Weibull parameters for brittle materials, Journal of Materials Science, vol. 41, pp. 5630–5638, 2006.

[159] M. Engelhardt, L.J. Bain, Simplified Statistical Procedures for the Weibull or Extreme-Value Distribution, Technometrics, vol. 19, pp. 323–331, 1977.

[160] M. Engelhardt, L. Bain, Some Complete and Censored Sampling Results for the Weibull or Extreme-Value Distribution, Technometrics, vol. 15, pp. 541–549, 1973.

[161] L. Bain, M. Engelhardt, Statistical Analysis of Reliability and Life-testing models; Theory and Methods, 2nd ed., Marcel Dekker, Inc, 1991.

[162] EN 12603, Glass in building — Procedures for goodness of fit and confidence intervals for Weibull distributed glass strength data, CEN European Committee for Standardization, 2002.

[163] ASTM C1239-13, Standard Practice for Reporting Uniaxial Strength Data and Estimating Weibull Distribution Parameters for Advanced Ceramics, ASTM International, pp. 1–17, 1993.

[164] DIN EN 843-5, Advanced technical ceramics - Mechanical properties of monolithic ceramics at room temperature - Part 5: Statistical analysis, Deutsches Institut Fur Normung, 2007.

[165] R.B. Abernethy, The New Weibull Handbook, 5th ed., Abernethy, Robert B., Florida, 2006.

[166] R. B. Abernethy, W. Fulton, New Methods for Weibull & Lognormal Analysis, ASME Paper No 92-WA/DE-14, 1992.

[167] R. Langlois, Estimation of Weibull parameters, Journal of Materials Science Letters, vol. 10, pp. 1049–1051, 1991.

[168] F.N. Nwobi, C.A. Ugomma, A Comparison of Methods for the Estimation of Weibull Distribution Parameters, Metodološki Zvezki - Advances in Methodology and Statistics, vol. 11, pp. 65–78, 2014.

[169] A. Khalili, K. Kromp, Statistical properties of Weibull estimators, Journal of Materials Science, vol. 26, pp. 6741–6752, 1991.

[170] I. Pobočíková, Z. Sedliačková, Methods for estimating the parameters of the Weibull distribution, Applied Mathematical Sciences, vol. 8, pp. 4137–4149, 2014.

[171] L. Makkonen, Problems in the extreme value analysis, Structural Safety, vol. 30, pp. 405–419, 2008.

[172] N.J. Cook, Rebuttal of " Problems in the extreme value analysis," Structural Safety, vol. 34, pp. 418–423, 2012.

[173] F.Q. Yuan, A. Barabadi, J.M. Lu, A.H.S. Garmabaki, Performance Evaluation for Maximum Likelihood and Moment Parameter Estimation Methods on Classical Two Weibull Distribution, pp. 802–806, 2015.

[174] H. Rinne, The Weibull Distribution: A Handbook, Chapman & Hall/CRC Press-Taylor & Francis Group, Giessen, Germany, 2009.

[175] GlasStress Ltd, Scattered Light Polariscope SCALP Instruction Manual, Version 5.5, 2013.

[176] M.H. Krohn, J.R. Hellmann, D.L. Shelleman, C.G. Pantano, G.E. Sakoske, F. Corporation, Biaxial Flexure Strength and Dynamic Fatigue of Soda – Lime – Silica Float Glass, Journal of the American Ceramic Society, vol. 85, pp. 1777–1782, 2002.

[177] MIL-PRF-13830B, Optical components for fire control instruments; General specification governing the manufacture, assembly and inspection of, U.S. Military Performance Specification, 1997.

[178] K.E. Cramer, M. Hayward, W.T. Yost, Quantification of residual stress from photonic signatures of fused silica, AIP Conference, vol. 1581 33, pp. 1679–1686, 2014.

[179] F. Veer, Y. Rodichev, Corrosion effects on soda lime glass, Challenging Glass 2 Conference, 2010.

[180] S. Jiang, D. Kececioglu, Graphical Representation of Two Mixed-Weibull Distributions, IEEE Transactions on Reliability, vol. 41, pp. 241–247, 1992.

[181] D.B. Kececioglu, W. Wang, Parameter Estimation For Mixed-Weibull Distribution, IEEE Annual RELIABILITY and MAINTAINABILITY Symposium, pp. 247–252, 1998.

[182] A. Karakoca, U. Erisoglu, M. Erisoglu, A comparison of the parameter estimation methods for bimodal mixture Weibull distribution with complete data, Journal of Applied Statistics, vol. 42, pp. 1472–1489, 2015.